PROCESSING OF ALUMIX 321 PM ALLOY AND ITS CORROSION BEHAVIOUR IN 3.5 WT% SALINE SOLUTION

by

Abdulwahab M. Ibrahim

Submitted in partial fulfilment of the requirements
for the degree of Doctor of Philosophy

at

Dalhousie University
Halifax, Nova Scotia
March 2013

DALHOUSIE UNIVERSITY

DEPARTMENT OF PROCESS ENGINEERING AND APPLIED SCIENCE

The undersigned hereby certify that they have read and recommend to the Faculty of Graduate Studies for acceptance a thesis entitled “PROCESSING OF ALUMIX 321 PM ALLOY AND ITS CORROSION BEHAVIOUR IN 3.5 WT% SALINE SOLUTION” by Abdulwahab M. Ibrahim in partial fulfilment of the requirements for the degree of Doctor of Philosophy.

Dated: March 11, 2013

External Examiner: _____

Research Co-Supervisors: _____

_____

Examining Committee: _____

_____

Departmental Representative: _____

DALHOUSIE UNIVERSITY

DATE: March 11, 2013

AUTHOR: Abdulwahab M. Ibrahim

TITLE: PROCESSING OF ALUMIX 321 PM ALLOY AND ITS CORROSION BEHAVIOUR IN 3.5 WT% SALINE SOLUTION

DEPARTMENT OR SCHOOL: Department of Process Engineering and Applied Science

DEGREE: PhD CONVOCATION: October YEAR: 2013

.....
Signature of Author

Dedication

I would like to dedicate this thesis to my parents, my wife, and my children. I would not be who I am today without their support.

LIST OF TABLES

LIST OF FIGURES

ABSTRACT

Aluminum powder metallurgy (PM) parts have found applications in automotive, aerospace and transportation. Sintered aluminum parts have been developed and compete with traditionally fabricated ingot metallurgy (IM) products for specific applications. To extend the range of application of (PM) alloys which offer the advantage of net and near net shape production, processing parameters and corrosion behaviour of the aluminum alloys need to be improved.

In this research, processing parameters and corrosion behaviour of a commercial Al-Mg-Si aluminum alloy (Alumix 321) were investigated. This alloy is the PM equivalent of wrought AA6061.

Four sintering temperatures (610 °C, 620 °C, 630 °C, 640 °C) and two pressing pressures (200 MPa, 400 MPa) were used and the optimum pressing and sintering procedure was selected. In addition to different processing routes of aluminum powder metallurgy alloys, a series of electrochemical experiments on both (IM) and (PM) aluminum alloy was performed with the aim of correlating corrosion behaviour with production techniques.

As a modification step, post sintering treatments and surface alteration techniques were applied. Hot rolling, hot swaging, repressing, resin impregnation and shot peening were performed and their effect on corrosion behaviour was investigated; their effect on density, hardness, and microstructure was also studied. Hardness after hot swaging and hot rolling increases and near full density was achieved (> 99%), while for resin impregnation and shot peening surface nature and roughness were affected, respectively. Electrochemical techniques such as open circuit potential (OCP), Tafel extrapolation (TE), cyclic polarization (CP) and stair step polarization (SP) were performed on the ingot, wrought, and post sintered alloys immersed in a 3.5 wt% NaCl solution. Electrochemical experiments show that corrosion current decreases as a result of post sintering treatments. The electrochemical experiments also show different corrosion mechanisms that were later confirmed by the metallographic analysis. The corrosion product and corroded surfaces of the alloys were characterized by optical microscopy, scanning microscopy (SEM), energy dispersive spectroscopy (EDS), wavelength dispersive spectroscopy (WDS), and X-ray diffraction (XRD). Results show that pitting is the main corrosion mechanism of the wrought alloy. However, powder metallurgy alloys show pitting, crevice, and intergranular corrosion.

LIST OF ABBREVIATIONS AND SYMBOLS USED

AES	Auger electron spectroscopy
APM	Aluminum powder metallurgy
ASTM	American society for testing and materials
AC	Alternating current
AA	Atomic adsorption spectroscopy
A	Area
CR	Corrosion rate
CE	Counter electrode
CIP	Cold isostatic pressing
CV	Cyclic voltametry
DB	Dog bone
DSC	Differential scanning microscopy
EW	Equivalent weight
E_{pit}	Pitting potential
EIS	Electrochemical impedance spectroscopy
EPMA	Electron probe micro analysis
EDXA	Energy dispersive x ray analysis
E_{app}	Applied potential
E_{corr}	Corrosion potential
E_{pro}	Protection poential
f	Frequency
FRA	Frequency response analyzer
HR	Rockwell hardness
IM	Ingot metallurgy
IGC	Intergranular corrosion
I	Current
i	Current density
i_{corr}	Corrosion current density
K	Kilo
LPS	Liquid phase sintering
LSV	Linear sweep voltammetry
L_f	Final length
L_i	Initial length
M_{air}	Weight of sample in air
M	Molarity
MAP	Mechanical alloying and processing
MPY	Mils penetration per year
M_{water}	Weight of sample in water
MRF	Materials research furnace

MEC	Mineral engineering centre
NDT	Non destructive testing
N	Normality
N	Number of electrons
OM	Optical microscopy
OAL	Overall length
OCP	Open circuit potential
PM	Powder metallurgy
RE	Reference electrode
RSP	Rapid solidification processing
SCC	Stress corrosion cracking
Sec	Second
SEM	Scanning electron microscope
SIMS	Secondary ion mass spectroscopy
SCE	Saturated calomel electrode
TRS	Transverse rupture strength
TGA	Thermal gravimetric analysis
TD	Theoretical density
t	Time
TEM	Transmition electron microscopy
T	Temperature
W_{oil}	Weight of bar impregnated in oil
$W_{oil\&water}$	Weight of oil impregnated bar immersed in water
WDXA	Wave length dispersive x ray analysis
WE	Working electrode
W%	Weight percent
XPS	X ray photo electron spectroscopy
Z	Impedance
Z′	Real impedance
Z″	Imaginary impedance
θ	Phase angle
ρ_{water}	Density of water
β	Tafel constant

ACKNOWLEDGEMENTS

I would like to acknowledge the guidance, advice and support of Dr. G.J. Kipouros throughout the whole project. I would like also to thank Dr. D. Paul Bishop for providing help and assistance and being a co supervisor in this research. The other supervisory committee members, Dr. G. Jarjoura and Dr. J. Li also contributed in the direction of the work. The author is grateful to the whole staff members of Materials Engineering Program, Department of Process Engineering and Applied Science. I would like also to thank the Minerals Engineering Center (MEC) at Dalhousie University. Thanks to technicians at Dalhousie University, Ms. Patricia Scallion, Mr. Ray Dube, and Mr. Dean Grijm for their assistance. Thanks also go to Natural Sciences and Engineering Research Council of Canada (NSERC). Lastly, I would like to acknowledge the assistance of Mr. Abulmaali Taher and the help of the Powder Metallurgy Lab at Dalhousie University, Winston Mosher, Ian MacAskill, Hung-Wei Liu and Randy Cooke.

CHAPTER 1 INTRODUCTION

1.1 ALUMINUM ALLOYS SYSTEMS

The addition of some elements to the pure metal improves the properties. For this reason, mechanical, chemical and physical properties of aluminum alloys are greatly enhanced by alloying pure aluminum with other elements. Copper, magnesium, manganese, zinc and silicon are the most common elements added to pure aluminum. The total amount of alloying elements added to the wrought alloys reaches up to 7 % (in mass percent) and up to 20 % silicon to cast alloys [1].

1.1.1 *WROUGHT ALUMINUM SYSTEMS*

The production of aluminum alloys starts with melting pure aluminum, alloying additions and certain amount of scrap. The second step is to convert the ingot into semi finished forms. Prior to fabrication, the aluminum ingots are homogenized at temperatures in the range of 450-600 °C. The purpose of the homogenization process is to reduce the effect of micro segregation and assist to remove low melting eutectic phases. The next step is to convert the ingot into semi finished product. This step involves hot working to achieve uniform and more homogenized structure. The ingot can be further processed by cold working [2] .

Aluminum wrought alloys are divided into two main groups, heat treatable alloys and non heat treatable alloys. The heat treatable alloys are 2xxx, 6xxx and 7xxx series. The non heat treatable alloys are 1xxx, 3xxx, 4xxx and 5xxx series.

For wrought aluminum and aluminum alloys, four-digit numerical designation system is used in which the first digit indicates the alloy group [3]. Table 1-1 shows the four digit designation system for aluminum and its alloys.

Table 1-1 Four-digit system for aluminum and its alloys [3]**.**

Aluminum alloy	Numerical designation system
Aluminum ≥99.00%	1XXX
Copper	2XXX
Manganese	3XXX
Silicon	4XXX
Magnesium	5XXX
Magnesium and Silicon	6XXX
Zinc	7XXX
Other elements	8XXX
Unused series	9XXX

1.1.2 *CAST ALUMINUM SYSTEMS*

In addition to light weight, some other advantages can be found in aluminum castings. Aluminum alloys have relatively low melting temperatures, good fluidity and cast ability. A wide range of cast aluminum alloys are produced and available for commercial use. Aluminum castings can be produced by sand casting; permanent mold and pressure die casting. Other novel techniques have been used; these processes include rheocasting and squeeze casting. The most widely used aluminum cast alloys are Al-Si, Al-Si-Mg and Al-Si-Cu. Similar to wrought aluminum alloys, some cast alloys respond to heat treatment in which the heat treatment process involves solution treatment, quenching and aging. For non heat treatable alloys, the strengthening mechanism is due to the presence of intermetallic compounds.

So far, there is no internationally accepted system for identifying aluminum castings alloys. However, a designation system has been introduced by the aluminum association of the United States. This system uses four digit numerical system to identify aluminum castings and foundry ingots. The first digit indicates the alloy group, the second two digits identify aluminum alloy and the last digit indicates the product form. Four digit designation system for aluminum alloys is shown in Table 1-2.

Table 1-2 Four digit system for cast aluminum and its alloys [2]**.**

Alloy	Current designation	Former designation
Aluminum, 99.00% or greater	1XX.X	
Aluminum alloys grouped by major alloying elements:		
Copper	2XX.X	1XX
Silicon with added copper and/or magnesium	3XX.X	3XX
Silicon	4XX.X	1 to 99
Magnesium	5XX.X	2XX
Zinc	7XX.X	6XX
Tin	8XX.X	7XX
Other elements	9XX.X	7XX
Unused series	6XX.X	

1.1.3 *POWDER METALLURGY SYSTEMS*

Parts produced by powder metallurgy (PM) technology have a distinctive combination of properties. The combination of the attractive properties of aluminum alloys along with the advantages of powder metallurgy PM process has gained much attention recently. In addition to light weight, strength and good corrosion resistance, aluminum alloys produced by PM technology have a net or near net shape, more fine and homogenous microstructure and high quality product. Production and the demand of aluminum PM alloys are gaining increased interest, specifically for automotive and aerospace industry.

Conventional aluminum powder metallurgy alloys consist of blends of aluminum powders mixed with lubricant and other various alloying elements. Table 1-3 shows the composition of some aluminum PM alloys.

Table 1-3 Composition of some aluminum PM alloys [1]**.**

Alloy Designation	*Composition*
201AB (conventional alloy)	Al-4.4Cu-0.8Si-0.5Mg-1.5 other
202AB (conventional alloy)	Al-4.0Cu-1.5other
601AB(conventional alloy)	Al-0.25Cu-0.6 Si-1.0Mg-1.5other
602AB (conventional alloy)	Al-0.6Mg-0.4Si-1.5other
7090 (advanced alloy)	Al-8.0Zn-2.5Mg-1.0Cu-1.5Co-0.35o
7091 (advanced alloy)	Al-6.5Zn-2.5Mg-1.5Cu-0.4Co
X7090 (advanced alloy)	Al-0.12Si-0.15Fe-(0.6-1.3)Cu-(2-3)Mg-(7.3-7)Zn-(0.2-0.6)Co
X7091 (advanced alloy)	Al-0.12Si-0.15Fe-(1.1-1.8)Cu-(1-3)Mg-(5.8-7.1)Zn(0.2-0.6)Co
X7093 (advanced alloy)	Al-9.0Zn-2.2Mg-1.5Cu-0.14Zr-0.1Ni
8009 (advanced alloy)	Al-8.5Fe-2.4Si-1.3V
X8019 (advanced alloy)	Al-8.3Fe-4.0Ce

The most common commercially available alloys are equivalent to wrought 6061 and 2014. The heat treatable 601AB alloy has excellent corrosion resistance with moderate strength while the aluminum copper alloy 201AB has a significant higher strength and good mechanical properties. Mechanical properties of some conventional PM aluminum alloys are given in Table 1-4.

Table 1-4 Mechanical properties of conventional PM aluminum alloys [1]

Alloy	Compacting Pressure (MPa)	Tensile strength (MPa)	Yield strength (MPa)	Elongation (%)	Hardness (HRE)
601AB-T6	96	183	176	1	70-75
	165	232	224	2	75-80
	345	238	230	2	80-85
602AB-T6	165	179	169	2	55-60
	345	186	172	3	65-70
201AB-T6	110	248	248	0	80-85
	180	323	322	0.5	85-90
	413	332	327	2	90-95
202AB Compacts-T6	180	227	147	7.3	45-50
202AB Cold-formed 19% T6	180	274	173	8.7	85

New aluminum alloys have been developed recently. These alloys have properties that meet the demand of aircraft forgings. Superior properties such as ductility, strength, fracture toughness and resistance to stress corrosion cracking (SCC) were achieved. The basis for this group of alloys is the technology of rapid solidification processing (RSP). The rapid solidification during atomization is used to produce very homogeneous microstructure and composition that cannot be achieved by ingot metallurgy (IM) technology. This technology is different than the conventional (PM) technology and the group of these alloys is called wrought (PM) alloys [1]. The use of RSP has lead to the development of high strength aluminum alloys based on 7000 series, Al-Li and aluminum alloys for service at higher temperatures [4]. Table 1-5 shows the mechanical

properties of some mechanical alloying and processing (MAP) and rapid solidified powder (RSP) aluminum alloys.

Table 1-5 Properties of some MAP and RSP aluminum alloys [1]

Material	0.2% Yield strength (Mpa)	Ultimate tensile strength (MPa)	Elongation %	Young's modulus (GPa)
MAP AA2014 as extruded **MAP AA2014-T6** **MAP 7010, at room temperature**	412	450 563 498	1.85	74.2
RSP 7090	595	637	10	
RSP X7090-T6E192	641	676	10	73.8
RSP X7091-T6E192	558	614	11	72.4

1.2 PROCESSING OF ALUMINUM POWDER METALLURGY ALLOYS

1.2.1 *POWDER PRODUCTION TECHNIQUES*

The first commercial aluminum powder was produced as flakes. Safety and efficiency were some of the concerns regarding using this technique. The production process of aluminum flakes was dangerous due to the possibility of explosive mixture formation between air and aluminum. Significant improvement in aluminum powder production has been achieved by the introduction of ball mill and atomization [5].

Atomization by far is the most widely used technique to produce aluminum powder [6]. The process of atomization involves spraying of molten aluminum metal through a nozzle. One end of the nozzle is attached to the molten aluminum and the other end terminates in a small orifice, the very fine metal droplets are cooled very fast by gas or liquid. A cooling rate of 10^3 to 10^6 $Ksec^{-1}$ is obtained. Greater cooling rates were achieved by using splat cooling process, in which, the molten metal is sprayed or

dropped over a high thermal conductivity chilled surface. Figure 1-1 shows the schematic diagram of the powder atomization process.

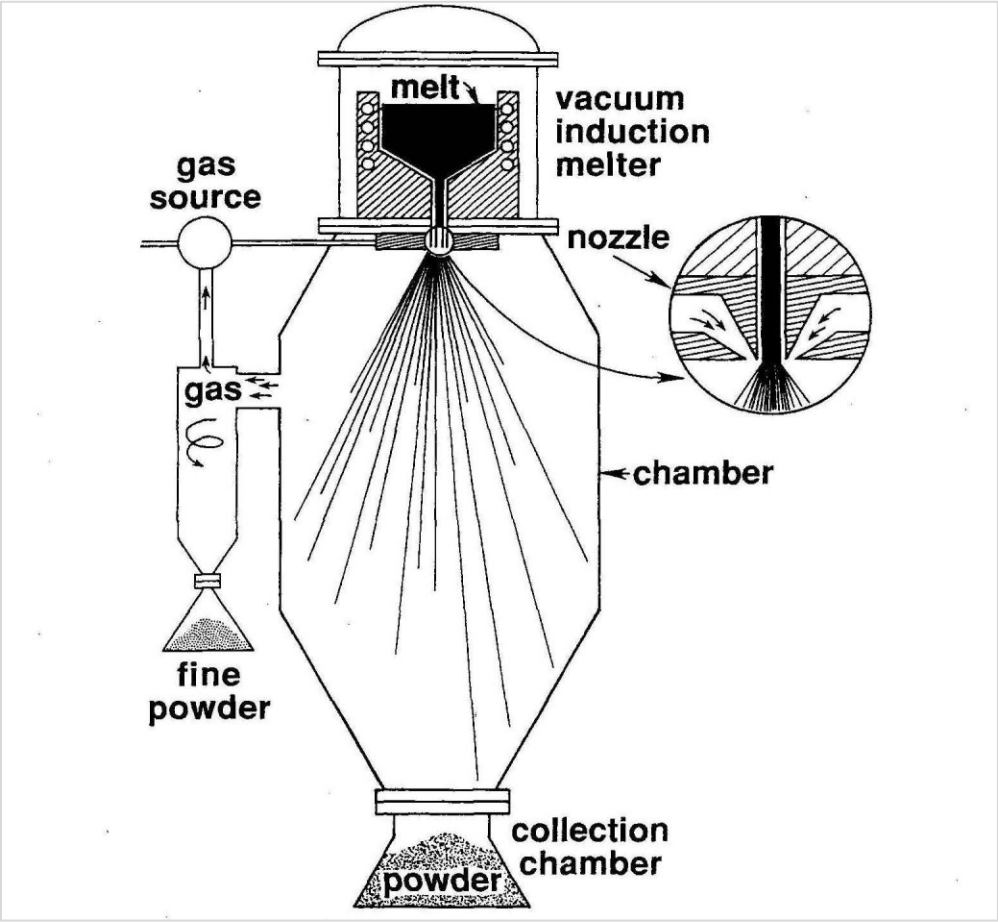

Figure 1-1 Schematic diagram of gas atomization process [7]**.**

1.2.2 *POWDER COMPACTION*

The goal of compaction is to compress the powder to produce the so-called green compact. Comparing to some other metals, aluminum is compacted at lower pressure. In addition to simple compaction process, complex parts with very fine details can be produced from aluminum powders as powder is easily flowing in the compression die. This response of aluminum powder is attributed to the easy flow of the powder in the compression die.

Die compaction is the highest production rate compaction method. This method of compaction involves applying a high uni-axial force along one axis of the die. The first step is to load the powder in a die cavity. After filling the die, either single action or double action can be applied. In single action, only the upper punch moves while in double action both the upper and lower punches move to press and compact the powder. At the end of the pressing step, the upper punch is removed and the lower punch is used to eject the piece. The die set up and the sequence of powder compaction cycle is shown in Figure 1.2 and Figure 1.3, respectively.

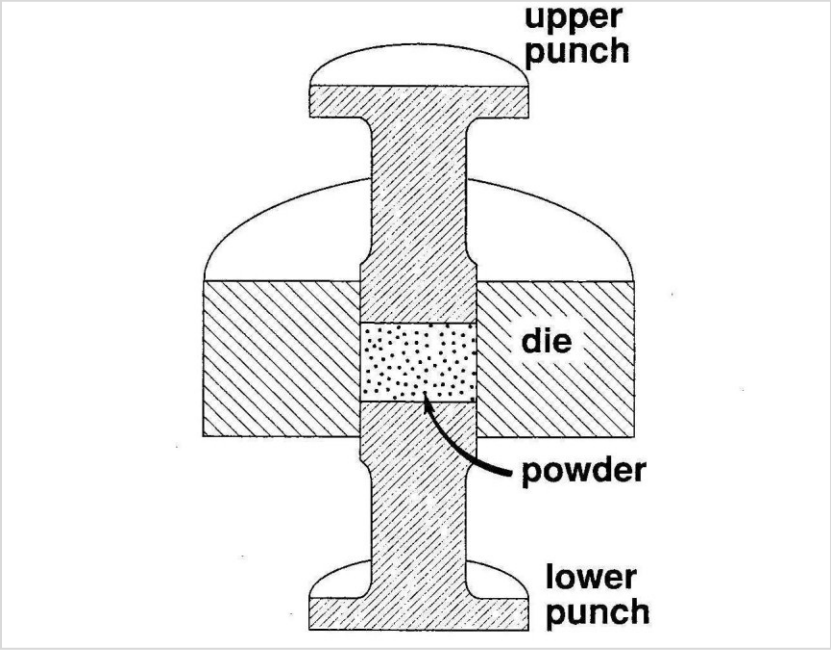

Figure 1-2 Punch and die set for powder compaction [8]**.**

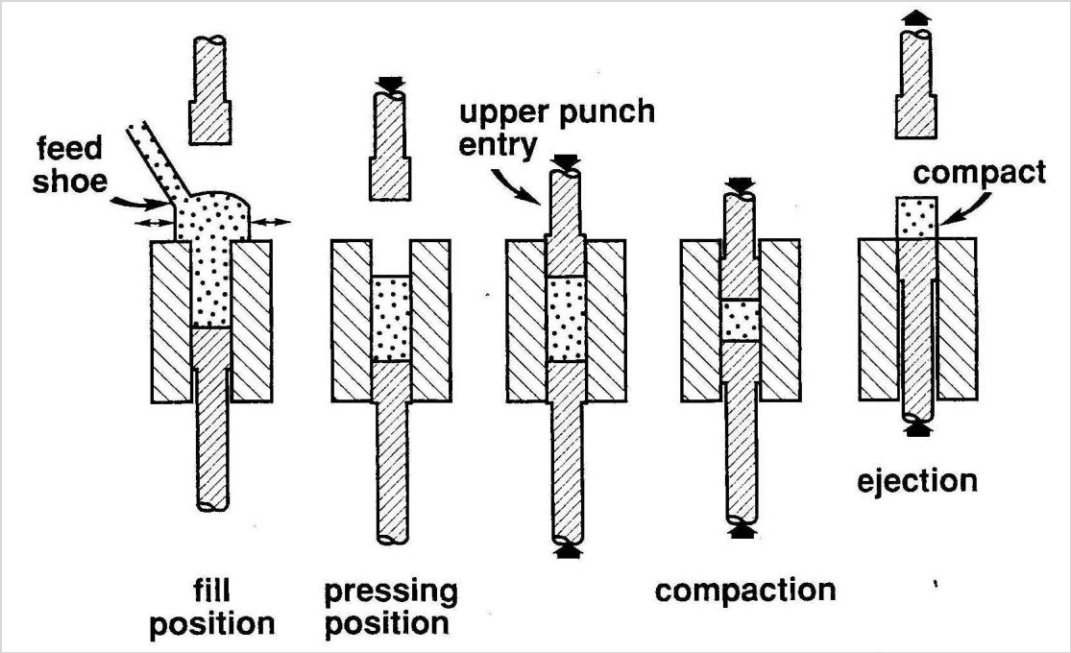

Figure 1-3 Double action compaction cycle [8]**.**

1.2.3 *SINTERING*

Sintering is defined by Kang as a processing technique to produce controlled density materials from metal or ceramic powders by applying thermal energy [9]. Basically, sintering can be categorized into two main types: solid state sintering and liquid phase sintering (LPS). Solid state sintering process occurs when the green compact is densified in a solid state, while liquid phase sintering occurs in presence or formation of a liquid phase in the powder compact. In addition to the two previous main sintering techniques, other types of sintering techniques can be utilized, for example, transient liquid and viscous flow sintering. Generally, most sintering is performed without applying an external pressure. For materials which are not suitable to traditional sintering techniques, pressure assisted sintering techniques can be utilized.

Solid phase sintering has gained the greatest consideration from the theoretical point view. This technique is applicable to pure substances such as nickel and copper. On the other hand and due to the cost and productivity advantages, the greatest level of

industrial sintering is performed using the liquid sintering technique. More than 70% of the sintered products are processed by liquid phase sintering technique [9].

Figure 1-4 shows the two sphere sintering model. This model has been proposed to explain the development of the interparticle bond during sintering. As the sintering process progress, bonds between particles will emerge and enlarge. The proceeding of sintering process will cause the two particles to coalesce into a single sphere. Generally, the process can be divided into three stages although it is difficult to distinguish between these stages. During the initial stage of sintering, a rapid growth of interparticle neck takes place. This stage is characterized by a small neck size ratio and small shrinkage. In the intermediate stage, pore becomes smoother and cylindrical nature develops. This stage is characterized by grain growth in which grain size becomes larger than the initial particle size. In the final stage of sintering, pores become closed and spherical, and grain growth is visible and clear.

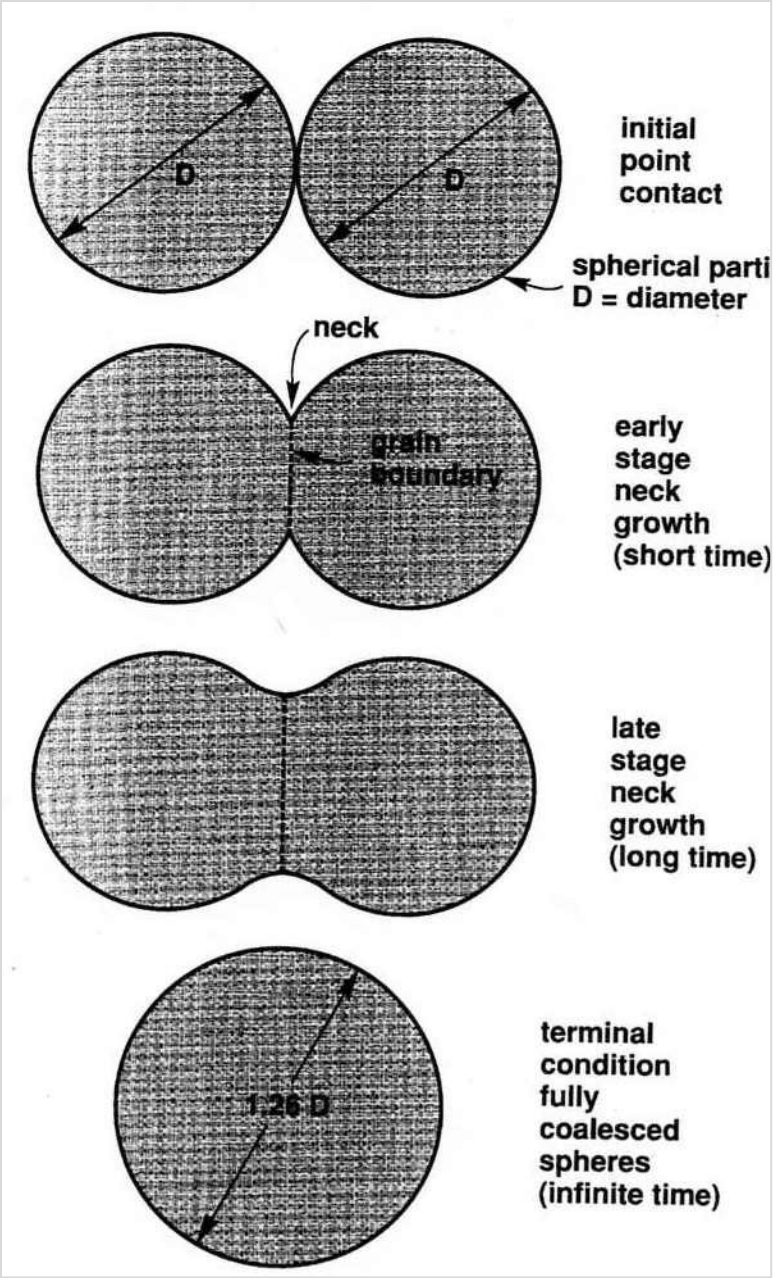

Figure 1-4 Two sphere sintering model[8]**.**

Compared to solid state sintering, the LPS densification rate is much higher since the liquid provides fast transport and therefore rapid sintering under certain conditions. Stages of LPS are shown in Figure 1-5.

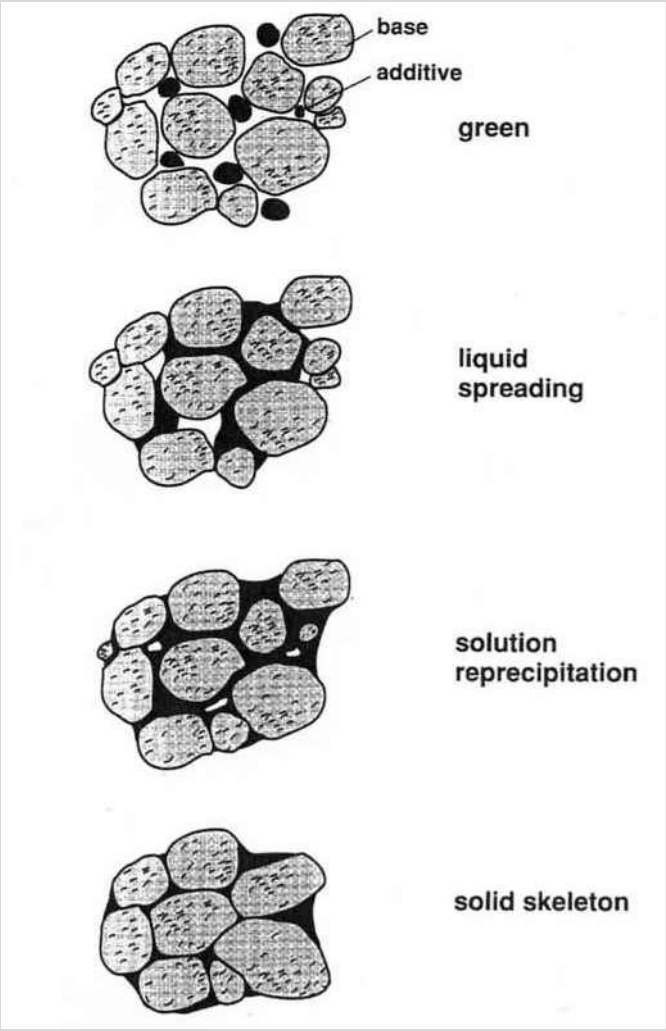

Figure 1-5 Stages of LPS using a mixture of two powders [7]**.**

Mixed powders are heated to a liquid formation temperature. During heating, solid state sintering takes place as well and driven by concentration gradient. Subsequent densification will be affected by the amount of liquid phase formed. After the liquid forms, three densification stages are encountered: rearrangement, solution reprecipitation and final stage sintering. Due to the capillary forces exerted by the liquid on the solid particles, densification takes place and the grains dissolve into the liquid. In the rearrangement stage, the compact will show a viscous response to the capillary action. This will result in a reduction of the densification rate and full density is possible by rearrangement if enough liquid is formed. As the densification process slows,

solubility and diffusion effects become dominant and this stage is termed as solution-reprecipitation. In the final stage, the sintering is controlled by densification in the solid structure. Densification process is slow due to the rigidity of contacting solid grains. Microstructural coarsening continues and remaining pores enlarge if they contain entrapped gas, resulting in compact swelling. Generally, prolonged final stage sintering degrades the properties of the most persistent liquid- phase sintered materials. Hence, practically, short sintering times are preferred.

Aluminum powder metallurgy (APM) parts can be sintered under various environments. Argon, vacuum, hydrogen, nitrogen and dissociated alumina have been used. APM parts sintered under nitrogen show better mechanical properties and hence, nitrogen is the preferred choice for aluminum sintering. Many researchers have agreed that the best way to get a successful sintering is to perform LPS. Better densification and performance of APM parts have been proven by using LPS. Sinter ability of APM preforms can also be enhanced by adding other alloying elements. Elements such as Sn, Pb, Bi, Sb have significantly improved the sintering. The best performance has been achieved by using magnesium. Aluminum sintering is difficult because of the presence of the oxide/hydroxide surface layer which prevents the powder particles to make contact. Magnesium reacts with aluminum oxide and forms a spinel phase ($MgAl_2O_4$) which breaks up the oxide layer and improve sinterability [10] [11] [12].

1.3 SURFACE ALTERATION PROCESSING OF POWDER METALLURGY ALLOYS

1.3.1 *ROLLING*

Powder rolling is the process in which a metal powder is compacted by rolling mills. In this technique, the metal powders are fed to a set of compaction rolls to produce a green compact. Further steps such as sintering or rerolling applied to produce a final product. Parts produced by this technique have uniform and reliable properties and many materials can be produced by this method. Examples of these products are nickel-iron strips, high purity nickel and nickel-iron-cobalt alloy.

Rolling can be applied for a green compact. The powder is first consolidated to a near theoretical density and the work piece is then subjected to rolling. Alloys processed by this technique include high strength aluminum alloys, high speed tool steels and super alloys.

1.3.2 *FORGING*

PM forging has been examined and tested as an alternative to the classical wrought forging alloys. PM forging offers many advantages over the conventional IM forgings. These advantages include final shape, fewer steps, less scrap and less manipulation. In this process, the processing sequence starts by the production of a preform with compaction and sintering to achieve a near theoretical density. The preforms then are subjected to forging in order to get a near net shape having almost the theoretical density. Figure 1-6 shows the process of preform forging. The process involves pore collapse as the forging progresses.

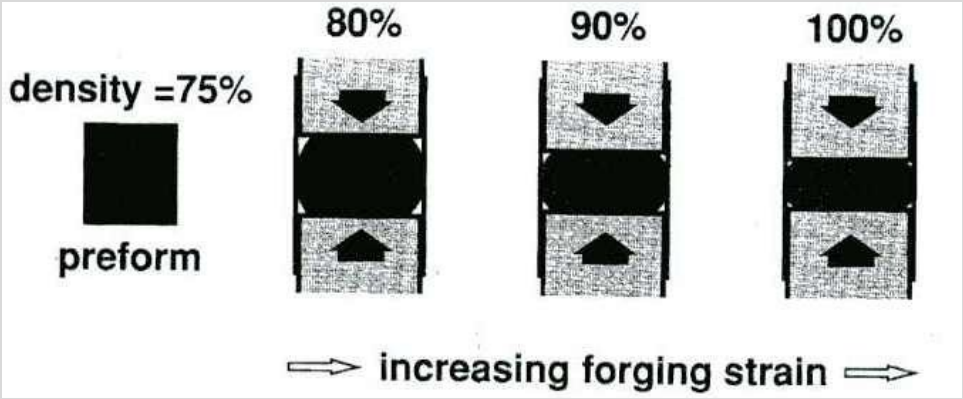

Figure 1-6 Powder forging process [8]**.**

In order to obtain a good part performance, some practical parameters need to be controlled. Firstly, die design and machining. In terms of final dimensions of the forged part, having a good die design of the forged part is very important. Advantages such as less cost and better dimensional tolerance are directly related to the die design step. Despite its difficulty, it is necessary to control the amount of the material in the die. Inaccurate calculation of the metal amount leads to die filling problems and flash presence complexity.

Powder forging is used to produce forgings from aluminum powders. A closed die forging technique was used to forge a rapid solidified 8009 Aluminum powder alloy. Superior properties have been obtained. Specifically, creep rupture behaviour of the forged parts was even better than the general aluminum alloys. Parts such as valve bodies, impellers and pistons were effectively forged from Al-Fe-V-Si PM alloy. Other forged parts were used in aerospace industry. Flap track and inboard main landing wheels were forged successfully from Al-Li alloys known as 644B and 622B [13][14] [15].

1.3.3 *EXTRUSION*

Extrusion is used to produce rods, tubes and honeycombs products from metal powder. Figure 1-7 shows a schematic diagram of the extrusion process. By this process dense products of various advanced materials such as refractory metals, composite and high temperature alloys are produced. Hot extrusion is used to produce fully dense billets

from tool steel powders. The extrusion technique can also be used for pre-compacted parts made of high speed steel. In this process, high speed steel is first compacted, sintered and then extruded. The compacted billet is then heated under a protective atmosphere and then extruded to the final shape [15].

Aluminum powder alloys are also suitable for extrusion. Prior to consolidation, the powder need to be degassed and adsorbed gases on the powder surface must be removed in order to produce a sound billet. After degassing, the surface temperature of the component is raised to the level that promotes sintering and then extruded.

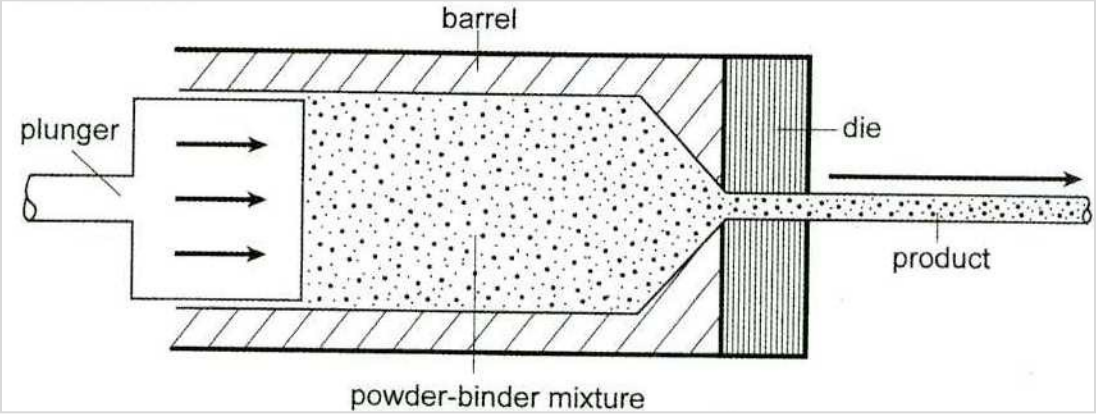

Figure 1-7 A schematic drawing of powder extrusion equipment set up [8]**.**

1.3.4 *REPRESSING*

The ASTM standard 243-10 defines repressing as “applying pressure to a previously pressed and sintered or presintered compact”. According to this standard, repressing includes restrike, coining and sizing [16]. Under certain conditions and requirements, post sintering sometimes is needed. Repressing or sizing is applied for two main functions, to improve the dimensional stability and to close off the subsurface porosity. The process involves applying a pressure that leads to a certain amount of strain. In addition to densifying the part, repressing can remove the distortion of heat treated or sintered parts. The process of repressing improves the uniformity of the sintered parts

dimensions. Figure 1-8 shows the effect of repressing on narrowing the size distribution of sintered components.

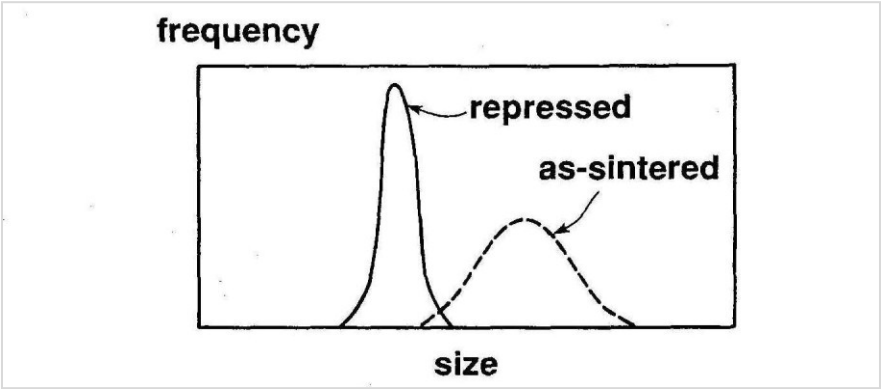

Figure 1-8 The effect of repressing on the size and uniformity[8]**.**

1.3.5 *SHOT PEENING*

One of the techniques used to improve fatigue life of components made from IM alloys is by shot peening. In this process, very small diameter metallic, glass or ceramic shots generate a compressive residual stress. Figure 1-9 represents a schematic sketch that shows the working theory of shot peening. As a result of bombarding the surface with the shots and in addition to the compressive layer, a densified layer is formed on the peened surface. The application of this technique has been extended to cover sintered PM parts. Appreciable fatigue strength improvement of shot peened sintered parts has been proven. An increase of 40 percent fatigue strength is obtained by shot peening 1.5 wt % carbon PM steel [7].

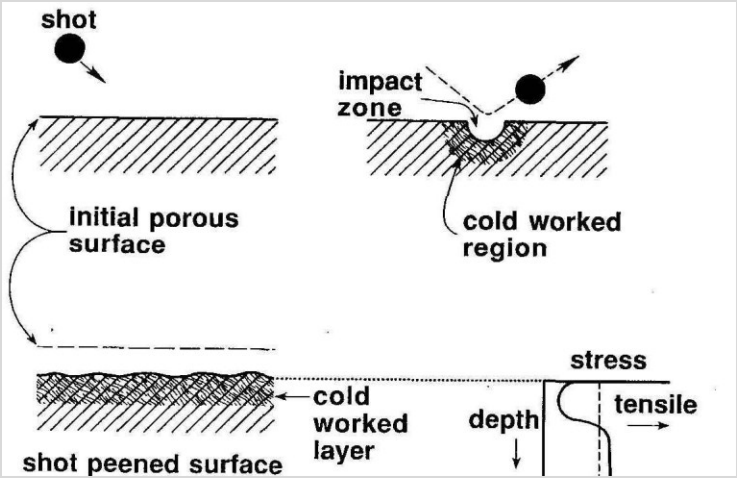

Figure 1-9 Schematic of shot peening technique [7]**.**

Pitting susceptibility of shot peened Al-Zn 7075-T651 was studied. The results show that there was a dramatic decrease in the number of surface pitting after shot peening treatment. Additionally, the fatigue stress limit of shot peened samples was increased [17]. Shot peening has been used to improve the fatigue properties of sintered aluminum parts. Increment of 10-15 percent in fatigue strength is achieved after shot peening of Alumix 431[18] .

1.3.6 *RESIN IMPREGNATION*

Resin impregnation can be defined as a process used to reduce and close the internal porosity of PM alloys by filling those pores with liquid resin. Resin impregnation has been used to enhance corrosion resistance, improve machinability and as a pretreatment before coating. Several types of resins have been used, the most common types being sodium silicate, low viscosity heat curable resins, low viscosity anaerobic resin and polyester resins [19].

The main techniques used for resin impregnation are; wet vacuum, dry vacuum pressure, wet vacuum pressure and pressure injection. In all these techniques, cleaning pretreatment is very important for better results. After curing, properties such as, adhesive strength, shrinkage on polymerization, temperature and chemical resistance are very important for better performance.

1.4 BACKGROUND ON CORROSION

1.4.1 *FORMS OF CORROSION*

Bruce Criage and Steven Pohlman defined six forms of corrosion. These forms include, uniform corrosion, metallurgical influenced corrosion, localized corrosion, mechanically assisted degradation and microbiologically influenced corrosion [20]. Based on the appearance, Fontana defined eight forms of corrosion. These eight groups can be categorized into two main categories: Intrinsic and extrinsic. Intrinsic mode can be defined as the mode of corrosion which is independent of design. In the extrinsic mode, the corrosion mode depends on the design.

The eight forms of corrosion can be identified as follow:

Uniform corrosion

Galvanic corrosion

Pitting corrosion

Intergranular corrosion

Stress corrosion cracking

Crevice corrosion

Erosion corrosion

Dealloying

1.4.2 *UNIFORM CORROSION*

Uniform corrosion is known also as general corrosion. This type of corrosion is characterized by a general attack and great loss of material. However, this type of corrosion can be predicted and catastrophic failures can be prevented. Generally, all metals are susceptible to uniform corrosion. The passive metals such as aluminum and stainless steel suffer other types of corrosion such as pitting. In addition to the well known atmospheric corrosion, other examples of uniform corrosion can be identified. These cases include rusting of steel, green patina on copper and silver tarnishing. Figure 1-10 shows the schematic diagram of the uniform corrosion.

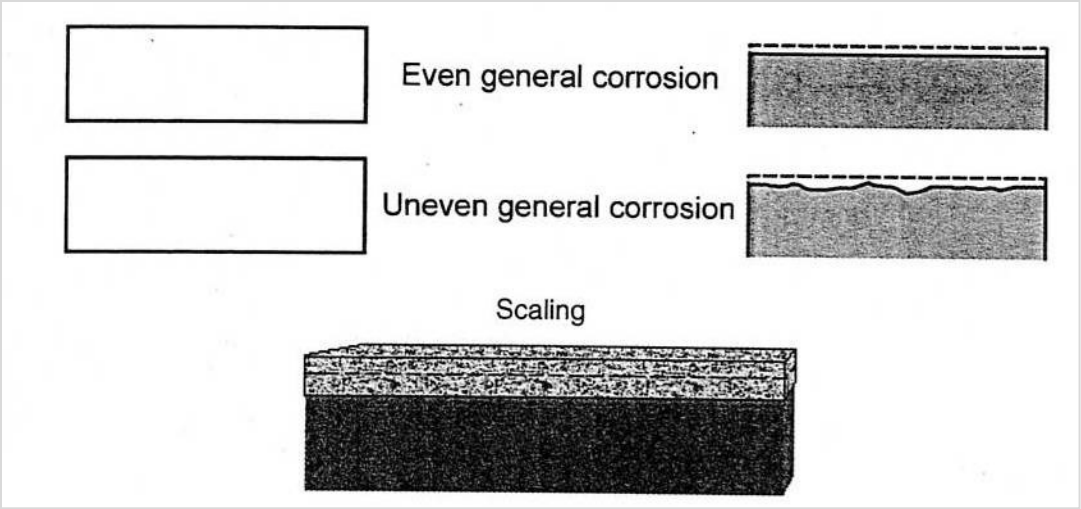

Figure 1-10 Uniform corrosion [20]**.**

1.4.3 *GALVANIC CORROSION*

This form of corrosion is also known as dissimilar or bimetallic corrosion. It happens when two metals with different potential are in contact with each other. When two dissimilar metals with different potential are in contact, the metal with the most negative and less noble potential will act as anode while the metal with the more positive potential will be the cathode.

Figure 1.11 shows a schematic presentation of galvanic corrosion of mild steel coupled to copper. From the design point of view, junctions between dissimilar metals are not recommended; instead, alloys with close values of potential can be used. In addition to the difference in electrochemical potential other factors that may lead to galvanic corrosion are difference in mechanical deformation, heat treatment, welding and microstructure.

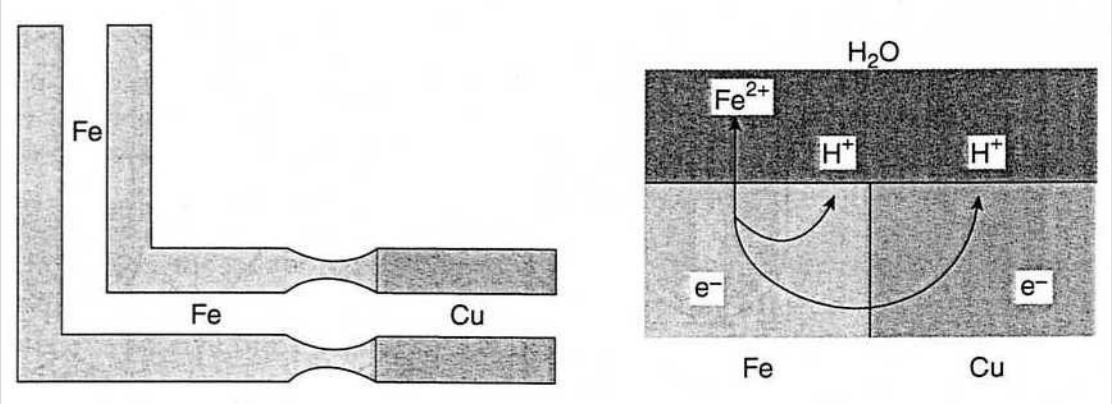

Figure 1-11 A schematic presentation of galvanic corrosion of steel coupled to copper[20]**.**

1.4.4 *PITTING CORROSION*

Pitting is an extreme form of localized attack. Most of engineering metals and alloys are susceptible to pitting corrosion. Pits initiate at some preferred sites. These sites include; localized rupture of the oxide film, local inhomogeneity and local loss of passivity. For those of passive alloys such as stainless steel and nickel chromium alloys, the local breakdown of the passive layer is the main cause of pitting. This breakdown happens at some preferred sites, these sites include scratches, impurities or any discontinuity in the passive film. Figure 1.12 shows different pits geometry.

The mechanism of pitting is self initiating and propagating. Directly, after pits have formed at those preferred sites, the sites behave anodically and become unstable. Dissolution takes place at those sites and the local environment becomes very corrosive.

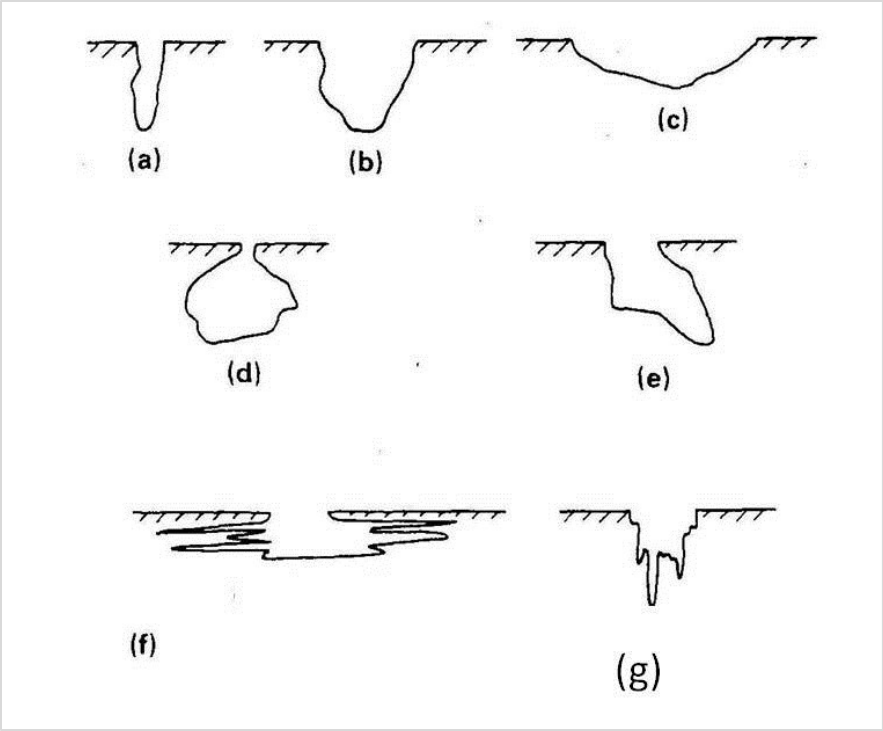

Figure 1-12 Different pits geometry. (a) Narrow and deep. (b) Elliptical. (c) Wild and shallow. (d) Subsurface. (e) Undercutting. (f) Horizontal. (g) Vertical. [21]**.**

1.4.5 *INTERGRANULAR CORROSION*

Intergranular corrosion cracking (IGC) is defined as a preferential attack of grain boundaries, or areas adjacent to grain boundaries. The grain boundary is a preferred place for impurities, precipitates and intermetallic compounds. This localized dissolution is attributed to the potential difference between these phases and the grain boundaries. Intergranular attack becomes very serious in the presence of composition dissimilarities. For example, austenitic stainless steel is well known for its tendency to IGC, the cause of the attack is being attributed to the presence of a chromium rich phase which precipitates along the grain boundaries. These precipitates are surrounded by a chromium depleted zone. In the presence of a corrosive environment, the depleted zones are more rapidly attacked relative to its adjacent areas.

In addition to stainless steel, copper, magnesium, and aluminum alloys are susceptible to Intergranular corrosion. Difference in potential between the grain boundaries and the

surrounded area is the main cause of Intergranular corrosion. Some aluminum systems such as, 2XXX, 5XXX, 7XXX are prone to IGC, other alloys such as 6XXX are generally resist such kind of attack. Other alloys such as, 1XXX, 3XXX are invulnerable to intergranular corrosion.

1.4.6 *STRESS CORROSION CRACKING (SCC)*

For a material to be susceptible to stress corrosion cracking, certain conditions must be met simultaneously. These conditions are: susceptibility of the material to SCC, crack promoting environment and tensile stress that should be higher than a certain threshold value. In addition to applied stress, even residual stress causes stress corrosion cracking. Stresses introduced by cold work, thermal treatments and welding are some sources of residual stress that may cause failure due to SCC. Two factors have a great affect on the susceptibility of the material to SCC. The first factor is the microstructure and the formation of second phases along the grain boundaries both being the sources of failure due to SCC. High strength aluminum alloys belong to 7XXX series found to suffer from SCC in T6 heat treatment condition. Performing overaging treatment was found to reduce the susceptibility of these alloys to SCC. The second factor is the chemical composition and distribution of second phases and impurities.

1.4.7 *CREVICE CORROSION*

Crevice corrosion is due to formation of a corrosion cell between the electrolyte within the crevice and the electrolyte outside the crevice. Oxygen inside the crevices is starved while the electrolyte outside is rich in oxygen. As a result, the material within the crevice will behave as the anode while the exterior part which is more aerated will act as a cathode.

Crevice corrosion takes place at narrow openings or gaps. Gaskets, flanges and O-rings are preferred places for crevice corrosion as well as threaded joints, lap joints and bolt holes which are introduced by design. Figure 1.13 shows the schematic of the mechanism of crevice corrosion. In the first stage, oxygen has been depleted within the crevice. The metal will dissolve according to the equation (1-1).

$$M \rightarrow M^{n+} + ne^{-} \quad (1\text{-}1)$$

This reaction happens inside the crevice and balanced by the cathodic reaction (1-2)

$$O_2 + 2H_2O + 4e^{-} \rightarrow 4OH^{-} \quad (1\text{-}2)$$

Metal ions will concentrate inside the crevice due to the oxidation reaction. Electrons produced from the oxidation are conducted through the metal to the external surface, where they are consumed by reduction reaction. In many aqueous environments, high concentration of Cl^- and H^+ were found to be developed inside crevices and lead to a very corrosive situation.

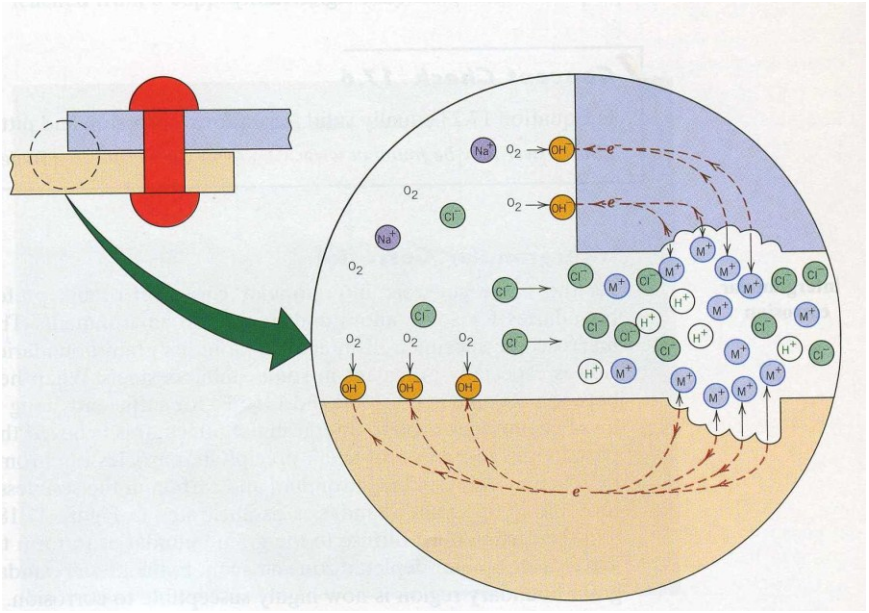

Figure 1-13 A schematic illustration of crevice corrosion mechanism[22]**.**

1.4.8 *EROSION CORROSION*

Erosion corrosion can be defined as a combination of mechanical wear or abrasive with corrosion. Combination of wear and corrosion results in a very severe attack than it would be realized with mechanical or chemical corrosive action alone. Erosion corrosion media include aqueous solution, gases and liquid metals. Alloys that depend on the protective film for corrosion resistance are most susceptible to erosion corrosion. For

example, the combination of hot gases and high fluid velocity blow off the metal protective corrosion product film. Eventually, the fresh alloy will be exposed to the corrosive media leading to erosion corrosion acceleration. Many factors affect the erosion corrosion behaviour. Fluid nature, velocity and the presence of suspended particles or bubbles may have a dramatic effect on the severity of erosion corrosion.

1.4.9 *DEALLOYING*

Dealloying is also known as a selective leaching or parting corrosion. It commonly occurs in solid solutions in which one element is selectively removed from the alloy as a consequence of corrosion. The mechanism of dealloying involves one of the following processes: selective dissolution of an anodic constituent or alloy dissolution and replating of the more cathodic element. The most common examples of dealloying are densification, and graphitic corrosion. In densification of brass, zinc is selectively removed from the alloy. This selected attack produces a weak and porous layer of copper and copper oxide. Under certain circumstances, the process continues and dealloying penetrates the metal structure and allows liquids or gases to pass through the porous remaining structure. Certainly, the formation of a porous mass of copper remains and impairs the mechanical properties of the alloy significantly.

Graphitic corrosion is another form of dealloying. It is a selective leaching of iron from gray cast iron, leaving a porous graphite network. The cathodic nature of the graphite with respect to iron is the reason behind this selective attack [21].

1.5 TRADITIONAL MONITORING AND CORROSION MEASUREMENT TECHNIQUES

1.5.1 *VISUAL EXAMINATION*

The simplest way to detect and monitor corrosion is by visual observation. In addition to corrosion evidence observation, this technique can be used to detect surface flaws, surface discontinuities and other joints discontinuities. Visual examination is normally conducted with microscopes. With the aid of borescopes, difficult to access parts can be monitored and detected. Borescopes can be used to inspect pipelines, tanks, inside walls and any difficult to reach regions. One of the main drawbacks of this technique is the human error. Moreover, it is considered as a qualitative method of analysis.

1.5.2 *GAIN AND LOSS IN WEIGHT METHODS*

Weight loss tests are considered as the most common of all types of corrosion testing. The emphasis is to use coupon specimens to measure the uniform corrosion. However, localized corrosion can be determined by using different samples and different evaluation techniques. Coupons are prepared from a sheet or plate, cleaned and then are subjected to uniform exposure to the environment. Figure 1-14 shows an immersion test set up. This setup has the facility to control the temperature, aeration, and reflux of vapor to reduce the effect of boiling and evaporation. Clean coupons are measured, weighted and then exposed to the corrosive environment for a certain time. The corrosion product then is cleaned off and the coupon is weighted again to determine the weight loss.

The corrosion rate from weight loss test can be calculated from equation (1-3).

$$CR = \frac{KW}{Atd} \qquad (1\text{-}3)$$

Where:

CR= corrosion rate.

K=constant, depending on the units.

W=weight lost in g.

A=area in cm^2.

t=exposure time in hours.

d=density in g/cm^3.

The corrosion rate in mils penetration per year (MPY) is the most widely used corrosion rate unit in the United States, and can be calculated from equation (1-4):

$$MPY = 534\frac{W}{Adt} \quad (1\text{-}4)$$

Where:

W=weight loss in mg

d=density in g/cm^3

A=specimen area in in^2

t=exposure time in h

Weight gain and lost corrosion experiments may be conducted in field or in laboratory. Laboratory tests are less expensive and easy to conduct. Because of the long time needed to conduct these experiments, accelerating factors such as temperature can be used. Despite the large number of samples needed, one of the main disadvantages is the lack of information about the mechanism of the corrosion process and the difficulty to distinguish between different types of corrosion.

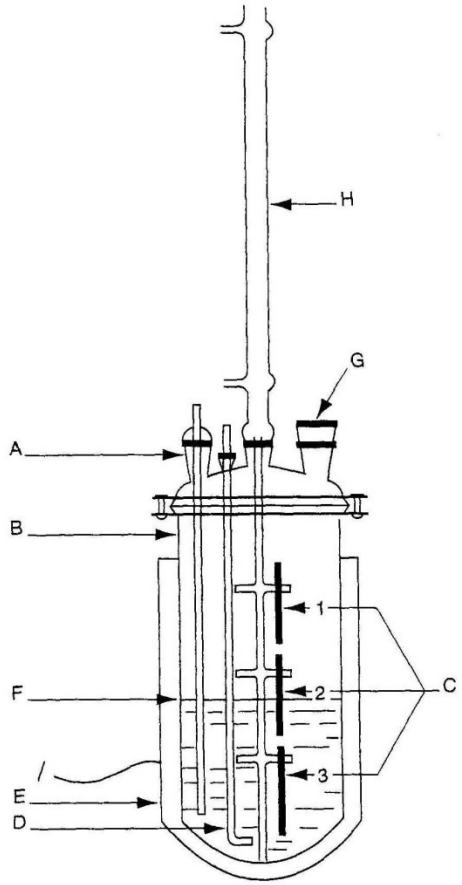

Figure 1-14 Immersion test setup, A, Thermocouple; B, resin flask; C, suspended specimens, D, gas bubbler; E, heating mantle; F, liquid surface; g, extra entry; H, reflux condenser[23]**.**

1.5.3 *ELECTRICAL RESISTIVITY CHANGE*

This method is based on the idea that the change of the area leads to the electrical resistance change which for any conductor is given by equation (1-5):

$$R = \rho \frac{L}{A} \qquad (1\text{-}5)$$

Were:

ρ = the resistivity

L = the length

A = cross sectional area

As the corrosion process proceeds, the area will be reduced and as a result R increases. This idea has been used to design electrical resistance probes. The wire sensing element can be used to detect and monitor corrosion rate. Electrical resistances probes shown in Figure 1-15 are flexible, easily installed and small. The main drawback is that only uniform corrosion can be measured.

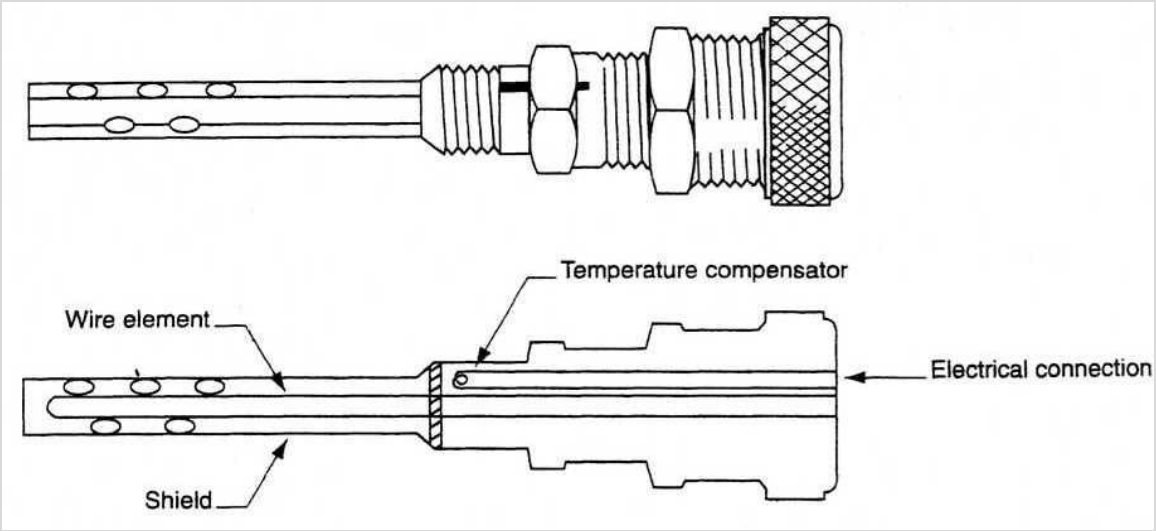

Figure 1-15 Electrical resistance probe for corrosion monitoring [23]**.**

1.5.4 *NONDESTRUCTIVE TESTING*

Many nondestructive testing techniques (NDT) can be used for corrosion detection. These techniques are quite helpful for detecting corrosion even at its early stages. Since some types of corrosion are visible to the unaided eye, for example, pits and rust are readily visible and relatively easy to detect. Visual inspection, magnetic particles, eddy current and dye-penetrant are commonly used for corrosion detection. However, each technique has some limitations and should be used under some precautions. Some techniques depend on measuring the corrosion product thickness and or the reduced thickness of the corroded part. These techniques involve ultrasonic, eddy current and X-ray radiography. NDT techniques can be used in field or in laboratory; the main drawback of these techniques is the difficulty to get quantitative evaluation of the corrosion process data.

1.5.5 *CHEMICAL ANALYSIS METHODS*

Chemical analysis techniques can be used to analyze corroded surfaces. These techniques are very efficient in terms of qualitative and quantitative analyses. Additionally, analyzing the corrosion product is very important to predict and understand the corrosion mechanism. Different analytical techniques and equipment have been used to offer and provide very valuable information about the composition of surface constituents.

Energy dispersive X ray spectroscopy (EDS) and wave length dispersive X ray spectroscopy (WDS) are used as accessories to the scanning electron microscopes (SEM) to offer simultaneous viewing and chemical analysis of the corroded samples. Other techniques are quite useful to detect the elements in extremely thin surfaces; Auger electron microscopy (AES), secondary ion mass spectroscopy (SIMS) and x- ray photo electron spectroscopy (XPS) are among those techniques.

Despite the simplicity and the large number of coupons used in non accelerating corrosion testing, some major disadvantages exist. The main disadvantage is that this type of testing is not used for real time monitoring, and gives only an average corrosion rate. Data from these tests do not provide information concerning the nature and the mechanisms of corrosion resistance. In using non accelerating corrosion tests developed for wrought alloys, difficulties arise when it is used for PM alloys. For example, weight loss measurements for wrought alloys are straight forward and easy to apply, while for PM alloys are more difficult in which test solution and corrosion product may trap inside the pores, making more difficult to record weight losses. Also, the surface area of PM parts is much larger than the nominal exterior surface area.

1.6 ELECTROCHEMICAL TECHNIQUES FOR MONITORING AND MEASURING CORROSION

1.6.1 *OPEN CIRCUIT POTENTIAL*

One of the important corrosion measurements is the determination of corrosion potential of the corroded metal. This potential normally called open circuit potential (OCP). J.R. Davis defines open circuit potential as the potential of an electrode measured with respect to a reference electrode or another electrode when no current flows to or from it [21]. Potential–time relationships have been frequently used to study and monitor the corrosion phenomena. Variation of corrosion potential as a function of time used to study film formation and film breakdown. It is worth noting that the corrosion potential measured from OCP can be different from that measured based on Tafel slopes, the difference depending on the immersion time and the conditions of metal solution interface.

1.6.2 *TAFEL EXTRAPOLATION*

In Tafel region, the relationship between applied potential and current density (*i*) can be given by the following relation:

$$E_{app} = E_{corr} - \beta_a \, log\left(\frac{i}{i_{corr}}\right) \quad (1\text{-}6)$$

for the anodic polarization curve, and for the cathodic polarization curve, the relation is given by:

$$E_{app} = E_{corr} - \beta_c \, log\left(\frac{i}{i_{corr}}\right) \quad (1\text{-}7)$$

Where:

E_{app}=applied potential

E_{corr}= corrosion potential

i= current density

i_{corr}= corrosion current density

β_c, β_a=cathodic and anodic slopes, respectively

Plotting of E_{app} versus log i is known as a Tafel plot. The above two equations can be used to calculate the corrosion current density and corrosion potential simply by

extrapolating the Tafel lines. Figure 1-16 shows the anodic and cathodic slopes in Tafel extrapolating technique. Moreover, corrosion current can be used to calculate the corrosion rate (CR) as follow:

$$CR = K1\frac{i_{corr}}{\rho}EW \quad (1\text{-}8)$$

Where:

CR is given in mm/y

i_{corr} in µA/cm^2

K_1= 3.27×10^{-3} mm g/µA/cm y

ρ =density in g/cm^3

EW=equivalent weight

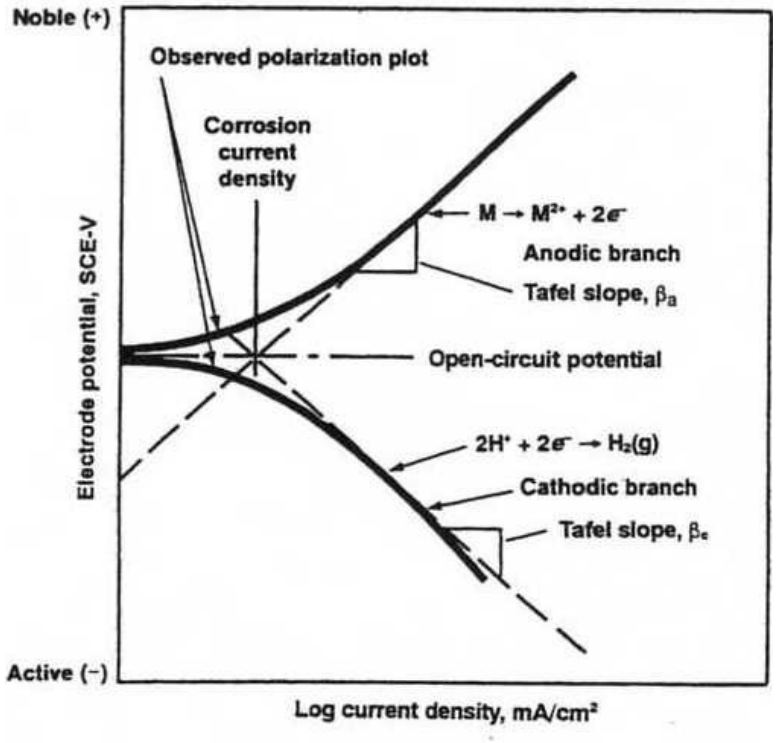

Figure 1-16 Cathodic and anodic slopes in Tafel extrapolation plot [21]**.**

1.6.3 *LINEAR AND CYCLIC VOLTAMMETRY*

Potential sweep voltammetry techniques are probably the most widely used techniques to study and investigate electrode process. In these techniques, a continuous, time linearly varying potential is applied to the working electrode.

Linear sweep voltammetry (LSV) and cyclic voltammetry (CV) were reported in 1938 and were theoretically described in 1948 by Randles and Sevcik [24]. For LSV, the current is monitored while the potential is scanned between two known points. The result is a linear sweep voltammogram. The difference between LSV and CV is that in the CV technique, the potential is swept back and forth cyclically between the two chosen points while current is recorded. The equipment used to carry out LSV and CV is illustrated in Figure 1-17.

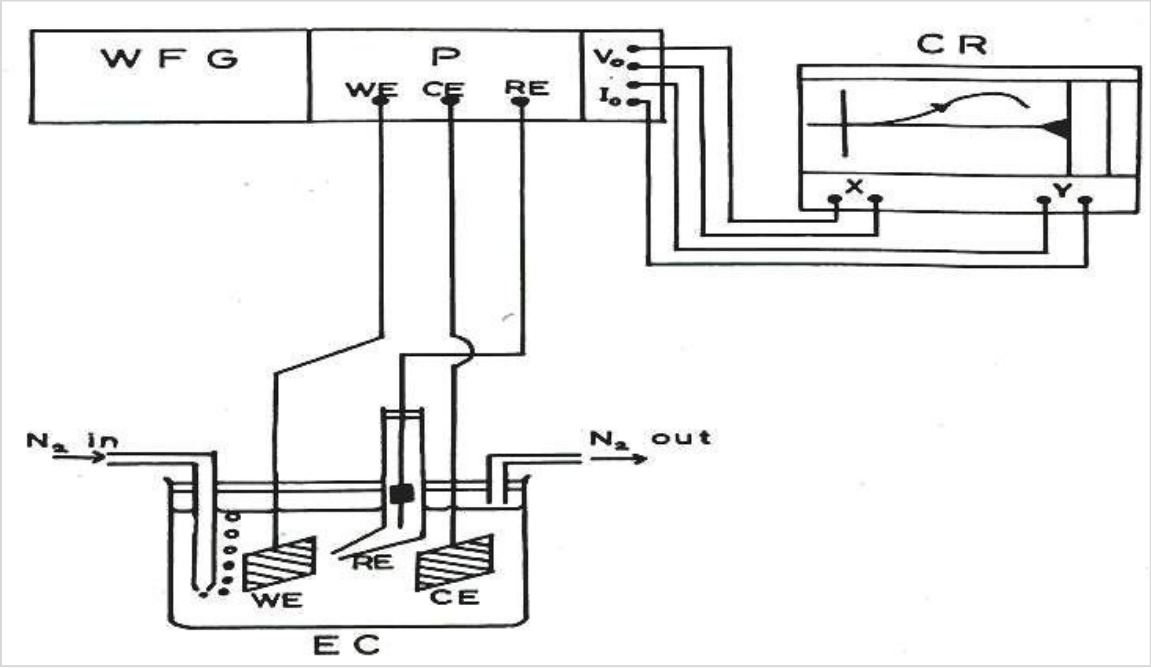

Figure 1-17 Schematic representation of the equipment necessary to perform linear sweep voltammetry(LSV):WFG wave form generator; p, potentiostat; CR, chart recorder; EC, electrochemical cell; WE, working electrode; CE, counter electrode; RE, reference.

The experimental setup consists of an electrochemical cell attached to a potentiostat. Normally, three electrodes are used in a standard cell: the working electrode (WE), the reference electrode (RE), and the counter electrode (CE). The potential at the working electrode is controlled with respect to the reference and the current is measured. Figure 1-18 and Figure 1-19 show the typical LSV and CV curves, respectively.

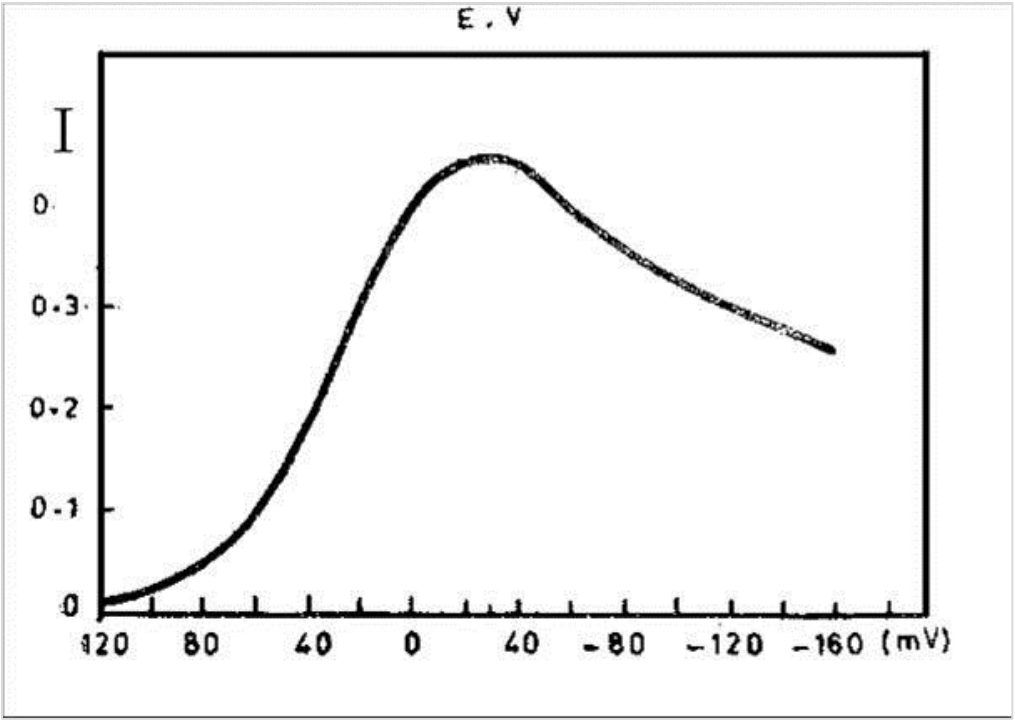

Figure 1-18 Typical linear potential sweep voltammogram[25]

In most of the cases, only qualitative information could be obtained from a full polarization scan. This qualitative information includes the change of passivation behaviour in the passive region and the change of pitting potential (E_{pit}) with alloying elements or inhibitors. However, it is possible to obtain quantitative information related to the corrosion kinetics and corrosion rate.

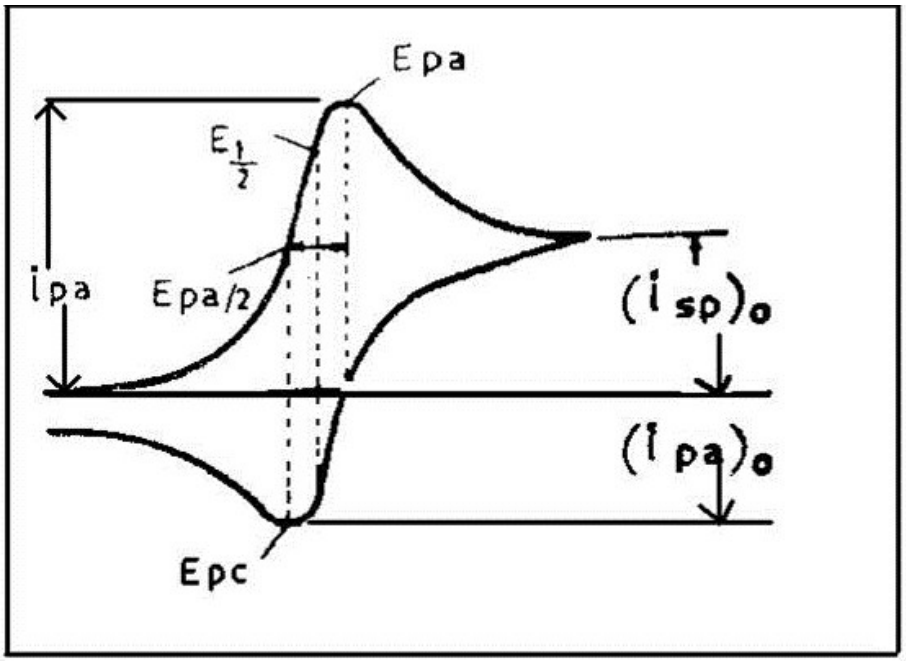

Figure 1-19 Typical cyclic voltammogram[25]**.**

1.6.4 *CYCLIC POLARIZATION*

This method is another variation of potentiodynamic polarization. This technique probably is the most well known technique to evaluate the pitting susceptibility of a material. In this technique, the potential is linearly swept from a low value to a higher value in the anodic direction and then the potential scan is reversed at some chosen current or potential toward the cathodic direction.

The resulting plot of the applied potential with respect to the reference electrode versus the logarithm of the current is shown in Figure 1-20. The potential at which the current is sharply increases is defined as the pitting potential (E_{pit}). The reverse scan will form a hysteresis loop, and the potential where the loop closes during the reverse scan is designated as a protection potential (E_p) [26].

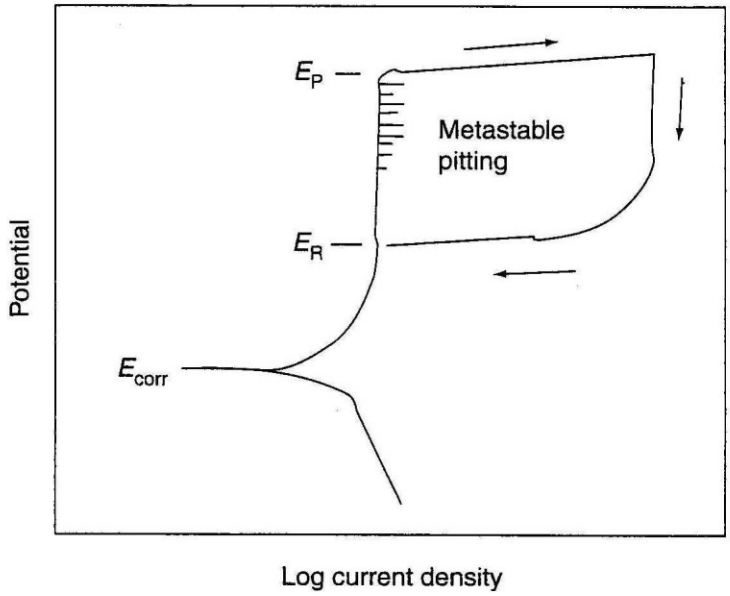

Figure 1-20 Cyclic polarization curve [1]**.**

1.6.5 *STEPWISE POLARIZATION*

This experiment sweeps the potential between separate potential set points in discrete potential steps. In this technique, instead of linear or cyclic scan, the potential is scanned in a form of steps. Unlike a smooth scan in linear or cyclic wave form, the potential applied is made up of small and discrete steps as shown in Figure 1-21.

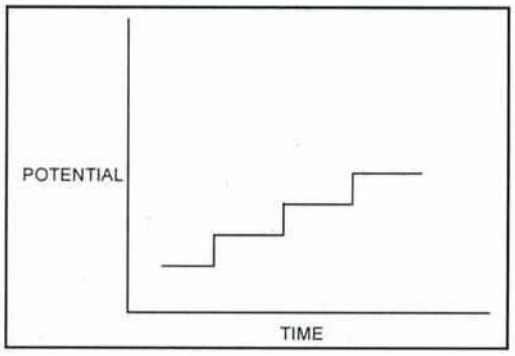

Figure 1-21 Stair case excitation waveform [26]**.**

1.6.6 *GAVANOSTATIC AND GALVANODYNAMIC TECHNIQUES*

In these techniques, which are also called chronopotentiometric, a constant current is applied and the potential is monitored as a function of time. A galvanostat is used as a source of current which is flowing between the working and the auxiliary electrode, while the potential is measured between the working and reference electrode. Figure 1-22 shows a schematic diagram for the apparatus used for chronopotentiometric measurements.

Different types of controlled current techniques can be applied. In constant current mode, the applied current will cause the electroactive species to be reduced to product at a constant rate, and after the flux of species becomes not enough to accept all electrons at the electrode surface, the potential will change to more negative values until a new reduction process takes place. In contrary of constant current, applied current could be changed as function of time. This technique is called programmed current chronopotentiometry. There is also another version of this technique, in which the current is reversed after some time and if the current is continuously reversed at each transition, cyclic chronopotentiometry is obtained.

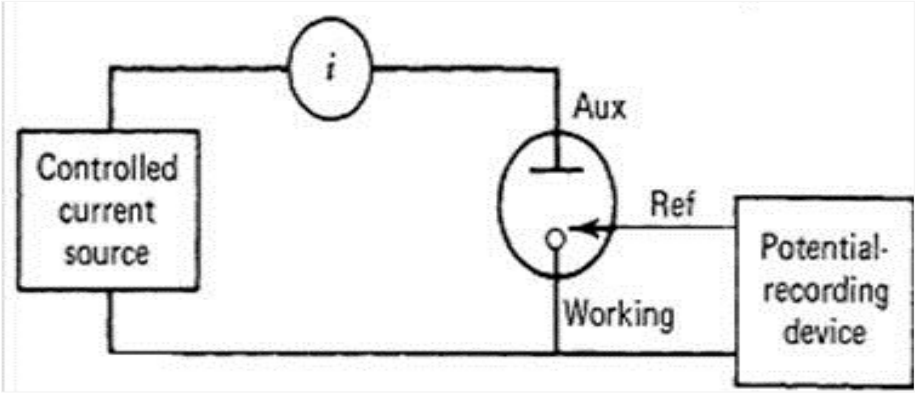

Figure 1-22 A schematic block diagram for chronopotentiometric measurements [27]**.**

1.6.7 *ELECTROCHEMICAL IMPEDANCE SPECTROSCOPY*

Electrochemical impedance spectroscopy (EIS) is a technique used for corrosion monitoring and to evaluate an electrode/electrolyte system. The principle of this technique is based on analyzing the impedance of the system as a function of the frequency of a small applied (AC) signal. The spectra obtained are evaluated as a function of frequency (*f*).

In the case of alternating current, the time dependent current response *I(t)* can be expressed as an angular frequency (ω) dependent impedance as follow:

$$Z(\omega) = V(t)/I(t) \quad (1\text{-}9)$$

Where:

t=time.

$V(t) = V_{\circ}Sin(\omega t)$.

$I(t) = I_{\circ}Sin(\omega t + \theta)$.

θ = is the phase angle between *V(t)* and *I(t).*

The impedance $Z(\omega)$ can be represented in terms of both, real $Z'(\omega)$, and imaginary $Z''(\omega)$ components according to the equation:

$$Z(\omega) = Z'(\omega) + Z''(\omega) \quad (1\text{-}10)$$

Nyquist and Bode plots are the most common ways to plot the impedance (Z). In nyquist plots $Z''(\omega)$ is plotted as a function of *Z'(w)*. This plot shows a semicircle that has two characteristic points. At low frequency values, the plot shows the sum of a solution resistance and a polarization resistance, while at high frequency range, only the resistance of the electrolyte appears. In Bode plots, the experimental spectra are evaluated as a function of frequency *(f).* In such a plot, the phase angle (log θ) and the logarithm of the impedance log |Z| are plotted versus frequency *(f)* where $\omega = 2\pi f$. Maxima and minima of θ, as well as their positions at certain frequency are used as indicators of the properties of the system [28]. Figure 1-23 and Figure 1-24 show the basic types of impedance spectra and their equivalent circuits.

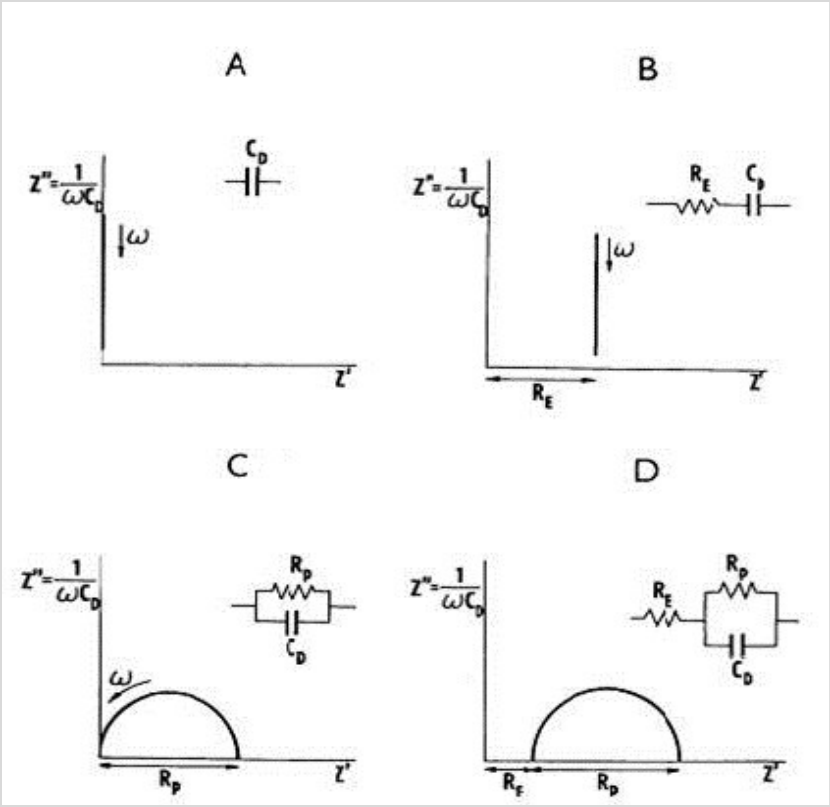

Figure 1-23 Basic types of impedance spectra and their corresponding equivalent circuits; A, capacity of electrical double layer alone; b, capacity of the electrical double layer when the electrolyte has an ohmic resistance (R_E); C, double layer capacity (C_D) and similtieous electrode reaction with polarization resistance (R_P); D, the same condition as C where the ohomic resistance of the cell (RE) is included [29]**.**

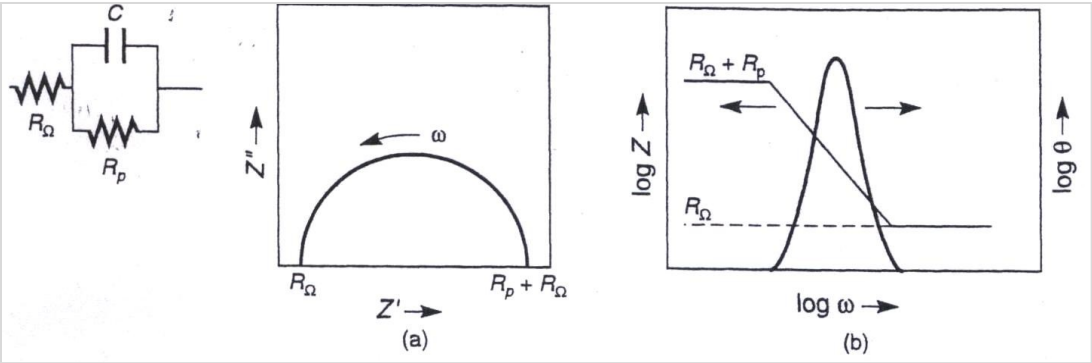

Figure 1-24 data display for EIS for a corroding electrode; a, Nyquist plot; b, Bode plot [29]

The equipment used to analyze the dynamic behaviour of an electrochemical system consists of a frequency response analyzer (FRA) and a spectrum analyzer or network analyzer combined with digital regulation device for collection of data and analysis of experimental impedance. Figure 1-25 shows a typical arrangement for EIS, the setup contains a potentiostat, a frequency analyzer FRA, a computer and a software for data collection and processing. A flat cell with three electrodes is commonly used to reduce the electrochemical noise.

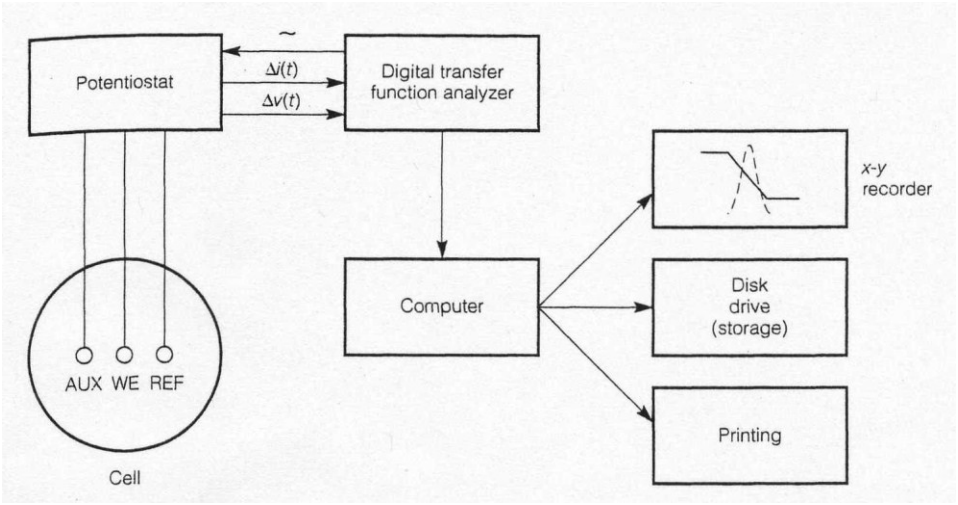

Figure 1-25 Typical arrangement of EIS.

Normally, impedance spectra become more complex than the examples shown in Figure 1-23. The center is often depressed below the axis, and the semicircular plot could be

distorted. EIS is a very efficient technique, it is sensitive, applicable in the laboratory and the field and it can be used to investigate many electrochemical and corrosion systems. However, the cost, maintenance and the difficulty of data interpretation are among the most common disadvantages of this technique.

1.6.8 *COMPARISON OF ELECTROCHEMICAL TECHNIQUES*

Each electrochemical technique is used for a specific purpose. Measurements of potential- current relations under controlled conditions may provide information on corrosion behaviour of materials. Electrochemical techniques can yield information on passivity, pitting tendency, corrosion rate, coatings as well as on the corrosion mechanisms. Table 1-6 shows the plots and results that are obtained from different electrochemical techniques.

Table 1-6 Electrochemical techniques.

Electrochemical Technique	**Applied**	**Plots**	**Obtained Results**
Open circuit potential (OCP)	Open circuit	E vs. t	Open circuit potential
Linear sweep polarization (LSP)	Potential	E vs. log (i)	Passivation potential range
Tafel extrapolation (TE)	Potential	E vs. log (i)	Corrosion rate
Cyclic polarization (Cp)	Cyclic potential	E vs. log (i)	Pitting tendency
Step wise polarization(SW)	Step potential	E vs. log (i)&t	Pitting tendency
Electrochemical impedance spectroscopy (EIS)	Ac with wide range of frequency	Real vs. imaginary impedance (z' vs. z'')	Evaluation of electrode /electrolyte system

CHAPTER 2 BACKGROUND

2.1 CORROSION OF ALUMINUM AND ITS ALLOYS

Aluminum is known for its corrosion resistance. This good corrosion resistance is attributed to the natural passive layer that inhibits metal oxidation. The good corrosion resistance enables aluminum to be used in many applications, such as buildings, construction, ship industry, transportation, beverage and aerospace industry. As shown in Figure 2-1, the protective layer is composed of two distinct layers. The inner oxide layer has a compact and amorphous nature while the outer layer has an amorphous nature and forms mainly of hydrated oxide [30].

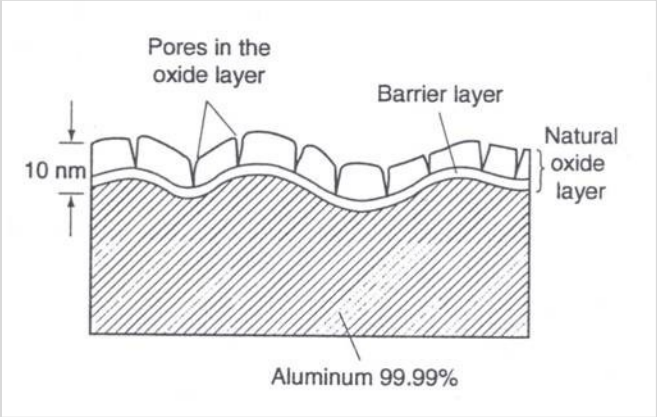

Figure 2-1 Schematic of the passive oxide film that forms on aluminum [30]**.**

The passivation behaviour can be observed in a typical polarization curve shown in Figure 2-2. The curve shows that the active stage in which the current density increases with increasing potential until a passivation potential is reached. To produce passivation, the current must reach or exceed the passivation current value and the potential must be kept in the passive region. However, the passive layer may undergo a local breakdown at higher potentials and the alloy experience a localized type of corrosion such as pitting or crevice corrosion.

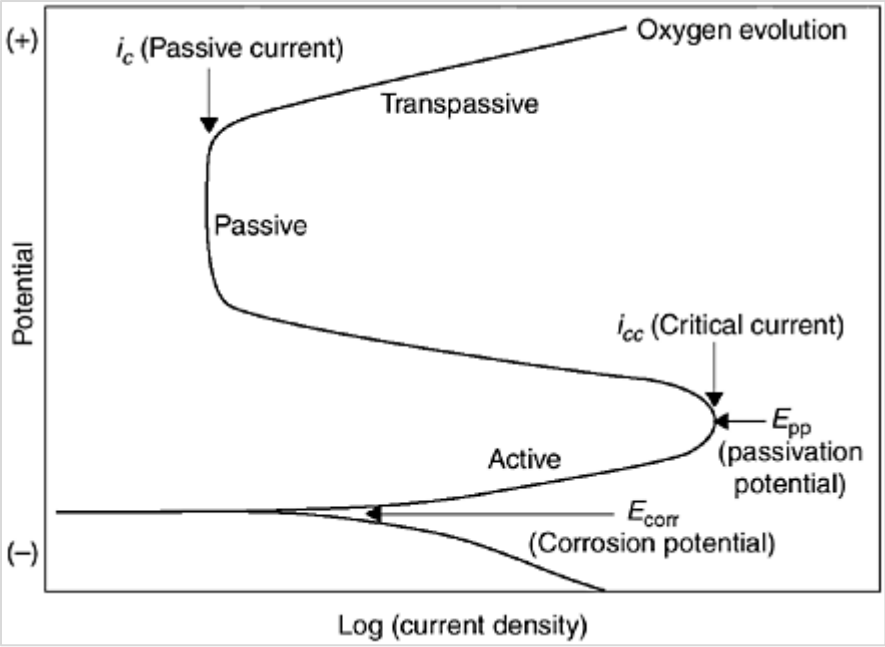

Figure 2-2 Typical passivation curve [31]**.**

Pitting is one of the most common corrosion attacks on aluminum alloys. Pits initiate at localized discontinuities in the protective film. The halide ions are known to assist in the breakdown of the protective aluminum oxide layer, and chloride (Cl^-) has been the most frequently encountered in service. In some aggressive environments such as halides containing environments, growth of pitting is autocatalytic. The local conditions inside the pits are very severe because of the increase in chloride ions concentration and the decrease in pH [32] [33]. Z. Szklaraska has proposed a model of pitting corrosion that involves four stages [34]. The Four steps are: processes occurring on the passive film, processes occurring within the passive film, formation of the metastable pits and finally stable pit growth. The first two steps are related to the breakdown of the passive oxide film. Since these two stages happen within the passive film and at the interface between the film and the solution, these stages are strongly related to the composition and the nature of the oxide film as well as the electrolyte composition. Metastable pits are very small in size and have the ability to survive for a short time. The metastable pitting happens at a potential close to the pitting potential and is characterized by an increase in current as the pits nucleate followed by a sharp decrease in current after a short time. Stable pits grow above the pitting potential and the growth depends on many factors

such as, alloy composition, pit environment, and pit potential. Some studies relate the pit growth phenomenon to the pits number, depth and radius as a function of time [34]. D. Buzza and R. Alkire studied the pits growth of pure aluminum using a laser technique to initiate artificial pits in an 1M NaCl as a corrosion environment. In addition to the relation between the pit shape and the applied potential, the authors proved that the pit depth is a function of time [35].

The other main localized type of attack in aluminum alloys is the crevice corrosion. Crevice corrosion occurs when an electrolyte exists in narrow fissures where the solution is stagnant and the oxygen access is limited. Such conditions exist at joints, bolts, flanges, and poor quality welds.

The mechanism of crevice corrosion has been studied by many researchers. A. j. Betts and L. H. Boulton [36] have concluded that crevice corrosion is related to alloy composition, applied potential, bulk solution and the crevice geometry. Additionally, these authors proposed a deoxygenation-acidification model to explain the crevice mechanism. This mechanism consists of two steps, initiation and propagation. The initiation step is characterized by a minor attack and can be divided into deoxygenating, hydrolysis-acidification and activation. Deoxygenating happens when the diffusion of oxygen inside the crevices is slower than the depletion through the cathodic reactions.

$O_2 + 4H^+ + 4e^- \rightarrow 2H_2O$ In acidic solution (2-1)

$O_2 + 2H_2O + 4e^- \rightarrow 4OH^-$ In neutral/alkaline solutions (2-2)

As a result of oxygen depletion, oxygen reduction is limited to the external surfaces and metal dissolution continues within the crevices according to this reaction:

$M \rightarrow M^{n+} + ne^-$ (2-3)

In the case of aluminum, the anodic reaction is as follow:

$Al \rightarrow Al^{+3} + 3e^-$ (2-4)

As a result of cation accumulation, metal hydrolysis forms according to the following reaction:

$M^{n+} + 2H_2O \rightarrow M(OH)^{(n-1)} + H_3O^+$ (2-5)

The hydrolysis reactions lead to acidification and pH decrease inside the crevice. In order to maintain the electroneutrality, chloride ions migrate from the bulk solution into the crevice. As a result of the deoxygination-acidification stage, the environment inside the crevice becomes very aggressive due to low pH and high chloride ion content. The conditions inside the crevice are strong enough to breakdown the protective passive layer. The propagation stage follows the initiation step. It involves a rapid increase in corrosion current and corroded area. Finally, corrosion product such as a salt film may form at a crevice mouth and the corrosion rate decreases.

Incubation and propagation stages model has been proven by M. Baumgärtner and H. Kaesche [37]. They studied the nature of crevice corrosion of pure aluminum in 1 N sodium chloride solutions. The samples were polarized potentiostatically. Incubation and propagation stages were apparent in current time plots. A similar model has been proposed by N. Sridher and others [38]. In their proposed model, they explained the crevice process based on four steps, deoxygenating, increase of salt and acid concentration, depassivation and propagation. Figure 2-3 shows the steps of this model.

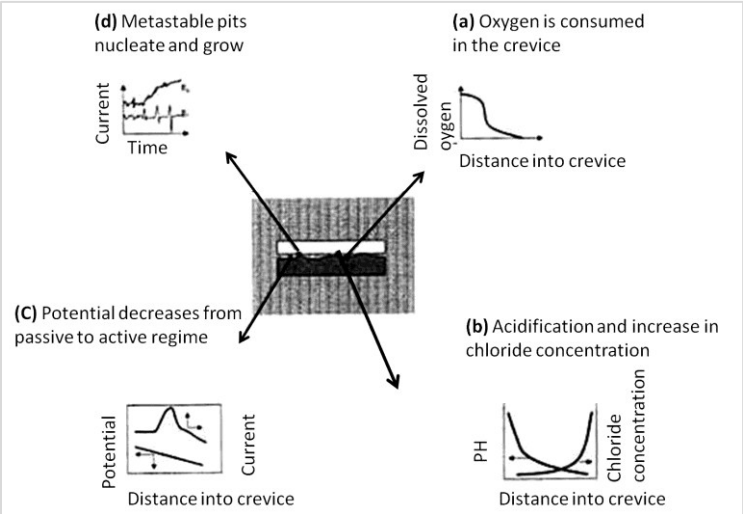

Figure 2-3 Processes leading to crevice corrosion [38].

2.2 CORROSION OF AL-MG-SI ALLOYS

2.2.1 *PITTING CORROSION*

Alloys in this series are known for their moderate strength and good corrosion resistance. This group of alloys is heat treatable and the basis of the heat treatment response is the presence of Mg_2Si . Copper while improving the mechanical properties of Al-Mg-Si, results in a deterioration of corrosion resistance. Some copper containing alloys such as 6013, 6111, 6065 show a lower resistance to pitting and intergranular corrosion.

Corrosion behaviour of wrought 6061 in 3.5wt % NaCl solution was studied by A. Ulhamid [39] who conducted his study using electrochemical techniques such as open circuit potential, cyclic polarization and Tafel plots. In deaerated solution, results obtained show that the open circuit potential of 6061 alloy was more negative compared to aluminum, while in aerated solution the results show a positive potential with respect to aluminum. A similar trend has been proven by P. Trazaskoma and his group [40]. Susceptibility to pitting corrosion was indicated using cyclic polarization for 6061 in both T4 and T6 tempers, where the plots show no passive region in aerated solutions. Under deaerated conditions, the alloy investigated show a clear passive region along with protective potential, and the pitting potential (E_{pit}) found to be -746 mv/SCE.

D. Aylor [41] studied the pitting behaviour of 6061 aluminum alloy foils and 6061-T6 conventional wrought alloy plates in sea water. Results show that the average corrosion potential (E_{corr}) of 6061 foil was significantly smaller than that for 6061-T6 plate: corrosion potential values reported were -0.860 V/SCE and -0.750 V/SCE, respectively. Foil samples were also kept for 2-3 days for stabilization and then cyclically polarized in deaerated solution. Similar pitting characteristics for foil and plate samples were observed on both samples and show a presence of pitting and protection potential. However, the increase in foil pitting corrosion resistance relative to plate samples was attributed to the large potential difference between E_{corr} and E_{pit}. In addition to the electrochemical experiments, marine exposure tests were performed on foil and plate

6061 samples. After one year exposure, foil samples experienced no pitting penetration while 60 days were enough to create pitting in 6061 plate samples. D. Aylor attributed this difference to the amount of cold working. Pitting susceptibility of 6056-T6 aluminum alloy was studied by C. Blanc and G. Mankowski [42]. In addition to aluminum, magnesium and silicon, this alloy contains copper and has been developed to replace the well known traditional 2024- T3 aluminum alloy in some aerospace applications. The pitting susceptibility was studied at different chloride concentrations. For low chloride ion concentration, the 6056 alloy shows a less resistance to pitting than 2024 alloy but its resistance to pitting was much better for the high chloride concentration. These authors used X- ray photo electron spectroscopy (XPS), SEM and transmission microscopy to study the oxide film, the polarized surfaces and the precipitates nature, respectively. The study concluded that there was no alloying elements enrichment of the passive film and no significant dissolution of the coarse particles. For that reason, the variation of pitting susceptibility of 6056 was similar to pure aluminum. On the other hand, 2024 shows a considerable dissolution of coarse particles and deposition and therefore, a considerable peak of pitting susceptibility was observed at low potential.

2.2.2 *EFFECT OF ALLOYING ELEMENTS AND MICROSTRUCTURE*

The basic understanding of the corrosion phenomenon is based on the fact that the corrosion process happens due to dissolution of pure, homogeneous and uniform metals. Practically, this situation does not exist and instead, conditions such as, dissimilar alloys, variable environment and surface layer are normally prevail. Additionally, the corrosion process is affected by other metallurgical factors; these factors are grain boundaries, second phases, impurities and alloying elements. In general, the corrosion behaviour of aluminum is related to the metallurgical factors. Aluminum alloys contain additional elements, precipitated phases, impurities and intermetallic particles. Precipitated phases and intermetallic particles may behave either anodically or cathodically and sometimes switch between the two [34, 43, 44].

Magnesium and silicon are the main alloying elements in Al-Mg-Si system. Copper and/or manganese sometimes are added. This system is heat treatable with Mg_2Si precipitates playing the major role in strengthening. Most Al-Mg-Si alloys provide good corrosion resistance. However, copper containing alloys show poorer corrosion resistance. Copper containing alloy 6056 was studied by C. Blank and G. Mankowski [42] who suggests that the geometry of the intermetallic particles affects the pitting susceptibility. They separated the intermetallic particles into four types based on their size. Some particles exist in a large number and precipitate along the grain boundaries. In addition needle like shape, globular, and very large particles were observed. The authors [42] attributed the better performance of this alloy compared to 2024 to the negligible dissolution of the coarse particles. B. Shaw et al [45] reported that copper concentration affect the susceptibility of Al-Mg-Si alloys to intergranular corrosion. The samples were anodically polarized at -300 mV/SCE in 0.05 M HCl. For copper free samples, the corrosive attack is largely uniform. However, samples containing copper show a very clear intergranular attack. Figure 2-4 shows the effect of copper concentration on the degree of intergranular corrosion. The explanation of the role of copper is based on the grain boundary depleted zone theory. The general mechanism involves a formation of a copper- depleted zone that develops along the grain boundaries which is preferentially attacked compared to the copper rich matrix and the copper containing boundary particles.

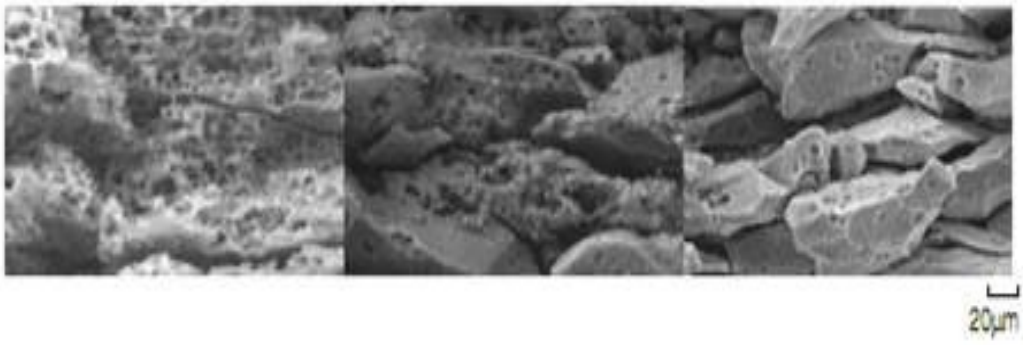

Figure 2-4 SEM micrograph showing the degree of intergranular corrosion of Al-Mg-Si alloy in 0.05 MHCL; (left) 0% copper, (middle) 0.7% copper, (right) 1.5 % copper[45]

In aluminum alloys, Intermetallic phases are either developed by design to obtain the desired microstructure and consequently certain mechanical properties or either exist in the alloys as impurities. Depending upon the alloy system, different second phases may exist. Phases such as, Al_6Fe, Al_3Fe, AlMg, AlMnMg, αAl_3Fe, αAl(Fe,Mn)Si, AlCuFe and AlCuMg have been reported [34] . As mentioned earlier, intermetallic particles play a major role in the localized corrosion of aluminum alloys. Relative to the aluminum matrix, intermetallic particles can be further characterized either active or noble. For example, Al_2CuMg and Mg_2Si were found to be active to the matrix while, Al_3Fe, $Al_{20}Cu_2(Fe,Mn)_3$ and Al_7Cu_2Fe are noble to the matrix. R. Buchheit has compiled the corrosion behaviour of various intermetallic phases in aluminum alloys [46]. The data reported by Buchheit show that different intermetallic particles show a different electrochemical behaviour. Table 2-1 shows the corrosion potential for intermetallic particles that exist in aluminum alloys.

Table 2-1 Corrosion potential for intermetallic compounds common in aluminum alloys [46]**.**

Phase	Stoichiometry	Corrosion potential (V_{sce})	Environment	Aeration	Other data reported
θ	Al_2Cu	−0.44	53 g/liter NaCl + 3 g/liter H_2O_2	Open to air	—
θ	Al_2Cu	−0.76	1.0 *M* NaCl	N_2 sparged	AP, CP, RRDE
θ	Al_2Cu	−0.45 to −1.1	Sulfate solutions *vs.* pH	N_2 sparged	AP, CP, RRDE
θ	Al_2Cu	−0.64	1.0 *M* NaCl	N_2 sparged	AP, CP
θ	Al_2Cu	−0.70	0.5 *M* NaCl	Open to air	—
θ	Al_2Cu	−0.64	53 g/liter NaCl + 3 g/liter H_2O_2	Open to air	—
θ	Al_2Cu	−0.68	0.2 *M* NaCl	Not stated	AP, CP
θ[b]	Al_2Cu	−0.621	3% NaCl	Not stated	—
θ	Al_2Cu	−0.59	1.0 *M* NaCl	N_2 sparged	AP, CP
θ	Al_2Cu	−0.13 to −1.23	Cl^--free buffers	Ar sparged	AP, CP
θ[a]	Al_2Cu	0.04 to 0.02	Dilute HF	Open to air	CP
θ	Al_2Cu	−0.38	Dilute HF	CO_2 sparged	CP
η_2	AlCu	−0.49	0.5 *M* NaCl	Open to air	—
δ	Al_2Cu_3	−0.36	0.5 *M* NaCl	Open to air	—
γ_2	$AlCu_2$ (Al_9Cu_4)	−0.32	0.5 *M* NaCl	Open to air	—
β	$AlCu_3$	−0.26	0.5 *M* NaCl	Open to air	—
—	Al-14Cu	−0.620	0.6 *M* NaCl	N_2 sparged	GC
—	Al-18Cu-5Fe	−0.670	0.6 *M* NaCl	N_2 sparged	GC
—	Al-24Cu-5Fe	−0.675	0.6 *M* NaCl	N_2 sparged	GC
T_1	Al_2CuLi	−1.094	0.6 *M* NaCl	N_2 or Ar sparged	AP
T_1	Al_2CuLi	−1.096	0.6 *M* NaCl	Open to air	AP
T_1	Al_2CuLi	−0.803	ASTM G69	Open to air	—
S	Al_2CuMg	−0.89	1.0 *M* NaCl	Open to air	AP
S	Al_2CuMg	−0.920	0.5 M NaCl	N_2 sparged	—
S	Al_2CuMg	−0.910	53 g/liter NaCl + 3 g/liter H_2O_2	Open to air	—
β	Al_3Fe	−0.470	53 g/liter NaCl + 3 g/liter H_2O_2	Open to air	—
β	Al_3Fe	−0.585	Borate buffer pH 7	Air sparged	AP, CP, EIS
β	Al_3Fe	−0.650	0.1 *M* NaCl	Air sparged	CP
β	Al_3Fe	−0.78	0.1 *M* $AlCl_3$	N_2 sparged	AP,CP
β	Al_3Fe	−0.910	0.5 *M* NaCl	N_2 sparged	—
β	Al_3Fe	−1.05	0.1 *M* NaOH	Deaerated	AP, CP
β[b]	Al_3Fe	−0.39 to −0.58	3% NaCl	Not stated	—
—	Al_3Fe(Mn)	−1.10	0.1 *M* NaOH	Deaerated	—
—	Al_6(Mn, Fe)	−1.20	0.1 *M* NaOH	Deaerated	—
—	Al_6Mn (Fe)	−1.50	0.1 *M* NaOH	Deaerated	—
—	Al_6Mn	−1.70	0.1 *M* NaOH	Deaerated	—
—	Al_6Mn	−0.76	53 g/liter NaCl + 3 g/liter H_2O_2	Open to air	—
—[b]	Al_3Mn	−0.51 to −0.86	3% NaCl	Not stated	—
—	αAl(Fe, Mn)Si	−1.15	0.1 *M* NaOH	Deaerated	AP, CP
—	δAlFeSi	−1.40	0.1 *M* NaOH	Deaerated	AP, CP
β	Mg_2Si	−1.59	?NaCl	Deaerated	
β[b]	Mg_2Si	−1.53 to −0.68	3% NaCl	Not stated	—
M	$MgZn_2$	−0.96	53 g/liter NaCl + 3 g/liter H_2O_2	Open to air	—
β	Al_3Mg_2	−1.15	53 g/liter NaCl + 3 g/liter H_2O_2	Open to air	—
—	Al_8Mg_5	−1.13 to −1.34	Sulfate solutions pH 3 to 13.8	N_2 sparged	—
—	Al_8Mg_5	−1.05	1.0 *M* NaCl	N_2 sparged	—
—	Al_8Mg_5	−1.15	ASTM G69	Open to air	—
δ	AlLi	−1.96	0.6 *M* NaCl	Deaerated	—
β	Al_3Ta	−0.05	Borate buffer pH 7	Aerated	CP, EIS
β	Al_3Ta	−0.24 to −1.28	Cl^--free buffers pH 3 to 12	N_2 sparged	CP, EIS
β	Al_3Ta	−0.800	0.5 *M* NaCl	N_2 sparged	—
β	Al_3Zr	−0.625	0.5 *M* NaCl	N_2 sparged	—
β	Al_3Zr	−0.28	Boric acid pH 5	Ar sparged	CP
β	Al_3Ti	−0.880	0.5 *M* NaCl	N_2 sparged	—
—	Al_3Ni	−0.43	53 g/liter NaCl + 3 g/liter H_2O_2	Open to air	—
—	Al_3Ni	−0.74 to −0.72	3% NaCl	Not stated	—
α	Si	−0.17	53 g/liter NaCl + 3 g/liter H_2O_2	Open to air	—

The role of copper on intergranular corrosion of Al-Mg-Si alloy was studied by M. Larsen et al [47]. The effect of different tempers on IGC was also investigated. In their research, these authors carried out their corrosion experiments on samples that contained different copper concentrations. Samples with 0.02, 0.18 and 0.7 wt % copper were tested in 30 g NaCl/l + 1 vol % HCl nitric acid followed by 24 h immersion in 30 g NaCl/l + 1 vol % HCl. Results show that copper increases the susceptibility to IGC, while the

lowest copper containing alloy was resistant to IGC. The susceptibility to IGC in the underaged tempers was attributed to the formation of a noble copper film that forms a micro galvanic cell between the film and a solute depleted zone. On the other hand, artificially aged samples showed a reduced susceptibility to IGC. This behaviour was attributed to the loss of the copper rich film. As a general conclusion, the authors suggested that the high IGC resistance and good mechanical properties can be obtained by optimizing the artificial aging process. This optimization can be achieved by a favorable precipitation formation at the grain boundaries and grain interior. In another publication [48], the same author studied the effect of excess Si/Mg composition ratio on the IGC. Corrosion experiments were performed for copper containing samples which were compared to copper free samples with a large excess of Si, all samples were heat treated to similar tempers. Similar results were obtained that the copper containing alloy was significantly more prone to IGC compared to the copper free alloy. Copper free alloy with excess Si shows a lower response to IGC. Similar to other reports, the higher tendency to IGC was caused by a continuous copper-rich film. Additionally, the copper free silicon excess alloy showed a complete resistance to IGC by removing the cathodic particles by selective etching.

Other forms of corrosion were evaluated as a function of silicon excess content. Silicon content effect on exfoliation corrosion of Al-Mg-Si alloy was studied by F. Eckermann et al[49]. Exfoliation is a form of intergranular corrosion that occurs at boundaries of the grains elongated in the rolling direction. In their research, this group of researchers performed corrosion tests on a commercially available AA6061 aluminum alloy with higher silicon content. They concluded that the severity of exfoliation corrosion is related to the silicon content variation in solid solution. Moreover, they proved that the exfoliation attack does not follow grain boundaries and intermetallic phase's orientation.

The role of iron containing phases on corrosion is reported to be significant. The effect of these phases is attributed mainly to their cathodic nature. F. Eckermann [50] used X-ray microtomography to study the effect of iron containing intermetallic phases on the

initiation of IGC. Work performed on heat treated AA6061 samples showed that IGC was initiated at a broken Fe containing phase. Atomic force microscopy (AFM) was used by J. Park [51] to study the influence of Al_3Fe on local dissolution and pit imitation of 6061 aluminum alloy. The authors reported that the dissolution of the aluminum matrix occurs adjacent to the inclusions and that effect was found to be related to the size of the inclusion. Large cavities found to form around large inclusions. Additionally, pH measurements near the inclusions were conducted using scanning micro sensor measurements. The measurements show that pH as high as 11 was recorded. Moreover, the cathodic nature of the inclusions was further proven by potential measurements.

2.2.3 *EFFECT OF SURFACE FINISH*

Although the effect of surface finishes on corrosion resistance is very well known, different authors reported different conclusions. A. Aballe et al [52] studied the effect of degree of polishing on the pitting susceptibility of AA5083 aluminum alloy. They reported that samples polished to 1200 grit show a greater susceptibility to the localized corrosion than the samples polished to 80 grit. According to these authors localized alkaline corrosion (LAC) was observed where the corrosion occurs due to the increase in the alkalinity of the area around Al(Mn,Fe,Cr) particles. The authors interpreted their results based on the density of the iron containing particles as a function of the polishing process. On the contrary, A. Bastaweesy [53] reported different results who used Tafel plot and cyclic polarization techniques to evaluate the effect of surface roughness on corrosion behaviour of 6061-T6 aluminum alloy in saline solution. The author used emery papers and endmil machine to prepare different samples with different roughness. Results show that smother surfaces show lower corrosion rate and better pitting corrosion resistance than rough surfaces. The corrosion potential of the surface obtained by grinding on 1000 grit emery paper was found to be -783mV/SCE, and the corrosion rate of the same smooth surface reported to be 2.39 mpy. For the coarse endmil, the surfaces corrosion potential of -685 mV/SCE was recorded. The author attributed the weak performance of the rough surfaces to the formation of deep surface irregularities and micro defect which will accelerate the corrosion process.

2.2.4 *EFFECT OF INHIBITORS*

Corrosion resistance of aluminum and aluminum alloys can be improved by using inhibitors. Molybdates, sulphates and chromates have been used to reduce and inhibit corrosion of aluminum and its alloys. The effect of dichromates on the corrosion behaviour of 6061 aluminum alloy was studied by W. Badway [54]. The inhibition effect was studied using X-ray photoelectron spectroscopy, SEM in addition to potentiodynamic polarization. Comparing to sulphates and molybdates, dichromates show better performance. The inhibition effect of dichromate found to be dependent on the concentration, the inhibition efficiency increases as the dichromates concentration increases from 0.01 M to 0.1 M. The better performance of dichromates was attributed to the accommodation of dichromates on the active sites and their ability to inhibit the galvanic couples between the cathodic sites and the matrix. There was also evidence that the passive film incorporates Cr, which consequently, lead to a remarkable corrosion inhibition efficiency. In a similar work, W. Badawy and F. Kharafi [55] studied the effect of the same inhibitor on the same aluminum alloy but at different pH. In this research, a solution of pH=2 was used. A similar conclusion has been obtained, in which the positive effect of dichromate was proven.

The effect of various anions on the corrosion behaviour of 6061 aluminum alloy was studied by J. Datta et al [56]. The effect of Cl^-, Br^-, NO^{-3} and $SO4^{-2}$ was investigated. Potentiodynamic polarization, electrochemical impedance spectroscopy and immersion tests have been applied. It was concluded that the dissolution of the matrix was reduced in the presence of Br^-, NO^{-3} and $SO4^{-2}$, while the presence of the Cl^- found to accelerate the corrosion process by penetration into the protective oxide film. The effect of $SO4^{-2}$ on passivity was very obvious, the passivity of the 6061 aluminum samples in presence of $SO4^{-2}$ was extended over a wide potential range and polarization beyond the pitting potential was needed to breakdown the passive layer. Cerium chloride was used by H. Allachi [57] to protect AA6060 aluminum alloy in a marine environment. According to the results obtained, the addition of cerium chloride to aqueous 3.5 wt% NaCl solution found to reduce the pitting and general corrosion of AA6060 alloy. This beneficial effect

was attributed to the precipitation of cerium compounds on the cathodic α-Al(Fe, Mn)Si intermetallic phase.

2.3 CORROSION OF ALUMINUM PM ALLOYS

Corrosion of powder metallurgy is a new area of research. Even for sintered stainless steel which is historically older than PM aluminum, some topics have not been covered. Despite the little work, most of the research for PM aluminum alloys was conducted using simple immersion tests. However, electrochemical techniques have been used as well.

As mentioned previously, aluminum and its alloys are known for their good corrosion resistance which is attributed to the formation of a passive protective layer that forms on the surface. However, in the case of aluminum parts prepared by powder metallurgy techniques, pores are an essential microstructural feature and have a tremendous effect on the corrosion behaviour. These pores act as initiation sites for corrosion.

2.3.1 *EFFECT OF POWDER PROCESSING PARAMETERS*

Among other factors, limited solubility of some alloying elements in aluminum matrix is the main restriction toward better properties. A new technology has been used recently to overcome this restriction, this approach is known as rapid solidification (RS). In addition to higher solubility, RS can provide fine microstructure, reduced segregation and fine precipitated intermetallic compounds.

The effect of rapid solidification on the corrosion behaviour of Al-Zn-Mg produced by PM and cast alloys has been studied by A. Sameljuk et al [58]. The PM alloy shows a better performance in 0.3 wt% NaCl solution compared to the cast alloy. The improved performance of the PM alloy to localized corrosion is attributed to its microstructure. The precipitates in the rapid solidified PM alloy are significantly refined. In addition, the difference between the alloying content between the matrix and the precipitate is less than in the case of cast alloy. In addition to the difference between cast and PM alloys, the author studied the effect of the production route on crevice susceptibility of the PM alloy. Two different approaches were used to prepare the PM alloys: some samples

were prepared by cold pressing of the dried powder into a compact of 30% porosity, while other samples were prepared by hot pressing, consolidation and then hot extrusion to produce a pore free microstructure. Both, the extruded and the cold pressed alloys reveal a wide passive range, but the current density of the cold pressed samples was higher compared with the extruded alloy.

In another publication, the effect of rapid solidification on the corrosion behaviour of Al-5Zn-3Mg-0.6Cu-0.8Zr-0.25Cr-0.15Ni-0.15Ti in 3 wt% NaCl solution was studied [59]. The authors concluded that PM and cast alloys have similar phase composition, but they differ in morphology, size and distribution of precipitates. Furthermore, they confirmed that the localized corrosion initiates at the cathodic particles. Intermetallic Size, morphology and distribution found to affect the corrosion behaviour of cast and PM alloys. Cast alloy shows a decrease in corrosion resistance because of the presence of large and inhomogeneously distributed particles.

S. Sunada et al investigated the corrosion behaviour of an Al-Mg-Si alloy produced by ingot and powder metallurgy [60] in sulfuric acid solution of 0.5 kmol/m^3. The potentiodynamic polarization curves of the IM and PM alloy were quite similar.

An Al-Mg alloy prepared by mechanical alloying and known as IN-9052 was studied by J. Mcintyre and et al [61] for the pitting behaviour and compared to AA6061-T6 and AA5086-H32. Pitting susceptibility was evaluated using potentiostatic and potentiodynamyic polarization in 3.5 wt% deaerated NaCl solution. The study showed that the pitting potential of the three alloys was similar. However, the alloy IN-9052 showed a larger difference between pitting potential and the open circuit potential than the other two alloys. This difference makes the IN-9052 alloy to have a better pitting resistance than AA6061 and AA5068. The potentiostatic test showed that the current density of IN-9052 was more stable than the AA6061 alloy. In the case of AA6061, the current density increased rapidly and then remained high for the duration of the test. This behaviour indicates that pitting initiation was much slower on IN-9052 than AA6061. The surface investigation conducted on the corroded samples after 5 weeks of exposure to the solution showed the appearance of different corrosion product

appearance, and the thickness of the corrosion layer on AA6061 was much greater than the layer formed on IN-9052. The corroded surface examination also revealed that the pits formed on AA6061 were much larger and deeper than the pits formed on IN-9052.

The corrosion rate of AA6061 PM Alloy with 5, 10, 15 wt% $CuAl_2$ was calculated by O. Vanegas and others [62]. PM samples were prepared by blending, pressing and sintering under vacuum. Tafel plots showed that the corrosion resistance of 5% $CuAl_2$ AA6061 reinforcement samples was the poorest, while the samples with 15% $CuAl_2$ showed the best performance and lower corrosion rate.

The effect of sintering parameters on the corrosion behaviour of 2124 aluminum PM alloy has been studied by S. Majado et al [63]. Variables included, sintering temperature, time and atmosphere. Sintering temperature was varied between 750°C and 610°C, while the sintering atmosphere used was N_2 or N_2-H_2. The sintering time used was one and two hours. Surprisingly, the author concluded that sintering conditions variation does not affect the corrosion behaviour. The polarization experiments conducted in 3.56 wt% NaCl solution showed that the corrosion potential for all the samples was similar. Tafel plots were used to measure the current density in which the corrosion current density of wrought alloy was higher than that of the PM alloy. The authors attributed the similar corrosion behaviour of the PM alloys to the microstructure. They concluded that all the PM samples have the same type of particles with the same shape, distribution and population density. The authors also attributed the different behaviour between the wrought and the PM alloys to their microstructure. In the case of the PM alloy, the Al-Fe-Mn-Si-Cu particles were scattered within the aluminum matrix, while there was a clear clustering and banding of the Al-Fe-Mn-Si-Cu particles in the wrought alloy. These scattered particles impede the propagation of the corrosion from one particle to another and lead to a lower corrosion current. Moreover, the population density of the particles in the PM alloy is lower than for wrought alloy. In addition to the differences in particle size and number, their chemistry was also found to be different. Both, PM and wrought alloys have the same matrix composition, but the content of some alloying elements in these particles was higher for wrought alloy than

in the PM alloy. This difference in composition between the matrix and these particles leads to enhance pits formation through galvanic cells.

Similar sintering effect on corrosion resistance was found by D. Bishop et al [64]. The authors conducted their corrosion study on PM 2014 aluminum alloy. Sintering variables included time, and temperature. There was only a small difference in corrosion potential as a function of sintering time that varied at 0.5 h, 1h and 2h. Similarly, the corrosion potential of the PM and wrought alloy was the same. In terms of corrosion current, the wrought alloy shows a greater corrosion current than the PM alloy. The authors also studied the effect of sintering time on Ag-modified PM 2014 aluminum alloy. The results showed that samples sintered at 4 hours show a higher corrosion current than those sintered for 16 hours.

2.3.2 *EFFECT OF CHEMICAL COMPOSITION*

Stress corrosion cracking is probably the reason for most of aluminum alloys corrosion failures in aircraft industry. It is known that microstructural and compositional modifications that used normally to improve the mechanical properties often lead to a higher SCC susceptibility [4]. Consequently, most of research on high strength aluminum alloys is devoted to SCC.

One way to improve the SCC behaviour of high strength aluminum alloys is by adding grain refiner elements. The PM microstructure can be refined by adding cobalt as grain refiner leading to better mechanical properties while maintaining good stress corrosion resistance. L. Christodoulou et al investigated the effect of Co content on the SCC behaviour of 7091 PM alloy [65]. SCC behaviour of samples prepared from 7091 PM alloy with different cobalt content was tested. The study proved that increasing cobalt content improves the SCC resistance. This increase in SCC resistance was attributed to the cobalt content and not to the grain refining effect. The authors explained this effect on the formation of Co_2Al_9 particles, as these particles work as cathodic sites and blunt the stress corrosion cracks. The presence of the cathodic particles leads to localized matrix dissolution around these particles, which eventually reduce the curvature crack tip.

Comparing to cobalt effect, other elements found to have an adverse effect on the corrosion resistance of Al-Zn-Mg PM Alloy. The effect of zinc content on pitting susceptibility of Al-Zn-Mg PM alloy in 3.5 wt% NaCl solution was studied by E. Lunarska et al [66]. The detrimental effect of zinc was attributed to the formation of $MgZn_2$ at which pits nucleate at their vicinity. Pitting susceptibility increases with the zinc content of the alloy. Alloys with 12.5% Zn were more susceptible to pitting than the two other alloys (8.8, 9.0 %).

Another approach to study the corrosion behaviour of Al-Zn-Mg-Cu alloy has been used by M. Topolski et al [67] who studied the corrosion behaviour of a PM duplex composite alloy prepared from Al-Zn-Mg-Cu alloy and Al-Mn alloy. Corrosion experiments showed that the volume fraction of the two alloys can be modified to suppress the corrosion process. No current flow between the two alloys was observed in a couple of 70% Al-Zn-Mg-Cu and 30% Al-5% Mg. Also, it was proved that each electrode surface had suffered from corrosion. The Al-Mn alloys had undergone pitting corrosion while the Al-Zn-Mg-Cu alloy had undergone intergranular corrosion.

2.3.3 *EFFECT OF HEAT TREATMENT*

The effect of heat treatment on the corrosion resistance of sintered Al-Cu-Mg PM alloy was studied by S. Majado and others [68]. Al-Cu-Mg prealloyed powder was uniaxially pressed, sintered in N_2 for 60 minutes and then heat treated into T4 and T6 conditions. Corrosion behaviour then was evaluated using potentiodynamic polarization in a dilute Harrison solution of a composition 0.35 wt% $(NH4)_2SO_4$ and 0.05 wt% NaCl which is similar to the atmospheric environment for the aircraft. The authors have concluded that the corrosion behaviour of the sintered Al-Cu-Mg alloy is similar or even better than its commercial wrought equivalent. It was also concluded that the heat treatment can improve the corrosion performance of the sintered Al-Cu-Mg alloy. As sintered alloy and its equivalent wrought alloy showed a very similar i_{corr} values, which in turn, found to be higher than those of heat treated samples. Sintered samples heat treated to T6 developed a higher i_{Corr} than that for the T4 state. Since alloys treated in T4 and T6 state presented similar particles density, this conclusion can be explained based on the

copper content difference between the particles and the matrix. Samples in T6 condition showed a major copper content difference between the matrix and the cathodic particles which lead to pit formation through a galvanic cell mechanism.

Saito and Latanision reported the corrosion behaviour of aluminum alloys 2618 and 2024 produced by ingot metallurgy and by hot extrusion [69]. The alloys were tested in the as extruded condition and after natural and artificial aging. The potentiodynamic polarization was performed in a deaerated 0.1 N H_2SO_4 and 0.5 N Na_2SO_4 solution to which of 1000 ppm NaCl was added for pitting studies. The results showed that the fine dispersion of the cathodic $FeNiAl_9$ particles was thought to be the reason behind the slightly better corrosion performance of the powder metallurgy samples. The passive current of the 2618 PM samples found to be similar and increased slightly with increased aging temperature. In chloride containing solution, pits in the naturally aged samples powder alloys were initiated at the interface between the $FeNiAl_9$ and the aluminum matrix, but in the artificially aged PM samples the grain boundaries were the preferred sites for pitting initiation. Pitting potentials of the 2024 PM and conventional aluminum samples were found to be almost constant and no effect of different aging treatment was observed.

2.4 THE PURPOSE OF THE RESEARCH

The purpose of this research is to study the processing and corrosion behaviour of the Alumix 321 aluminum powder metallurgy alloy in 3.5 wt% NaCl solution. The objective is to prepare and process PM samples using different production routes and to study how different processing techniques would affect the corrosion behaviour. The research plan was divided into four main steps:

1-To characterize and study the corrosion behaviour of the commercial wrought aluminum alloy AA6061 which is equivalent to the aluminum powder metallurgy alloy Alumix 321. The corrosion behaviour was studied using open circuit potential (OCP), Tafel extrapolation (TE), cyclic polarization (CP) and electrochemical impedance spectroscopy (EIS). Surface and microstructure of the corroded samples were

characterized. The characterization techniques include optical microscopy (OM), SEM, EDS, X-ray diffraction, and (EPMA).

2-To process, produce and characterize the lab-made aluminum powder metallurgy alloys using Alumix 321 powder. Different production routes were used and their effects on corrosion behaviour were studied.

3-To characterize and study the corrosion behaviour of the PM surface altered lab made samples. Different surface alteration techniques will be used and their effect will be studied. Shot peening, hot rolling, hot swaging, repressing, and resin impregnation will be used in this stage.

4-To compare the corrosion behaviour of the above three systems (wrought, synthesized, and surface altered). The comparison was performed based on their electrochemical behaviour, corroded samples morphology, and the microstructure of the corroded samples.

CHAPTER 3 METHODOLOGY AND EXPERIMENTAL TECHNIQUES

3.1 METHODOLOGY

In the first part of this research, commercially available AA6061 aluminum samples manufactured by ingot metallurgy were prepared for corrosion experiments. The preparation steps involved, cutting, grinding, polishing and cleaning. After sample preparation, corrosion experiments were performed using different electrochemical techniques and then corrosion surface of the corroded samples was analyzed using optical microscope, SEM and EPMA. The second part involved using powder metallurgy technique to prepare samples made of commercially available Alumix 321 powder. Powder samples uniaxially pressed, sintered and then heat treated. Similar to AA6061, the experimental work included studying the corrosion behaviour of sintered powder metallurgy samples and characterization of the corroded surfaces. The electrochemical behaviour of the PM samples was compared to that of the IM 6061.

The third part of this work was devoted to study the effect of post sintering treatments on the corrosion behaviour of powder metallurgy samples made of Alumix 321 alloy. Shot peening, hot swaging, hot rolling, sizing and resin impregnation were used. For peened, rolled, sized and resin impregnated samples, the uniaxial pressing machine was used, while the cold isostatic pressing machine was used to press samples prior to swaging and the effect of these treatments on corrosion behaviour was investigated. After the corrosion experiments, optical microscopy, SEM and EPMA were used to study the corroded samples. The electrochemical behaviour of the surface modified Alumix 321 samples was compared to the PM Alumix 321 alloy to deduce the effect the surface modification has on the corrosion behaviour.

3.2 POWDER CHARCTERIZATION AND SINTERABILTY

3.2.1 *POWDER CHARACTERIZATION*

The powder used for this research was provided by Ecka Granules Inc. It is a commercially available aluminum alloy powder known as Alumix 321. The powder was

pre-blended and contains ~ 1.5 % Licowax as a lubricant to assist in reducing die wall friction. Prior to use, certain characteristics were analyzed and tested. Firstly, chemical analysis was performed to confirm the composition of the as received material. Atomic Adsorption Spectroscopy technique was used for an accurate chemical analysis. The morphology and size of the as received powder were performed using the SEM.

3.2.2 *POWDER BLENDING*

The Alumix 321 powder was received pre-blended and mixed with the lubricant, but due to the possibility of particle setting, blending was performed to ensure powder homogeneity. Figure 3-1 shows a Turbula Model T2M Mixer used to conduct blending. Nalgene bottles having a capacity of 1 liter were used and about 1/3 of its size was occupied by powder. Blending was performed for 20 min.

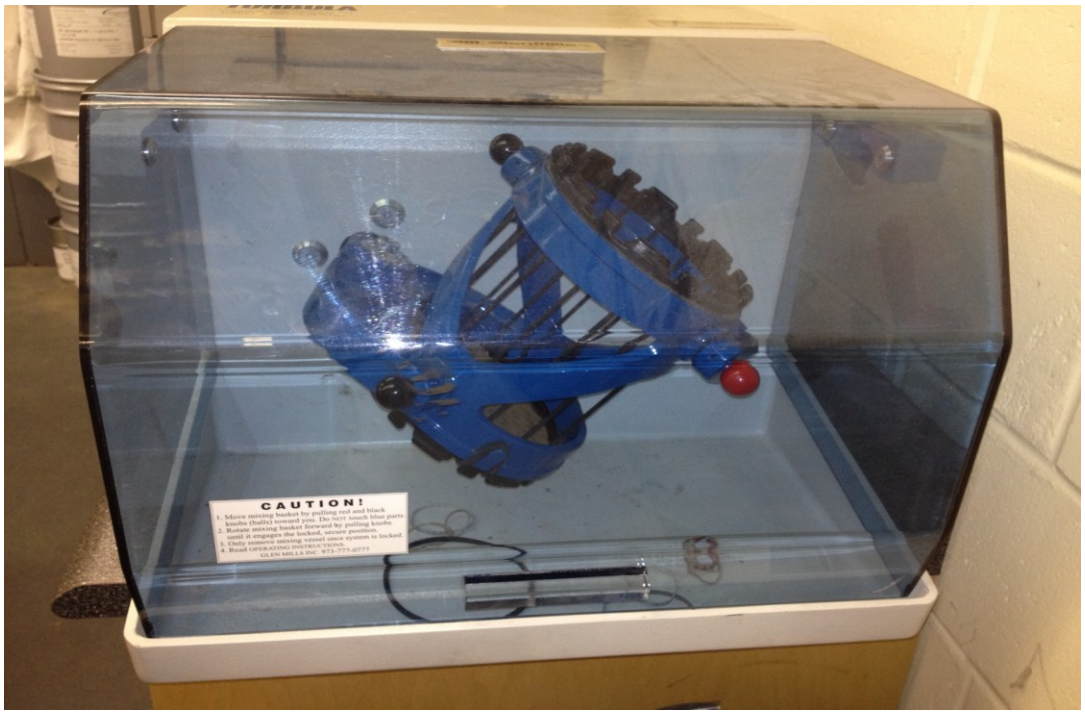

Figure 3-1 Turbula Model T2M Mixer.

3.2.3 *POWDER COMPACTION*

Powder compaction was carried out to produce four different samples geometries. These were transverse rupture strength (TRS), 15mm cylinders (pucks), dog bone (DB) samples and cold isostatic bars (CIP). TRS bars were used for general sintering response evaluation, heat treatment and hardness measurement. The 15 mm pucks were pressed using 2.5 grams of powder and used to evaluate the effect of pressure on sintered density and corrosion study. The DB samples were prepared by pressing 7 grams of powder and used for tensile properties characterization. CIP was used to prepare samples designed for swaging. The cold isostatically bars were pressed using 84 grams of powder using the cold isostatic machine shown in Figure 3-2.

Figure 3-2 Cold isostatic machine.

TRS bars, cylindrical bucks and dog bone samples were pressed uniaxially. Instron SATEC model 5594-200 HVL 1 MN load frame and self contained rigid tooling has been used as shown in Figure 3-3.

Figure 3-3 Instron load frame and self contained DB (left) and TRS (right) tooling.

Green density and green strength were used to evaluate the response of the powder to compaction pressure. Green density measurements were conducted according to MPIF standard # 42 for determination of density of compacted or sintered powder metallurgy products [70]. Green density measurements were performed on TRS bars using a Mettler Toledo AB204-S scale. Firstly, the mass of the samples were measured in air (M_{air}). Next, the samples were hung by a copper wire and submerged in water, and then the measured mass of the samples in water (M_{water}) was obtained. The following equation was used to calculate the green density.

$$Green\ Density\left({}^{g}/_{cc}\right) = \frac{(M_{air} X \rho_{water})}{(M_{air} - M_{water})} \quad (3\text{-}1)$$

Where:

M_{air} =Weight of TRS bar in air (g)

M_{water} =TRS bar weight in water (g)

ρ_{water} =Density of water at the temperature measurements (g/cc)

Three point bend test was used to conduct the green strength tests. TRS bars pressed at different loads were used. The tests were conducted in accordance with MPIF standard# 15 [71] .

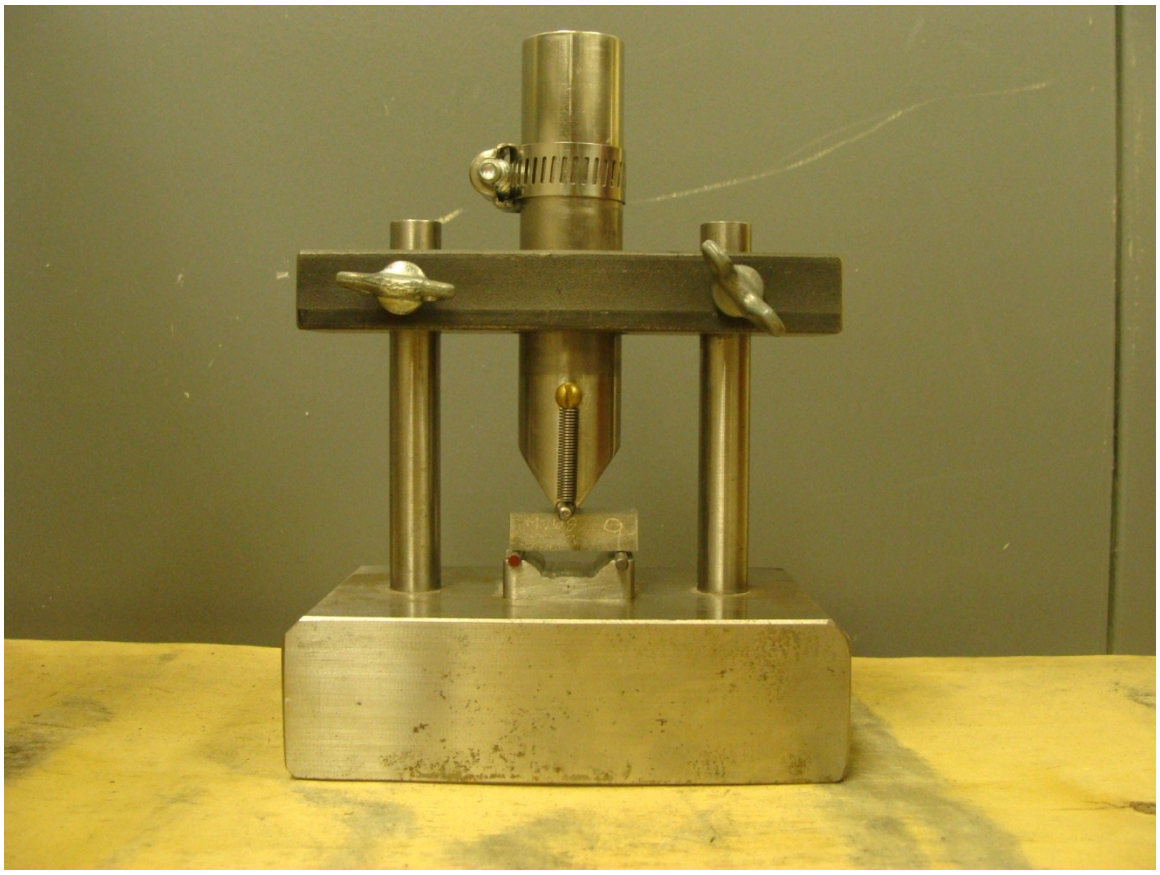

Figure 3-4 Transverse rupture strength test fixture used to measure the green strength

Green strength measurements were conducted using the load frame and the transverse rupture test fixture shown in Figure 3-3 and Figure 3-4, respectively. All samples were loaded to failure and peak load was recorded. The following equation was used to calculate the green strength.

$$S = \frac{3 \times P \times L}{2 \times d^2 \times W} \quad (3\text{-}2)$$

Where,

P =force in required to rupture (N)

L =length of specimen span of fixture (mm)

d=thickness of specimen (mm)

W =width of specimen (mm)

3.2.4 *SINTERING AND SINTERING RESPONSE*

The sintering of green compacted samples was performed in a bell-jar furnace manufactured by Materials Research Furnaces (MRF) shown in Figure 3-5. In all experiments, the samples were set in a stainless steel tray that was then placed at the center of the furnace to minimize temperature fluctuation under 99.999% pure nitrogen atmosphere. The heating process can be divided into three steps: de-lubrication, sintering, and cooling. In the first heating stage, the samples were held isothermally at 390°C for de-lubrication for 30 min. Sintering process consisted of an isothermal hold and was done in the range of 610-640°C for 30 min, post sintering cooling involved a furnace cooling to a temperature less than 100°C.

Figure 3-5 Materials research furnace used for sintering.

3.2.5 *DIMENSIONAL MEASUREMENT*

Dimensional measurement, sintered density and apparent hardness were used to evaluate the general sintering response. In the former, the dimensions of samples were measured before and after sintering and the dimensional change was calculated according to the following formula.

$$Dim.\,Change = \frac{(L_f - L_i)}{L_i} \times 100\% \qquad (3\text{-}3)$$

L_f =Final length

L_i =Initial length

Overall length, width and thickness variation were used to evaluate the dimensional change of the sintered samples. Mass variation of the sintered samples was also used as

another tool of sintering evaluation. Mass of the samples was measured before and after sintering, and then mass loss percentage was recorded.

3.2.6 *SINTERED DENSITY MEASUREMENT*

The density of the sintered samples was conducted using the oil impregnation technique. TRS bars were first weighed in air (W_{air}) and then impregnated in oil under vacuum. After 25 min, the vacuum was released and the samples were cleaned with a Kim wipe and weighed again (W_{oil}) in air. Finally, the samples were hung with a thin copper wire, and then weighed while immersed in water ($W_{oil\&water}$). The process was conducted according to MPIF Standard #42 [70] and the following equation was used to calculate the sintered density.

$$Density\left({}^{g}/_{cc}\right) = \frac{(W_{air} \times \rho_{water})}{(W_{oil} - W_{oil\&water})} \quad (3\text{-}4)$$

W_{air} =Weight of bar in air (g)

ρ_{water} =Density of water (g/cc)

W_{oil} =Weight of bar impregnated with oil (g)

$W_{oil\&water}$ =Weight of oil impregnated bar immersed in water (g)

3.2.7 *HARDNESS AND TENSILE TESTING*

Figure 3-6 shows a LECO R600 hardness tester. This machine was used for apparent hardness measurements. All tests were performed using the HRE scale. In this scale a 100 kg load and an 1/16 inch indenter were used. Prior to testing, samples were lightly ground using a 250 grit silicon carbide grinding paper to help flatten the surfaces and remove any scale formed. Apparent hardness was performed in the as sintered and in T6 condition. Four TRS bars were used per sintering condition. For each bar, two readings were taken on the top of each bar and two on the bottom. This yielded an average of 16 hardness readings.

Figure 3-6 LECO hardness tester.

The tensile testing was conducted on flat dog bone samples in accordance with MPIF standard 10 [72]. Prior to testing, the reduced sections of the tensile samples made of Alumix 321 were lightly ground with 240 grit SiC paper to remove any lip. Cross sectional dimensions measurements were taken at three points along the reduced section, the closer point to the fracture point was used for calculation purposes. All samples were loaded until fracture using self locking flat grips on a hydraulic load frame. An Epsilon 3542 extensometer with a gauge length of 25 mm was attached to the specimens and Partner software was used to record stress and strain.

3.2.8 *HEAT TREATMENT*

Al-Mg-Si alloys are well known for their excellent response to heat treatment. Usually, the heat treatment process is conducted in three steps; solutionizing, quenching and aging. In PM alloys, the most common heat treatment processes are T1 and T6 which refer to as sintered and artificially aged condition, respectively. The Solutionzing step was performed by holding the sintered samples for one hour at 530°C under regular atmospheric conditions. Figure 3-7 shows a Lindberg Blue M Box furnace used to conduct the solution heat treatment.

Figure 3-7 Lindberg furnace used for solution heat treatment before aging.

Artificial aging then carried out using a Fisher Scientific Isotemp oven mechanical convection furnace, shown in Figure 3-8. The aging process involved an isothermal hold

at 160°C for 18 h. In addition to the built in thermocouple an external thermocouple was used to control the temperature.

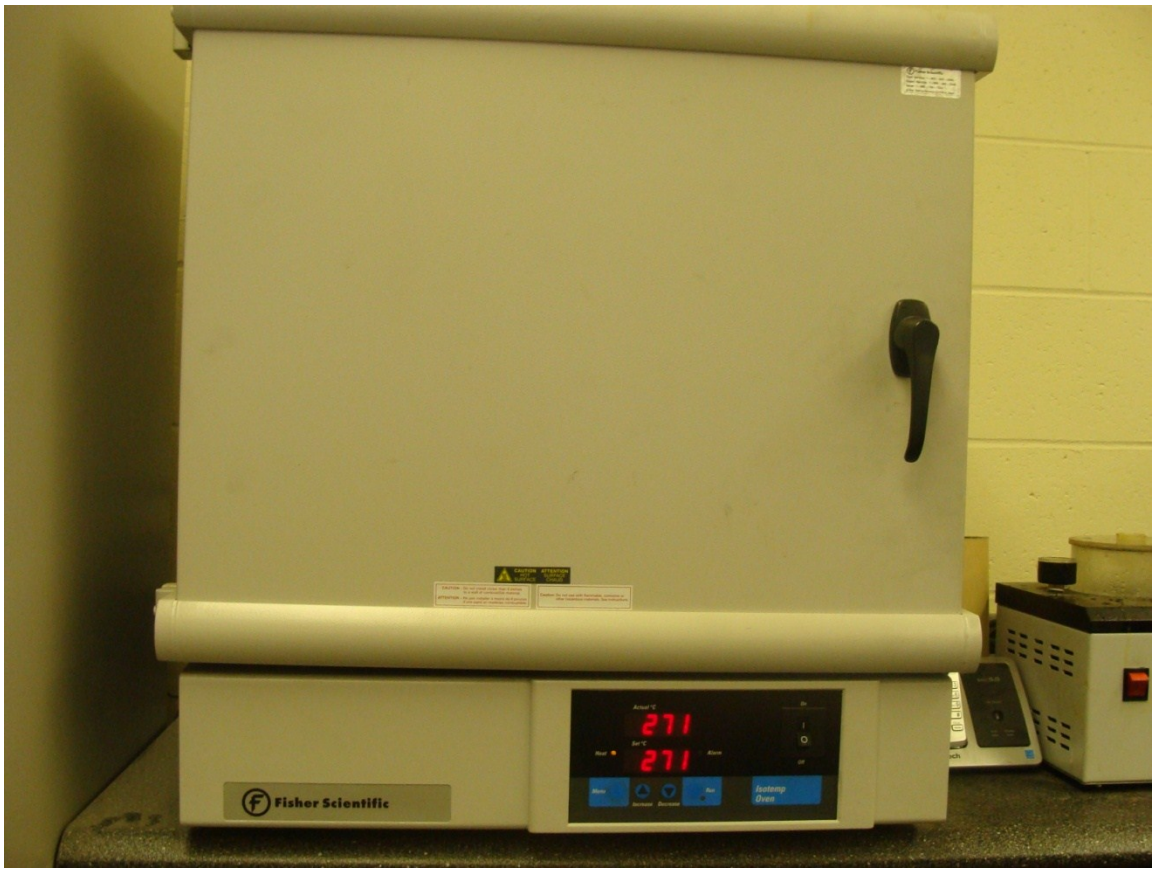

Figure 3-8 Isotemp oven used for aging treatment.

3.3 MICROSCOPY

3.3.1 *OPTICAL MICROSCOPY AND IMAGE ANALYSIS TECHNIQUE*

For metallographic analysis, samples were mounted, ground and then polished samples are mounted in backelite, while for green and fragile samples cold mounted was performed in an epoxy resin under vacuum. The samples then were ground using SiC grinding paper in the range 240-600 grit, and then polished using diamond paste of 9, 6, 3, and 1 µm to obtain scratch free surfaces. Samples then were rinsed in distilled water and dried. It is worth noting that no chemical solvents agents were used to clean the samples for corrosion experiments.

An Olympus BX51-TRF optical microscope shown in Figure 3-9 was used with a built-in digital camera type Olympus DP71. An Image analyzing technique was used to obtain quantitative data from the microstructure. The quantitative metallographic analysis was performed using Image–Pro Plus software version 6.3.

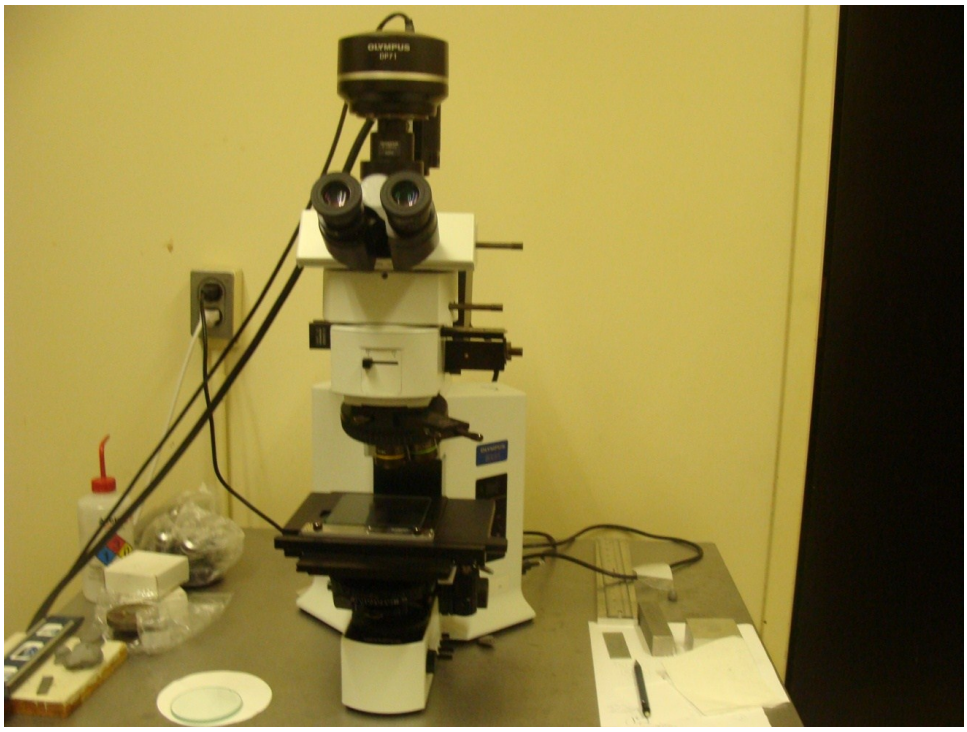

Figure 3-9 Olympus BX51 microscope used for optical microscopy analysis.

3.3.2 *SEM AND CHEMICAL ANALYSIS*

In addition to optical microscopy, a Hitachi S4700 Cold Field Emission scanning electron microscope shown in Figure 3-10 was used to analyze the morphology and size of the raw powder and the sintered and surface modified samples. In terms of corrosion experiments, SEM was used to evaluate the extent and the type of corrosion attack.

The raw powder was prepared for SEM by sprinkling a small amount of powder over a silver paste and dried for one hour. The use of SEM offered information about the morphology and size of the powder. Sintered and surface modified samples were mounted and then analyzed at different directions and images obtained at different magnifications. Corroded samples were dried before the examination and then inserted in the machine and photographed. Some corroded samples were slightly polished and then analyzed to offer a better understanding of the corrosion process and to get more information about the corrosion attack. Energy dispersive X-ray Spectroscopy analyses were performed on all samples using an Oxford X-Sight 7200 Energy Dispersive Spectroscopy system. This was used to determine phases present within sintered samples and corrosion products in corroded samples.

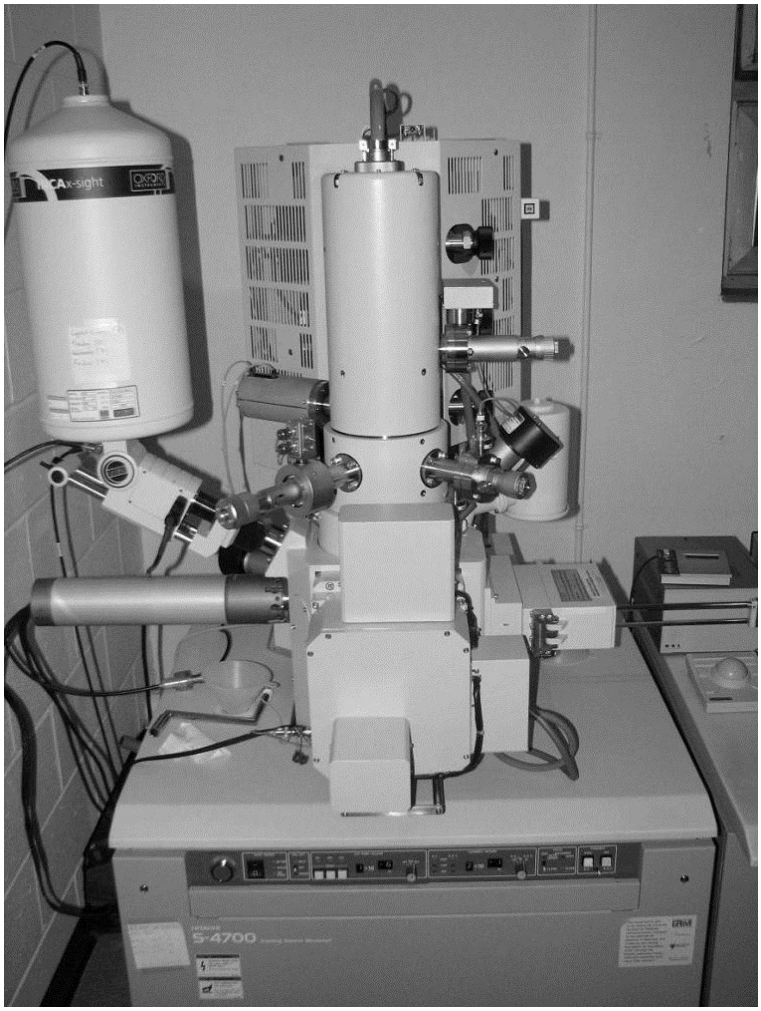

Figure 3-10 Hitachi S4700 SEM and EDS apparatus.

3.4 X- RAY DIFFRACTION

X-ray diffraction was conducted on the raw powders as well as sintered and heat treated samples. It is also used to analyze the corrosion products of corroded samples. Figure 3-11 shows a Bruker AXS D8 Advance x-ray analysis apparatus with a copper X-ray source. All samples were placed in the proper sample holders and a tube voltage of 40 KV and of 40 mA current was used. Samples were then analyzed using EVA analytical software.

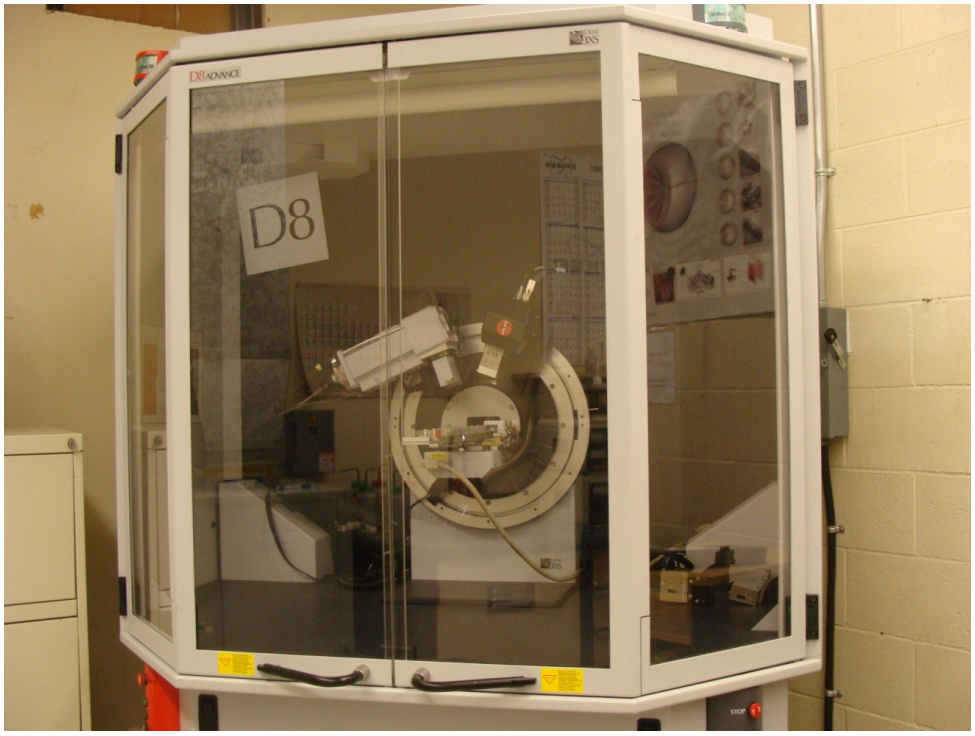

Figure 3-11 Bruker D8-Advance XRD machine used for phase analysis.

3.5 ELECTRON –PROBE MICRO ANALYSIS

Samples were prepared for (EMPA) using the same procedure that was used for metallography. EPMA was performed using JEOL JXA-800 WDS/EDS shown in Figure 3-12. The instrument was calibrated using a set of elemental standards with known values. The elements used for calibration were, Al, Mg, Si, Fe, Cu, and Mn. Back scattered electron images were obtained and the chemical analysis was performed for the matrix, grain boundaries, and intermetallic phases. A minimum of three analysis points were taken for each metallurgical feature of interest and then the average values were reported.

Figure 3-12 EPMA instrument showing sample chamber, spectrometer, and analysis system.

3.6 THERMAL ANALYSIS

3.6.1 *DSC AND TGA*

Differential scanning calorimetry (DSC) and thermal gravimetric analysis (TGA) were performed to offer better understanding of the sintering process of the green compact. This system measures the heat flow and the weight change and offers valuable information about the phase changes. Green samples were cut and ground from the middle of TRS bars into small cylinders of about 4 mm in height and 3 mm in diameter. TA instrument SDT-Q600 shown in Figure 3-13 was used to conduct these experiments. Pure aluminum samples were used for base line, the base line was later subtracted from green samples heat flow obtained. The samples were placed in the instrument and high purity nitrogen gas was passed at a flow rate of 100 ml/min while the sample is then subjected to the desired thermal profile. The temperature profile used was similar to the one used for sintering and the heating rate was 10°C /min.

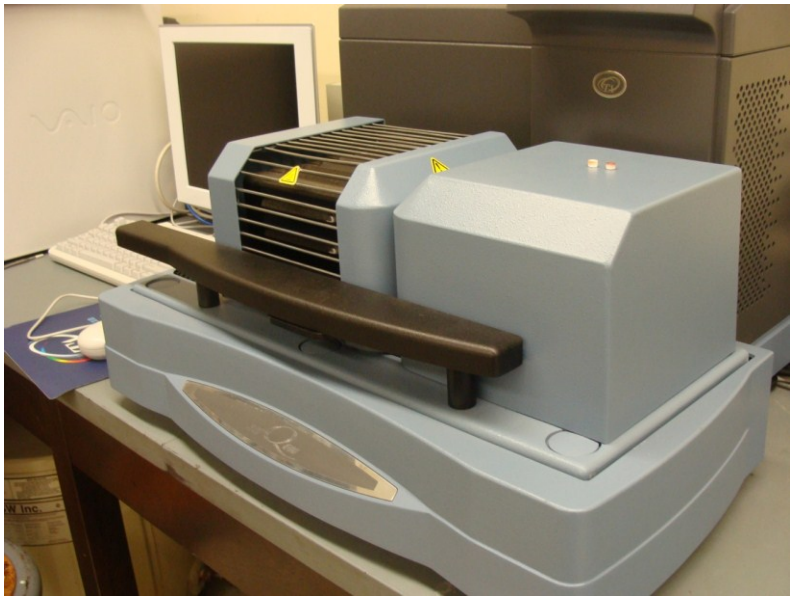

Figure 3-13 Differential Scanning Calorimeter.

3.7 SURFACE ALTERATION TECHNIQUES

3.7.1 *SHOT PEENING*

The shot peening technique was applied to study the effect of shot peening on the corrosion performance of sintered samples. Sintered sample surfaces were shot peened using the Canablast shot peening machine manufactured by international surface technological IST INC, shown in Figure 3-14. Samples were first pressed and then sintered. Prior to peening, sintered samples were ground, polished, and then cleaned using the conventional metallographic preparation techniques.

A sample holder made of steel shown in Figure 3-15, was used to mount the sintered samples. Once the samples were placed into the sample holder, the die was attached to a movable aluminum ram inside the peening chamber which was controlled by an automated actuator system. Magnet was inserted in the chamber to collect any source of iron contamination. Operating parameters were chosen as follow; pressure=35 PSI, distance=6.5 inches, angle=90˚and number of passes were 2 passes. These parameters were chosen to obtain an intensity of 0.4 mm N. The peening media was zirconia (ZrO_2).

Figure 3-14 Canablast shot peening machine.

Figure 3-15 Samples holder used for shot peening.

3.7.2 *SWAGING*

Hot Swaging was performed on a sintered compact billet prepared by cold isostatic pressing. In cold isostatic pressing, a rubber tube was first filled with 85 gram of powder and then sealed using adhesive tape. After the compressing chamber was filled with water, the sealed tube was placed in a steel container that fit inside the compressing chamber. Pressure used was increased up to 30,000 PSI and kept at that value for about 1 minute. Figure 3-2 and Figure 3-16 show the CIP machine and the rubber tubes used, respectively.

Figure 3-16 Rubber mould used for cold isostatic pressing.

The green billet obtained after cold isostatic pressing had an average diameter of 21.65 mm and later it was subjected to hot swaging process. Swaging machine and swaging die are shown in Figure 3-17 and Figure 3-18, respectively.

Swaging is the process used to deform the work piece diameter by passing it through a number of dies. As the billet is forced through a four segment dies, its diameter reduced and the sample elongates.

Figure 3-17 Swaging machine.

Prior to swaging, the green billets were placed in a furnace set to 500 °C for 1 h. After the billet got homogeneous, the heated billet was swaged and returned back to the furnace for the next swaging step. Five sets of decreasing diameters dies were used for a total cross sectional reduction of approximately 34%. As the desired diameter was obtained, swaged bars were machined into disks and then heat treated into T6 condition.

Figure 3-18 Four segment die used for swaging.

3.7.3 *SIZING*

Sizing is a post sintering process in which low strain is used to adjust the final dimension of the compact. In all the sizing experiments, sizing was performed on samples after sintering. The 15 mm cylindrical bucks were initially pressed and sintered and then sized using a universal testing system SATEC (5594-200 HVL). Sizing was done using the same machine and the same die as for pressing. Prior to sizing, the 15 mm pucks were slightly

ground using a 230 grit SiC paper and then soaked in sizing lubricant for about 2 minutes, the lubrication being used to reduce the friction effect and ease sized pieces removal from the die. The sizing load was in the range of 50-180 MPa and the percentage of the reduction in thickness was kept in the range of 2-5%.

3.7.4 *ROLLING*

Slabs were prepared first by pressing and sintering. Forty grams of powder was used to produce slabs with dimensions 92.45 mm X 20.40 mm X 8.26 mm. Green compacts were pressed at 500 MPa using a universal testing system SATEC (5594-200 HVL). Green slabs were then sintered and hot rolled using a rolling machine. Prior to rolling, the sintered slabs were heated in a furnace set at 500°C for 1 hour and then placed between the rolling mills. The rolling process was performed through sequential steps, and each step was controlled by adjusting the distance between the rolling mills. In total, the thickness of the sintered slab has been reduced from 8.26 mm to 6.03 mm resulting in 27% reduction.

3.7.5 *RESIN IMPREGNATION*

Resin impregnation was used to study the effect on the corrosion resistance of filling the pores with the epoxy resin. It is also used to study the effect of surface area on corrosion resistance. For this experiment a castable vacuum system from Buehler was used. The set up contains two chambers, one to evacuate the samples and the other was to hold the resin, the two chambers are connected by a plastic tube which is controlled by a valve. Figure 3-19 shows the impregnation unit. Samples were pressed at 100 MPa and then sintered. Prior to resin impregnation, the samples were ground, polished and then cleaned. The impregnation procedure was performed in many steps; the first step was to place the samples in a vacuum chamber and then apply vacuum to remove adsorbed air from the pores. Samples were kept under vacuum for about 10 minutes. The second step was to transfer the resin to the vacuum chamber by opening the valve that connects the two chambers, and the process of impregnation continues until the samples get covered. In the next stage the vacuum was released and pressure

was applied on the sample. Finally, the samples were removed and cleaned with a tissue and slightly polished, photographed and then tested for corrosion. The epoxy resin used in this experiment was provided by Buehler and used originally for samples mounting. It is known as Epo colour dye enhanced epoxy. The resin composes of Bisphenol, Alkyl glycidyl ether, and Acrylic ester. The hardner composes of poly a mine, diethylen etriamine, and Triphenyl.

Figure 3-19 A castable vacuum system used for resin impregnation.

3.8 SURFACE CHARACTERIZATION AND METROLOGY

3.8.1 *PROFILOMETRY*

Profilometry was applied for shot peened samples in order to follow the effect of peening on surface morphology and roughness. Optical profilometry is one of the non contact surface metrology techniques and used to scan surfaces and provide information about sample's topography. Prior to scanning, pressed and sintered samples where ground, polished, and then cleaned. In case of shot peened samples no further preparation was performed. The samples were scanned before and after peening. After scanning, roughness was recorded and images of samples surface topography were taken.

An optical profilometer manufactured by Nanovea model P550 is shown in Figure 3-20 and was used to conduct the profilometry measurements. The machine was attached to a high resolution optical sensor and 1.2 mm optical pen with a resolution of 0.1 µm was used to scan the samples.

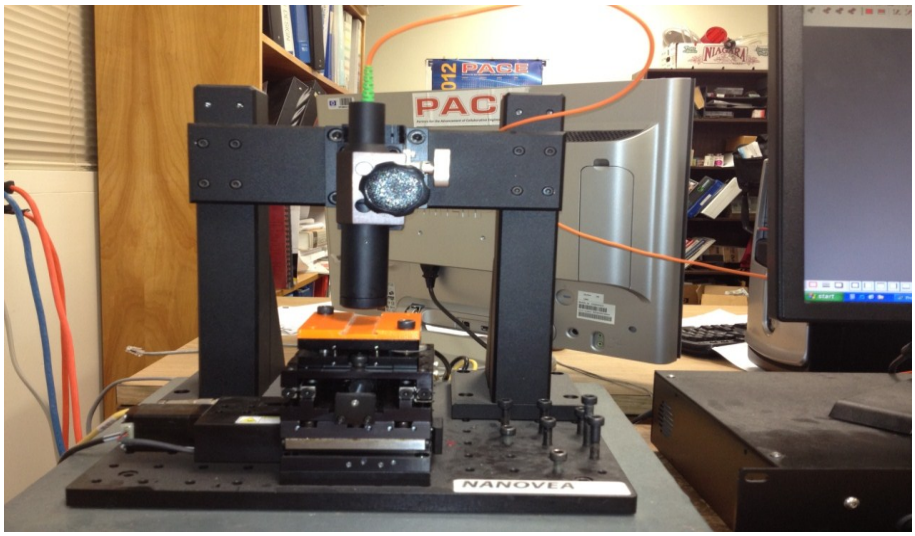

Figure 3-20 P550 optical profilometer.

3.9 CORROSION PERFORMANCE

3.9.1 *ELECTROLYTE PREPERATION*

In this research all the corrosion experiments were conducted using a synthetic electrolyte consisting of a solution of 3.5 wt% analytical grade NaCl in deionized water. The NaCl obtained from Fisher Scientific and the deionized water was provided by the Mineral Engineering Center at Dalhousie University. The pH of the solution was between 6.2 and 6.8. All the experiments were performed at a controlled temperature of 22±1 °C using a Dyna-Sence thermo regulator control system.

3.9.2 *ELECTROCHEMICAL CELLS AND ELECTRODE SET UP*

Standard electrochemical cell was used in this research. The cell is shown in Figure 3-21 and known as a bulb cell, and has been standardized by ASTM. The working electrode assembly is shown in Figure 3-22.

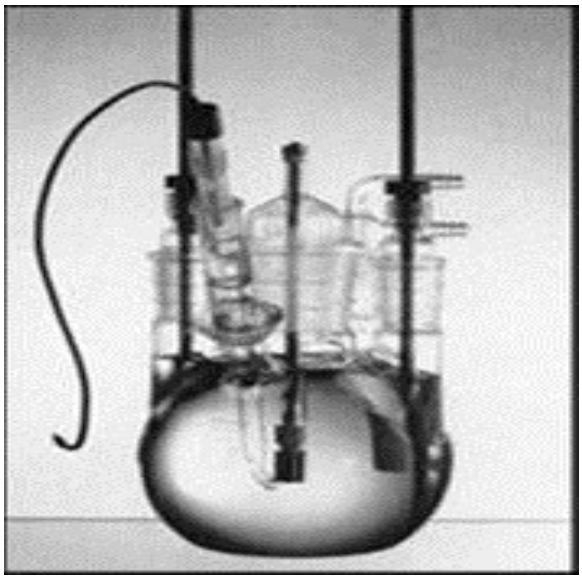

Figure 3-21 The three electrode traditional cell.

It consists of an electrode holder made of Teflon and is designed to accept specimens of 1.5 cm in diameter, at the top of the sample holder there is a threaded hole where a stainless steel bar fitted in a Pyrex tube is threaded in. The sealing washer was made of Teflon and exposes 1 cm^2 of the sample to the test solution; the washer has a knife edge

design in order to minimize the crevice effect. The potential of the working electrode is measured using a saturated calomel electrode (SCE) reference electrode through a Luggin capillary. A graphite rod of surface area 3.85 cm^2 was used as a counter electrode.

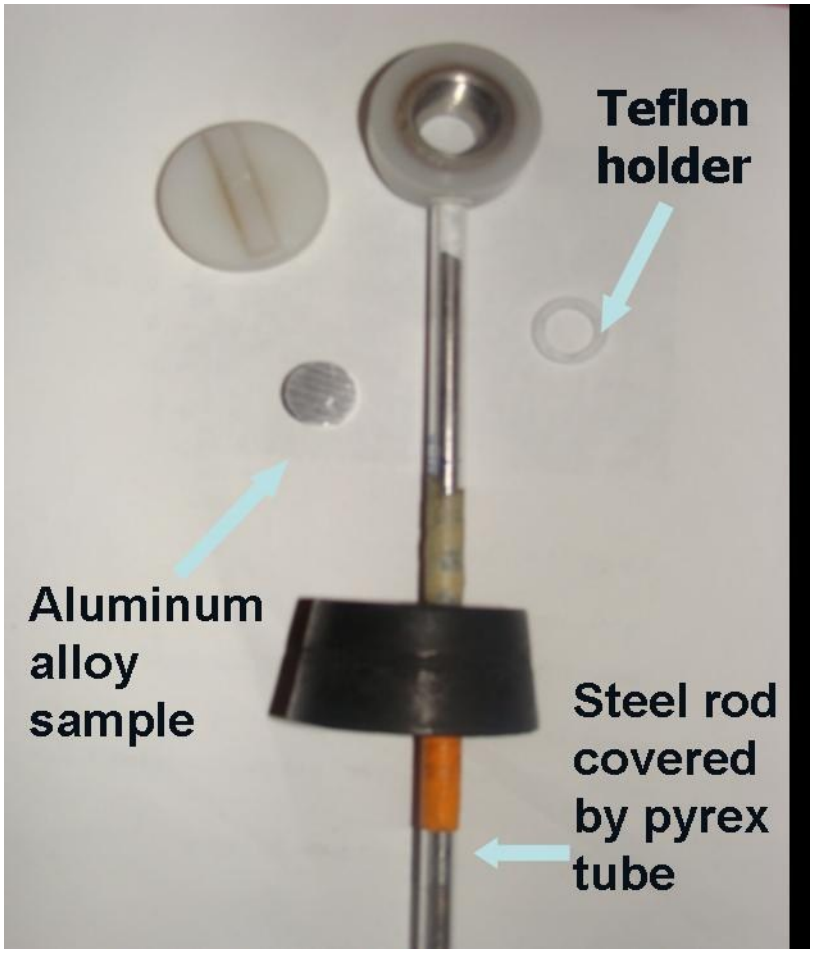

Figure 3-22 The asembly of working elctrode.

Samples used for corrosion testing were wrought, sintered, and surface modified sintered alloys. Wrought samples were cut from a AA6061-T6 15 mm diameter rod. Each sample was cut into 6mm thick disks using a isomet Low-speed cut-off machine. Sintered and surface altered samples made of Alumix 321 were already pressed using 15 mm disk die and there was no need for further machining. Except for shot peening in which the samples tested in the as peened condition, disc samples were ground sequentially from 240 to 600 grit using abrasive SiC paper. The test samples were then

polished with a diamond suspension solution at 9, 6, 3 and 1µm. Finally, the samples were cleaned using deionized water, dried and tested. A potentiostat EG&G PARC model 273A, Princeton Applied Research, USA was used to perform Tafel extrapolation, Cyclic polarization, and Stair case polarization. The instrument was controlled by a corrware software which was provided by Scribner Association, Inc. Figure 3-23 shows the potentiostat.

Figure 3-23 EG&G 273 A potentiostat.

3.9.3 *OPEN CIRCUIT POTENTIAL*

Open circuit potential experiments were performed prior to each electrochemical experiment. In this kind of experiments, the working electrode was exposed to the electrolyte in the open circuit condition until the measured potential reached equilibrium. The open circuit potential was monitored as a function of time until almost a constant potential was obtained. Wrought samples were kept for 1 hour. In the case

of sintered powder samples and due to its nature, the samples were kept in the electrolyte for 24 hours and then OCP was recorded for 2 hours.

3.9.4 *TAFEL EXTRAPOLATION TECHNIQUE*

The Tafel extrapolation technique was used to measure the corrosion current and potential; the former can be used to calculate the corrosion rate. In Tafel extrapolation experiments, the working electrode was polarized in the range of -1 V/SCE and 0 V/SCE. A scan rate of 0.1667 mV/S was used in all experiments. The corresponding current density was recorded as a function of applied potential and the resulting curve is a plot of potential vs. the logarithmic of measured current. Corrview software was used to analyze the resulting curves and corrosion current and corrosion potential were obtained by superimposing a straight line along the cathodic and the anodic part of the plot.

3.9.5 *CYCLIC POLARIZATION*

The purpose of cyclic polarization is to measure the pitting tendencies of a metal in a given environment. The working electrode was polarized in the forward direction from an initial potential of -1.25 V/SCE, and when the scan reached 0 V/SCE, it was reversed and began scanning in the negative direction. The final potential of the scan was -1.5 V/SCE.

3.9.6 *STAIR STEP POLARIZATION*

Slower scan rate has been achieved using the stair step polarization. In this technique, the potential was scanned in a form of stairs and the potential was kept at that potential for a certain amount of time. The potential was initially scanned from -1 V/SCE and the final potential was -0.65 V/SCE. Step size used was 10mv and the potential was kept at each potential increment for 2500 sec. This procedure offers a very slow scan rate and 24 hours were needed to complete one experiment.

CHAPTER 4 RESULTS AND DISCUSSION

4.1 MATERIALS

The powder material used in this research is a commercially available alloy known as Alumix 321. The raw material is obtained in a form of powder and was provided by Ecka Granules Inc. Alumix 321 is the powder commercial equivalent to AA6061 aluminum alloy. The powder in its as received condition has been characterized prior to use. Initially, chemical analysis was performed by Atomic Adsorption Spectroscopy (AA). The results of the as received Alumix 321 powder are given in Table 4-1. The complete chemical analysis is shown in Appendix A.

Table 4-1 Chemical analysis of as recieved Alumix 321 raw powder.

Element	Mg	Si	Cu	Fe	Bi	Sn	V	Al
Wt-%	1.31	0.5	0.32	0.10	0.01	0.03	0.01	Bal

The main alloying elements in this system are magnesium and silicon. These two elements are the basis of the heat treatment of this system. They form Mg_2Si intermetallic phase which improves the mechanical properties. Copper is also responsible to improve mechanical properties. Iron exists as an impurity and forms different intermetallic phases which affect corrosion and mechanical properties, while Sn, V, and Bi were added to improve sinterability of the powder.

In addition to the chemical analysis, size and morphology assessment has been performed using the SEM. Figure 4-1 shows the size and morphology of the Alumix 321 powder. Slightly spherical particles with a diameter of about 35 µm were observed along with some of more elongated particles as shown in Figure 4-2. This variation in shape is an indication of different techniques used to produce the blend. Spherical particles are typical of gas atomized, while the irregular shape is due to some other powder production method such as mechanical or chemical techniques.

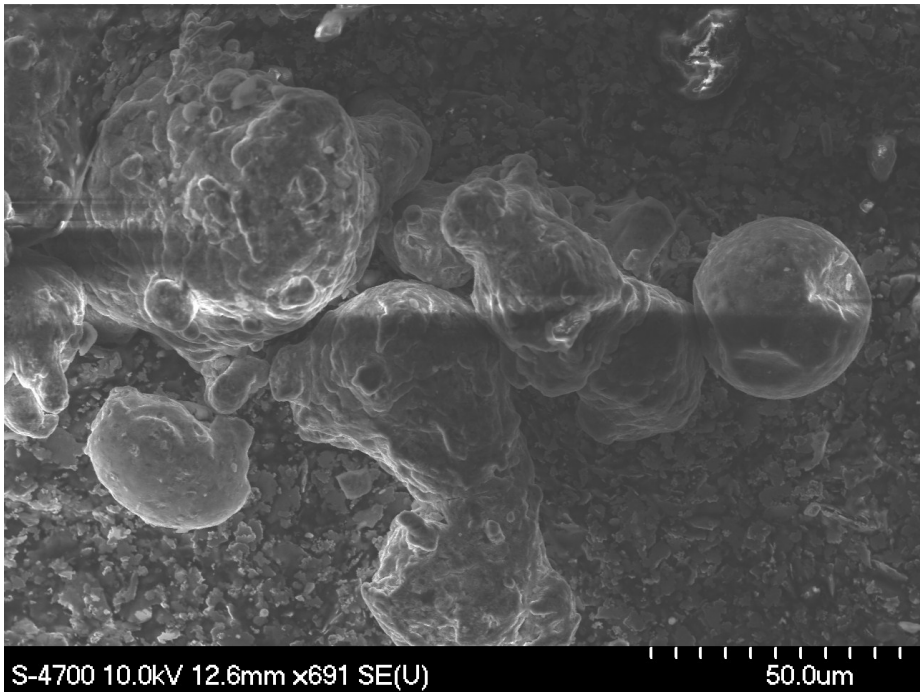

Figure 4-1 SEM micrograph of the as recieved Alumix 321.

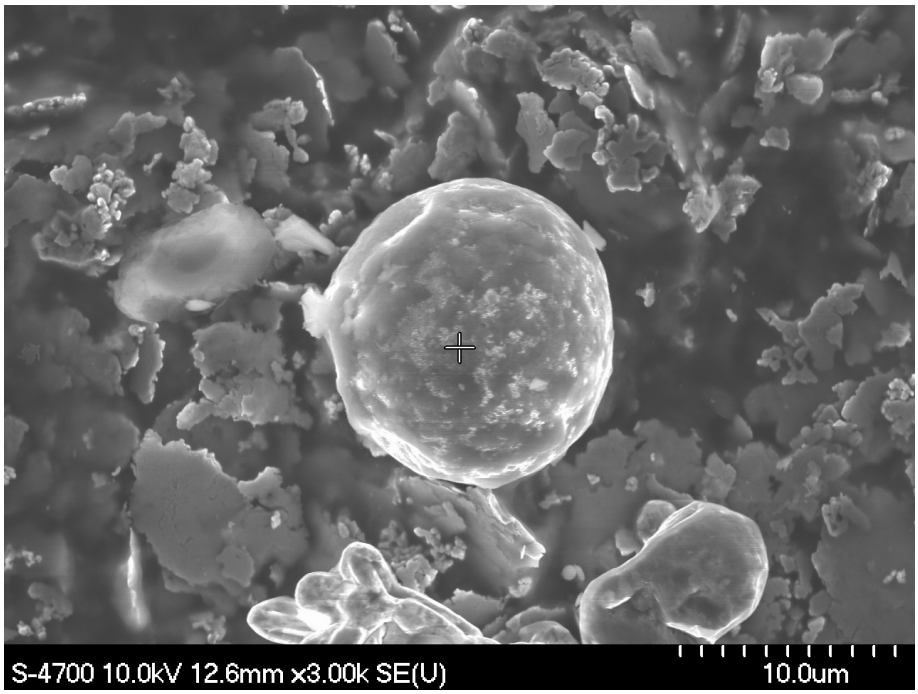

Figure 4-2 SEM image shows spherical and elongated particles.

For more assessment of these kind of powders EDS analysis was performed. Figure 4-3 shows the line scan through the two types of powders. The EDS spectra show that the spherical particles are composed of magnesium while the irregular particles show the presence of aluminum and silicon. For more evaluation and understanding of this blend, the green compact was mounted, polished and scanned via the scanning electron microscope. The results confirmed the presence of Al-Si master alloy while, aluminum, magnesium and copper were added in elemental form.

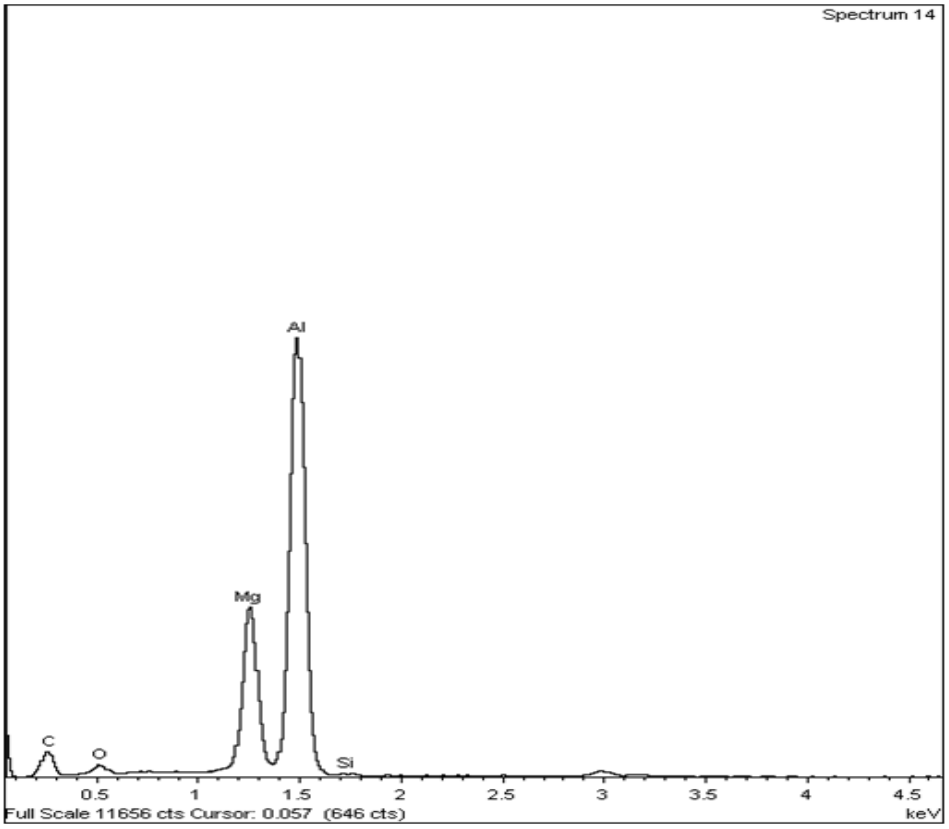

Figure 4-3 EDS spectrum through two types of powder.

4.2 COMPACTION RESPONSE

Initially, the compressibility of the as received Alumix 321 powder was studied. The compressibility of the powder was studied by pressing the powder in the range of 100-500 MPa and the response was characterized using green density and green strength.

4.2.1 *GREEN DENSITY*

Figure 4-4 shows the variation of the green density as a function of the compaction pressure. It is clear that the green density increases steeply with the compaction pressure and then gradually levels off, it is worth noting that any increase in pressure beyond 500 MPa will not yield any significant increase in green density; contrary, higher pressure would begin to become less practical due to die wearing problems.

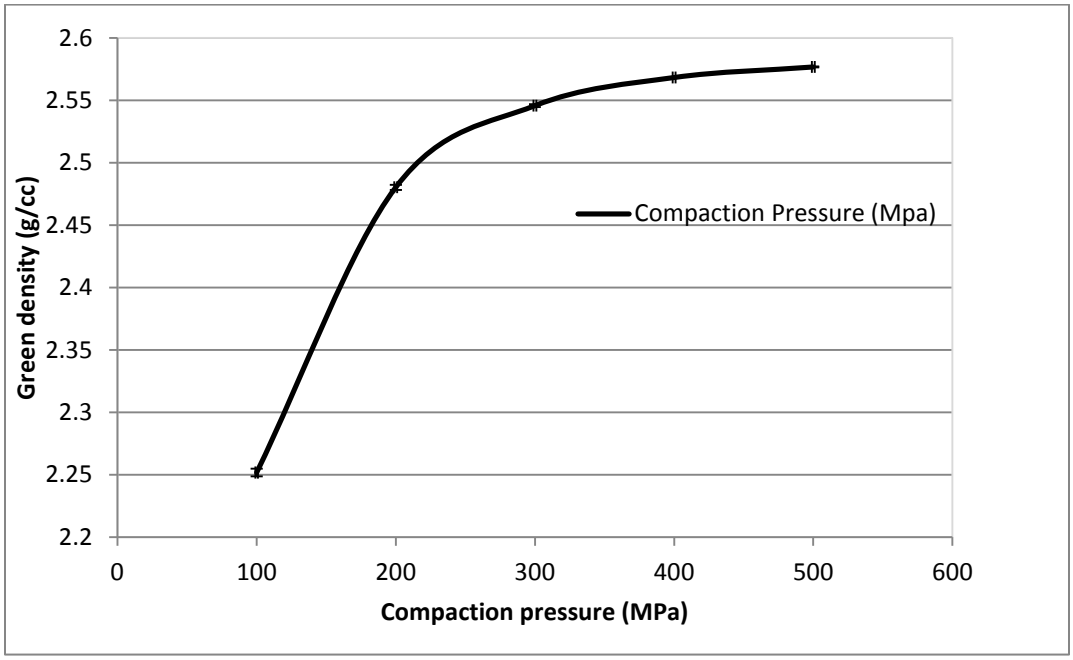

Figure 4-4 Compaction curve of Alumix 321.

4.2.2 *GREEN STRENGTH*

Data on green strength as a function of compaction pressure are shown in Figure 4-5. The curve demonstrates a similar trend to that of the green density variation. However, the plateau appears between 200-400 MPa and then a slight increase in strength appears at 500 MPa. The overall relation between the two parameters appears to be linear and seems comparable to the green density variation.

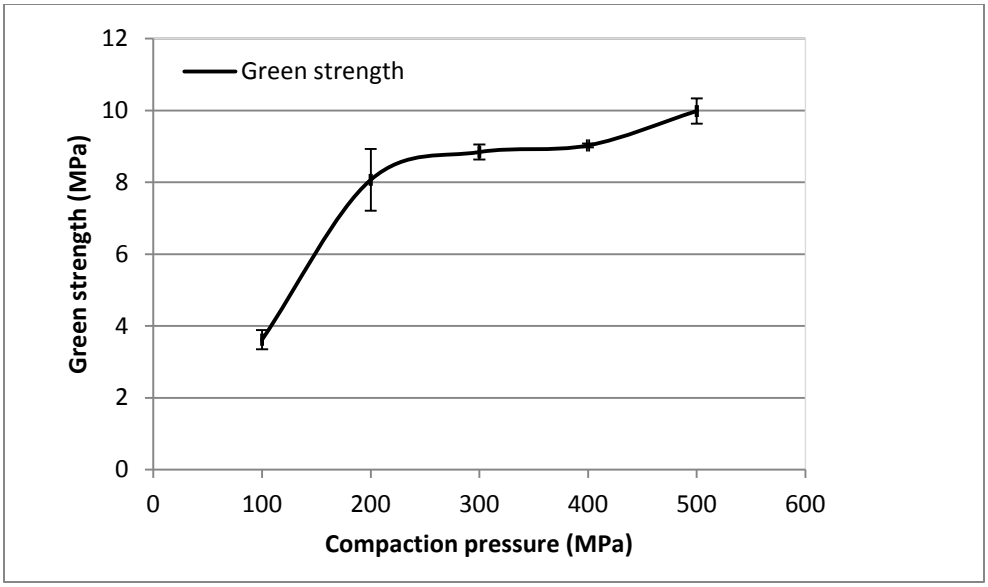

Figure 4-5 Green strength as a function of compaction pressure.

4.3 SINTERING RESPONSE

4.3.1 *EFFECT OF COMPACTION PRESSURE AND SINTERING TEMPERATURE*

Initially, the effect of sintering temperature on Alumix 321 alloy to yield the best possible performance of the material was evaluated. This was performed by evaluating the sintering response of Alumix 321 pressed at 200 and 400 MPa and sintered at four different temperatures ranging from 610-640 °C at increments of 10 °C. For this, TRS bars were used and the assessment included the measurement of dimensional change, sintered density and apparent hardness.

The dimensional variations at each sintering temperature were measured in three orientations. Figure 4-6 and Figure 4-7 show that the percentage of reduction recorded was 2.5% and 4% for samples pressed at 200 MPa and sintered at 630 °C and 640 °C respectively, while samples pressed at 400 MPa showed a smaller amount of shrinkage. The largest amount of shrinkage obtained was 2% and associated with sintering at 640 °C. Data for width and length changes were almost similar especially at lower sintering temperatures (610, 620, 630 °C), while the dimensional changes in the overall length (OAL) shows the largest variation across the spectrum of sintering temperatures. From

the results it became clear that the largest amount of shrinkage and robustness occurred at 630 °C and 640 °C.

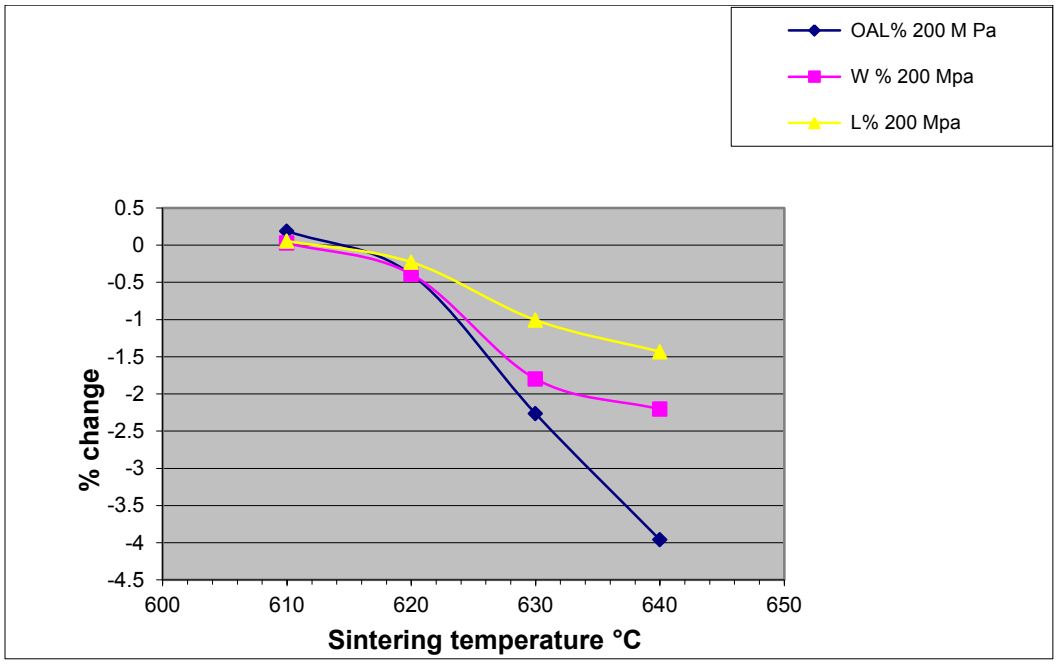

Figure 4-6 Dimensional change of Alumix 321 as a function of sintering temperature.

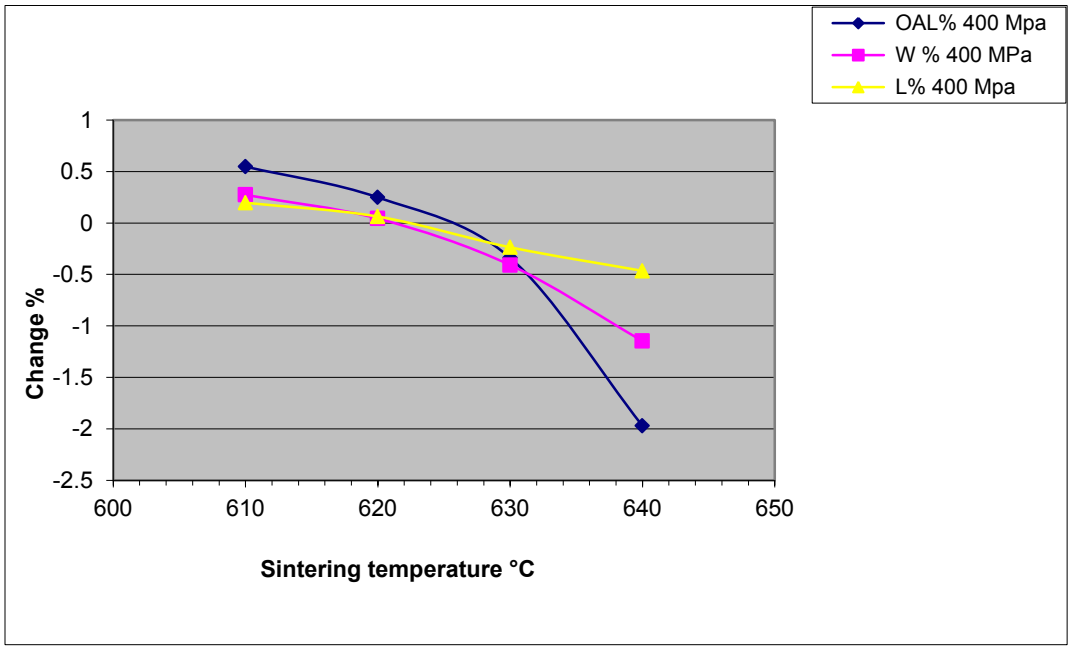

Figure 4-7 Dimensional change of Alumix 321 a function of sintering temperature.

In addition to dimensional changes, density measurement was also conducted on samples from each of the four sintering temperatures. Figure 4-8 illustrates the density variation of sintered samples pressed at 200 and 400 MPa. The sintered density at higher temperatures shows higher values compared to those sintered at lower temperatures. Data demonstrated that sintering temperature of 610 °C and 620 °C was too low and resulted in samples of significantly reduced density relative to the samples sintered at higher temperatures (630 °C, 640 °C). It can be concluded that at higher temperatures, a larger amount of liquid is produced which will lead to a larger amount of shrinkage as shown in Figure 4-6 and Figure 4-7, consequently, improving the densification mechanism and higher density values produced. On the other hand, the effect of compaction pressure is not clear. Figure 4-8 illustrates that the relation between pressure and density is linear for samples pressed at 200 MPa and sintered at lower temperatures (610 °C, 620 °C). An adverse effect has been observed for samples pressed at 400 MPa and sintered at 630 °C and 640 °C, in which higher pressure resulted in lower density. The non linear relation between sintered density and compaction pressure suggests that although the sintering treatment cycles have been performed under the exact same conditions, some other factors such as, local temperature inhomogeneity, chemical composition inhomogeneity and green density distribution may play a role.

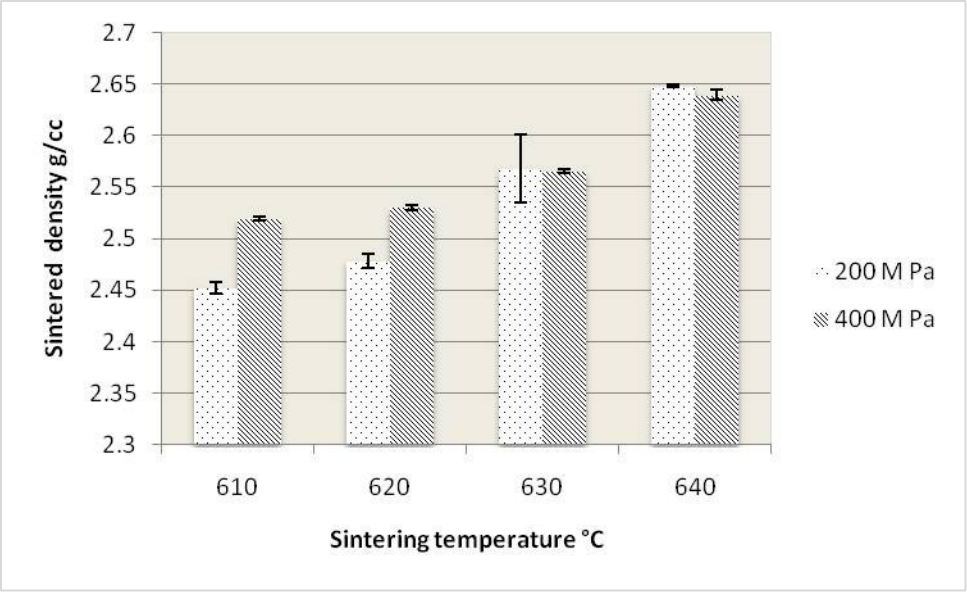

Figure 4-8 Variation of sintering density as a function of pressure and temperature.

One option used to minimize the density variation was to reduce the sample size. A different die has been used to produce disk samples with smaller size (15mm diameter and 7mm thickness). Another sintering profile has been performed based on the disk samples through the range of sintering temperatures and pressures. Figure 4-9 illustrates the effect of sintering temperature and pressure on Alumix 321 pressed into the disk shape. In this profile, the samples were pressed between 100 to 500 MPa and sintered at different sintering temperatures. The important conclusion about the behaviour of the disk samples in contrast of the TRS samples is the linear variation of density as a function of pressure. It is clearly seen that samples pressed at higher pressure and sintered at higher temperature showed a better densification. The plot shows that samples sintered at industrially sintering temperature (630 °C) [73] show the density gradient that is a function of pressure. A theoretical density (TD) of 98.4 % was obtained at 500 MPa and 630 °C, this value was reduced to 95.6% for samples pressed at only 100 MPa. In addition to the effect of pressure, sintered density found to depend on sintering temperature: a similar trend has been observed for TRS samples.

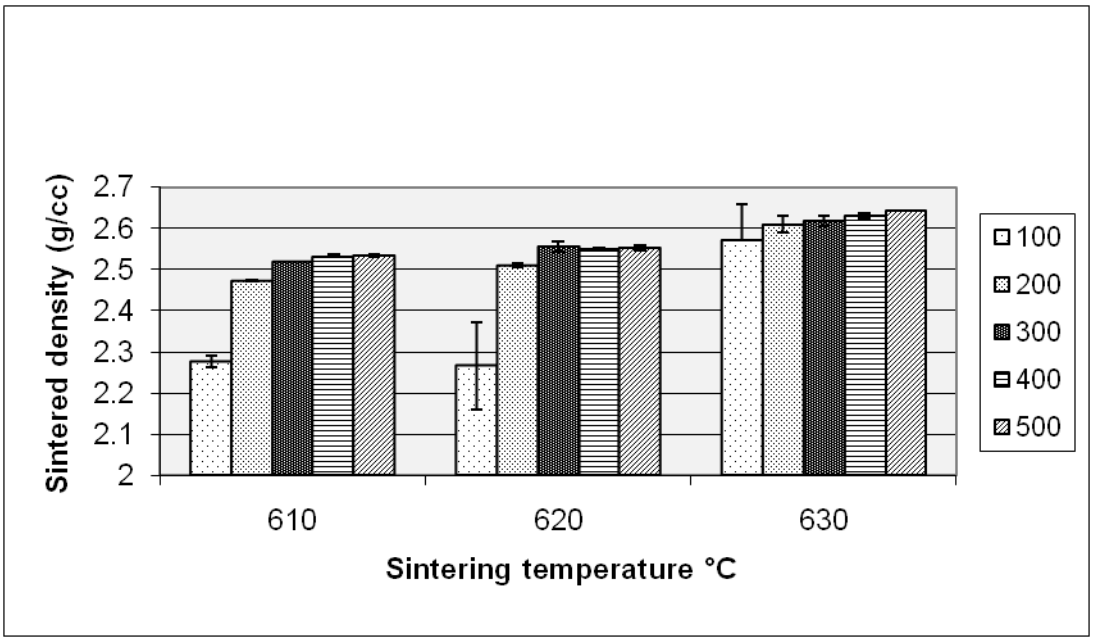

Figure 4-9 Effect of sintering temperature and pressure on density of Alumix 321 disk samples.

4.3.2 *HEAT TREATMENT AND MECHANICAL PROPERTIES*

In addition to the sintered density, a response to sintering was also assessed by conducting hardness measurements. Here, measurements were conducted in as sintered and aged condition. Figure 4-10 illustrates the variation of apparent hardness as a function of compaction pressure and sintering temperature for both as sintered and as aged conditions. The data show that the hardness of Alumix 321 under these two tempers increases as the sintering temperature is increased. For aged samples, almost equal values of 98 HRE were obtained at 640 °C by pressing at 200 and 400 MPa respectively, while at the lowest sintering temperature (610 °C) and at the same pressing pressure (200, 400 MPa), hardness obtained was 81 and 87 HRE, respectively. For those set of samples pressed and sintered to similar industrial conditions (200-400 MPa, 630 °C), hardness values are very close to the values published by the Ecka granules company [73]. The linear relation between sintering temperature and hardness has also been observed for the as sintered samples. The hardness values obtained at 640 °C were 47 and 43 HRE for samples pressed at 200 and 400 MPa, respectively. Lower values were obtained at lower sintering temperatures. Only 19 and 27 HRE were

obtained by sintering at 610 °C and pressing at 200 and 400 MPa respectively. Interestingly, hardness follows the same trend observed by density as shown in Figure 4-7. The effect of pressure on the hardness clearly appears at lower sintering temperature, while at higher sintering temperatures, the effect does not exist. Despite the general increase of hardness as a function of sintering temperature, solutionized and aged samples show a higher hardening response compared to the as sintered samples.

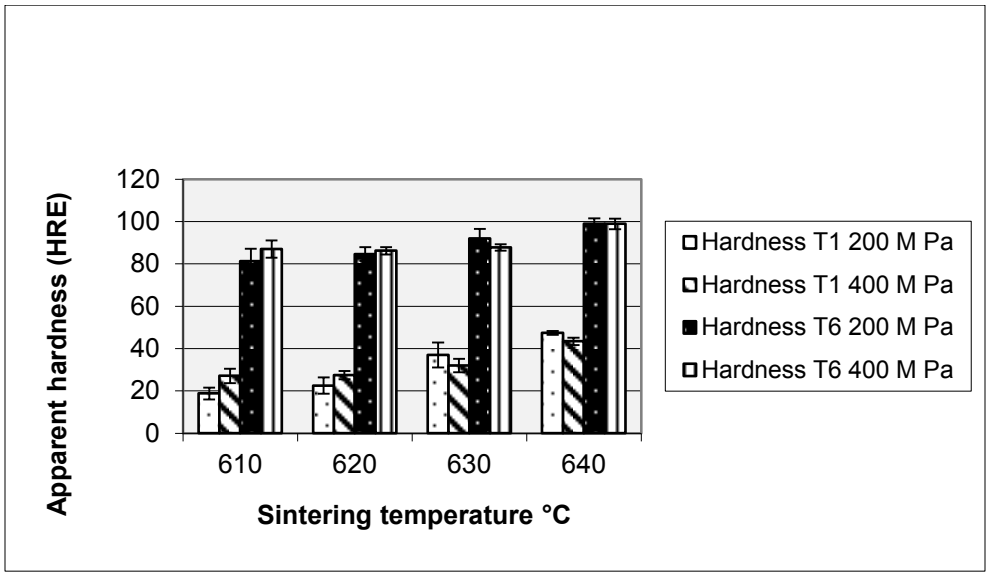

Figure 4-10 Variation of hardness and sintering temperature as a function of sintering temperature and compaction pressure.

For the tensile tests, Alumix 321 powder was compacted at 100, 200, 300, 400, 500 MPa and then sintered at 630 °C. The dog bone samples then heat treated into T6 condition and tensile tests were performed at room temperature. Figure 4-11 and Figure 4-12 show the average values of yield strength and ultimate tensile strength, respectively. The trends in tensile properties followed the same trend for green density, green strength and sintered density. Yield and tensile strength in T6 temper revealed an increase as a function of pressure. It can be noticed that for both of these properties, 100 MPa pressing pressure shows the lowest values, following that, slight increase in strength appears that levels off at 300 MPa and continues up to 500 MPa. This is in

agreement with the results of green strength and density in which further increase of pressure than 400 MPa does not show much increase in properties.

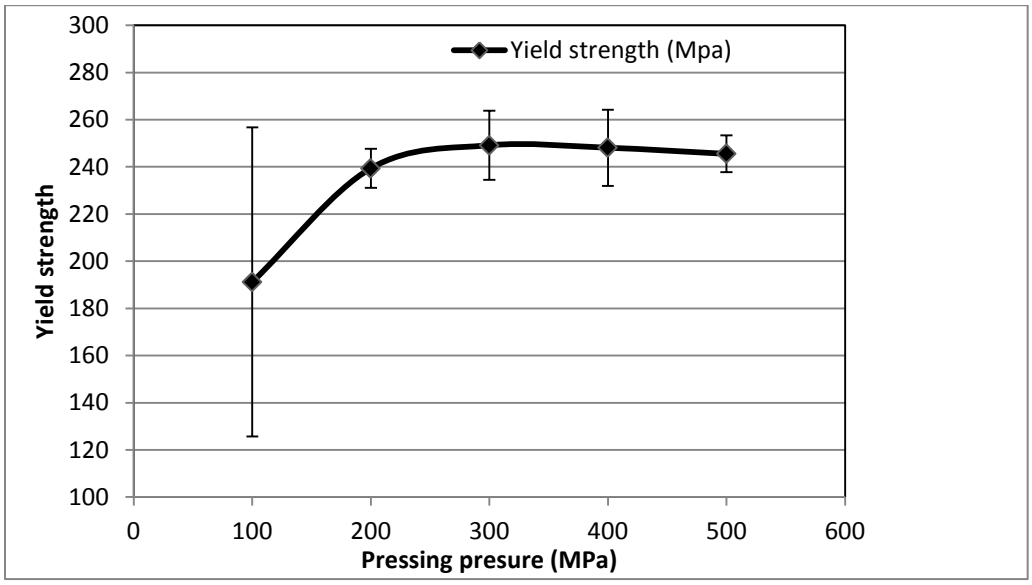

Figure 4-11 Yield strength of Alumix 321 as a function of compaction pressure.

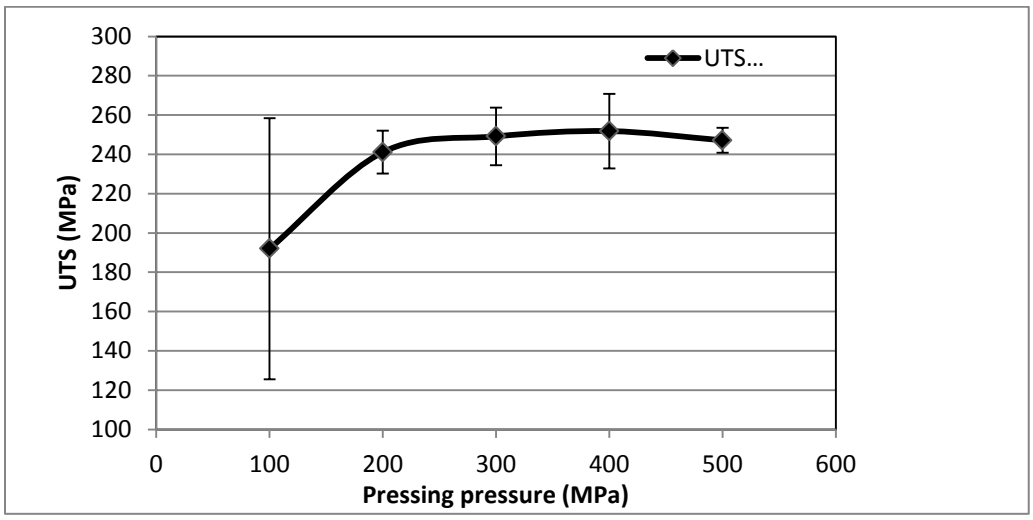

Figure 4-12 Ultimate tensile strength of Alumix 321 PM alloy as a function of compaction pressure.

In addition to yield and tensile strength, ductility was assessed during the tensile testing. This was measured using percentage of elongation to failure. Figure 4-13 shows the effect of compaction pressure on percentage of elongation. The overall trend shows

that the alloy showed low ductility which appears from the small percentage of elongation recorded. The data reveals that pressing at 500 MPa produced the highest percentage of elongation among the whole pressing range.

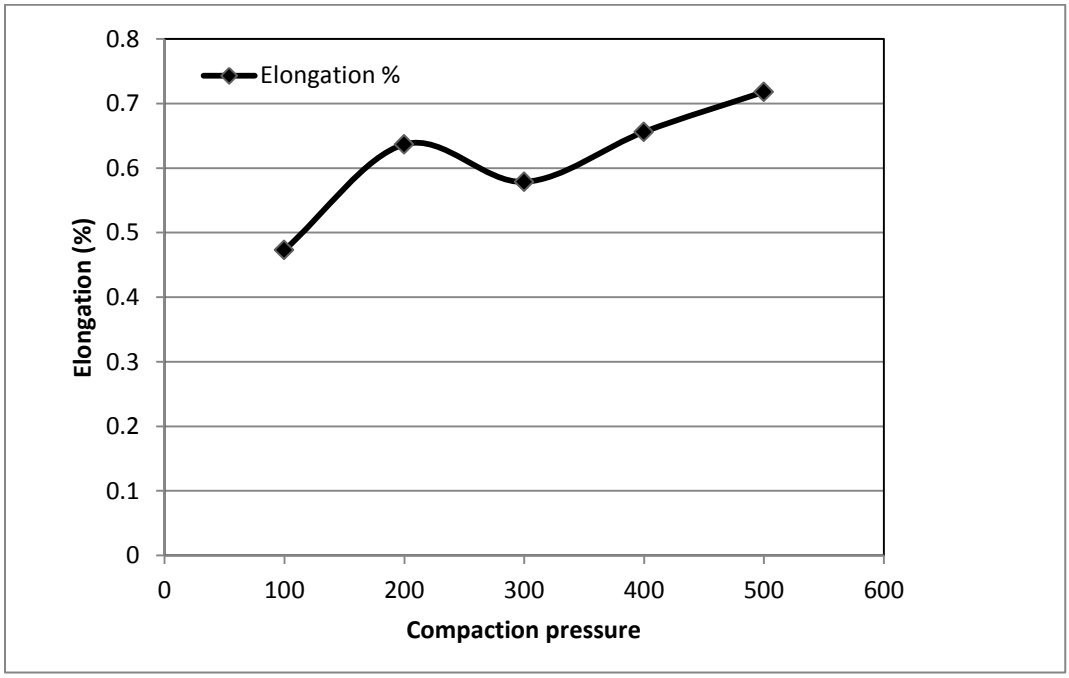

Figure 4-13 Elongation to failure of Alumix 321 as a function of compaction pressure.

Tensile properties of sintered Alumix 321 were compared against the standard properties established by commercial 601AB [5]. Table 4-2 illustrates the comparison between the two systems. It is clearly visible that Alumix 321 tensile properties were comparable to those published for 601 AB. Yield and tensile strength values were almost the same. However, there were notable differences observed in percentage of elongation. Consequently, all Alumix 321 samples show a very low ductility. This low percentage of elongation can be explained based on the experimental error during the experiments. It was noted that some sintered samples show a very clear warpage that affect grapping the samples to the tensile machine.

Table 4-2 Comparision of T6 tensile properties of Alumix 321 and the commercial alloy 601 AB.

Alloy	Compaction Pressure (MPa)	Offset Yield Strength (MPa)	Ultimate Tensile Strength (MPa)	Elongation to Failure (%)
Alumix 321-T6	100	191±65	192±66	0.5±0.3
	200	239±8	241±11	0.6±0.1
	300	249±15	249±15	0.6±0.1
	400	248±16	252±19	0.7±0.2
601 AB-T6	96	176	183	1
	165	224	232	2
	345	230	238	2

4.3.3 *THERMAL ANALYSIS*

Differential scanning calorimetry (DSC) was used to provide further understanding of the sintering process. It is used to evaluate and assist the reactions occurred during sintering. In this test, a small cylindrical piece of 4 mm in height and 3 mm in diameter was machined from a green TRS compact and sintered in DSC furnace under a nitrogen atmosphere. Figure 4-14 shows the variation of heat flow and weight as a function of temperature during the sinter cycle. The heat flow of the green compacted sample shows a very similar response to the sintering process. An endothermic peak A starts at about 340 °C indicates the de-lubrication stage, in which the lubricant vaporize from the sample, this process is combined by the weight loss. The second peak B initiates at ~ 583 °C and indicating a localized melting of the alloy. A secondary melting peak C appears at ~ 610 °C and it could be an indication of persistent liquid phase formation, which disappears at point D. As the sample cools down, another smooth thermal profile obtained that suggests that all reactions have been completed. Figure 4-14 also

illustrates the change in mass during sintering. The plot shows a large decrease in mass that corresponding to de-lubrication stage.

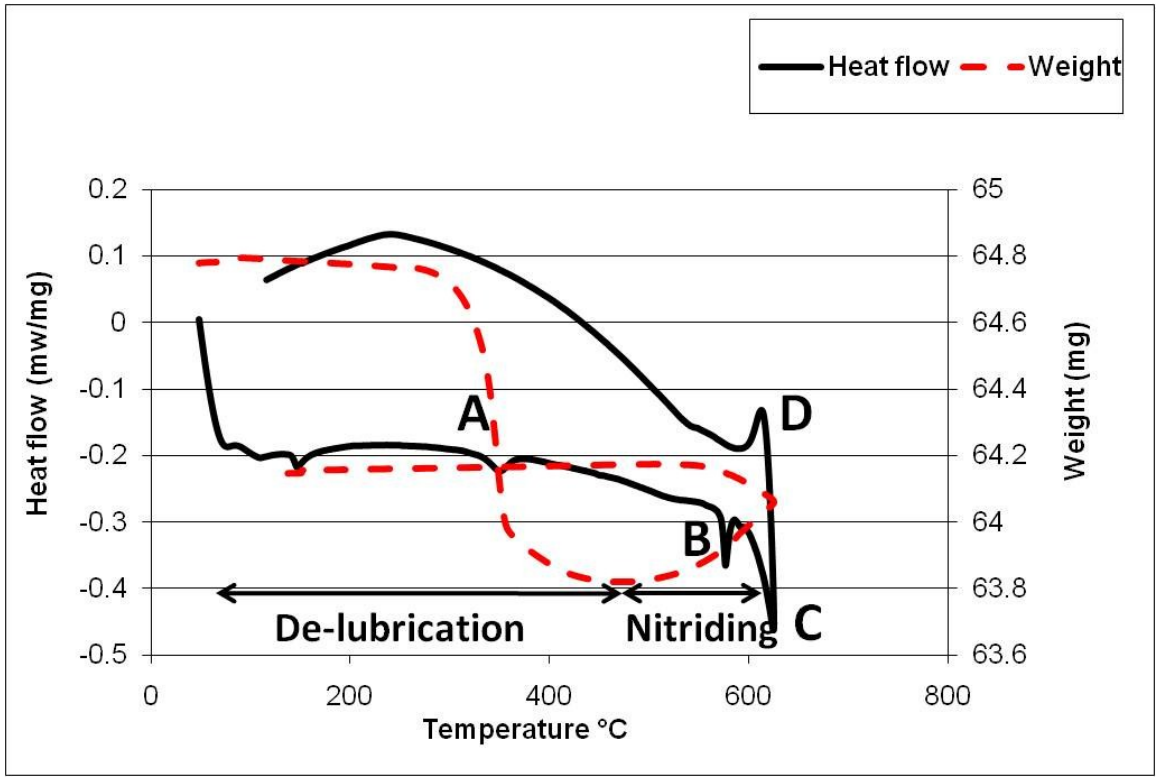

Figure 4-14 Heat flow and weight variation as a function of temperature.

It is worth to note that the total amount of the lubricant is 1.5% of the green compact weight. However, the maximum weight loss measurements show only 1.33 %. The reasonable explanation is that the gain in weight is due to the formation of aluminum nitride. Aluminum nitride forms at ~ 450 °C and begins after 63 minutes. The formation of aluminum nitride occurs due to the reaction between aluminum and nitrogen gas used in the DSC experiments.

4.4 MICROSTRUCTURAL CHARACTERIZATION

4.4.1 *OPTICAL MICROSCOPY*

For more understanding and a close insight on the Alumix 321, microscopy, chemical analysis and EPMA were performed on Alumix 321 samples. Figure 4-15 shows a microstructure of Alumix 321 sample pressed at 500 MPa in the as sintered condition.

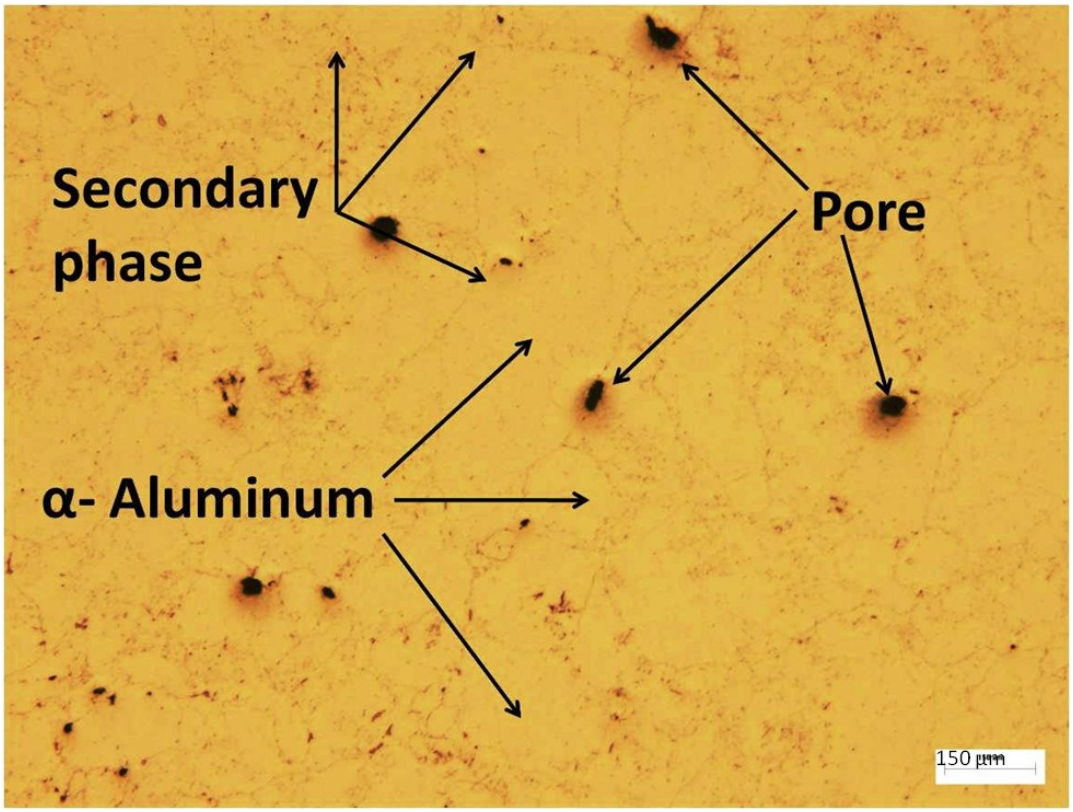

Figure 4-15 Optical micrograph of Alumix 321 PM alloy as-sintered.

From this image it was observed that the pores are round and a high degree of sintering was achieved which correlates well with the density measurements. The microstructure contains α- aluminum as a matrix and a secondary phase that outline the grains.

4.4.2 *SCANNING MICROSCOPY*

For closer examination SEM was performed on Alumix 321 samples in T1 and T6 tempers. The SEM micrographs, Figures 4-16 and 4-17 show very clearly that the microstructure of both tempers T1 and T6 exhibit the presence of gray intermetallic

compounds in addition to the other microstructural features such as the matrix and the pores. EDS analysis was also performed on different microstructural features to get some clue about the chemical nature of those phases. Figure 4-18 shows the spots used to conduct the chemical analysis where the spots numbers were chosen to include the matrix, gray elongated particles and round gray Particles.

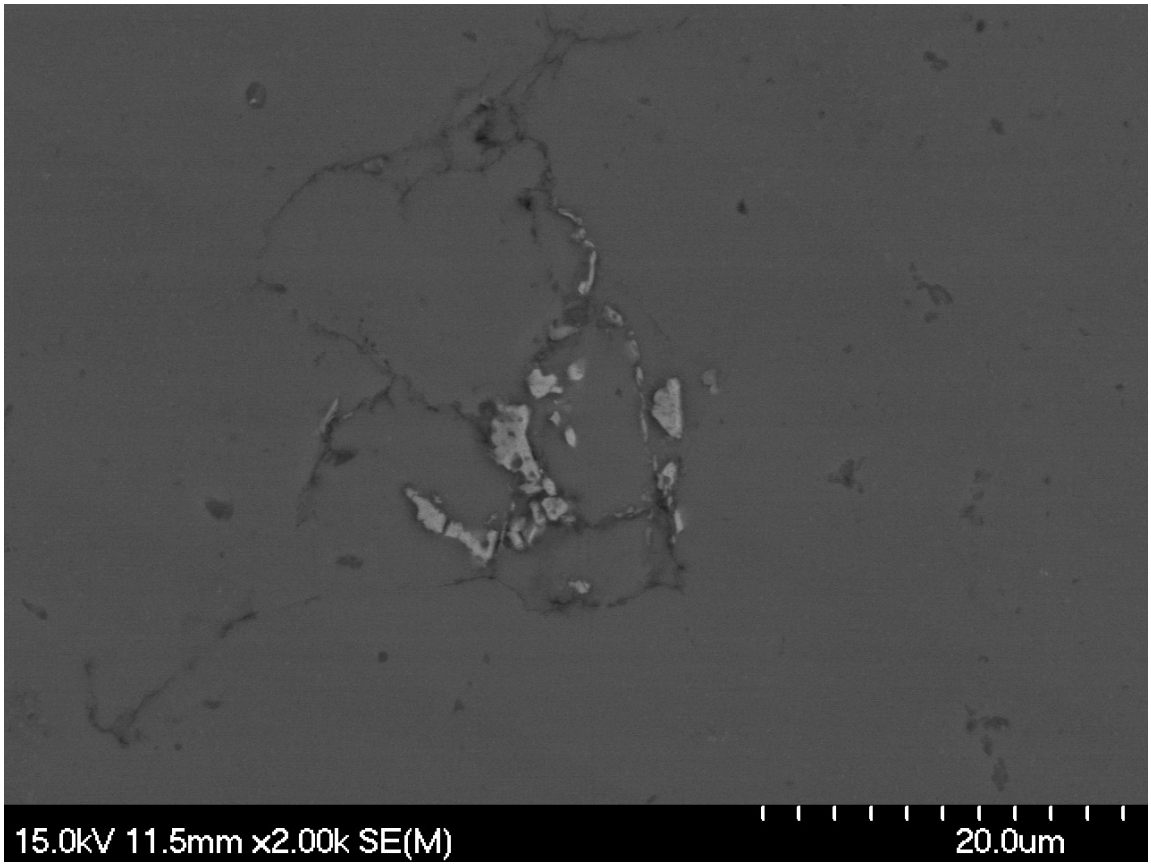

Figure 4-16 SEM micrograph of Alumix 321 T1.

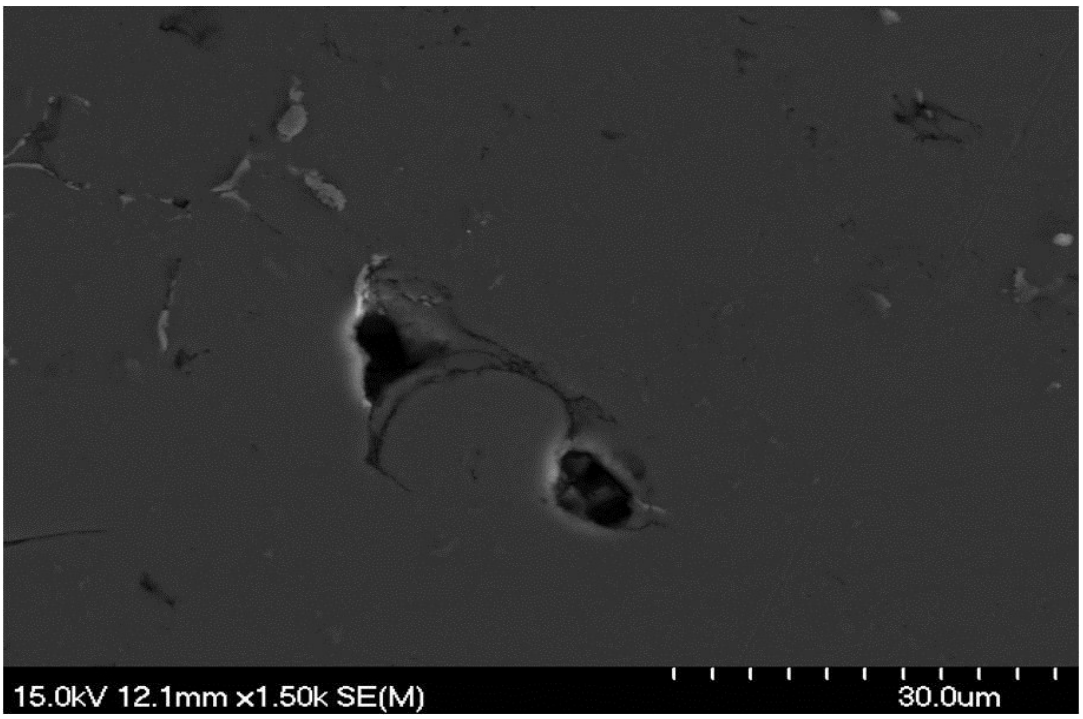

Figure 4-17 SEM micrograph of Alumix 321 -T6

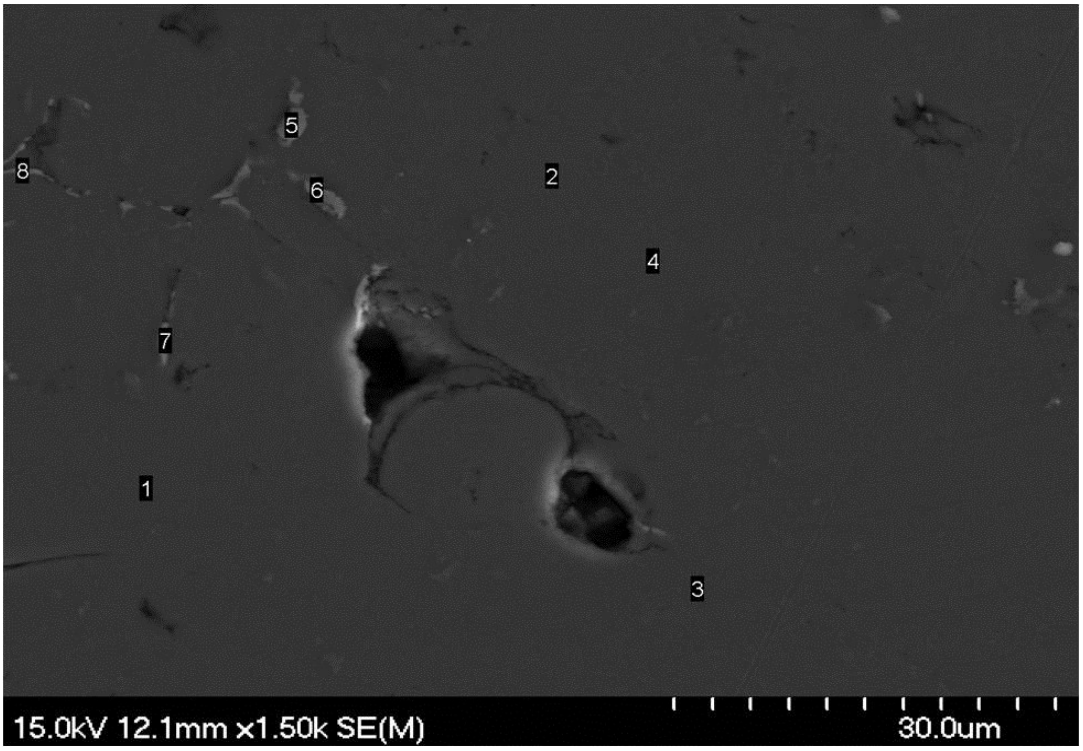

Figure 4-18 Spots used to conduct chemical analysis of Alumix 321-T6.

Chemical analysis results shown in Figures 4-19 and Figure 4-20 prove the presence of aluminum as a matrix in which some alloying elements were dissolved such as Mg, Si and Cu. The other features that were analyzed are the gray particles, in which the spectrum obtained shows the presence of iron which indicates that these particles are iron containing intermetallic compounds. Iron containing particles form during solidification of aluminum alloys and known to contain aluminum and iron with some other elements. The chemical composition of these particles will be examined in more details later in this report.

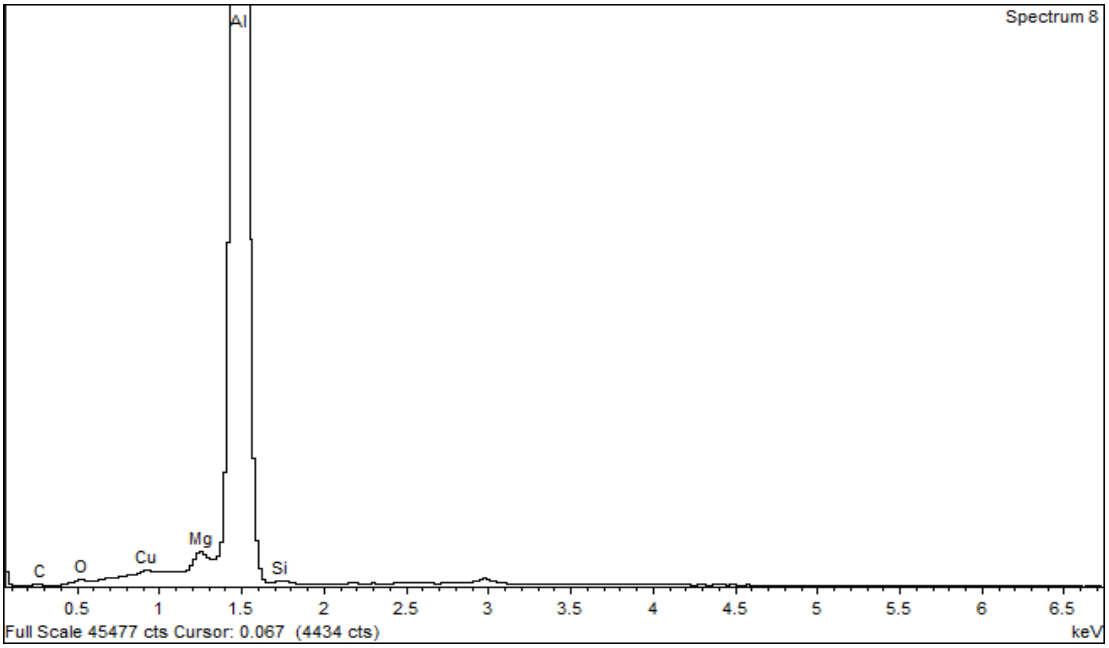

Figure 4-19 EDS spectrum of matrix grains of Alumix 321.

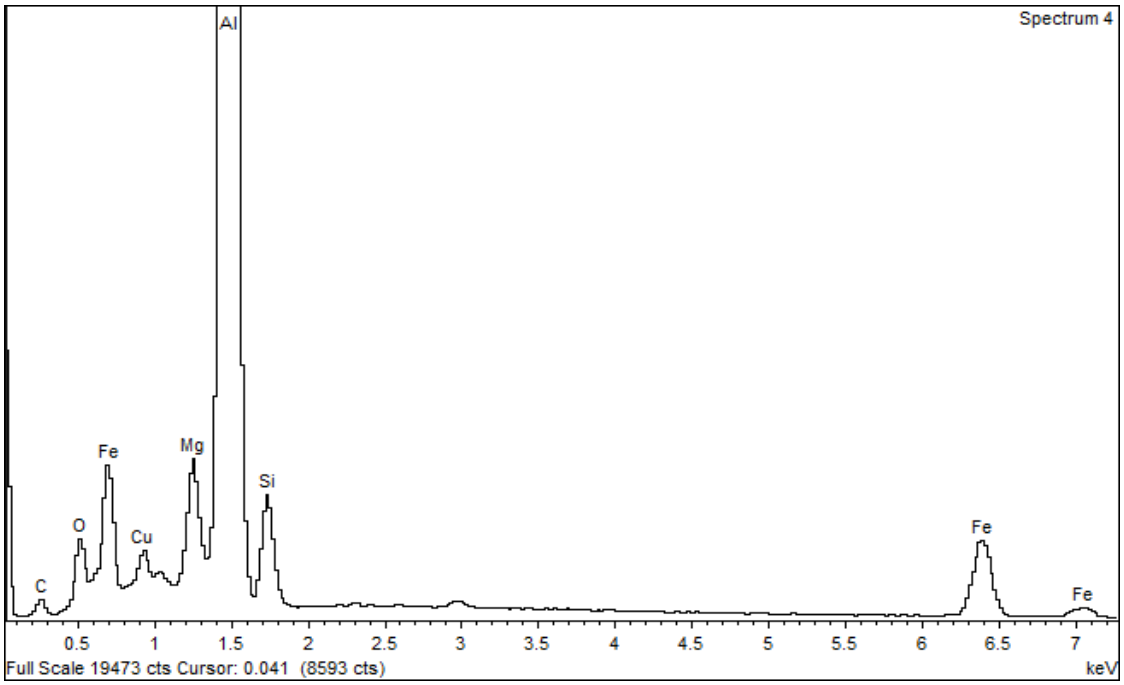

Figure 4-20 EDS spectrum obtained from gray intermetallic particels in Alumix 321.

In addition to the previous phases examined, images taken at higher magnification show the presence of a dark gray phase. The EDS analysis performed shows that the phases contain higher amounts of magnesium and silicon which suggest the formation of Mg_2Si (β phase). SEM micrograph and the EDS spectra are shown in Figures 4-21 and Figure 4-22, respectively.

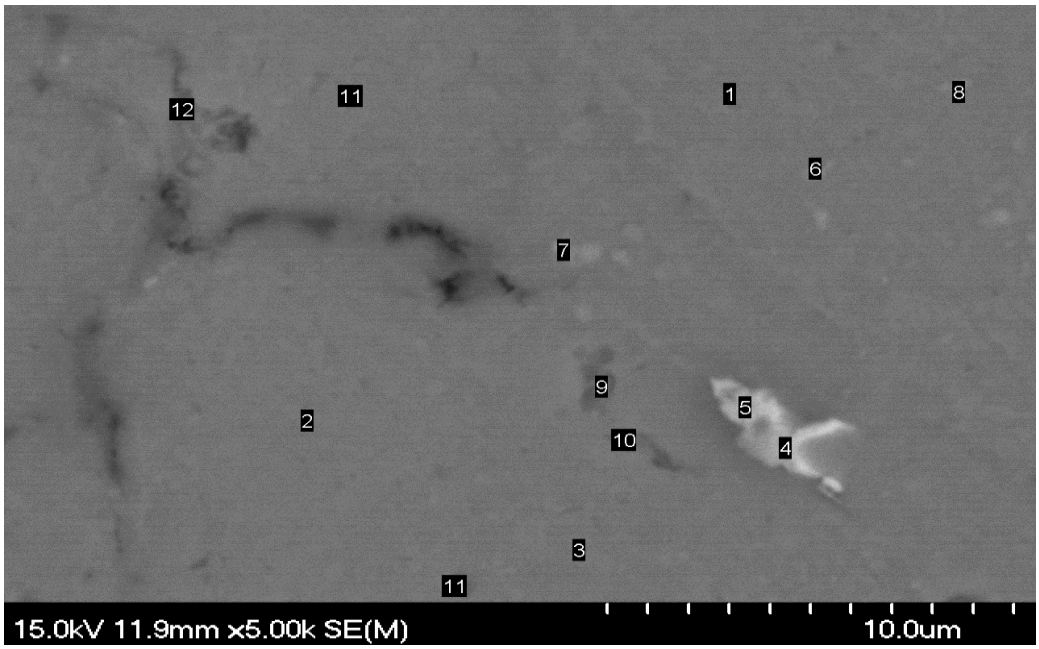

Figure 4-21 Higher magnification SEM micrograph of Alumix 321.

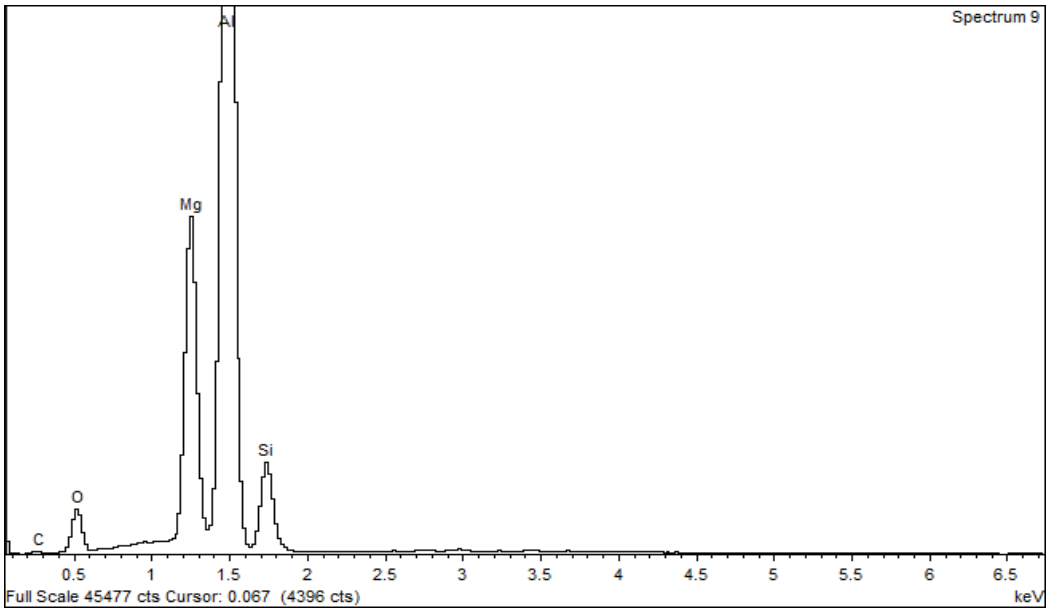

Figure 4-22 EDS spectra of Alumix 321 taken from spots 9, 10 and 12.

4.4.3 *ELECTRO-PROBE MICRO ANALYSIS (EPMA)*

As a further step to characterize the microstructure of Alumix 321 samples, EPMA was performed. The goal was to get quantitative chemical analysis results that would help to define the nature and chemical composition of the different phases that exist. EPMA analysis was performed on the matrix and intermetallics of Alumix 321 in T1 and T6 temper where an average of three readings was taken from each phase. Figure 4-23 shows the EPMA results for the Alumix 321 matrix in T1 and T6 temper.

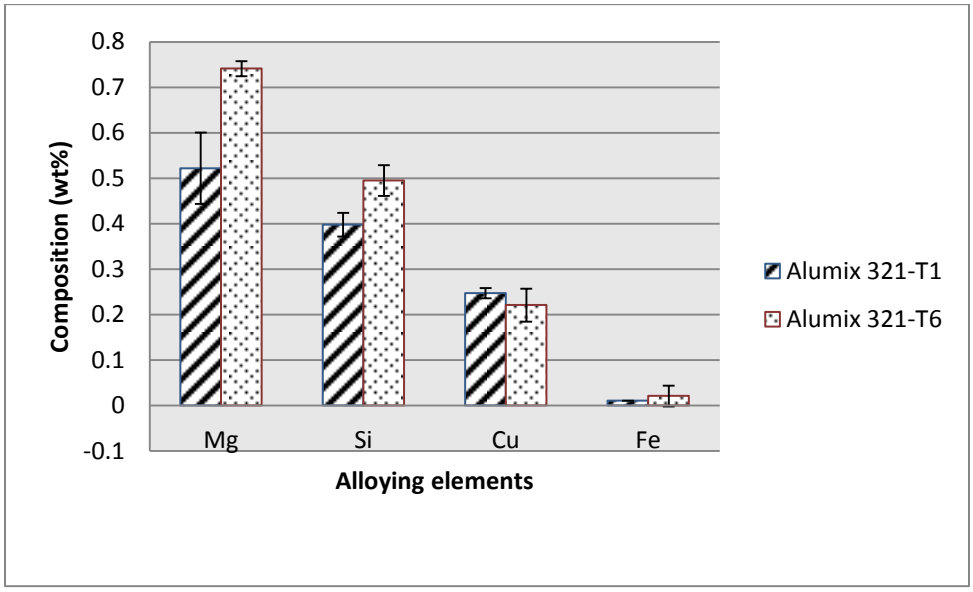

Figure 4-23 Average chemical analysis of matrix grains of Alumix 321 in T1 and T6.

Chemical analysis of the Alumix 321 matrix in T1 and T6 condition shows that the concentration of both Mg and Si is higher in T6 than in T1 samples. This variation in composition referred to the heat treatment by which these two tempers were obtained. For as received sintered samples the cooling time was moderately slow and the chance for those elements to migrate to the grain boundary is much higher. When the samples were heat treated, the solutionized time and temperature offered enough time for those elements to diffuse inside the matrix and most likely form Mg_2Si which explains the higher amount of those two elements. It is worth noting that the EPMA analysis also shows lower concentration of Mg comparing to the values obtained from the Atomic Adsorption Spectroscopy technique. In addition of the limitation of this technique to

offer very accurate chemical analysis, the formation of spinel phase ($MgAl_2O_4$) during sintering and the formation of Mg_2Si are possible reasons for this low Mg concentration. Also magnesium at its melting point has a high vapour pressure and some magnesium may have evaporated. Due to the very low concentration of copper, it is highly unlikely for copper to form any precipitate for this system, this would explain that the difference in copper concentration was not that much between as sintered and heat treated samples. Iron concentration also shows no difference between the two tempers. The analysis shows that the concentration of Iron found to be 0.01 and 0.02 wt% in T1 and T6 temper, respectively. Generally, iron has a very low solubility in aluminum and forms insoluble particles during early stages of aluminum production [74].

As was mentioned earlier in this chapter and in addition to other microstructural features, gray particles were observed using optical and scanning microscopy. The first step that was done and explained before is the EDS analysis which shows clearly the presence of iron. Due to the limit of EDS technique, EPMA was performed seeking more accurate quantitative analysis. Higher magnification using back scattered electron image shows that the gray particles can be further classified into two groups. Figure 4-24 shows the presence of small round particles in addition to elongated Chinese script particles.

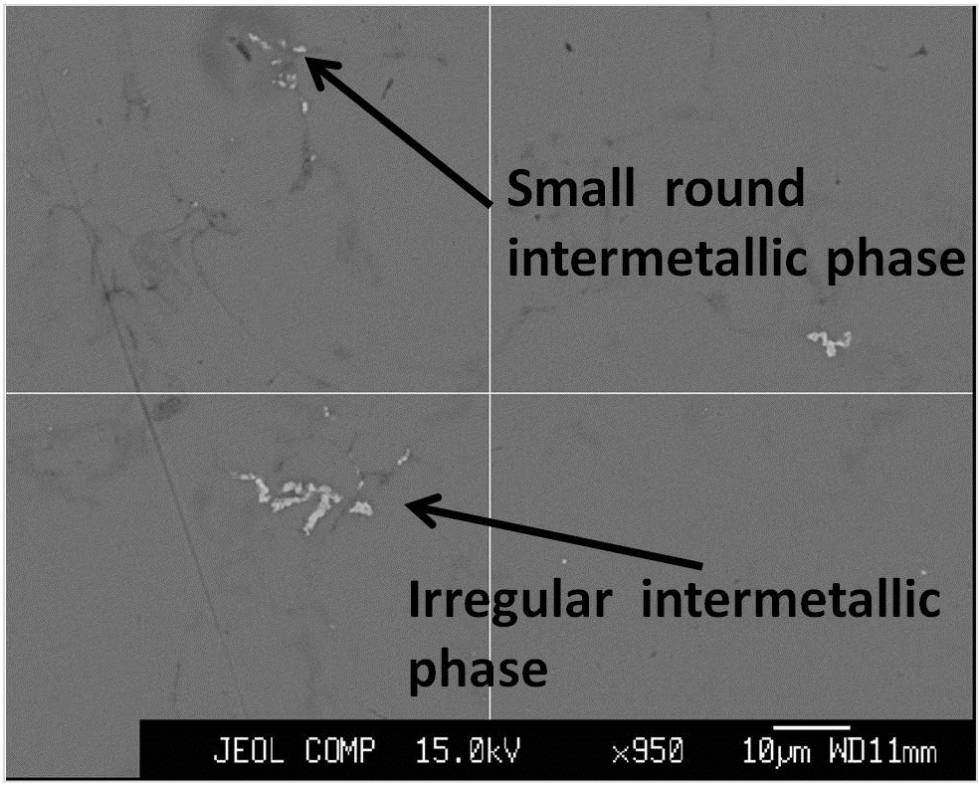

Figure 4-24 Backscattered electron image of Alumix 321-T6 shows two differnt types of intermetallic phases.

The Chemistry of both intermetallic particles shows a clear presence of Fe and Al along with smaller concentrations of Mg, Si and Cu. Figure 4-25 shows the EPMA results for the both round and irregular intermetallic phases.

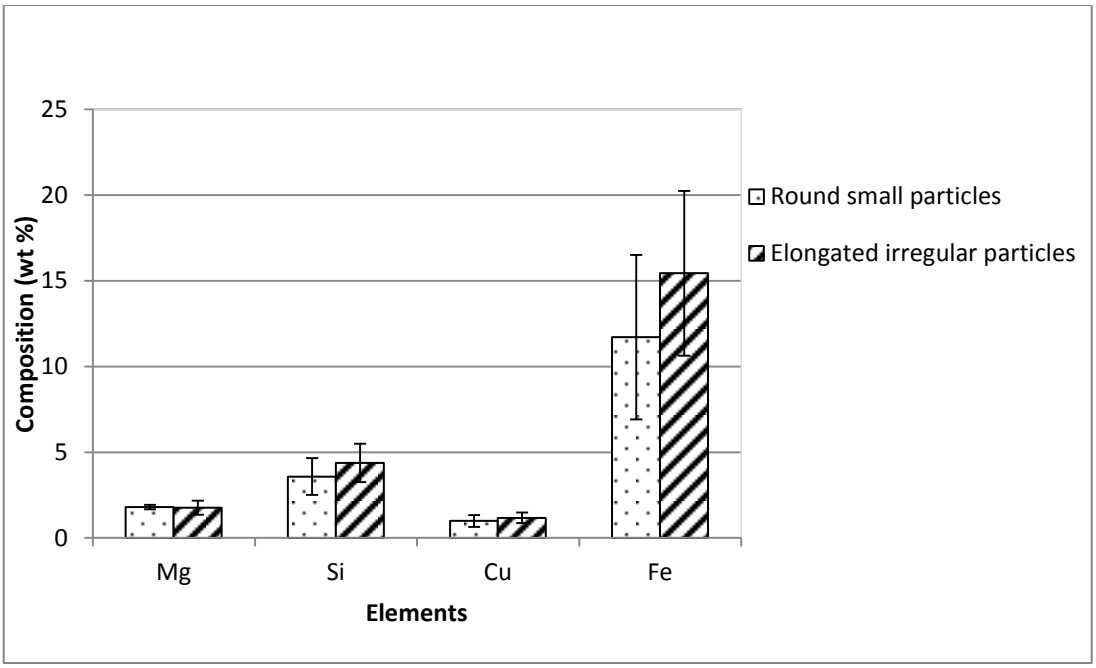

Figure 4-25 Average chemical analysis of small round and irregular particles observed in Alumix 321-T6 PM alloy.

It is worth noting here that there was a major error with most of the readings especially for small round intermetallic phases. This error is attributed to the very small size of the particles which have a size that in the same order of the beam width, causing the beam to excite some atoms surrounding in addition to the iron containing particles.

For more clarification and understanding of the nature of the phases and the intermetallic particles X-ray diffraction was performed on Alumix 321 in T1 and T6 condition. Figure 4-26 shows the diffraction patterns for two Alumix 321 samples in the T1 and T6 temper. The diffraction patterns show that the two samples exhibit almost the same diffraction pattern, the only difference being that peaks observed for T6 samples shows a small shift from the T1 samples. This can be explained based on the effect of heat treatment performed. Solution treatment for T6 samples provided enough time for the alloying elements to diffuse to the matrix which resulted in a small change in lattice dimensions. It was clearly seen that the main phase observed was aluminum in both samples and there was no clear evidence of any other phases.

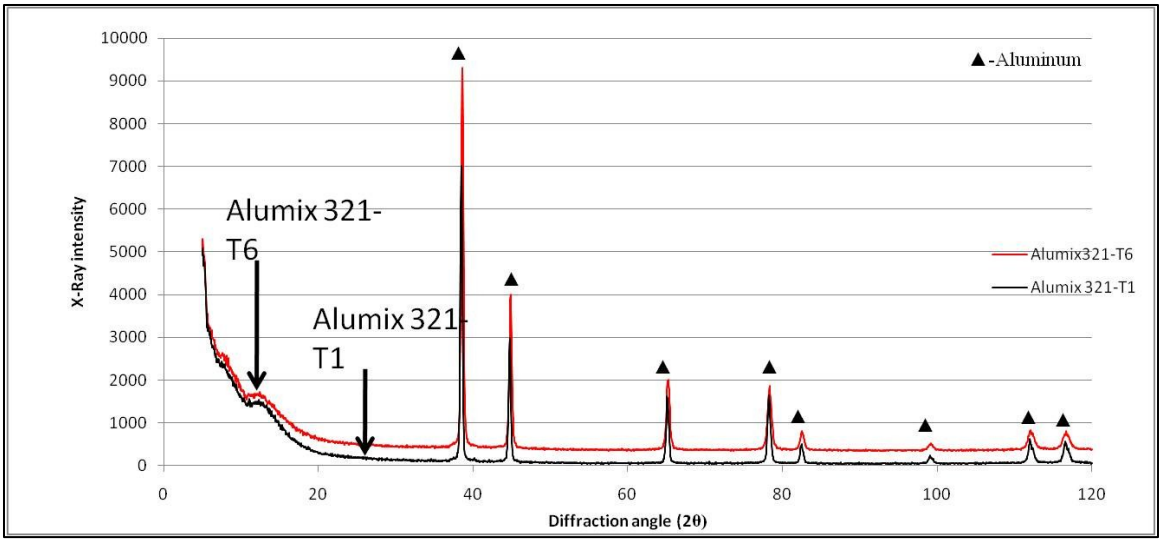

Figure 4-26 X-Ray diffraction dat for the Alumix 321 alloy in T1 and T6 condition.

As a further attempt to identify the nature of phases using an x-ray technique, slower scan rate of (0.02 sec/degree) was used. Two Alumix 321 samples in the T1 and T6 condition were examined, and the scanning was performed within the range of the expected strongest peak of Mg_2Si which probably the predominant phase exist in this system. Figure 4-27 illustrates the x ray diffraction pattern performed on Alumix 321 in T1 and T6 at a very slow scan rate. It was obvious that Alumix 321 sample in T1 condition shows a small peak at about 40 degree, this peak is corresponds to the strongest peak of Mg_2Si which forms exactly at 40.133 degree. In contrary, it was very hard to see any Mg_2Si visible peak in the T6 samples. The better explanation of this is due to the higher chance of a relatively coarse Mg_2Si formation during moderately slow cooling in the as sintered condition. In contrary, solutionzing treatment will help to dissolve most of magnesium and silicon in the aluminum matrix, and as a result aged T6 samples will form a very fine homogeneously distributed Mg_2Si which is very hard to detect. The evidence of Mg_2Si formation in the T1 condition was proved by EDS and EPMA.

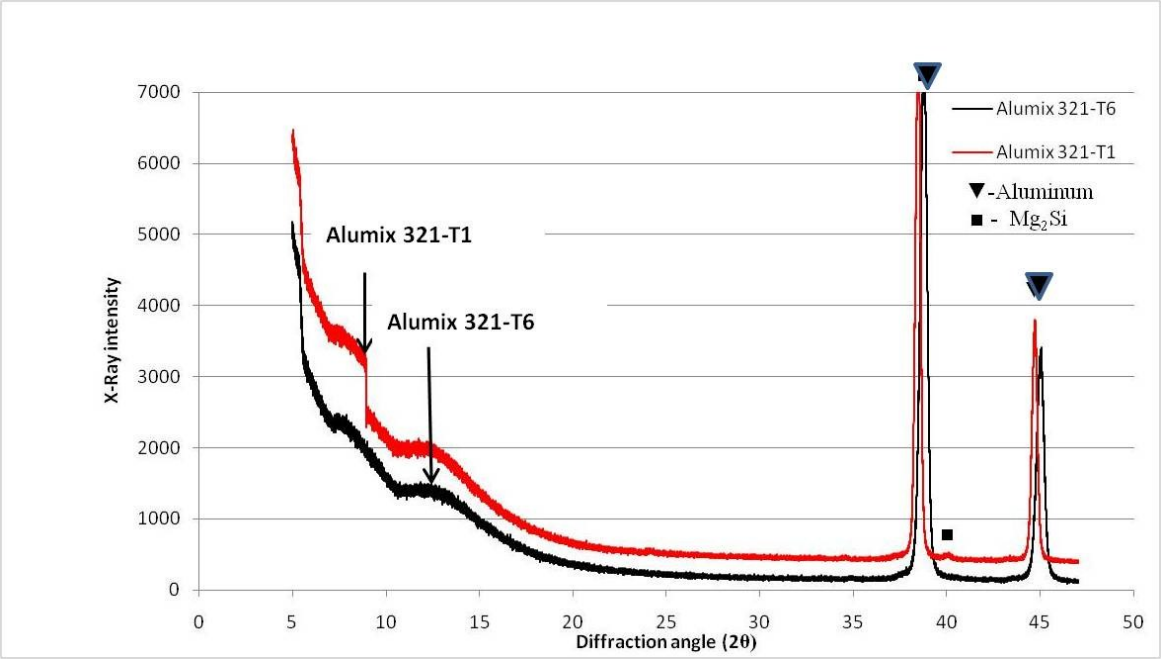

Figure 4-27 X-Ray diffraction data for Alumix 321 in T1 and T6 taken at a slower scan rate.

Unluckily, x- ray was unable to provide a convincing identification of the iron containing intermetallic phases observed in EDS and EPMA studies. This was probably due to the small amount of iron content which resulted in a smaller amount of iron containing phases.

4.5 POST SINTERING TREATMENTS

4.5.1 *HOT ROLLING*

Pre sintered prerforms made of Alumix 321 were subjected to hot rolling. Slabs made of Alumix 321 were pressed at 500 MPa, sintered and then hot rolled. Table 4-3 shows the rolling parameters used to perform the rolling process.

Table 4-3 Hot rolling paramteres used for Alumix 321 hot rolling process.

Material	Compaction Pressure (MPa)	Rolling Temperature (°C)	Initial Thickness (mm)	Final Thickness (mm)	Reduction Percentage (%)
Alumix 321	500 MPa	500	8.38	6.07	27

The impact of hot rolling on Alumix 321 was very obvious. The slabs were elongated and 27% reduction obtained as shown in Figure 4-28. In addition to the dimensions, hot rolling impact can be seen through both, density and hardness. Table 4-4 shows the variation of density and hardness before and after the rolling process. Hot rolling was very affective as a densification process, the density increases from 2.589±0.124 g/cc before rolling to a density of 2.665±0.004 g/cc after rolling, and as a result theoretical density increases up to 99.01%. In addition to the density measurement, the hardness in T1 and T6 was also measured. Similar to the results obtained for density, hardness values obtained after rolling were higher than those obtained before rolling. It is worth noting here that the highest hardness obtained was 106±6 HRE, this high hardness value is due to the combination of both densification and T6 heat treatment.

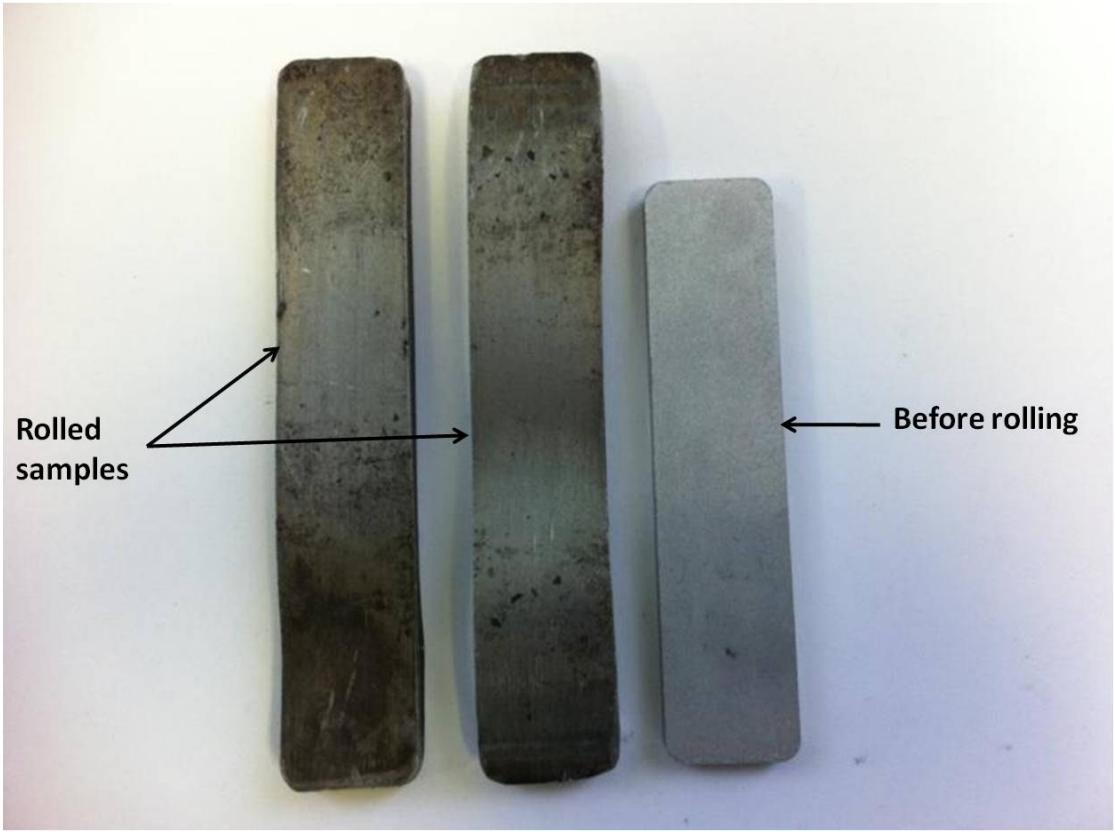

Figure 4-28 Effect of hot rolling on Alumix 321 PM alloy.

Table 4-4 Effect of hot rolling on density and hardness of Alumix 321.

Property	Density (g/cc)		Hardness (HRE)	
	Apparent	Theoretical	T1	T6
Before Rolling	2.589±0.124	96.2 %	30±2	93±3
After Rolling	2.665±0.005	99.10 %	53±8	106±6

The impact of hot rolling effect can also be seen through the microstructural changes. Figure 4-29 shows the transverse section optical micrograph of hot rolled sample. Deformed grains are clearly seen and only small amount of pores are observed.

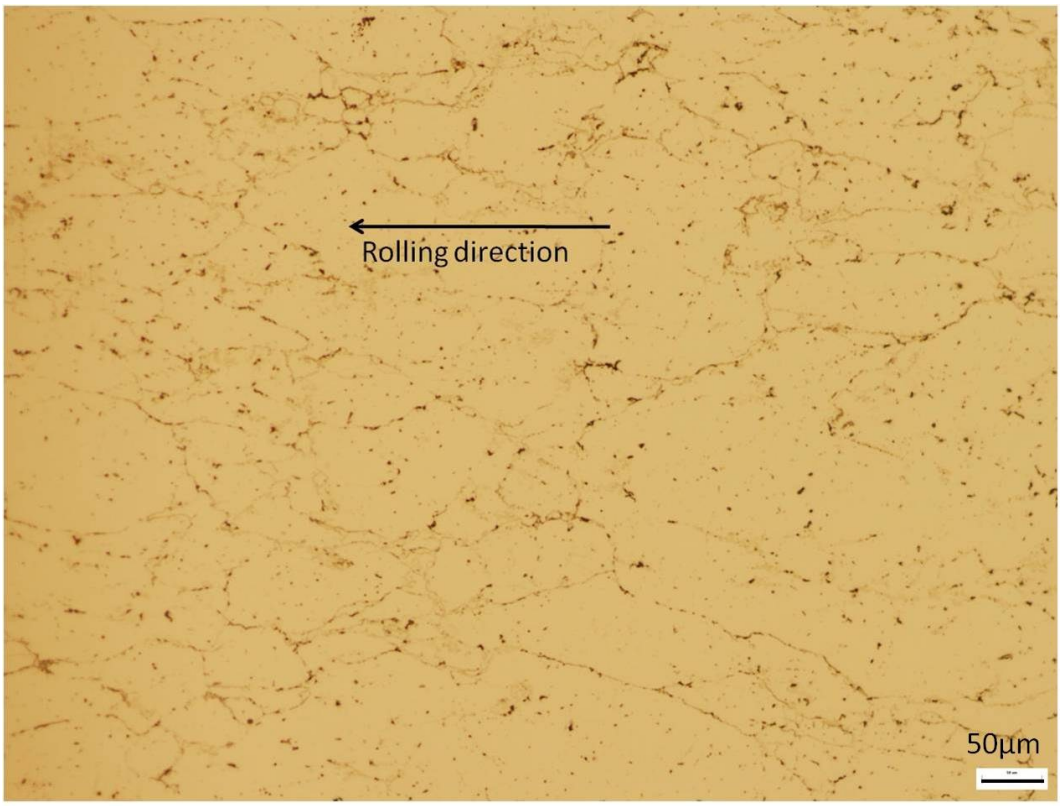

Figure 4-29 Optical micrograph showing the effcet of hot rolling on the microstructure of Alumix 321 PM alloy.

4.5.2 *HOT SWAGING*

Hot swaging (extrusion) is often used to produce parts with high performance and uniform cross section with full or nearly full density. Hot swaging was performed at 500 °C on Alumix 321 preforms sintered samples. Figure 4-30 show Alumix 321 preform before and after swaging, respectively. As a result of 5 steps of hot extrusion, the original billet diameter reduced from 21.65 mm to 15 mm, which produced a sectional reduction of 34%.

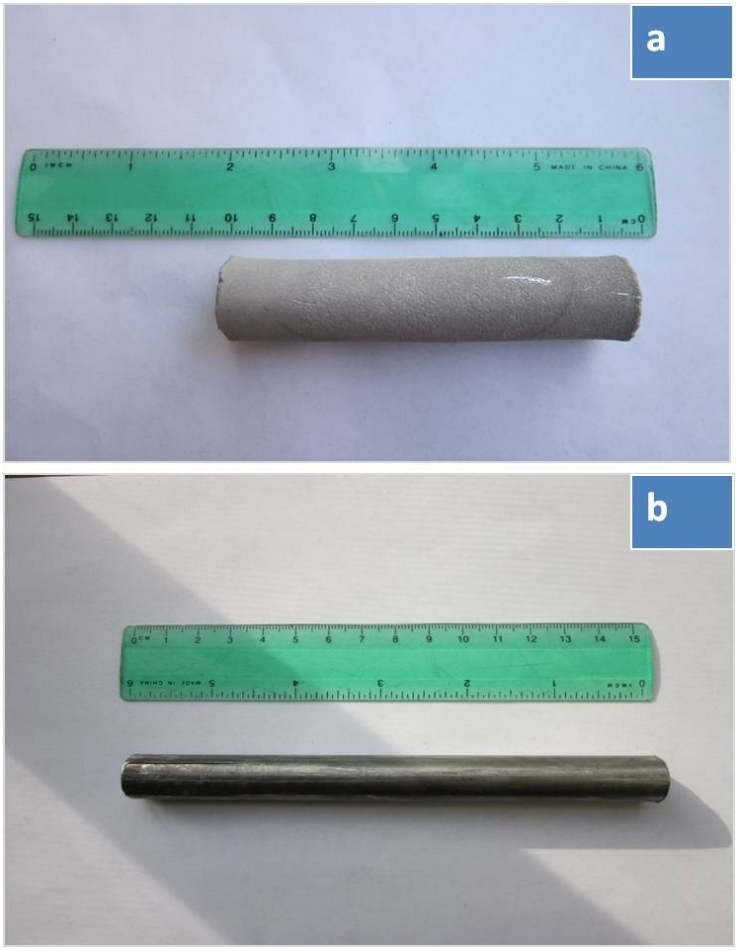

Figure 4-30 Effect of hot swaging on Alumix 321 PM alloy. a) before swaging, b) after swaging.

The effect of hot swaging on both density and hardness was very obvious. Table 4-5 shows that hot swaging was a very affective process and a sintered density of 2.673 (g/cc) was obtained which produces nearly a full dense structure with 99.39±0.67 theoretical density.

Table 4-5 Effect of hot swaging on density of Alumix 321.

Material	Alumix 321-As CIP and sintered	Alumix 321-As hot swaged
Density	2.485±0.022	2.673±0.002

In addition to the effect on density, hot swaging effect on hardness was also noticeable. An increase in hardness was achieved after hot swaging. Figure 4-31 illustrates that both

T1 and T6 hot swaged Alumix samples showed higher apparent hardness values than non swaged samples.

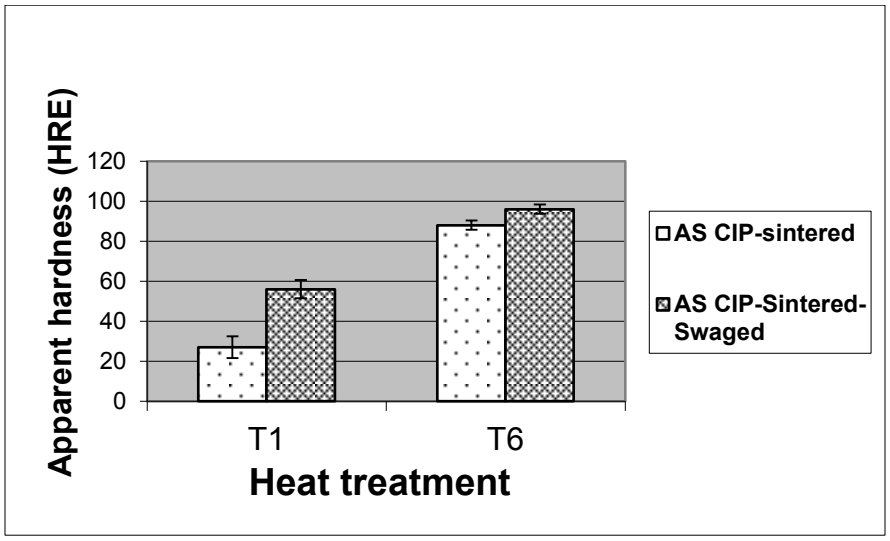

Figure 4-31 Effect of hot swaging on hardness of Alumix 321 PM alloy.

For more understanding of this process, hot swaged samples were prepared for metallographic examination. This test was chosen to offer more understanding of the hot swaging process and how it affects the microstructure and consequently the material properties. Alumix 321 samples from longitudinal and transverse directions were cut and examined using the optical microscope. Figure 4-32 shows two different Alumix 321 samples before and after swaging. The microstructure of the cold isostatically and sintered sample consists of the typical Alumix 321 microstructure. The microstructure consists of α-aluminum matrix, intergranular secondary phase and porosity. It is very visible that swaging has a very strong effect on the microstructure. The deformation applied during swaging was very effective in closing off those pores and produce an almost pore free microstructure. It can also been seen that the secondary phase is less visible and equally distributed in the aluminum matrix. This is attributed to the heat treatment applied after swaging in which a solutionizing temperature enables those secondary phases to dissolve in the matrix. These microstructural changes were reflected in an increase in theoretical density from 92.41 to 99.39 and an increase in hardness from 88 HRE to 96 HRE as was early mentioned in

the previous paragraph. Figure 4-33 illustrates the transverse section of hot swaged Alumix 321-T6 samples. It is clearly seen that the hot swaging produces squeezed and elongated aluminum grains in the deformation direction.

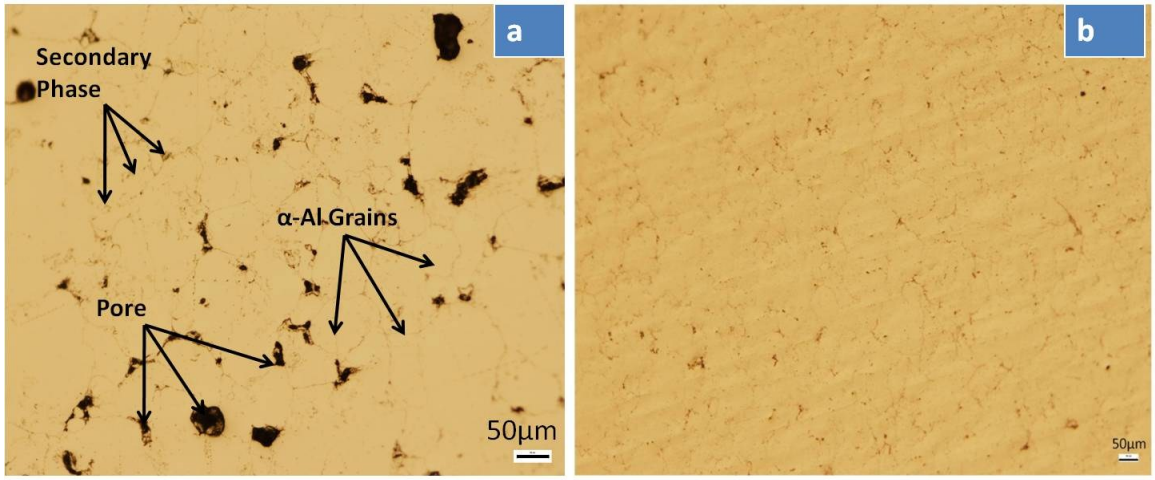

Figure 4-32 Optical micrograph of Alumix 321 (a) before swaging CIP-as sintered (b) after swaging-longitudinal direction-T6.

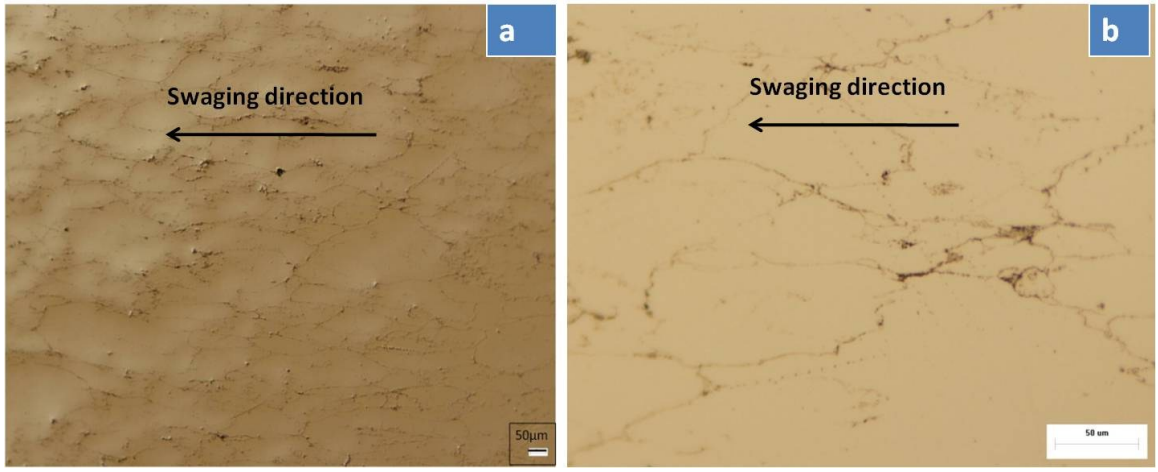

Figure 4-33 Optical microscopic images of Alumix 321 (a) after swaging-transverse direction-T6 (b) after swaging-transverse direction-T6.

4.5.3 *SIZING*

Sizing normally involves less deformation compared to processes such as rolling, extrusion and forging. The less amount of deformation helps to perform sizing of sintered products without much change in dimensions. In this regard, sizing was performed on two different sets of samples. The first set of samples pressed at 300 MPa and then repressed at 100 MPa, the second set was pressed at 500 MPa and then repressed at 180 MPa. Compared to other deformation processes, the percentage of reduction in sizing was smaller than that obtained with hot rolling and swaging in which the reduction percentage kept between 3 to 5 %. Sized samples showed generally an increase in both density and hardness. For the set of samples repressed at 100 MPa, density does not show much increase and retained almost the same. However, hardness increases from 16 HRE to 44 HRE. For samples repressed at 180 MPa, density and hardness increases from 2.539 g/cc to 2.565 g/cc and from 20 HRE to 48 HRE, respectively. In addition to the affect on density, hardness and reduction in thickness, sizing leads to reduce thickness variation. Figure 4-34 shows the effect of sizing on thickness variation of samples pressed at 500 MPa and repressed at 180 MPa, and among 4 samples tested three of them have almost the same thickness. This suggests the importance of sizing for narrowing the dimensional distribution of sintered parts which is very important to produce precise sintered components.

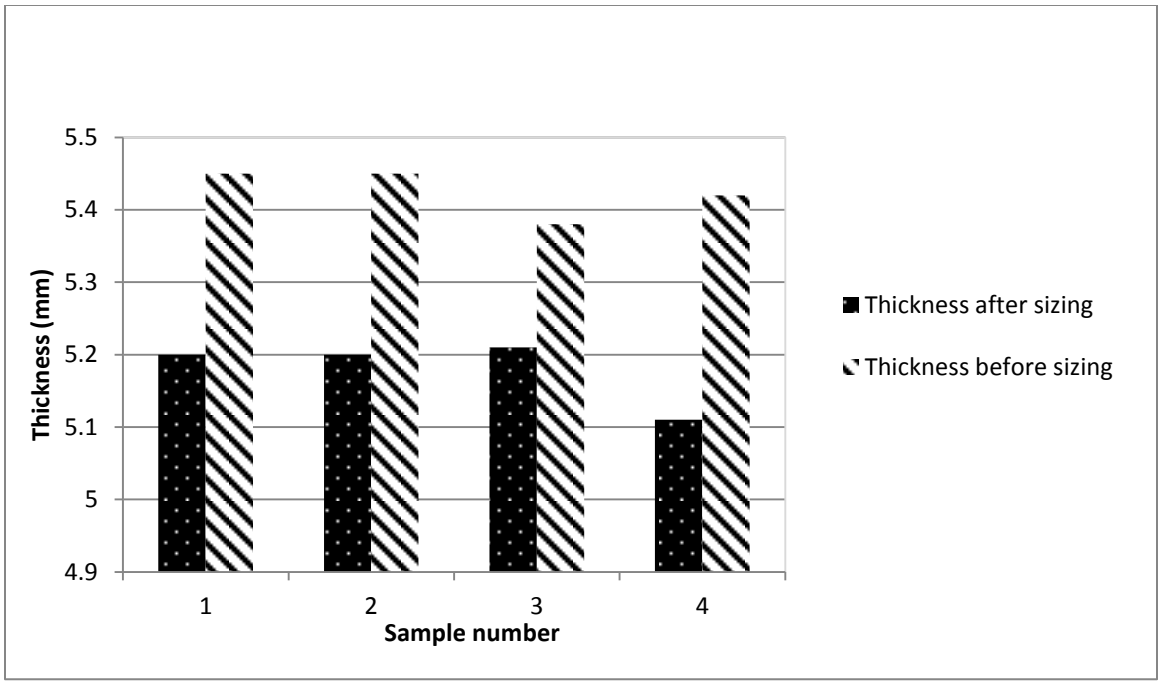

Figure 4-34 Effcet of sizing on thickness variation of Alumix 321 PM alloy.

The effect of repressing on the microstructure was not clear. Figure 4-35 shows that there was almost no evidence of elongated or deformed grains of the sized samples. The comparison of rolled and swaged Alumix 321 samples shown in Figures 4-28 and Figure 4-32 with repressed samples shown in Figure 4-35 shows major differences in microstructure. Rolled and swaged microstructure shows very obvious deformed grains. This can be referred to the amount of deformation performed. In the case of sizing, the percentage of reduction was kept in the range of 3-5% which seems not enough to cause visible changes in the microstructure. On the other hand, the percentage of reduction was 27% and 34% for the hot rolling and hot swaging, respectively.

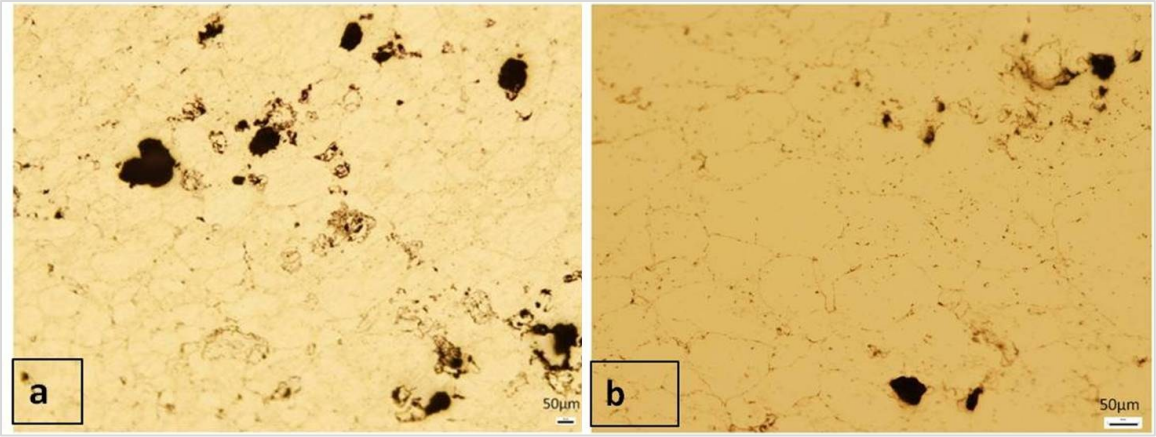

Figure 4-35 Optical micrograph of Alumix 321 PM alloy (a) repressed at 100 MPa, and (b) repressed at 180 MPa.

4.5.4 *SHOT PEENING*

Another type of treatment applied was the shot peening. Traditionally, this technique is used to improve fatigue resistance. However, this experiment was to apply this technique to treat the surface of sintered Alumix 321 samples and study its effect on the corrosion resistance. Figure 4-36 shows the effect of shot peening on the microstructure of Alumix 321.

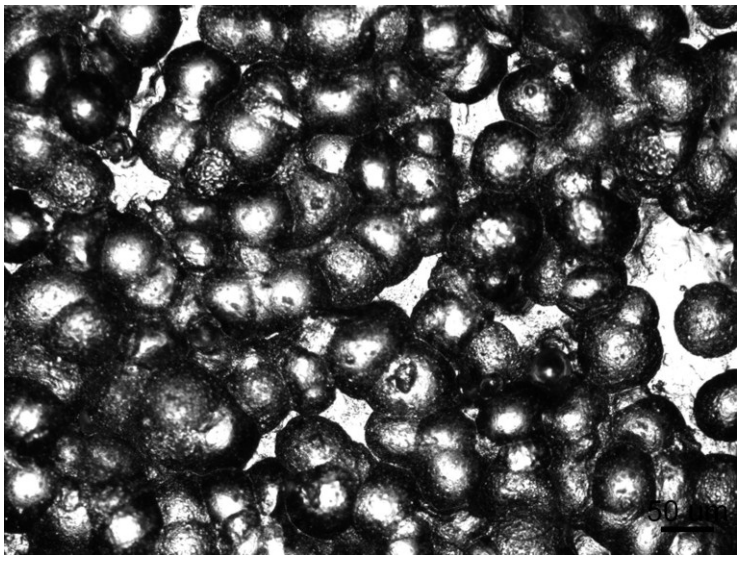

Figure 4-36 Optical micrograph of peened Alumix PM alloy after shot peening.

It is clearly visible from Figure 4-37 that the surface of shot peened sample was uneven and contains dimples. These dimples are due to the impact of shot balls on the Alumix 321 surface.

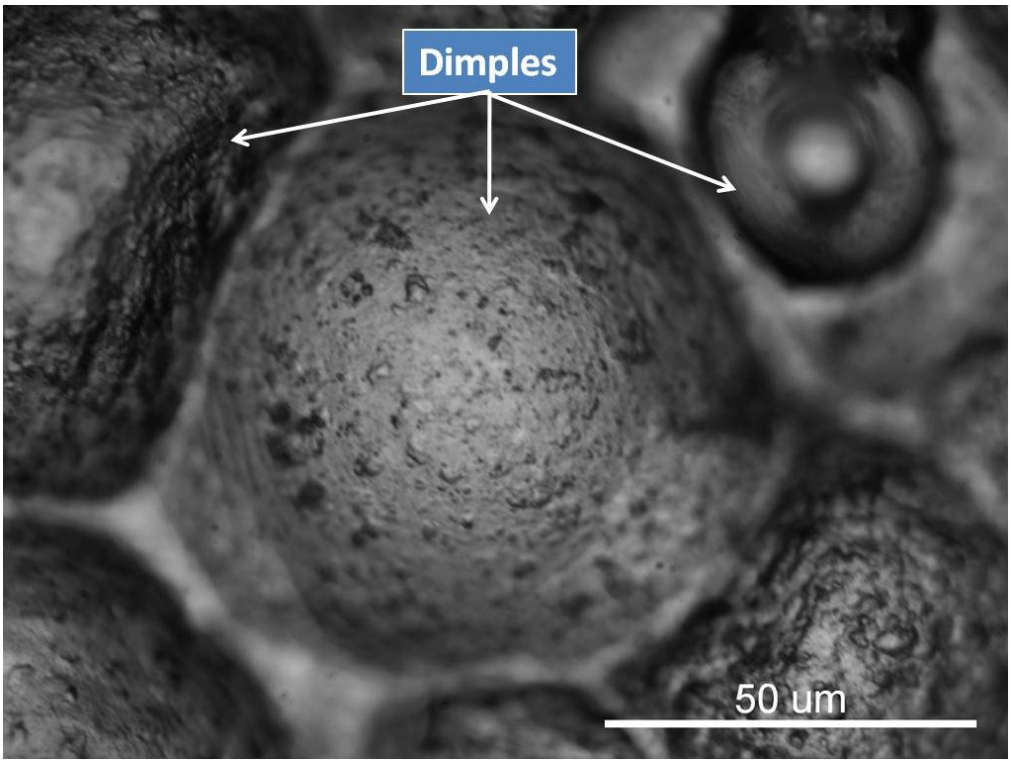

Figure 4-37 High magnification optical micrograph of shot peened Alumix 321 PM alloy.

In order to investigate the affect of peening on surface morphology, optical surface profilometry was conducted on unpeened and peened samples. Figure 4-38 and Figure 4-39 show the 3-D images of Alumix 321 material unpeened and peened to 0.4 mm N intensity, respectively.

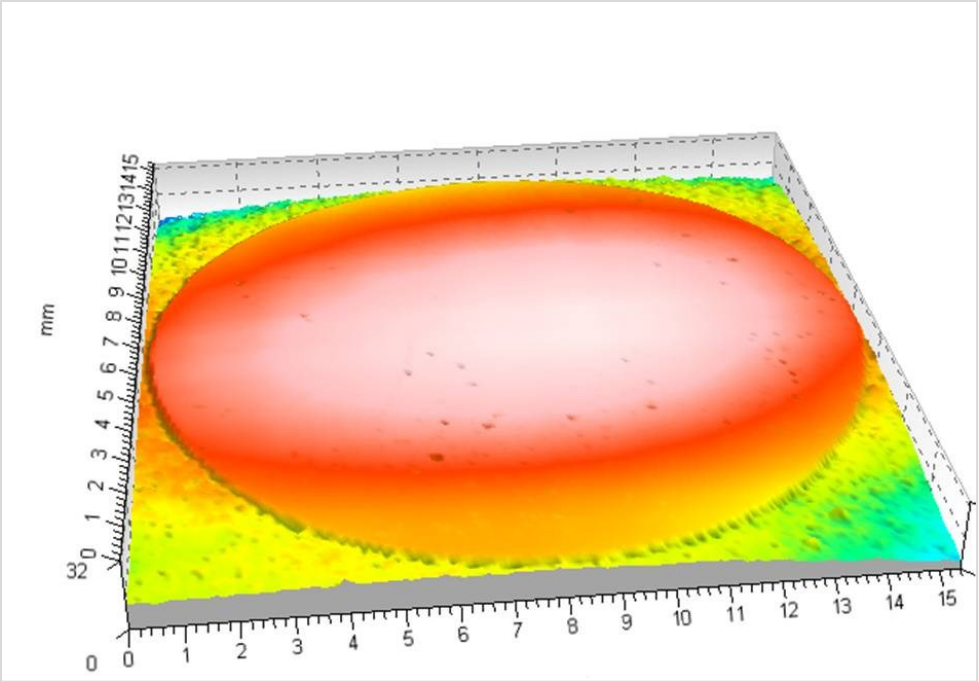

Figure 4-38 Surface topography of Alumix 321 before peening.

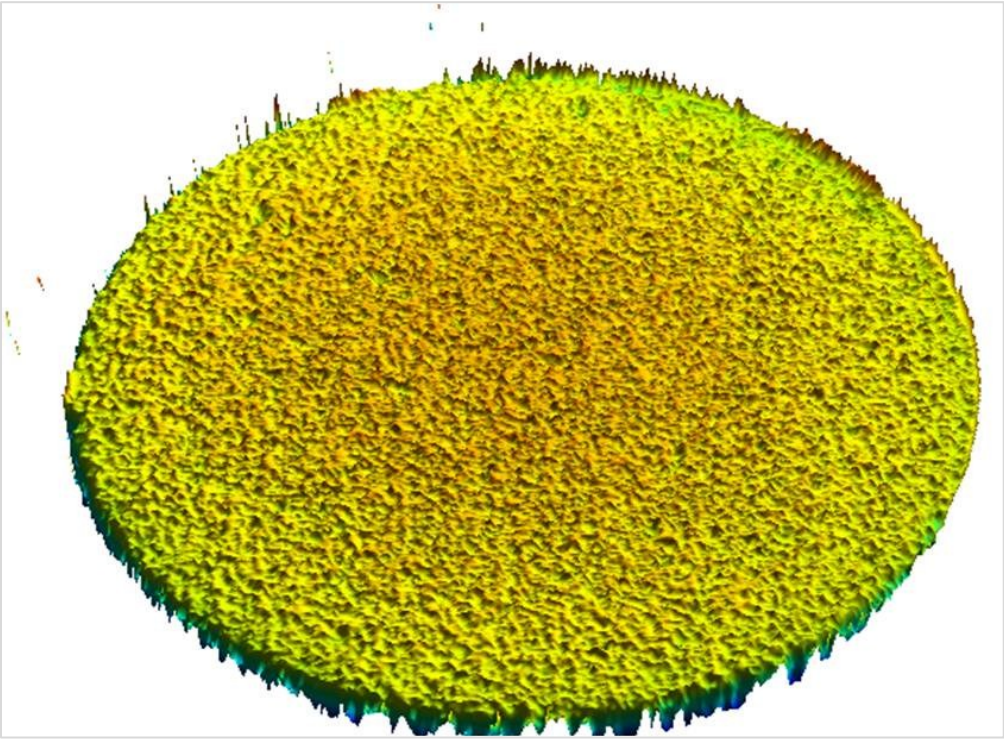

Figure 4-39 Surface topography of Alumix 321 after peening.

In addition to topography, it was quite logical to assume that shot peening affects the surface roughness as well. Figure 4-40 shows the profile scan of Alumix 321 samples before and after peening and wrought AA6061 alloy.

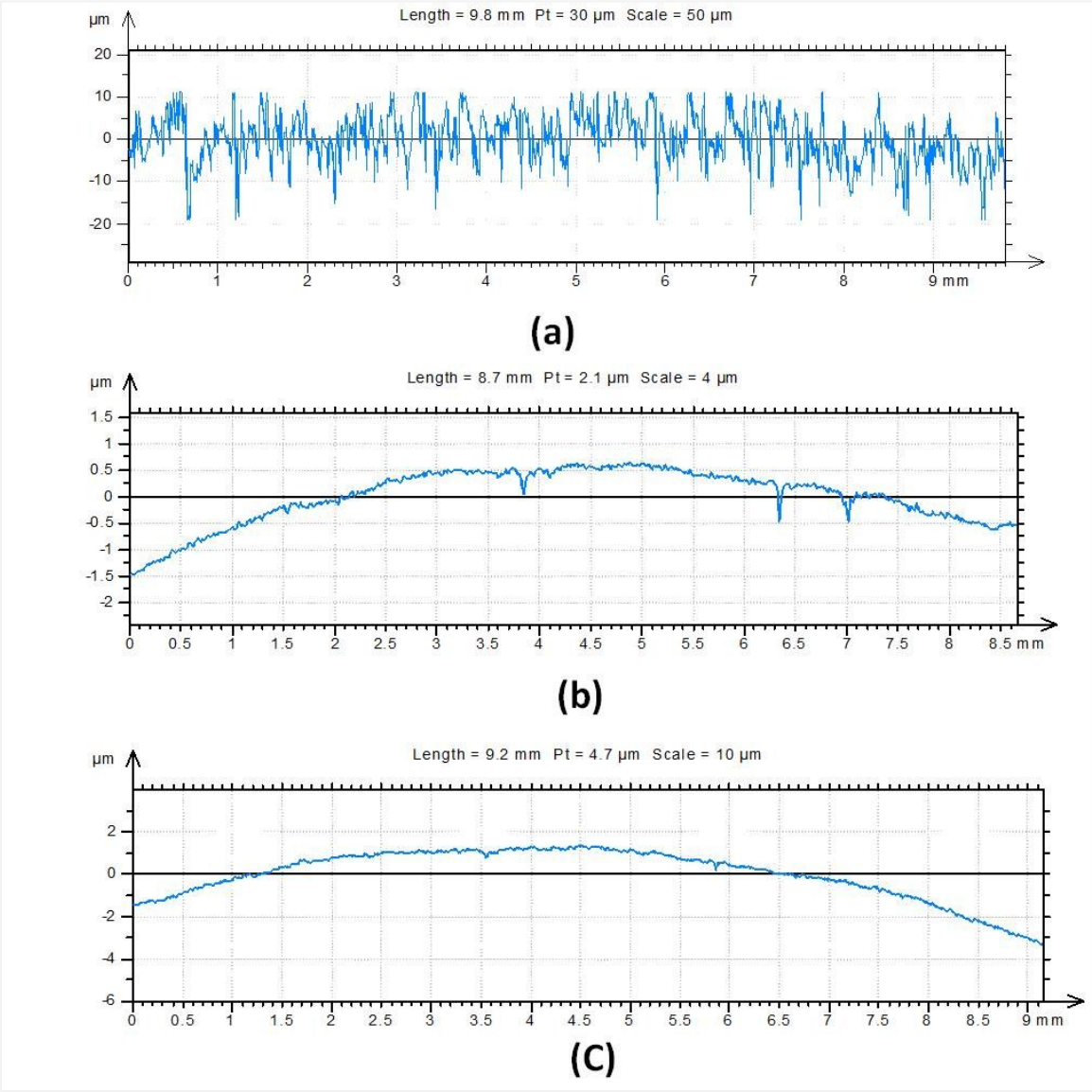

Figure 4-40 Profile scan of, (a) Alumix 321-peened, (b) Alumix 321-unpeened, and (c) wrought AA6061 alloy.

From the profile scan the average equivalent roughness (Ra) values were found and presented in Table 4-6.

Table 4-6 Roughness values of peened and unpeened Alumix 321.

Material	Alumix 321-Unpeened	Alumix 321-Peened	Wrought AA6061
Roughness (Ra)	0.033±0.003 µm	3.95±0.252 µm	0.034±0.004 µm

4.5.5 *RESIN IMPREGNATION*

Since it is concluded that the pores are very detrimental on corrosion resistance of sintered parts, resin impregnation was used to close off the porosity and study the effect of this process on corrosion resistance. The technique involves filling the porosity with epoxy resin and examines the effect that this process has on the corrosion behaviour of Alumix 321. In addition to that, resin impregnation was also used to study the effect of surface area on the corrosion resistance. Figure 4-41 illustrates the dark field illumination of Alumix 321 microstructure after impregnation. Resin impregnation technique was successful in closing the porosity. However, the impregnation process was performed more than one time to ensure that most of the pores were closed.

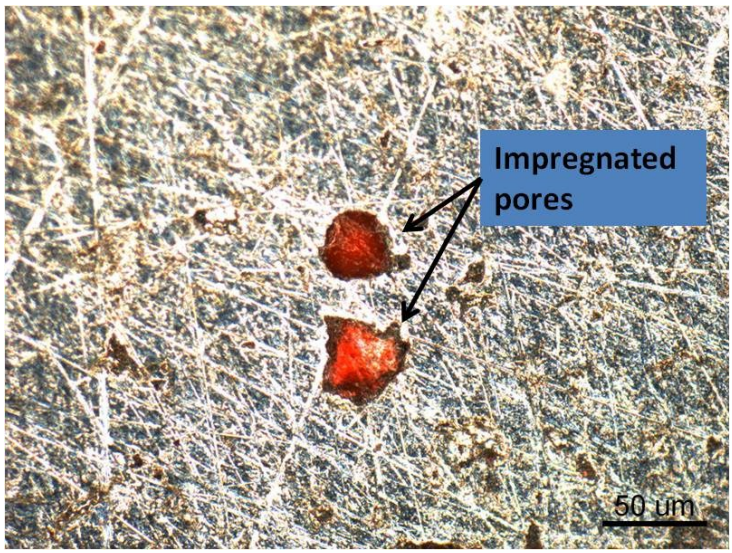

Figure 4-41 Dark field optical micrograph of Alumix 321 after resin impregnation.

4.6 CORROSION EVALUATION OF AA6061-T6

As was mentioned earlier, there is a lack of standards dealing with corrosion experiments of aluminum PM materials. Only a few scientific articles were published about this topic, and for most of the articles, there was a lack of complete description of the experimental conditions of corrosion of aluminum sintered materials. Due to these issues and as a first step corrosion evaluation experiments were conducted on the wrought AA6061 which is the equivalent of Alumix 321 PM alloy.

4.6.1 *OPEN CIRCUIT POTENTIAL (OCP)*

Open circuit potential is the potential of the sample when no current or potential is applied. Prior to electrochemical experiments this value needs to be measured because electrochemical testing parameters are related to this value. Figure 4-42 shows the open circuit potential of AA6061 aluminum alloy immersed in 3.5 wt% NaCl solution. The graph shows that OCP started with a higher initial open circuit potential before the potential gets stabilized and attained a stable open circuit potential at -0.736±0.004 V within 45 minutes and hence, this time was chosen as a time required for stabilization prior any electrochemical experiments. This value was in a good agreement with the work of other researchers [75] .

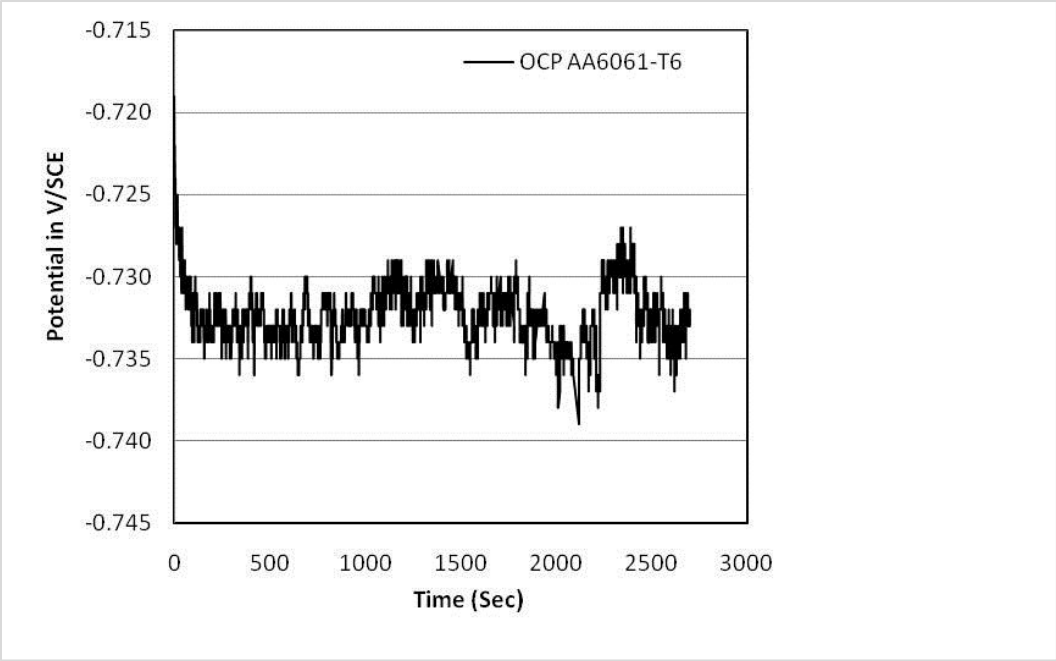

Figure 4-42 Open circuit potential variation Vs. exposure time of AA6061-T6.

4.6.2 *TAFEL EXTRAPOLATION (TE)*

Tafel plot was used to measure the corrosion current and consequently the corrosion rate of AA6061 samples. The plot as shown in Figure 4-43 was generated by scanning the samples ±250 mv vs. OCP. Both cathodic and anodic portion of the curve were extrapolated and the corrosion current I_{corr} can be estimated. Results show that the I_{corr} found to be 1.767E-06 A/cm^2. The corrosion rate was calculated according to the ASTM standards G 102-89 (2004) and equation (1-8) [76].

According to this equation, the corrosion rate found to be 19X10^{-3} mmpy. This value is very close to the value obtained by Ul-Hamid, 11X10^{-3} mmpy, under similar conditions [39]. On contrary to these results, the corrosion rate of AA6061 was found to be 63X10^{-3} mmpy [77]. The higher value obtained in [77] is attributed to the different environment used (seawater) in which the electrolyte was flowing with a velocity 10.0 ft/sec.

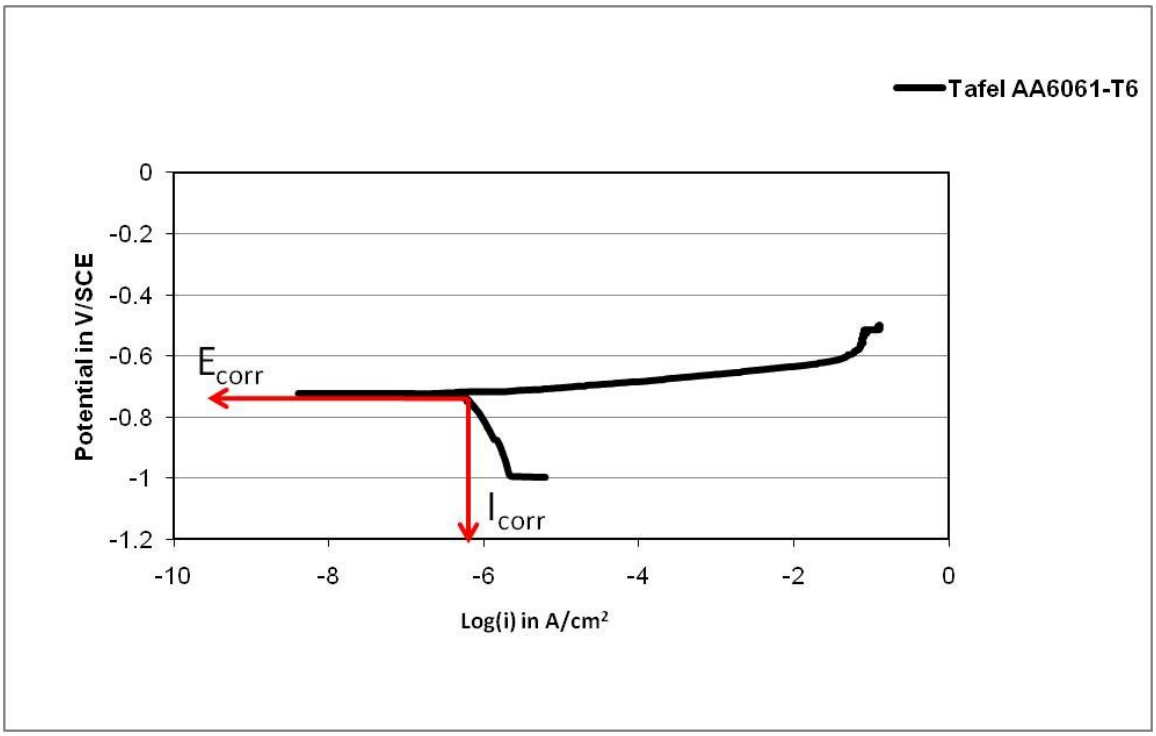

Figure 4-43 Tafel plot of AA6061-T6 aluminum alloy in 3.5 wt% NaCl solution.

4.6.3 *CYCLIC POLARIZATION (CP)*

Cyclic polarization experiments were conducted on AA6061 samples to provide information about pitting susceptibility. Cyclic polarization plots can offer practical information about pitting potential E_{pit} and protection or repassivation potential E_{rep}. Figure 4-44 illustrates a cyclic polarization graph of AA6061-T6 aluminum alloy immersed in 3.5 wt% NaCl solution. Pitting susceptibility can be evaluated from the anodic section of the scan. The anodic portion of graph does not show a classical passive region and instead shows that the current density increases dramatically within a very small potential range. It is found that there was an increase in current density from about $1x10^{-7}$ A/cm^2 to 0.1 A/cm^2 within only 100 mV/SCE. This remarkable increase in current density within a very small potential range is known to be a sign of pitting. Pitting potential is located at the same potential of the corrosion potential -0.714$\pm$ 0.003 V/SCE. The fact that pitting potential coincides with the corrosion potential was confirmed by other researchers [39, 53, 75, 78] . Furthermore, this fact was further

confirmed and explained by metallographic analysis and will be discussed later in this chapter. The cyclic polarization plot shows also another characteristic point, this point is the repassivation potential. Repassivation or protection potential (E_{pro}) is defined according to NACE/ASTM G193-10b standard as the most noble potential at which pitting or crevice corrosion will not propagate in a specific environment [79]. The repassivation potential of AA6061-T6 under current testing conditions was -1.039± 0.005 V/SCE. Corrosion parameters of AA6061-T6 in 3.5 wt% NaCl solution are shown in Table 4-7.

Table 4-7 Corrosion parameters of AA6061-T6 in 3.5 wt% NaCl solution.

Material	E_{ocp} V vs. SCE	E_{corr} V vs. SCE	I_{corr} A/Cm^2	E_{pit} V vs. SCE	E_{rep} V vs. SCE	C_R mmpy
AA6061-T6	-0.736±0.004	-0.714 ±0.003	1.77X10^{-6}	-0.714±0.003	-1.039±0.005	19X10^{-3}

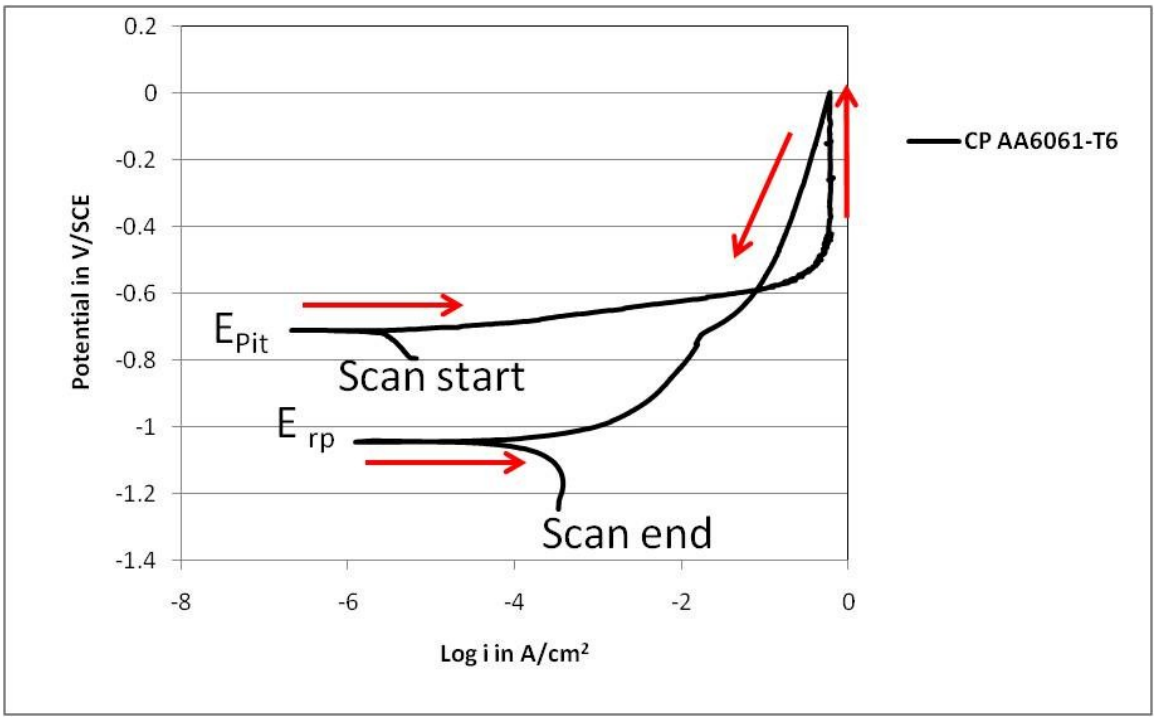

Figure 4-44 Cyclic polarization plot of AA6061-T6 alloy in 3.5 wt% NaCl solution.

4.6.4 *CHARACTERIZATION OF CORRODED SAMPLES*

AA6061-T6 samples subjected to corrosion experiments were characterized and studied after the corrosion experiments. Techniques such X-ray, EMPA, optical and scanning microscopy were used to evaluate the microstructure and the corroded surfaces of the investigated samples. It was pointed earlier that the corrosion potential and the pitting potential coincide; this hypothesis suggests that pitting takes place at the corrosion potential. In order to verify this assumption, AA6061-T6 samples were kept at corrosion potential for 24 hours and then subjected to metallographic analysis.

Figure 4-45 shows the optical micrograph of AA6061 T6 sample after it was kept at corrosion potential in which pitting ccorrosion was clearly visible. The microstructure was also analyzed after the AA6061-T6 samples were polarized above the corrosion potential. Figure 4-46 shows that polarized samples contain large pits. The analysis shows that two types of pits were obtained as a function of the potential.

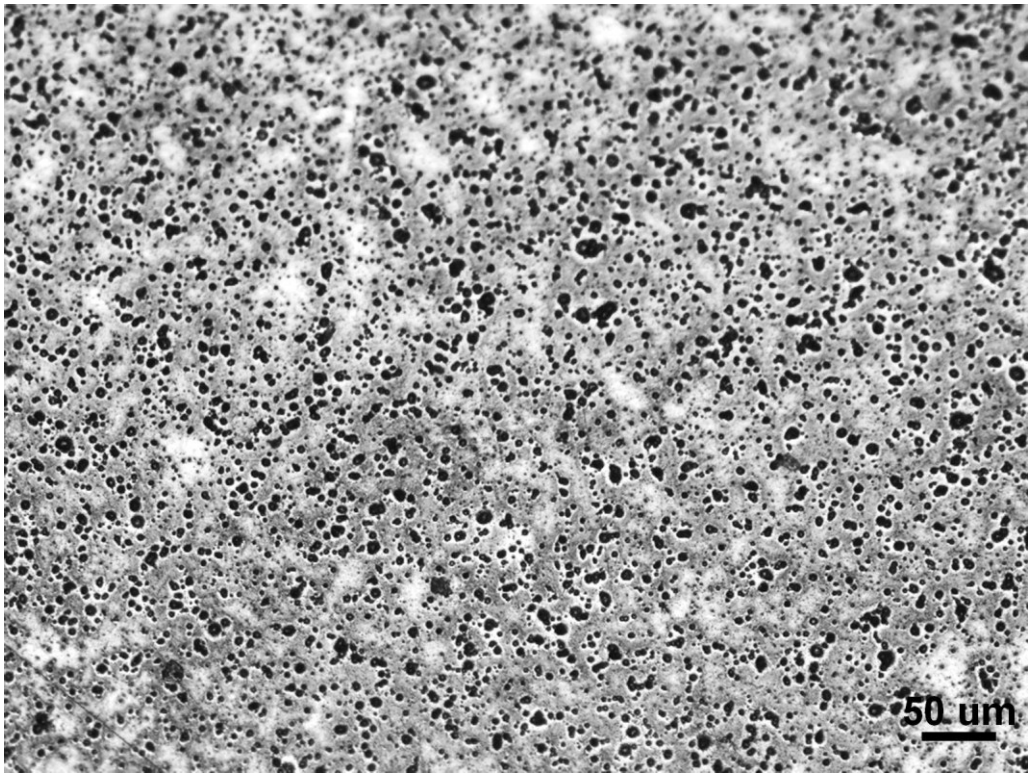

Figure 4-45 Optical micrograph of AA6061-T6 shows pitting corrosion.

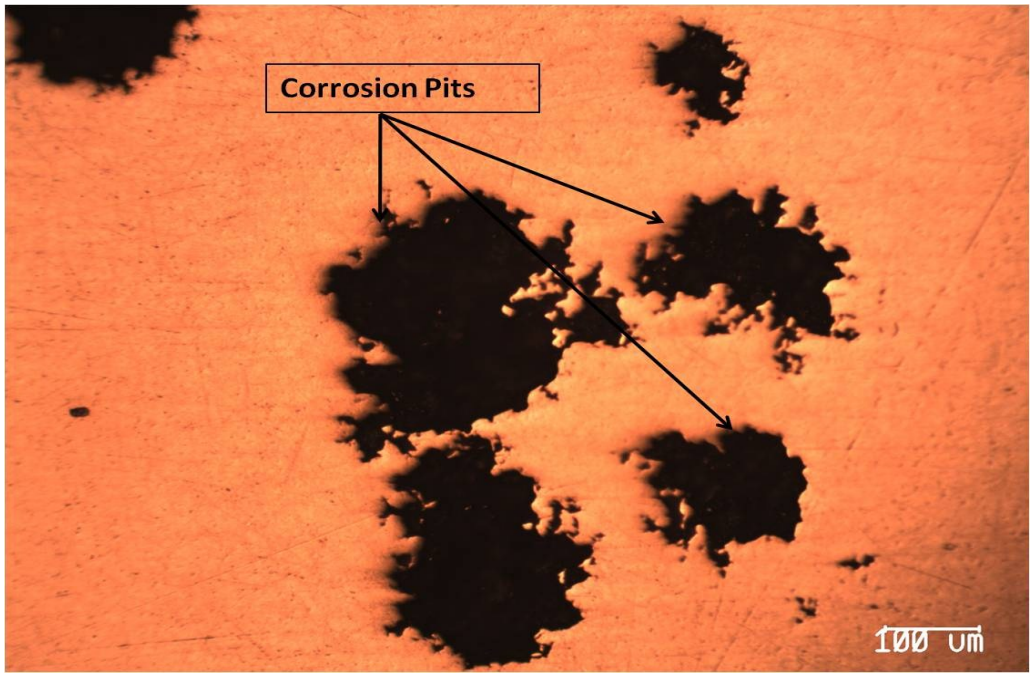

Figure 4-46 Pitting corrosion of AA6061-T6

Close examination using SEM shows that two types of pitting mechanisms observed, hemispherical and crystallographic. Figure 4-47 shows the SEM micrograph of hemispherical pitting which formed at the corrosion potential. In addition to the hemispherical pitting, large crystallographic pits were clearly seen on the AA6061-T6 samples polarized above the corrosion potential and shown in Figure 4-48.

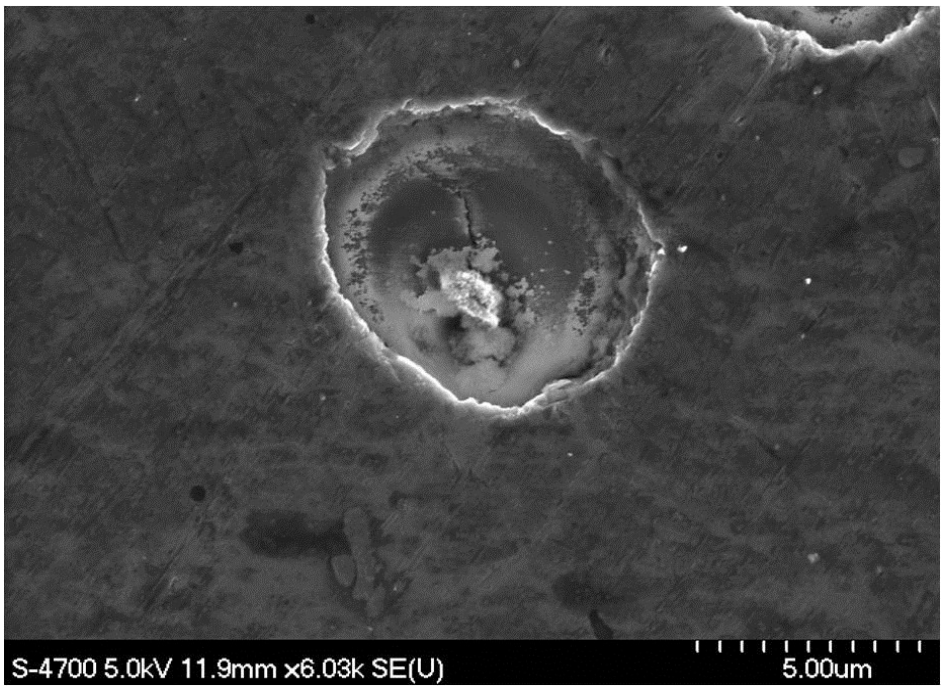

Figure 4-47 SEM micrograph of AA6061-T6 showing hemispherical pitting attack.

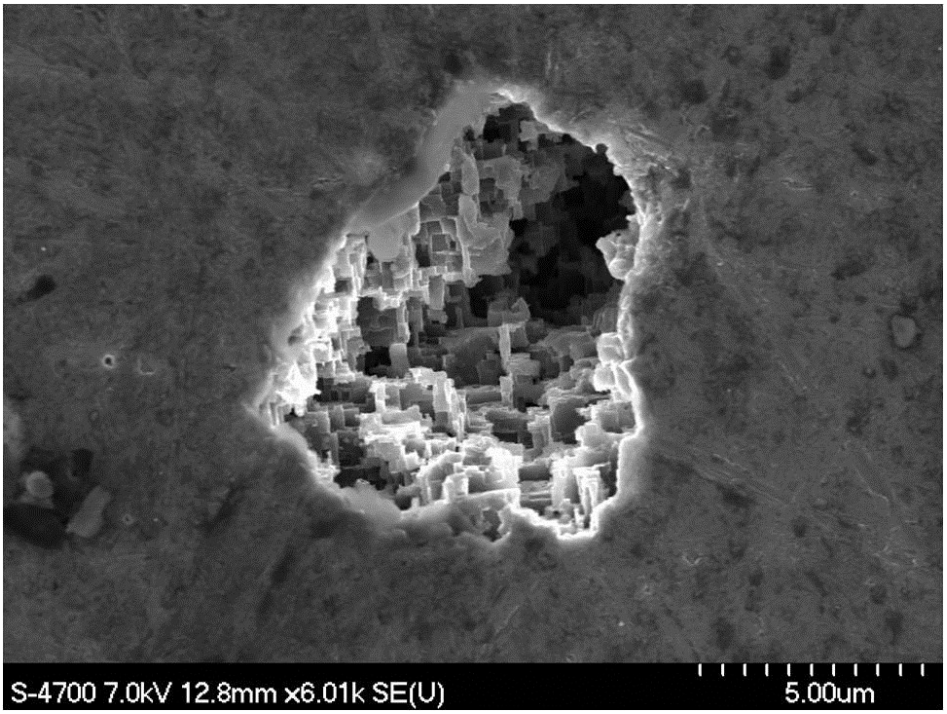

Figure 4-48 SEM micrograph of sample AA6061-T6 showing crystallographic pitting.

To trace the source of pitting corrosion, AA6061-T6 samples were kept in 3.5 wt% NaCl for 24 hours and then examined using SEM. Figure 4-49 shows the corrosion morphology of AA6061-T6 sample.

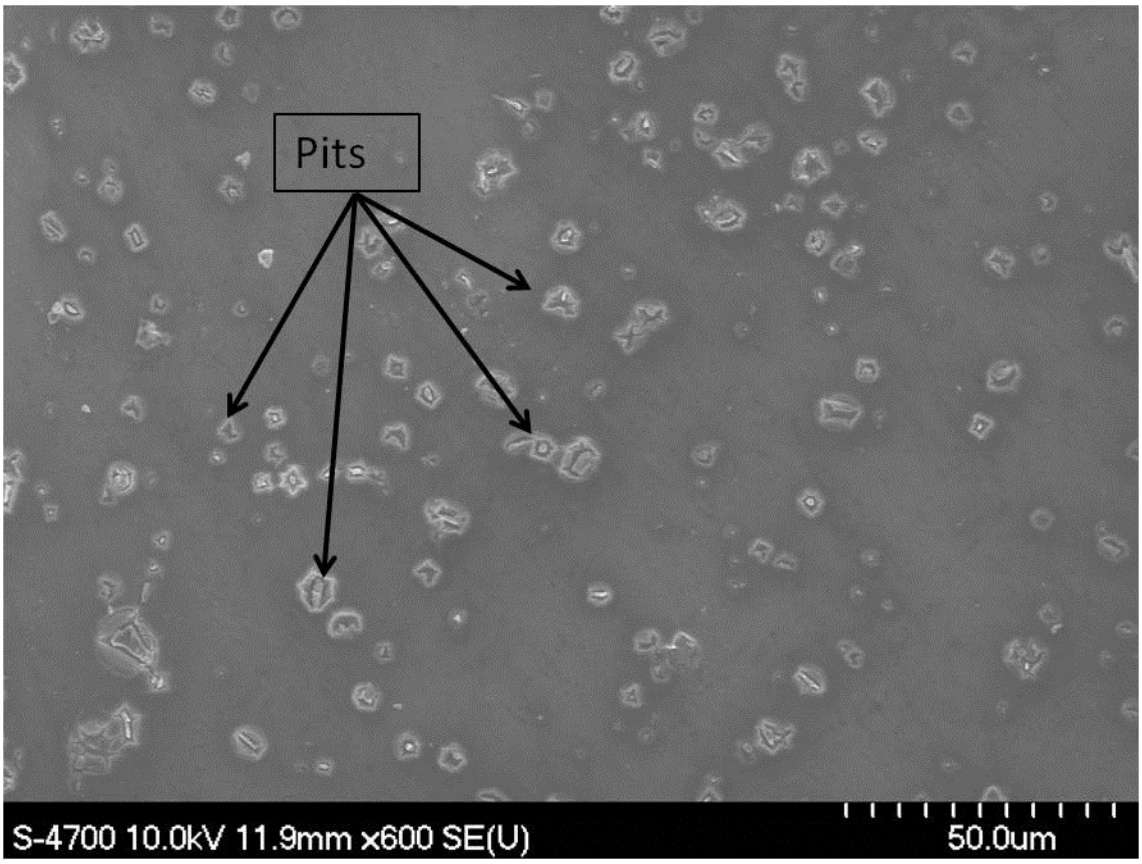

Figure 4-49 Low magnification SEM image showing pitting corrosion of AA6061-T6.

Higher magnification SEM images (Figure 4-50) shows breakdown of the film at certain spots and interaction points. This breakdown is attributed to the two stages of pitting, the first that occurring at the boundary between the solution and the passive film and the second that takes place within the passive film [32, 34].

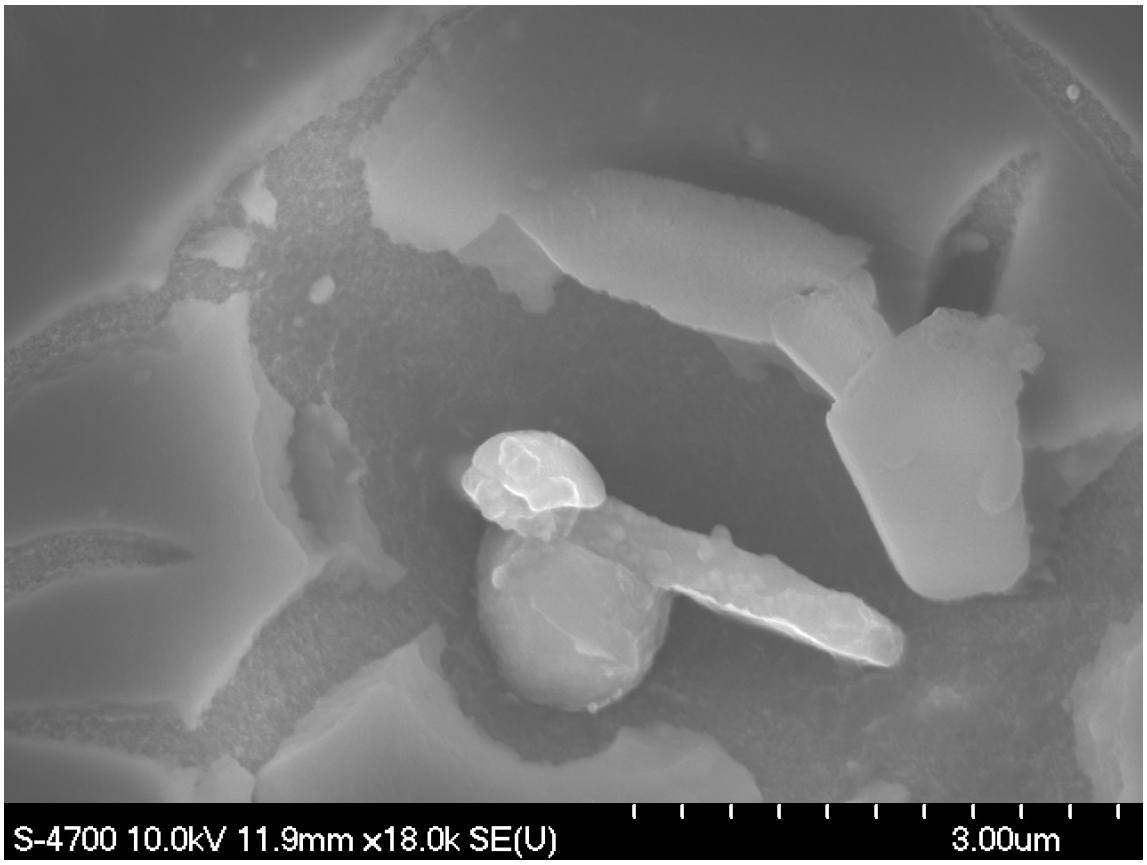

Figure 4-50 Higher magnification SEM micrograph showing breakdown of the passive film of AA6061-T6 sample.

The SEM images shown in Figure 4-51 indicates that the pits are formed at the vicinity of some type of particles. To understand the source of pitting and its relation to those particles, chemical analysis using EDS mapping analysis was performed and the results shown in Figure 4-52. In addition to other elements such as aluminum, silicon, magnesium, and copper the results of EDS map analysis prove the presence of iron as a primary component in this particle.

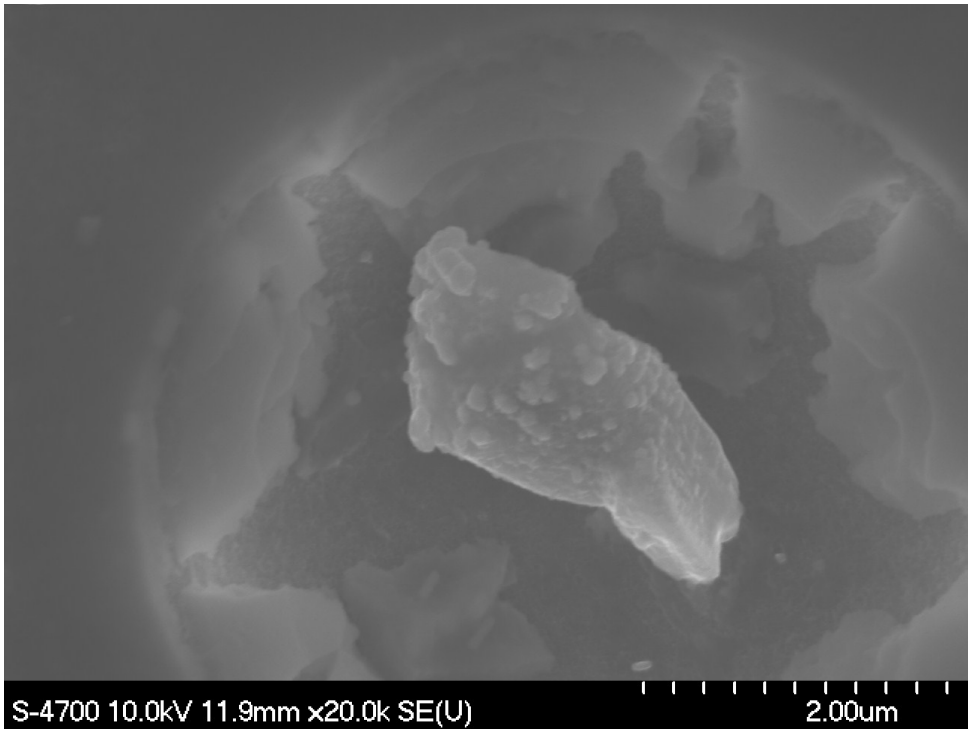

Figure 4-51 SEM micrograph of AA6061-T6 corroded sample showing initiation of pitting around particle.

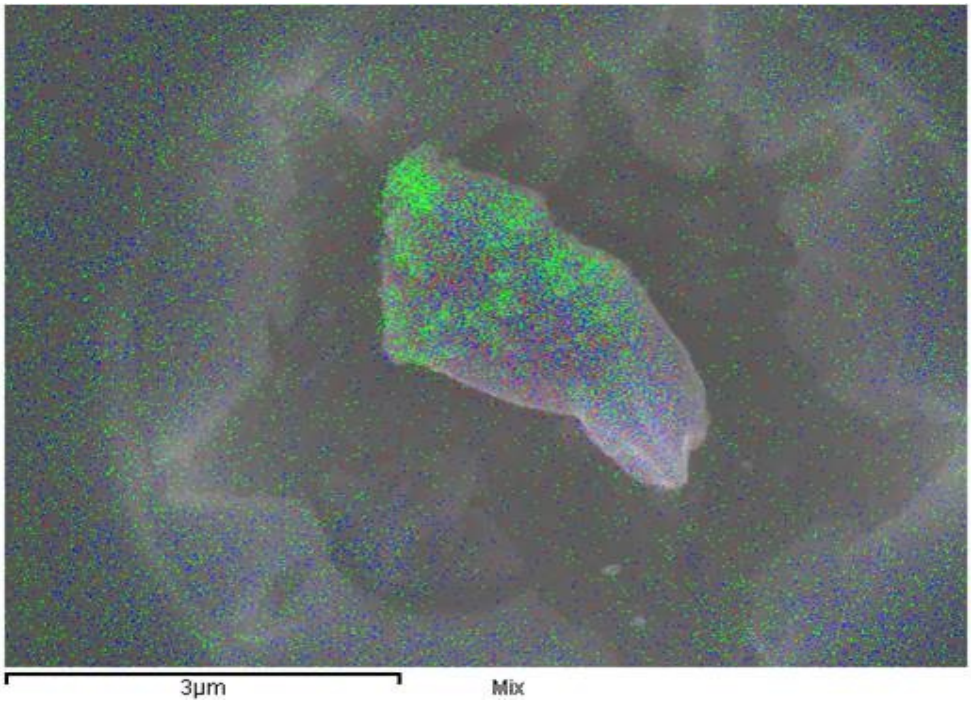

Figure 4-52 EDS map analysis of corroded AA6061-T6 showing the chemical composition of a particle and pit around it (Fe=red, Cu=green, Si=blue).

Based on the results, it is concluded that there is a relation between the particles and the pits form at their vicinity. For more and thorough investigation and understanding the role these particles play as a pitting imitation site, corroded AA6061 samples were slightly polished and then examined using SEM. Figure 4-53 shows how those pits form around secondary phase particles. Chemical analysis of those phases was analyzed using EDS and the results are shown in Figure 4-54.

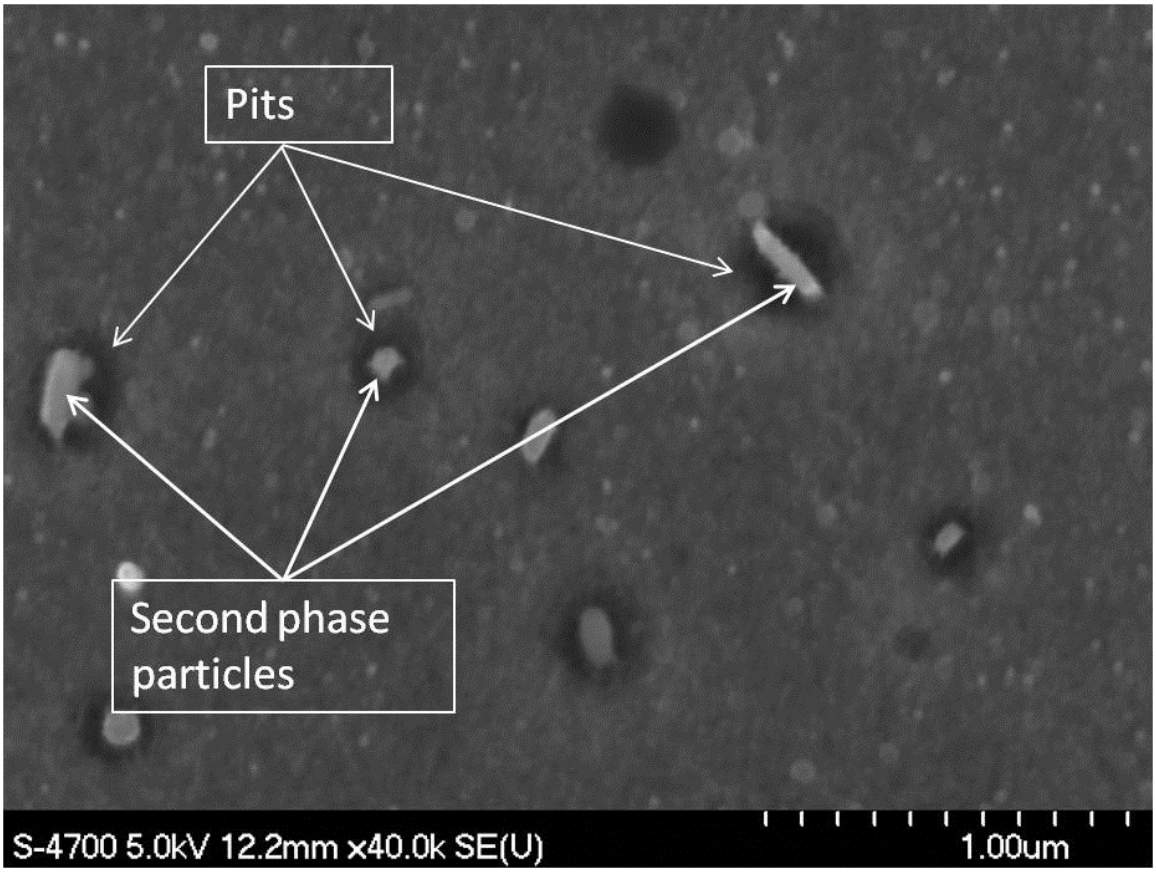

Figure 4-53 Initiation of pits around secondary phase particles.

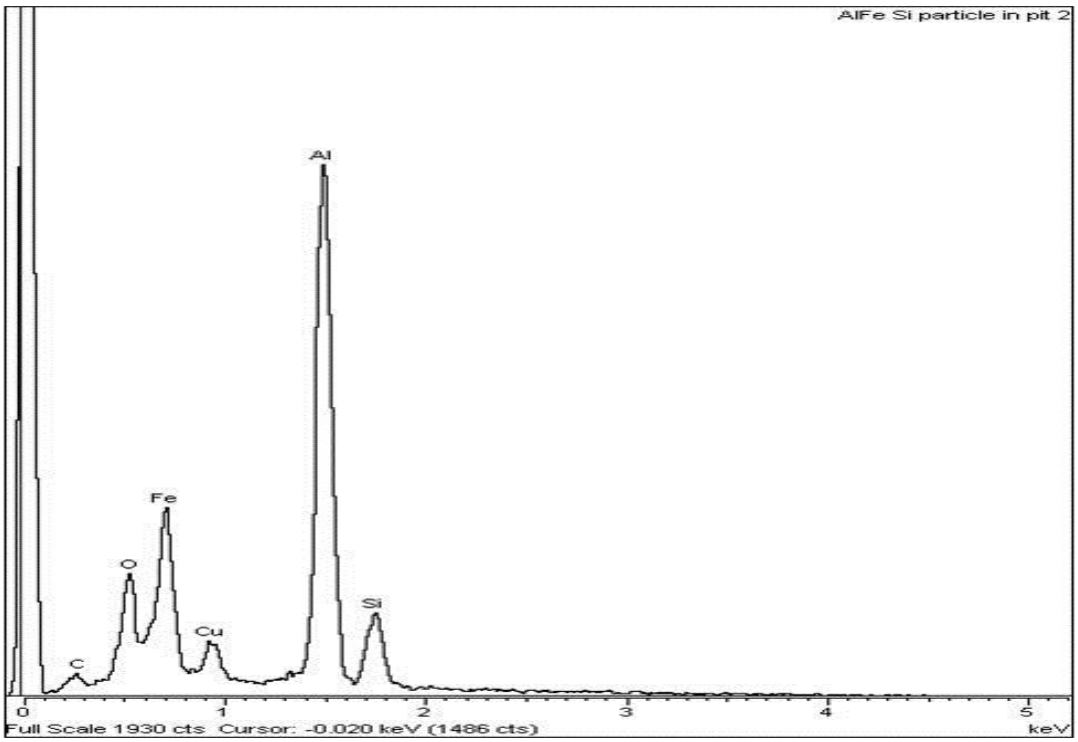

Figure 4-54 EDS spectrogram of the particles inside pits.

EDS analysis shows clearly the presence of iron as a major element in these particles.

To get more quantitative analysis of the second phase particles EPMA was used. Figure 4-55 illustrates the electron probe backscatter image of the AA6061-T6 microstructure on which EPMA was carried out. In addition to the aluminum matrix and iron containing particles, Mg_2Si was found. Close examination shows that the iron containing particles can be divided into two types, Chinese script like particles and small gray particles. EPMA analysis was performed on the entire matrix, iron containing particles and Mg_2Si and the results are presented in Table 4-8.

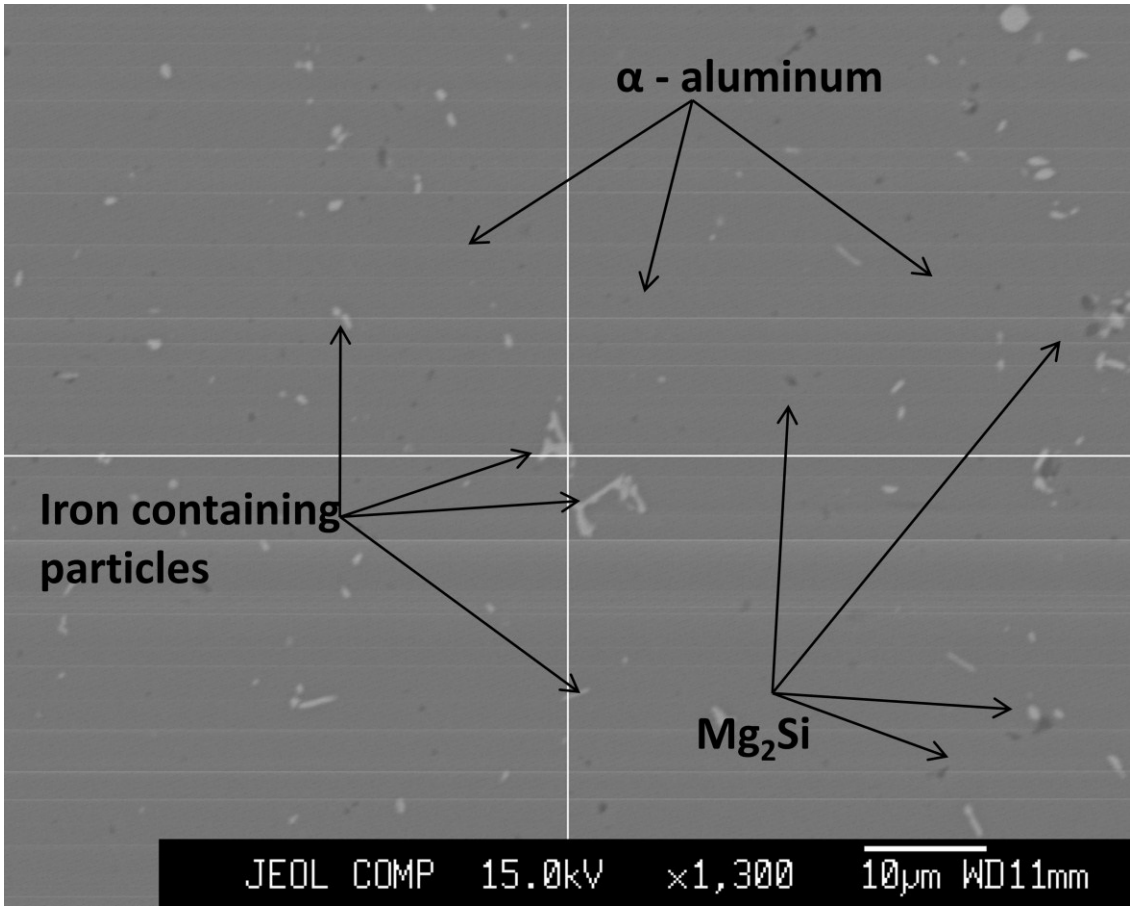

Figure 4-55 Backscattered electron image of AA6061-T6 microstructure.

Table 4-8 EPMA analysis of phases exist in AA6061-T6 alloy.

Phase	Chemical composition (wt %)				
	Al	Cu	Si	Mg	Fe
Matrix	98.03	0.29	0.53	0.74	0.05
Small gray particles	93.52	0.46	1.16	0.63	2.38
Chinese script particles	73.3	1.65	5.38	0.31	19.86
Mg_2Si	75.81	0.37	11.25	12.7	1.98

EPMA results suggest the presence of two types of iron containing particles with different iron content. It is very hard to identify the exact chemical formula of these

phases due to the reasons discussed earlier in this chapter, but the main conclusion here is that these are iron rich particles and contain silicon, aluminum. Smaller amount of magnesium and copper that detected suggests that these atoms were excited from the matrix and not from the particles themselves. These particles will be called AlFeSi particles. Transmition electron microscopy (TEM) analysis performed by D.M. Sun and others on a similar system shows very similar results and confirmed the presence of AlFeSi particles [80].

It has been reported by many researchers that iron rich particles such as AlFeSi , Al_3Fe and Al_6Fe are cathodic and more noble to the aluminum matrix, and have a detrimental effect on localized corrosion[30, 43, 81]. This explains clearly the reason behind pitting initiation at the vicinity of AlFeSi particles in AA6061 alloy that was shown in Figure 4-52 and Figure 4-53.

The corrosion attack and the corrosion product were also investigated. Figure 4-56 and Figure 4-57 show the optical micrograph and the SEM micrograph of corroded AA6061-T6 sample, respectively. It is obvious that the samples are preferentially attacked by corrosion along their longitudinal direction.

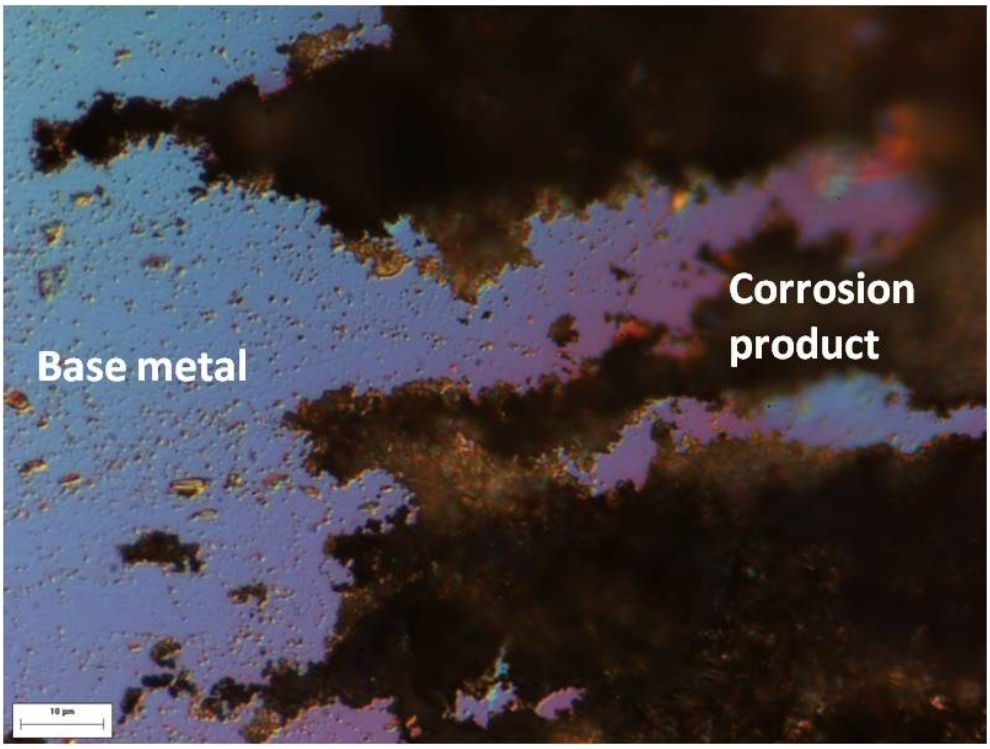

Figure 4-56 Optical micrograph of coroded AA6061-T6 sample showing the direction of corrosion attack.

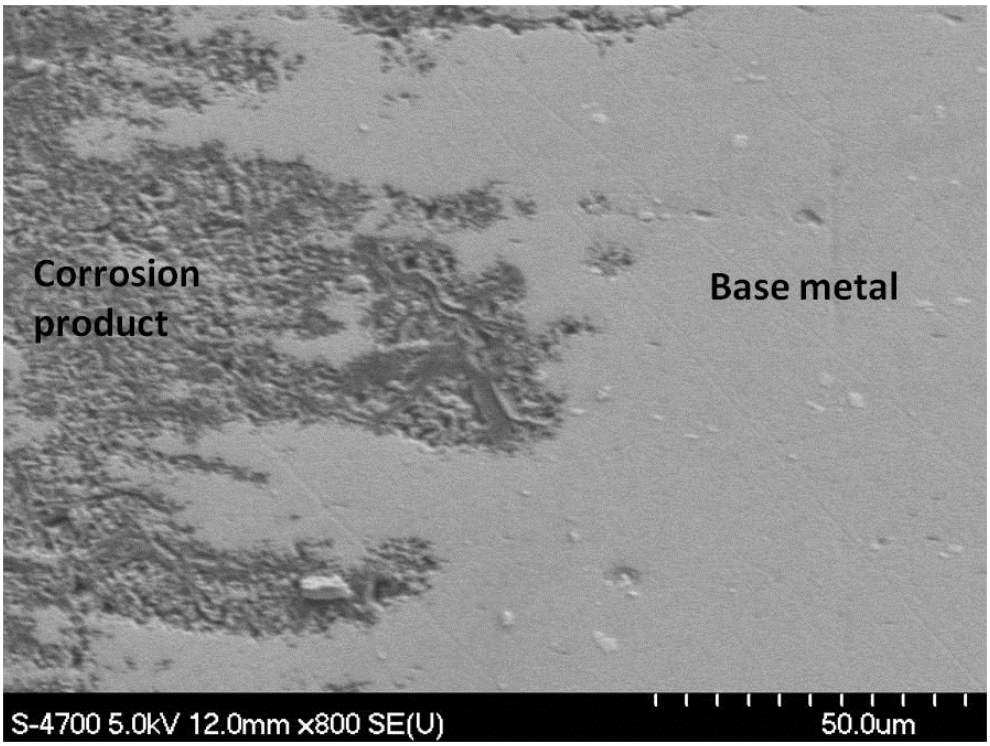

Figure 4-57 SEM micrograph showing the corosion attack of AA6061-T6 alloy.

Figure 4-58 shows the SEM micrograph of the corrosion product. The micrograph shows that the structure of the corrosion product is porous, non adherent and has a spongy nature**.** EDS analysis was performed on the corrosion product and the results show the presence of O, Na, Cl, and Al. XRD carried out on the corrosion shows a little success, because of the little amount of the corrosion product amount obtained. The diffraction pattern shown in Figure 4-59 indicates mainly the base metal in addition to small peaks of aluminum oxide and aluminum hydroxide.

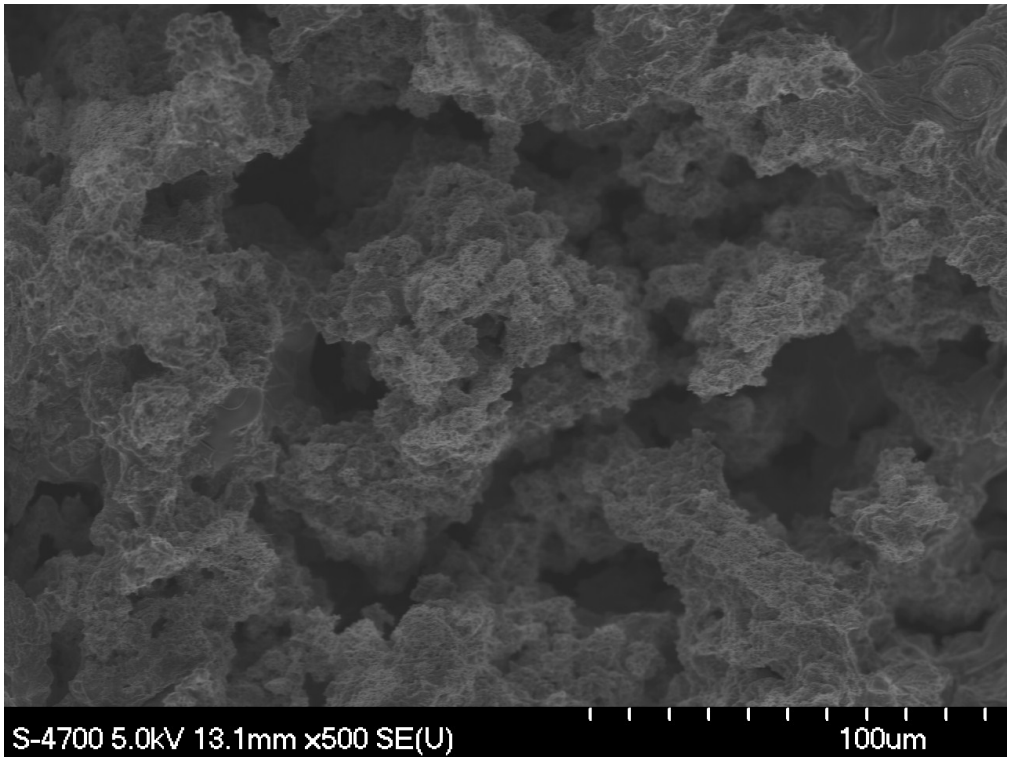

Figure 4-58 SEM micrograph of the corrosion product of AA6061-T6 alloy immersed in 3.5 wt% NaCl.

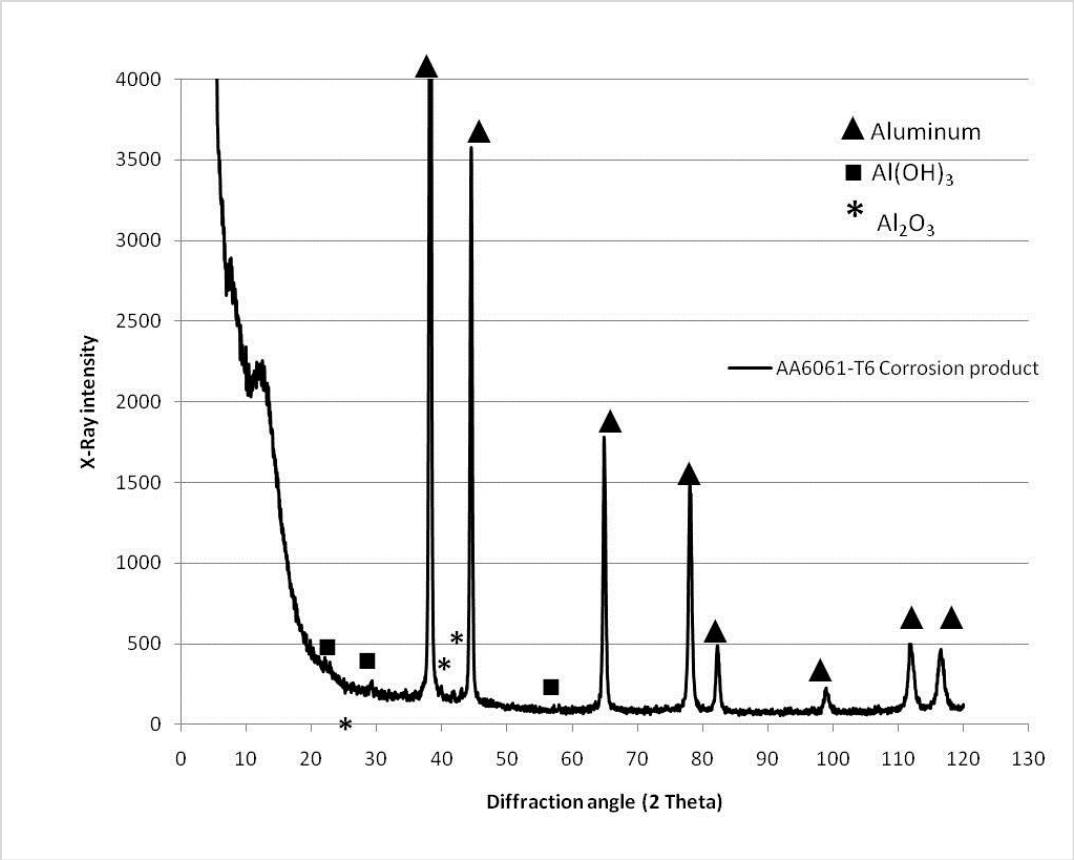

Figure 4-59 XRD diffraction pattern of the corrosion product of AA6061-T6 after exposing to 3.5 wt% NaCl.

4.7 CORROSION OF ALUMIX 321

4.7.1 *OPEN CIRCUIT POTENTIAL (OCP)*

Samples of Alumix 321 were pressed in the range of 100-500 MPa, then sintered at 630 °C, and they were tested for the OCP. Samples pressed at 200, 300, 400, and 500 MPa show a similar trend. The OCP graphs obtained for this set of samples were noisy with a very clear fluctuation in potential. Extending the stabilization time to 100 minutes was not enough to show a clear stability in potential. Interestingly, samples pressed at 100 MPa show a smother graph and more negative potential with a continuous decrease in potential as a function of time. Figure 4-60 shows the OCP graph of the samples pressed at 100 MPa and 500 MPa.

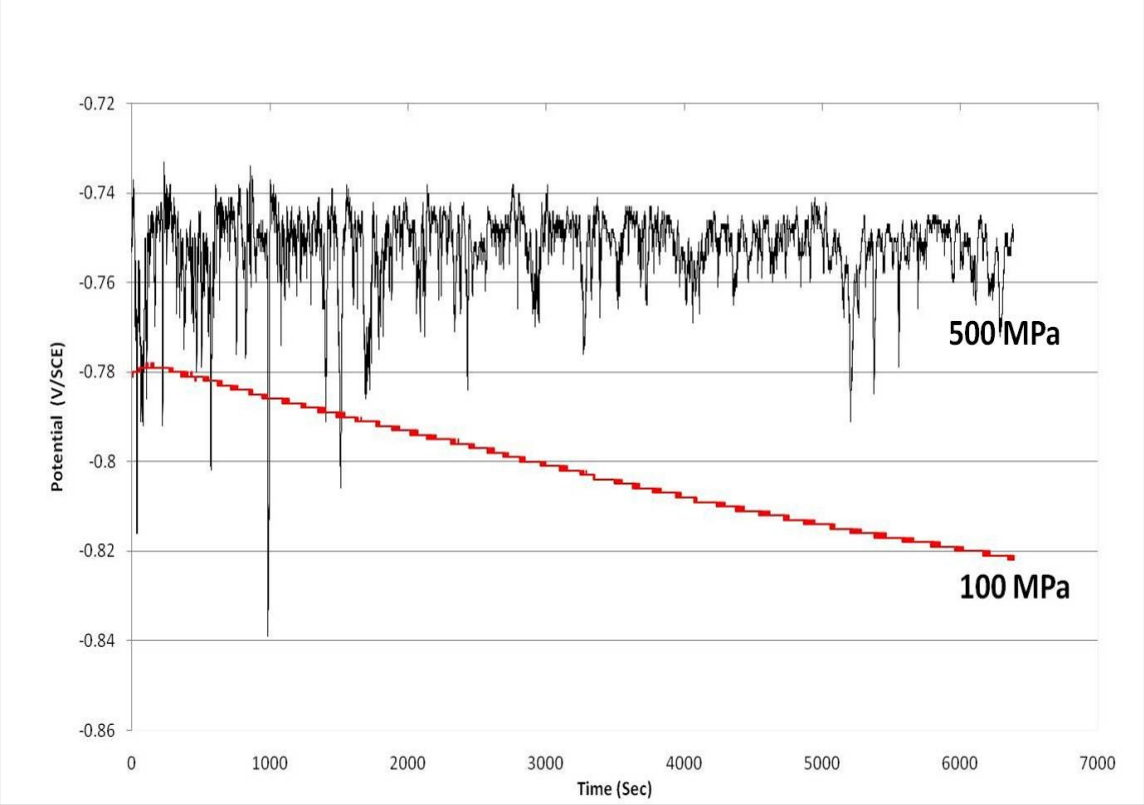

Figure 4-60 OCP variation vs. exposure time for Alumix 321 in 3.5 wt% NaCl solution.

Since two hours stabilization was not enough for steady state to take place, stabilization time was increased to 24 hours. Results of OCP after 24 hours stabilization show a much

less noisy graph and more stable and less fluctuated potential. Table 4-9 shows the variation of OCP as a function of pressing pressure.

Table 4-9 Variation of OCP as a function of pressing pressure of Alumix 321 in 3.5 wt% NaCl solution.

Pressure (MPa)	E_{OCp} (V vs.SCE)
100	-0.874±0.084
200	-0.761±0.002
300	-0.747±0.008
400	-0.748±0.004
500	-0.754±0.005

The general trend is that the samples pressed at higher pressure have less negative OCP. Interestingly, with the addition of more negative potential, samples pressed at 100 MPa show continuing drop in potential among the whole set of samples. Figure 4-61 shows the OCP variation of Alumix 321 samples pressed at 100 MPa and 500 MPa and were kept for 24 hours in 3.5 wt% NaCl solution.

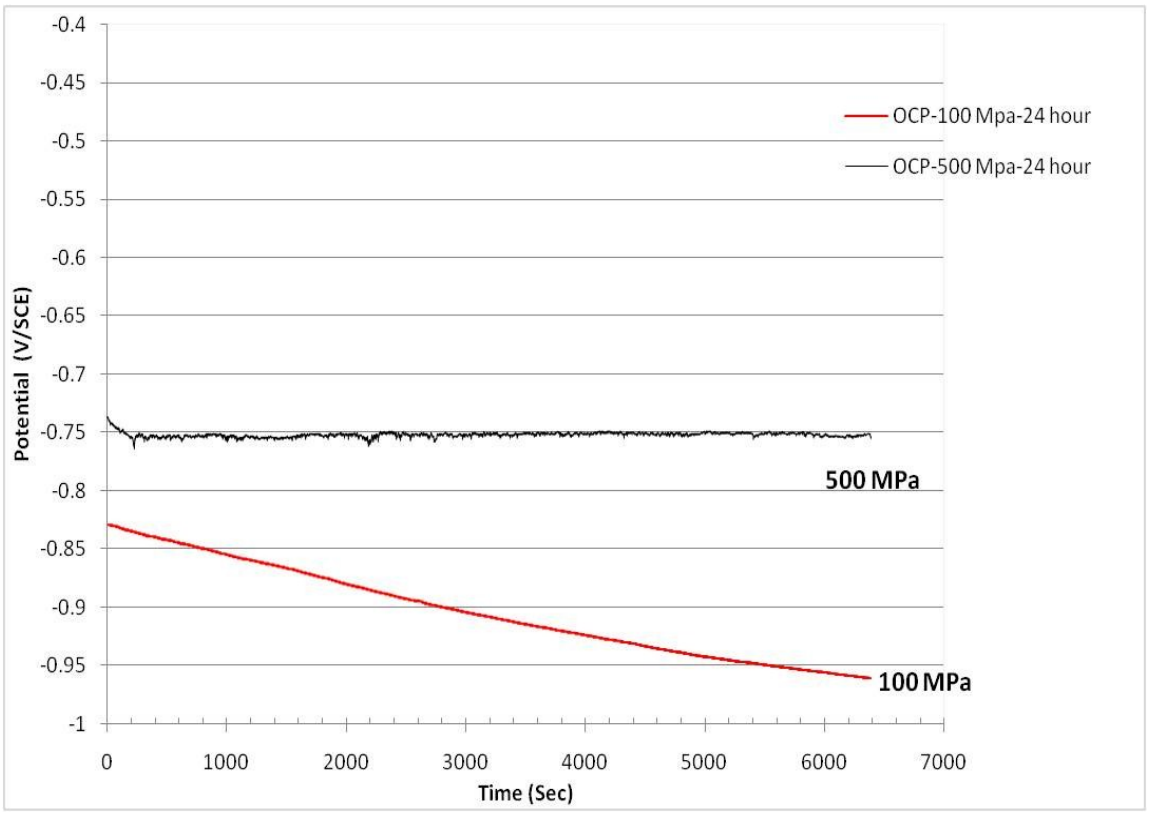

Figure 4-61 OCP variation of Alumix 321 as a function of time after 24 hours stabilization.

Y. L. Cheng [82] used the electrochemical noise technique (EN) to study the potential fluctuation of different aluminum wrought alloys in 3 wt% NaCl solution. The author related the EN to the micro galvanic cells that formed during the corrosion process. The continuously dropping in potential for the samples pressed at 100 MPa indicates that stability was difficult to achieve due to the nature of their porous structure. The samples pressed at this low pressure (100 MPa) have a low density and consequently the pores are of an interconnected nature and a very large inside surface area [83] [84]. Continuous drop in potential was also observed by F. Fedrizzi et al [85] when he studied the corrosion behaviour of AISI 316 sintered stainless steel in sodium chloride solution. It can be concluded that the interconnected pores nature and a large exposed area obtained in the low density samples lead to a very long penetration time of the testing solution into a sintered samples which result in a continues drop in potential.

4.7.2 *TAFEL EXTRAPOLATION (TE)*

Figure 4-62 shows the Tafel extrapolation graphs of Alumix 321 samples pressed in the range of 100-500 MPa. Samples pressed at 200, 300, 400, and 500 MPa show a similar trend in which very rapid increase in potential happens at the corrosion potential and this behaviour was similar to the behaviour obtained in AA6061 wrought alloy. On the contrary, samples pressed at 100 MPa show a different behaviour. Samples pressed at this low pressure show a low corrosion potential and gradual increase in current as a function of potential. This observation in addition to the previous obtained results from the open circuit potential suggests that the corrosion mechanism is different than the other samples pressed at higher pressures.

The extrapolation technique was applied to calculate the corrosion current. Results indicated that there was no clear relation between the corrosion current and pressing pressure and ranking the samples based on the applied pressure was not successful. The only conclusion here is that the samples pressed at low pressure shows a higher corrosion current among the all set of samples and hence lower corrosion resistance. The corrosion current found to be $1X10^{-5}$ A/cm^2. The set of samples that were pressed in the range of 200 to 500 MPa showed a very close density values and it is very hard to expect the pores morphology variation and pores distribution within that narrow range of density. The other factor is the uncertainty about the real surface area. The absence of a technique that enable us to measure the surface area of sintered samples led to the assumption that the exposed surface area is equal the nominal affected surface area of 1cm^2. This assumption is not true since the affected surface area of sintered samples is much larger than that of the nominal exposed area.

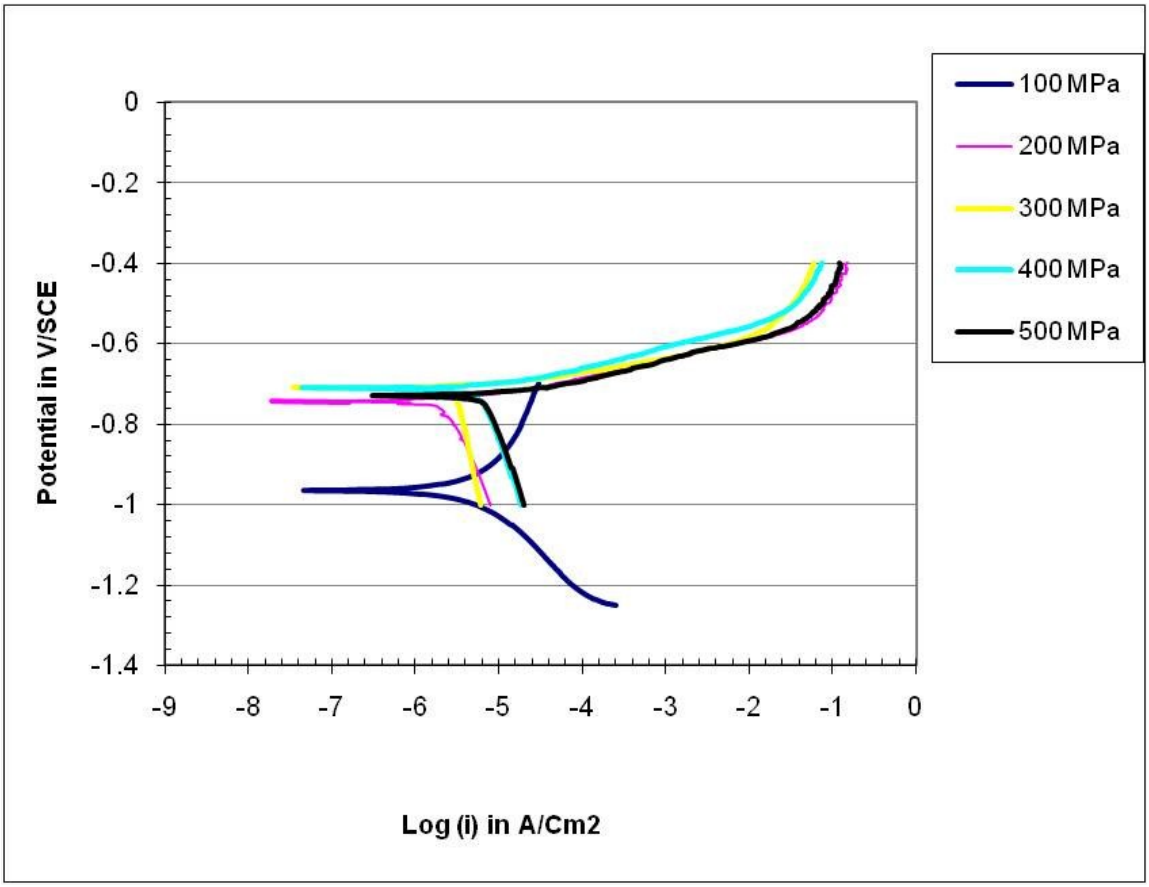

Figure 4-62 Tafel extrapolation plots for Alumix 321 in 3.5 wt% NaCl solution.

4.7.3 *CYCLIC POLARIZATION (CP)*

Figure 4-63 shows the cyclic polarization curves of Alumix 321 pressed at different pressure in 3.5 wt% NaCl solution. This test was used to study pitting susceptibility in which values of E_{pit}, E_{rep} were obtained from these plots. The main comment here is that during scanning from the negative to the positive potential stable pitting growth was not clear. Normally, stable pit starts at pitting potential and characterized with very sharp increase in current during forward scanning [26]. Similar to the behaviour of AA6061 wrought alloy, Alumix 321 PM alloy did not show a passive region and hence potential at which pitting started was not clear.

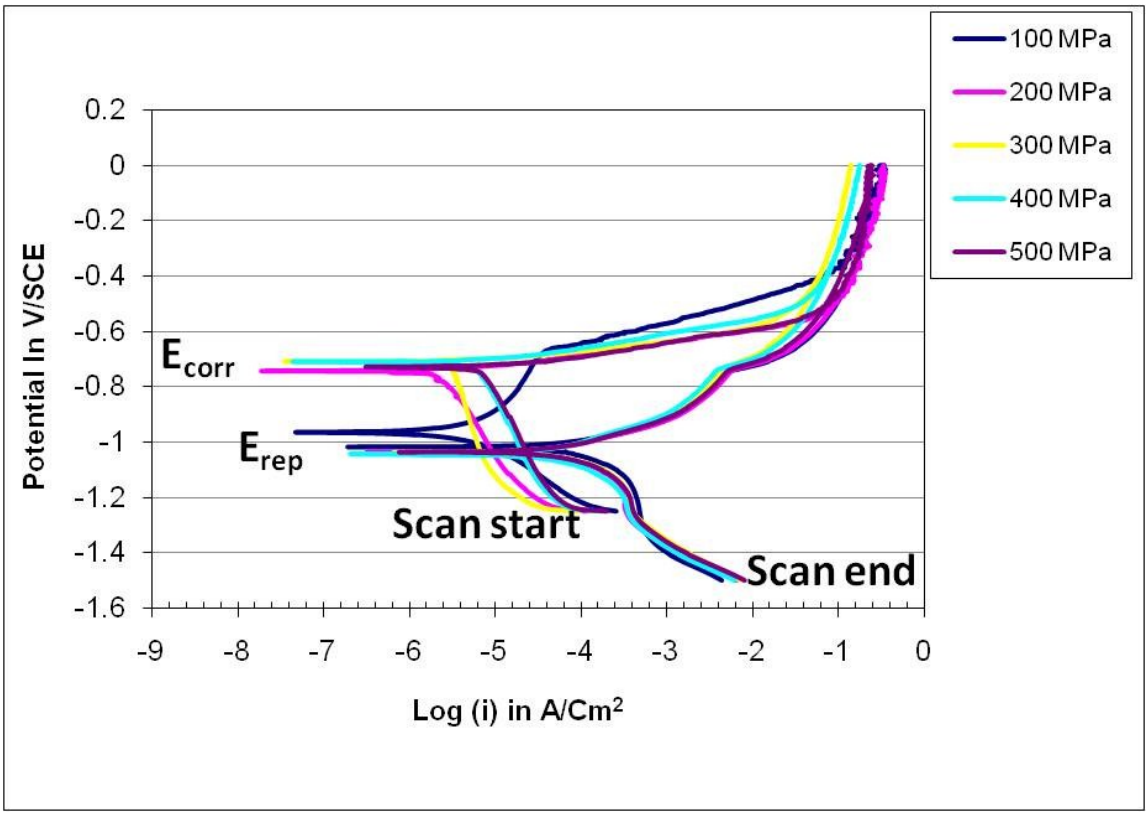

Figure 4-63 Cyclic polarization for Alumix 321 in 3.5 wt% NaCl solution.

The samples pressed in the range 200-500 MPa showed a similar trend. However, samples pressed at 100 showed a different behaviour. Figure 4-64 shows the cyclic polarization graphs for two Alumix 321 samples pressed at 100 and 500 MPa. It is clearly seen that the sample pressed at 500 MPa shows a larger tendency toward nucleation and growth of pitting. It is observed that pitting which is indicated by sharp increase in current happens at potential that coincides with the corrosion potential. On the other hand the anodic polarization curve of the samples pressed at 100 MPa shows a different behaviour of a gradual increase in current as a function of applied potential. Additionally, the potential corresponding to pitting was higher compared to that of the samples pressed at 500 MPa. This difference in behaviour suggests a different corrosion mechanism. Due to the low pressure used, samples pressed at 100 MPa showed lower density and hence, the pores exist are mostly interconnected and work as crevices sites, this microstructure offers a very large surface area for the corrosion reactions.

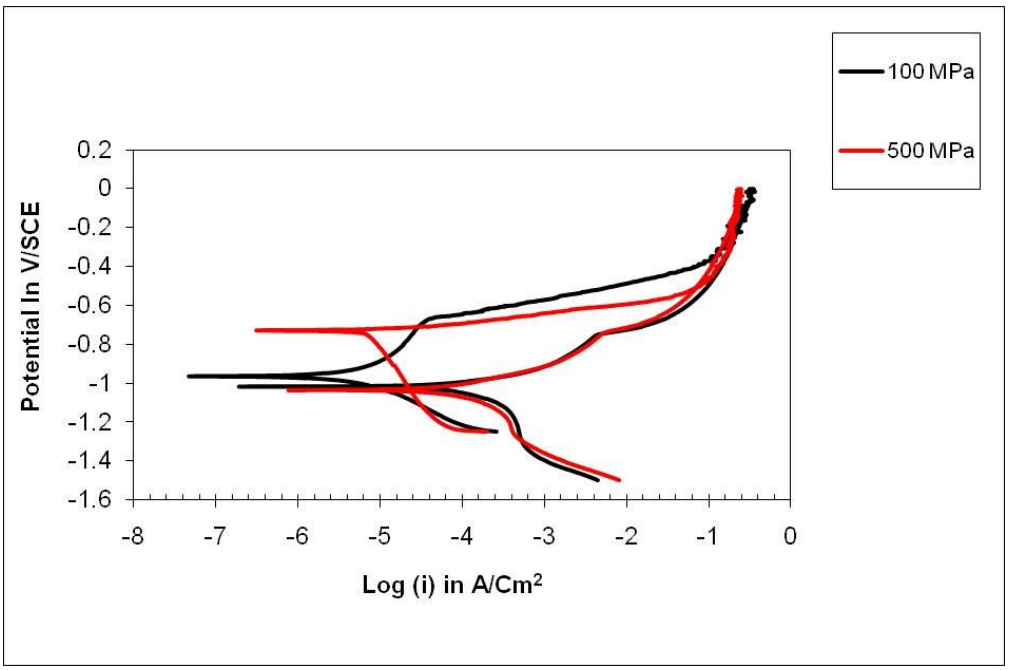

Figure 4-64 Cyclic polarization graph of Alumix 321 pressed at 100 MPa and 500 MPa in 3.5 wt% NaCl solution.

Figure 4-65 shows the variation of E_{corr} as a function of pressing pressure, which indicates that in agreement with the open circuit potential, the E_{corr} is higher at higher pressure and it can be deduced that samples at higher pressure exhibits an increased tendency toward passivation. The most active potential was recorded for the sample pressed at 100 MPa (-0.971 V/SCE), while the value recorded for the samples pressed at 500 MPa was -0.717 V/SCE.

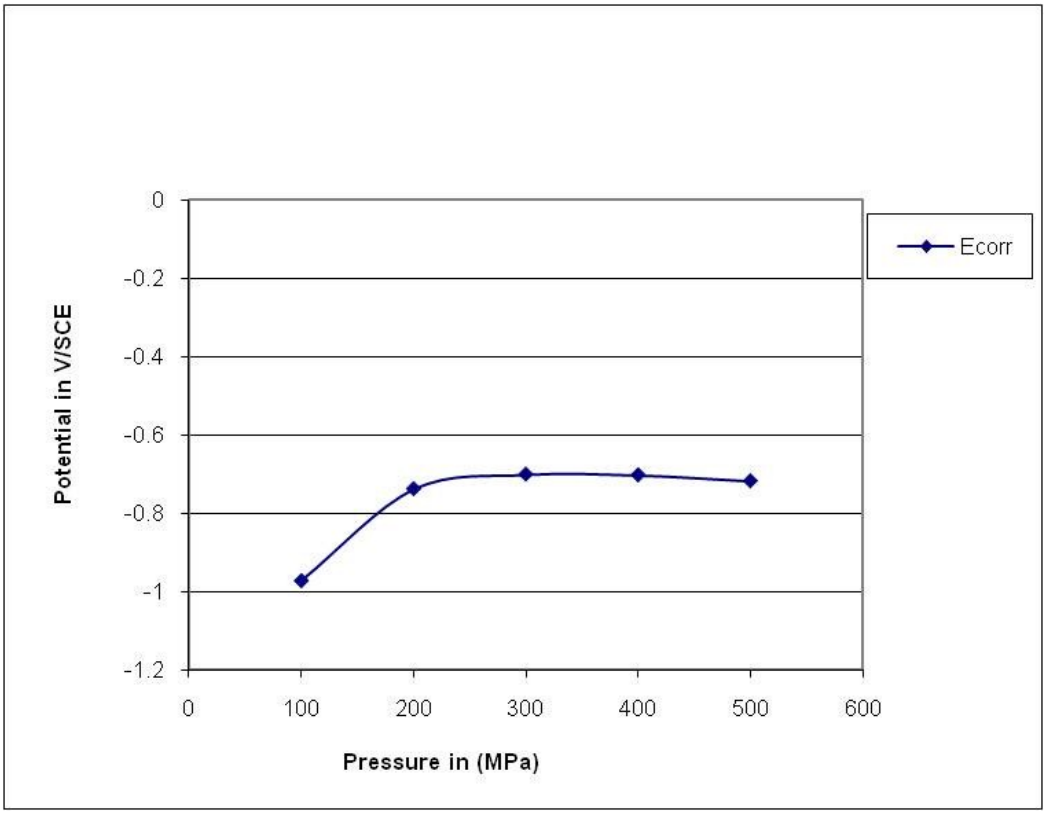

Figure 4-65 Variation of corrosion potential as a function of pressing pressure of Alumix 321 in 3.5 wt% NaCl solution.

In addition to the E_{corr}, the other characteristic point in the cyclic polarization graph is the repassivation or protection potential. The repassivation potential obtained from the cyclic polarization graph shows that pressing pressure does not have very much affect on E_{rep}, the average value recorded was -1.02±0.001 V/SCE. E_{rep} is defined as a potential below which pits repassivate.

In order to confirm the values of E_{pit} and E_{rep} those were originally determined by cyclic polarization test, a potentiostatic test was carried out to verify and confirm these two values. Samples held at less negative potential than E_{pit} should show pitting, while samples held at more negative potential than E_{rep} should show repassivation of pits and crevices. Figure 4-66 shows a cyclic polarization graph of Alumix 321 sample pressed at 500 MPa: it also shows the regions where the potentiostatic scan was performed. The idea behind this is to apply a scan at potential that is less negative than the E_{pit}, and at

potential that is more negative than E_{rep} and to observe the current variation as the scan is progressing.

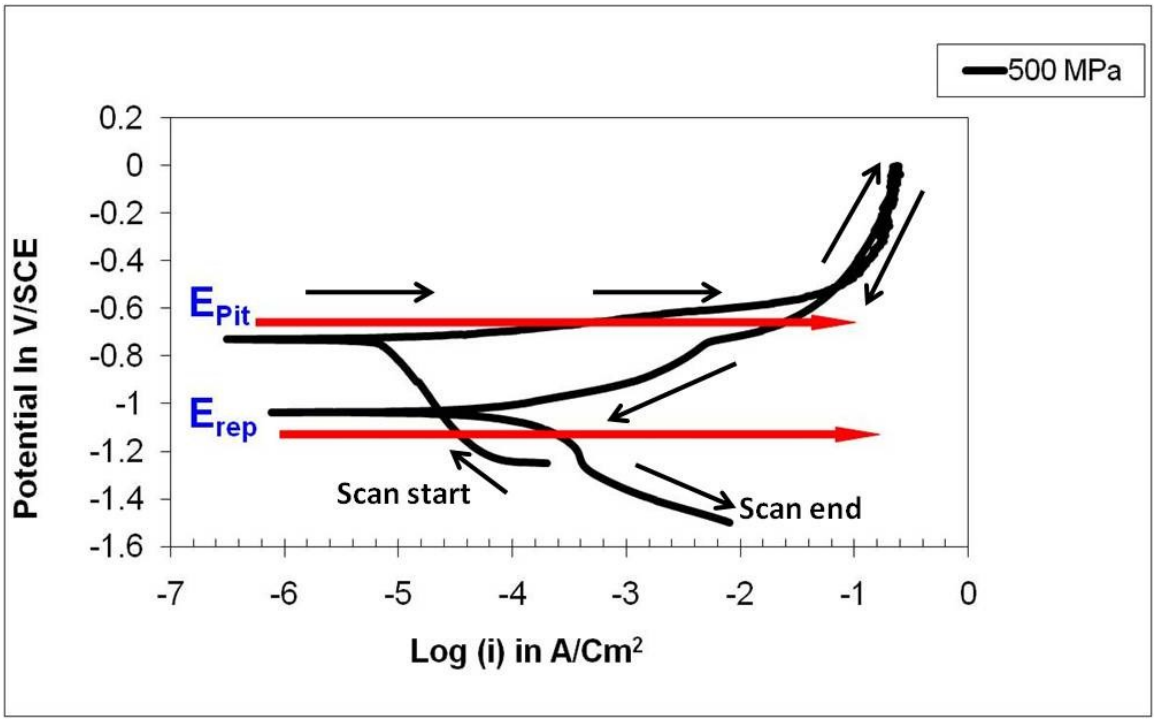

Figure 4-66 Cyclic polarization graph of Alumix 321 pressed at 500 MPa showing the position of the potentiostatic scan.

The potentiostatic scan was performed at -0.700 V/SCE and -1.08 V/SCE which are the potentials above the E_{pit} and below the E_{rep}, respectively. Figure 4-67 shows the variation of current as a function of time from the potentiostatic scan less negative than the E_{pit} and at a potential that is more negative than E_{rep},. The samples held at less negative potential than the pitting potential show an unstable current value with a noisy nature due to the pitting process [86]. On the other hand, the samples held at a potential that is more negative than the repassivation potential demonstrate very small current that is stable and decline with time.

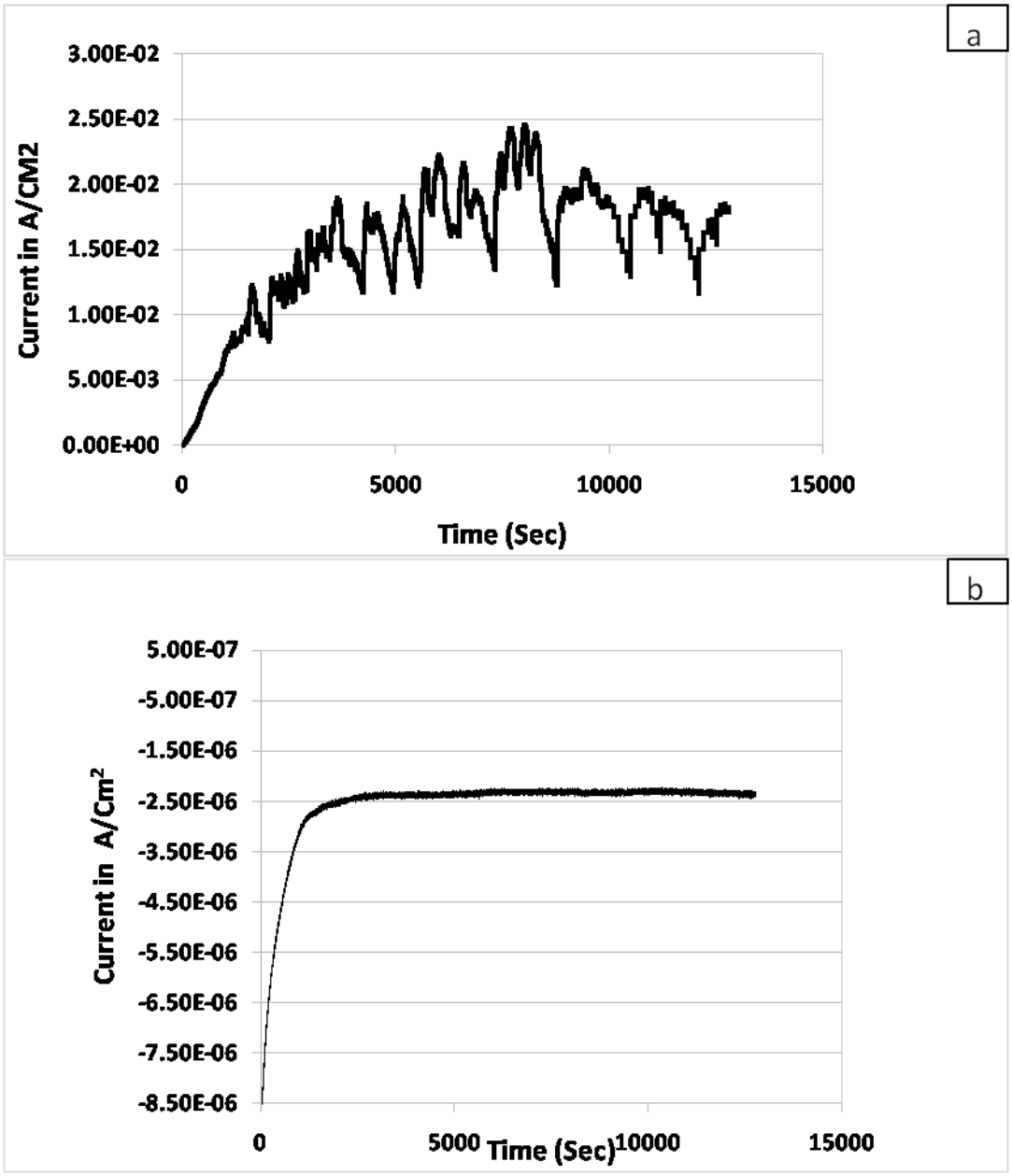

Figure 4-67 Plot of current vs time of Alumix 321 PM alloy in 3.5 wt% NaCl solution as a result of a potentiostatic scan, a) scan above pitting potential at -0.7 V/SCE, b) scan below repassivation potential at -1.08 V/SCE.

4.7.4 *STAIR STEP POLARIZATION (SP)*

It is known that pores in sintered metallic materials work as crevices. Crevice corrosion involves two main mechanisms, initiation and propagation. In the initiation step incubation or initiation time is needed to develop critical conditions in the crevices. It is hypothesized that accelerated polarization techniques may have not provided enough time for corrosion process to take place inside some crevices. Stair case polarization technique was used to reveal the crevice effect of pores. In this technique a very slow scan rate was used to offer enough induction time that is needed for crevice corrosion to take place.

Figure 4-68 shows the variation of potential as a function of time during stair step polarization. Figure 4-69 shows the variation of the potential as a function of time and current.

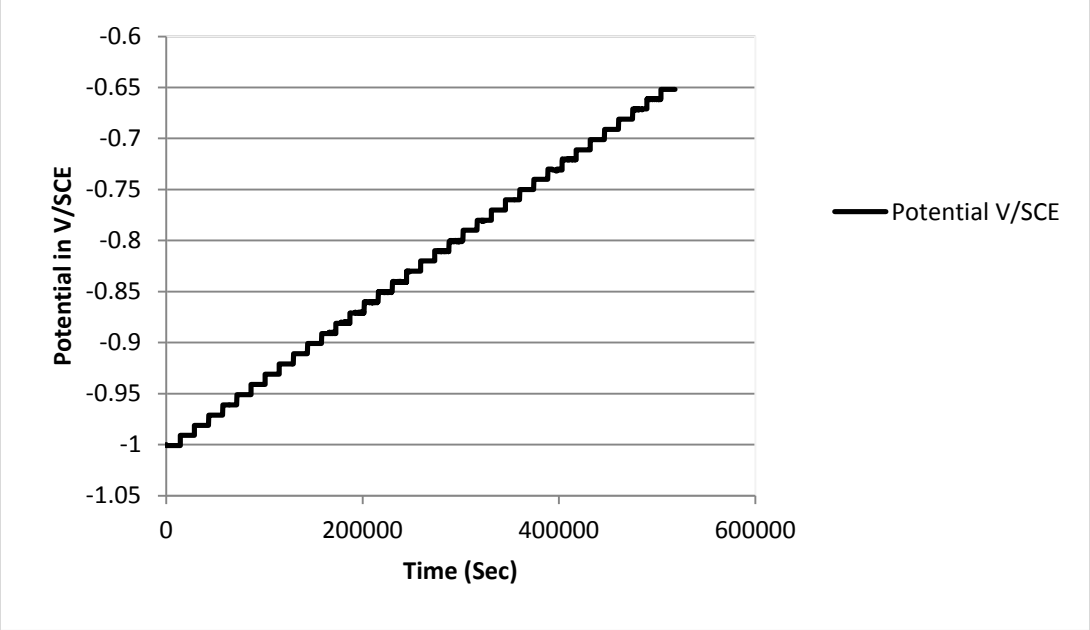

Figure 4-68 Variation of potential as a function of time for Alumix 321 in 3.5 wt% NaCl solution.

As the potential is raised in a step wise manner, the current was almost steady and constant until a certain potential was reached at which a fast increase in current can be

observed, this current is considered as pitting potential. Results obtained from this test did not show a clear variation between samples tested. Almost equal pitting potential was measured which was -0.730 V/SCE for the samples pressed in the range 100-500 MPa. This result is in agreement with the results obtained from the accelerated cyclic polarization plots. However, the current variation as a function of time was different from sample to sample but without clear trend. Figure 4-69 shows the stair step polarization plot. It compares two samples pressed at 100 and 500 MPa. The plot shows that the onset of the fast increase in current happens at the same potential which equal -0.730 V/SCE. The trend of current variation is similar to that obtained in cyclic polarization. The plot shows that the sample pressed at 100 MPa shows a gradual increase in current while the sample pressed at 500 MPa shows a fast increase in current after the pitting potential has reached. The reason behind this behaviour is not clear and difficult for interpretation due to the lake of previous work and standards that cover this type of testing.

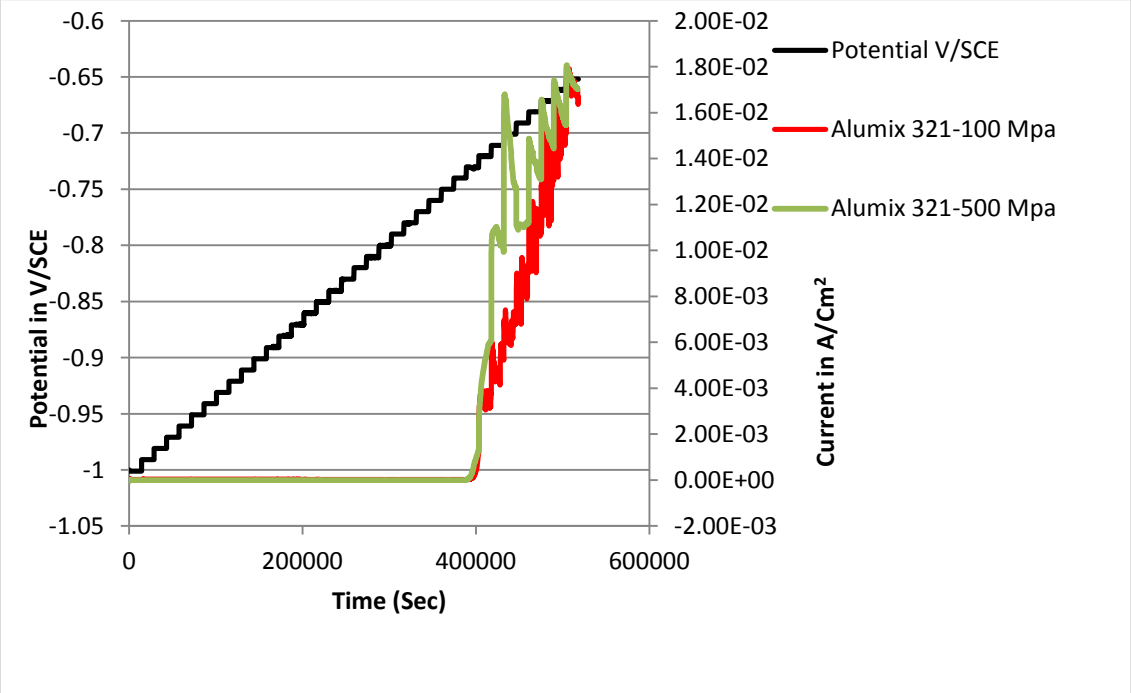

Figure 4-69 Stair step polarization plot in 3.5 wt% NaCl solution of Alumix 321 pressed at 100 and 500 MPa.

4.7.5 *CHARACTERIZATION OF ALUMIX 321 CORRODED SAMPLES*

Corroded samples prepared from Alumix 321 samples and pressed between 100-500 MPa were examined. The examination involved optical microscopy, SEM and chemical analysis. Figure 4-70 shows the corrosion morphology of Alumix 321 samples after exposing to 3.5 wt% NaCl for 48 hours.

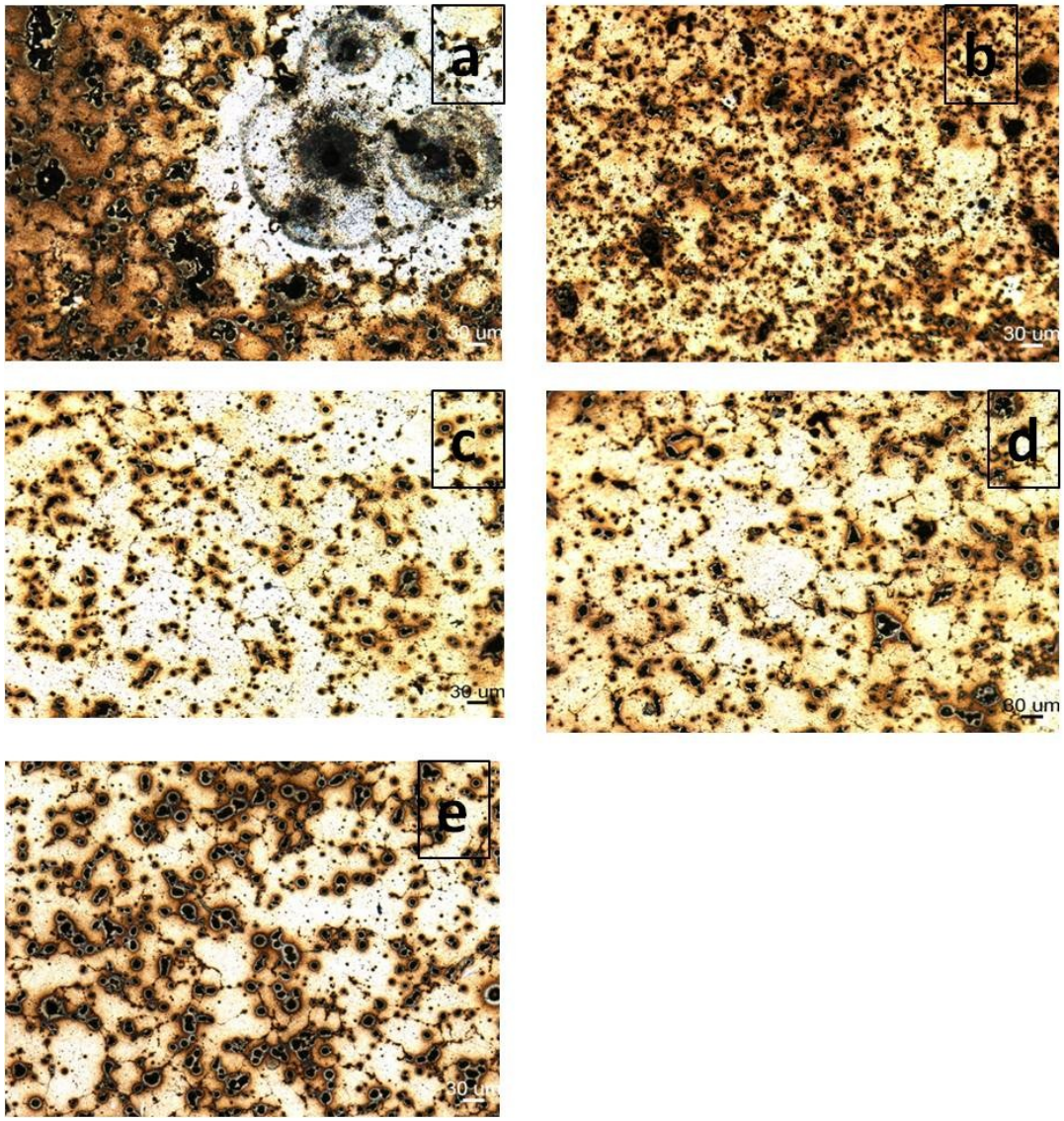

Figure 4-70 Optical micrograph of Alumix 321 pressed at, a) 100 MPa, b) 200 MPa, C) 300 MPa, d) 400 MPa, e) 500 MPa after 48 hours exposure in 3.5 wt% NaCl solution.

It is clearly seen that samples pressed at 100 MPa show different corrosion surface morphology in which most of the corrosion attack initiated at the large interconnected pores. These large interconnected pores offer a large surface area for corrosion process to take place and that effect was reflected in the highest corrosion current obtained during Tafel test. Only a few interconnected pores can be seen in the sample pressed at 200 MPa. Most likely, this pressure is the transition state between interconnected and round closed pores. For samples pressed at 300, 400 and 500 MPa most of the corrosion attack initiated in the closed round pores in which the corrosion reactions take place. The roundness of pores is very clear in these samples and indicates a high degree of densification. Despite the very clear and visible roundness of pores in the 500 MPa samples, pores in the samples pressed at 300, 400 and 500 MPa have almost the same degree of roundness. The similar microstructure obtained in this range of densities is in a good agreement to what was obtained from the electrochemical experiments. Tafel extrapolation and cyclic polarization experiments did not show a definite trend on how the corrosion current varies with density of Alumix 321 under these conditions. It is worth noting here that it was concluded from the electrochemical experiments that samples pressed at 100 MPa and samples pressed at 500 MPa corroded according to different mechanisms. The nature and size of the pores resulted from these samples suggest that the conclusion is probably true. For an insight investigation, two samples pressed at 100 MPa and 500 MPa were compared at higher magnification. Figure 4-71 shows the corrosion morphology of two Alumix 321 samples. The samples pressed at 100 MPa show large number of interconnected porosity. Some of these corroded pores were connected to other pores and form a tunnel like attack which outlines the grain boundaries and lead to a sever corrosion attack. Only minor attack was observed on the surface where pitting of the surface took place. On the other hand, most of corroded pores in the 500 MPa sample were spherical and have a round opening. These pores are isolated and due to the small number most of the sample surface remains free of corrosion. However, some very small pits on the matrix surface can be seen. Contrary to the sample pressed at 100 MPa, the corrosion attack at the grain boundaries is minor

and it does not show any tunnel like attack. Definitely, after sintering some retained pores exist and mostly accumulate at the grain boundaries. During exposure to the saline solution, these types of pores corroded and some of them become interconnected to other closed pores but with a much smaller severity compared to sample pressed at 100 MPa.

Figure 4-72 shows the SEM images for the corroded surface of two Alumix 321 samples pressed at 100 and 500 MPa. Alumix 321 samples pressed at lower pressure (100 MPa) showed a severe corrosion attack at the interconnected large pores. However, some pitting and intergranular corrosion were also observed. On the other hand the sample pressed at higher pressure (500) MPa showed much less corrosion attack. There is some evidence of corrosion in the interconnected pores but to a less degree compared to 100 MPa sample. The morphology of the corrosion surface also shows signs of pitting that took place on the surface. There were also indications of intergranular corrosion but with a less extent and severity. Figure 4-73 shows the corrosion surface of AA6061 and its equivalent Alumix 321 after the exposure to 3.5 wt% NaCl solution. Generally, the corroded surface morphology of Alumix 321 PM alloy was similar to AA6061 wrought alloy although other evidence of corrosion attack at the grain boundaries and at the interconnected pores can be seen. It can be concluded from this comparison that the samples pressed at higher pressure show corrosion morphology that is comparable and to some extent similar to the wrought AA6061.

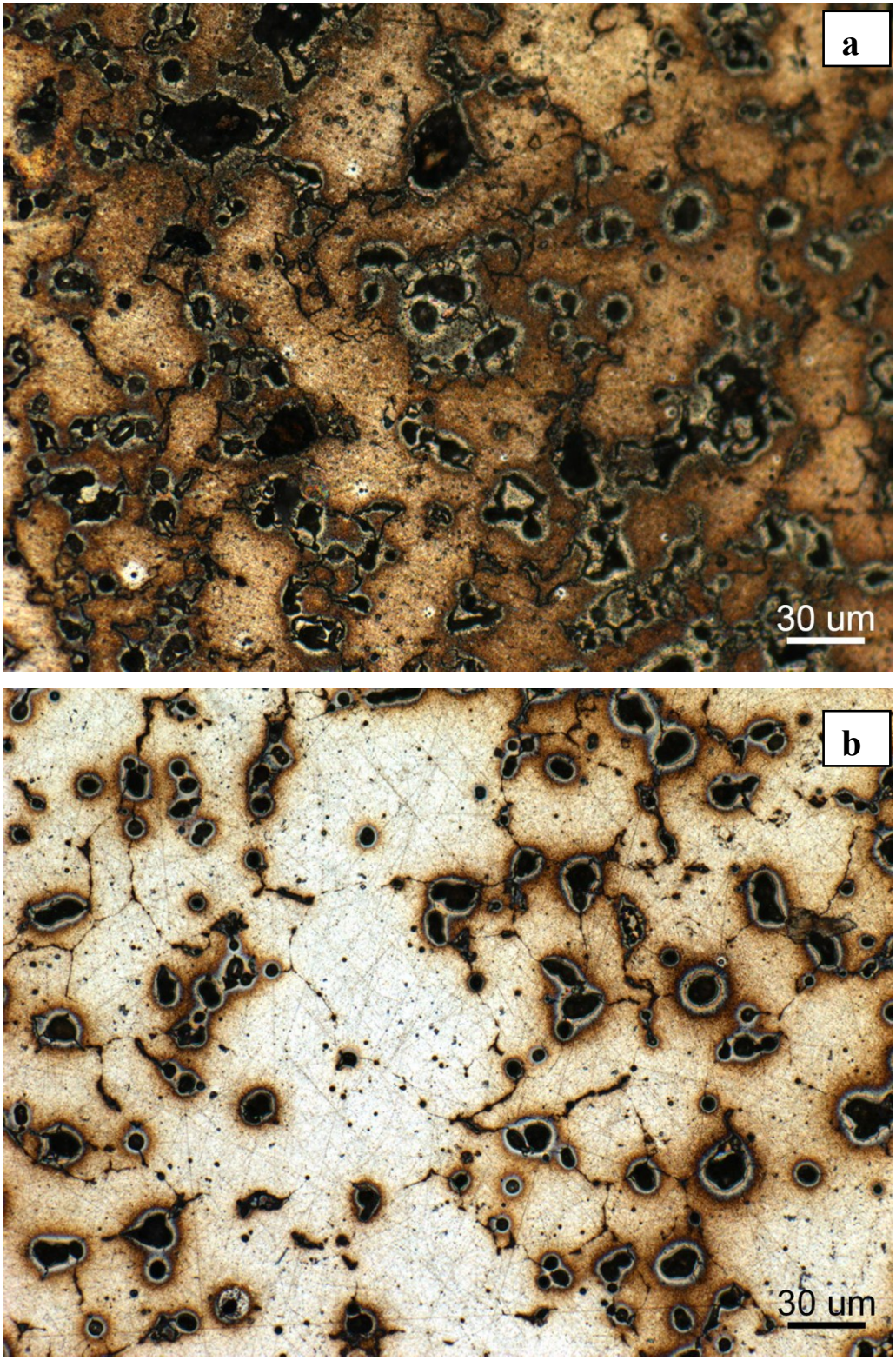

Figure 4-71 Optical micorgraph showing the morphology of corrosion attack of Alumix 321 after 48 hours exposure in 3.5 wt% NaCl solution a) 100 MPa, b) 500 MPa.

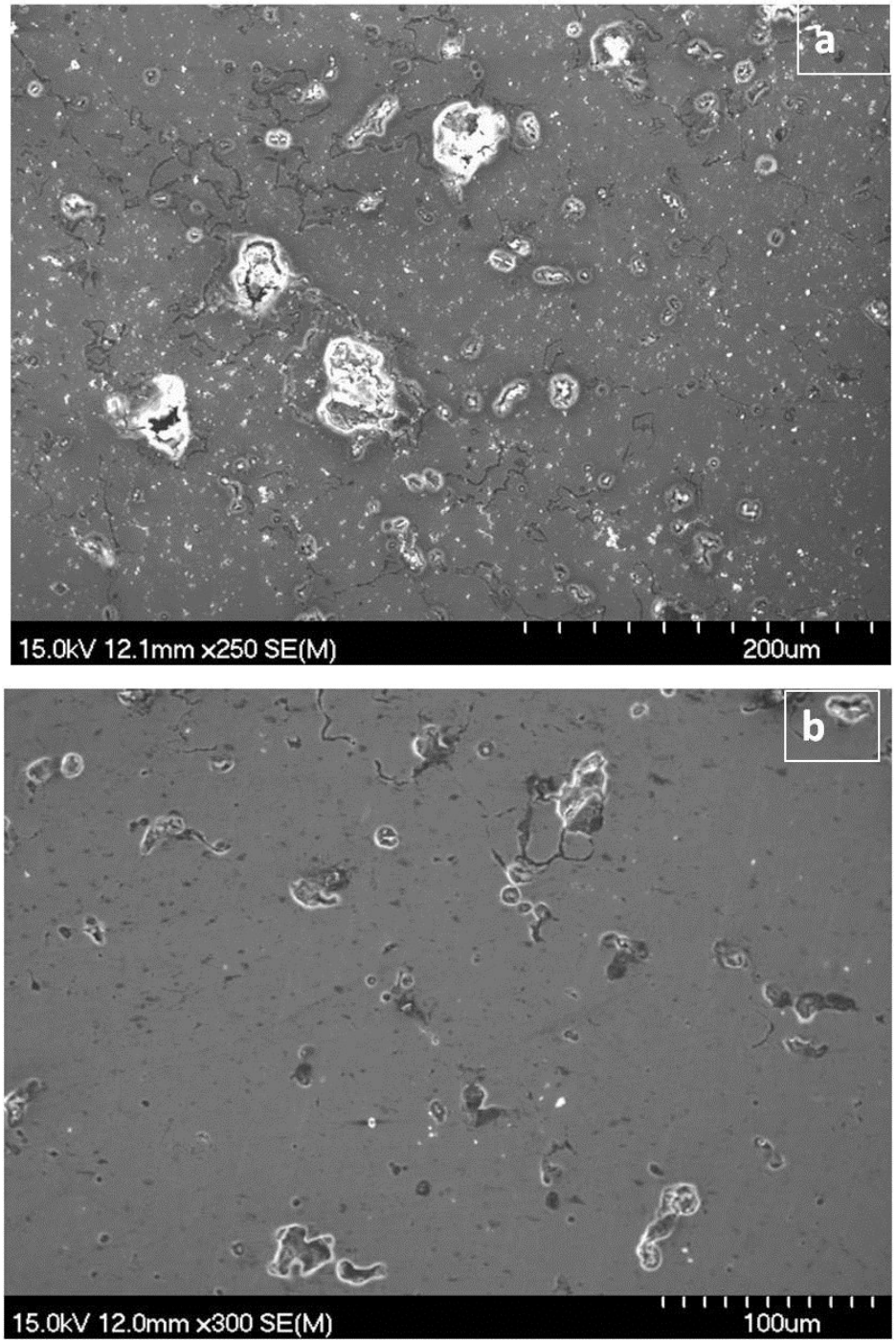

Figure 4-72 SEM micrographs show the corrosion morphology of Alumix 321 after exposure to 3.5 wt% NaCl a) pressing pressure=100 MPa, b) pressing pressure=500 MPa.

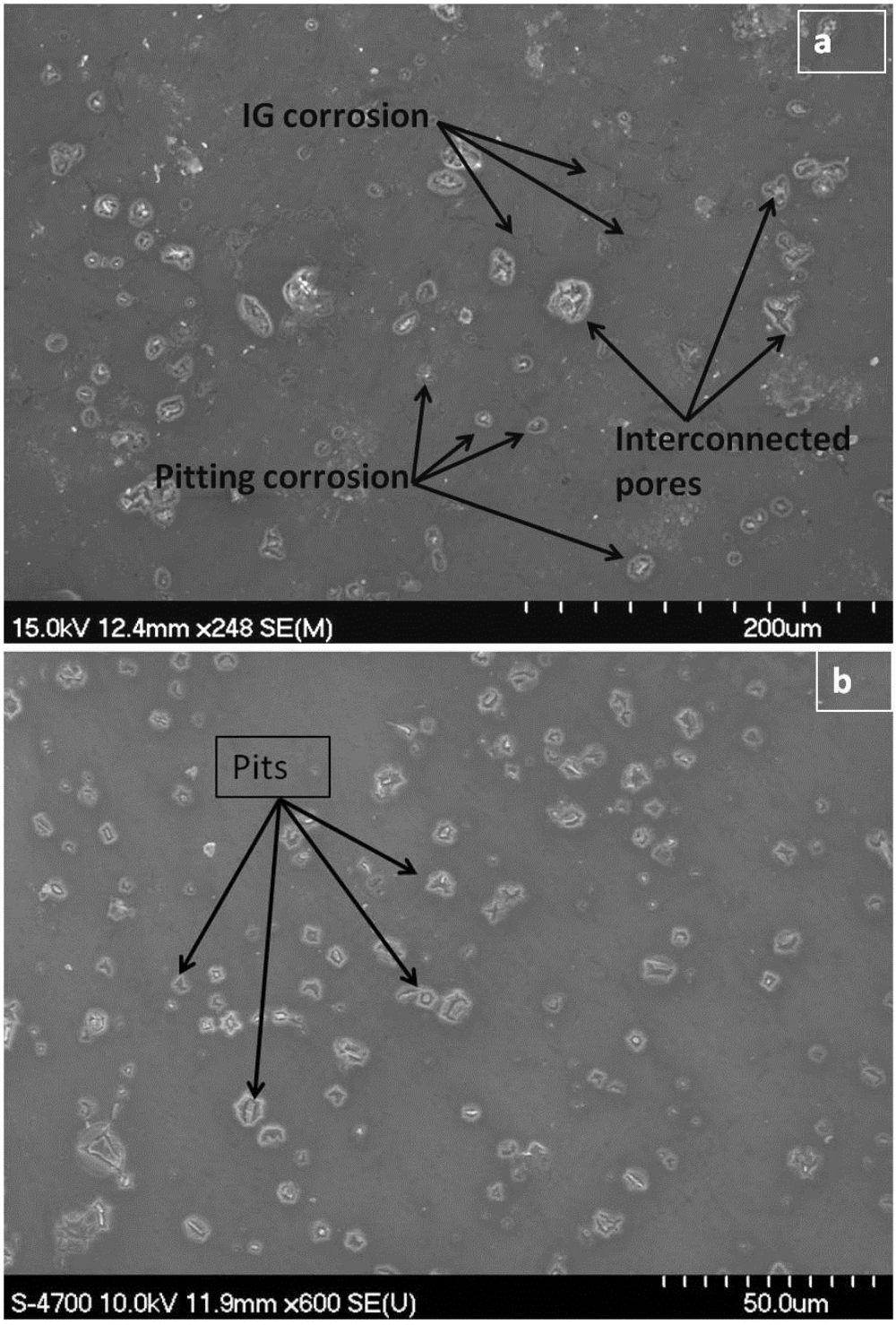

Figure 4-73 SEM micrographs of coroded samples a) Alumix 321 PM alloy pressed at 500 MPa, b) AA6061 wrought alloy after exposure to 3.5 wt% NaCl solution.

Figure 4-74 shows a higher magnification SEM image of the corroded surface of Alumix 321 pressed at 500 MPa. In addition to pitting, crevice and intergranular corrosion can be detected.

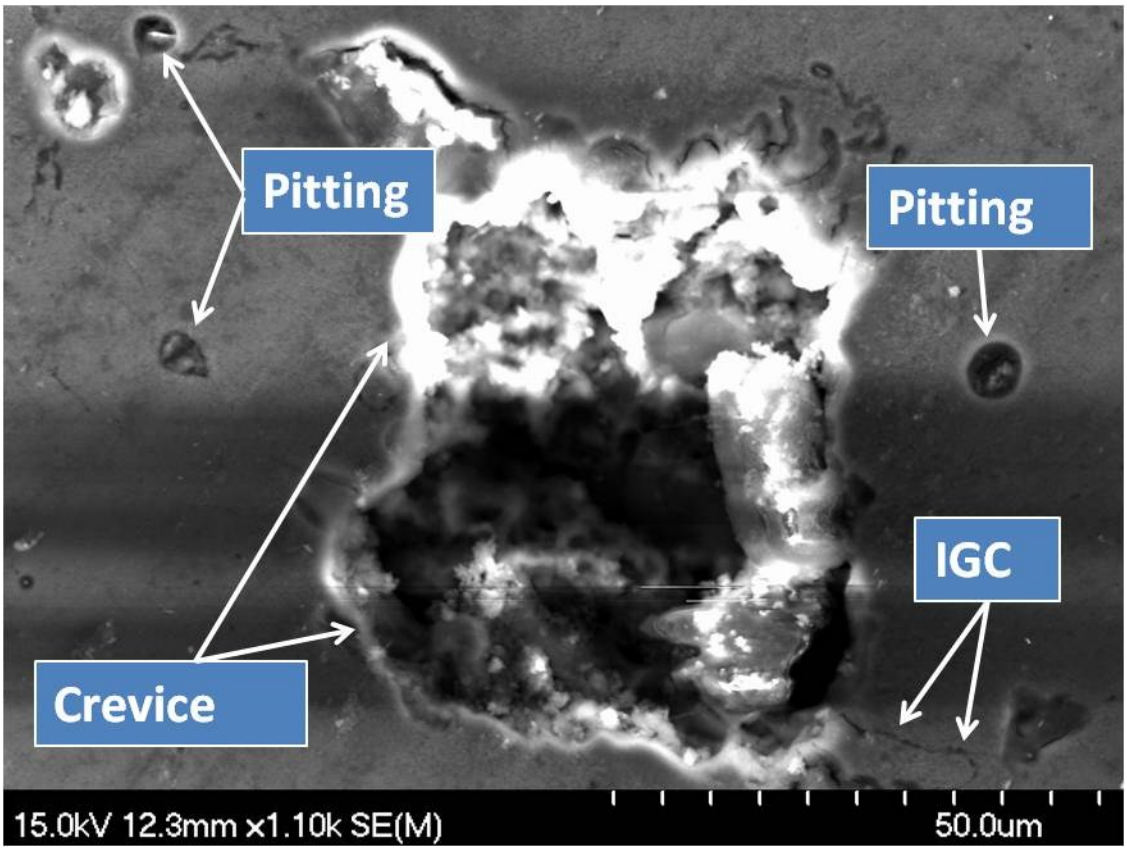

Figure 4-74 SEM micrograph of Alumix 321 corroded surface showing different types of corrosion after exposure to 3.5 wt% NaCl solution showing, pitting, crevice and IGC.

Close examination of the SEM images shows a similar observation to what we have seen in AA6061 corroded samples. It is clearly seen that in both AA6061 and Alumix 321 pitting initiation is related to the intermetallic particles. Figure 4-75 show the SEM micrographs of corroded AA6061 wrought alloy and Alumix 321 PM alloy. The similarity of the pits in both images suggests a similar pitting mechanism. In both cases the pits were hemispherical and have a smooth opening.

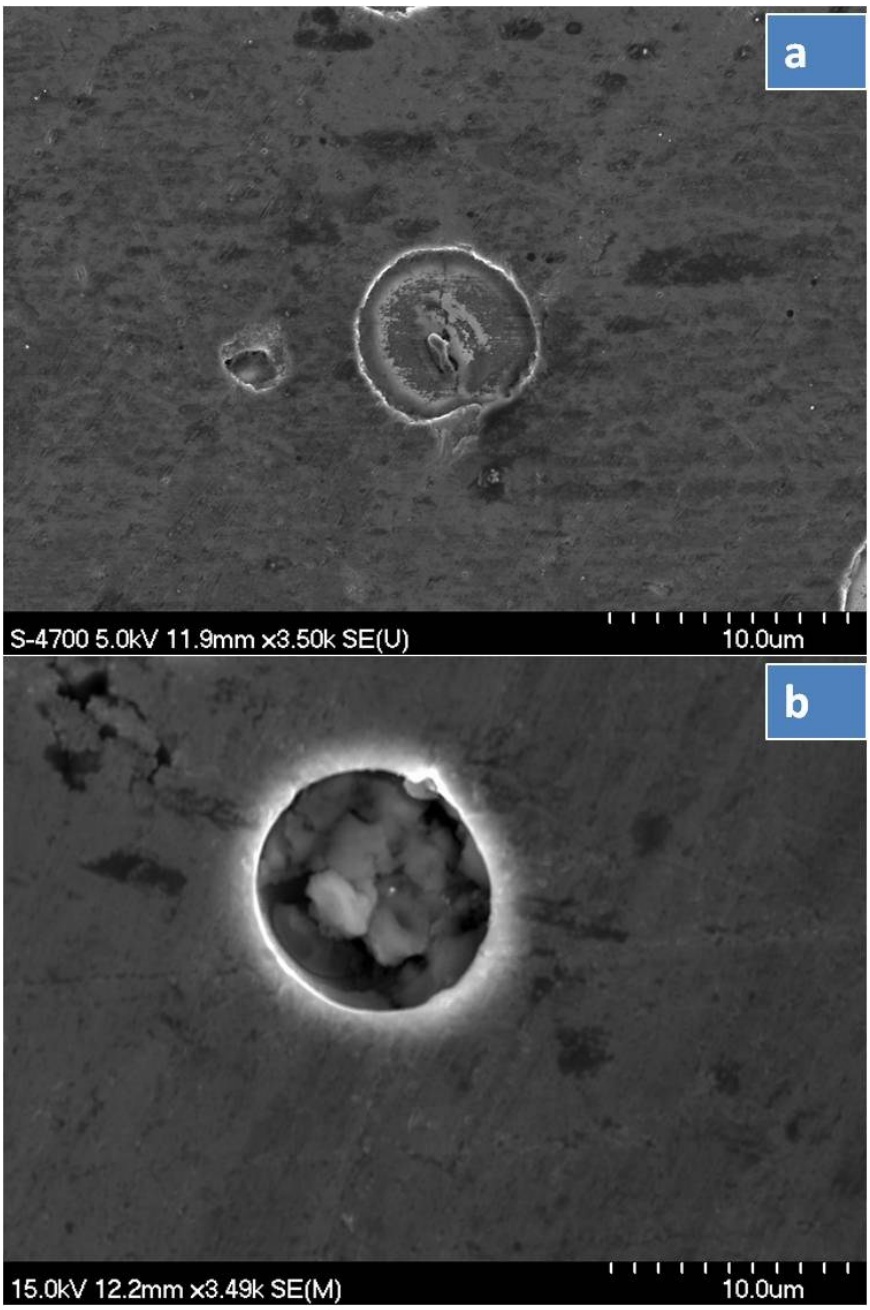

Figure 4-75 SEM micrographs showinh pitting a) AA6061 wrought alloy, b) Alumix 321 PM alloy after exposure in 3.5 wt% NaCl solution.

Figure 4-76 shows a pitting initiated at the vicinity of the intermetallic particles. To understand the chemistry of these intermetallic particles EDS was used.

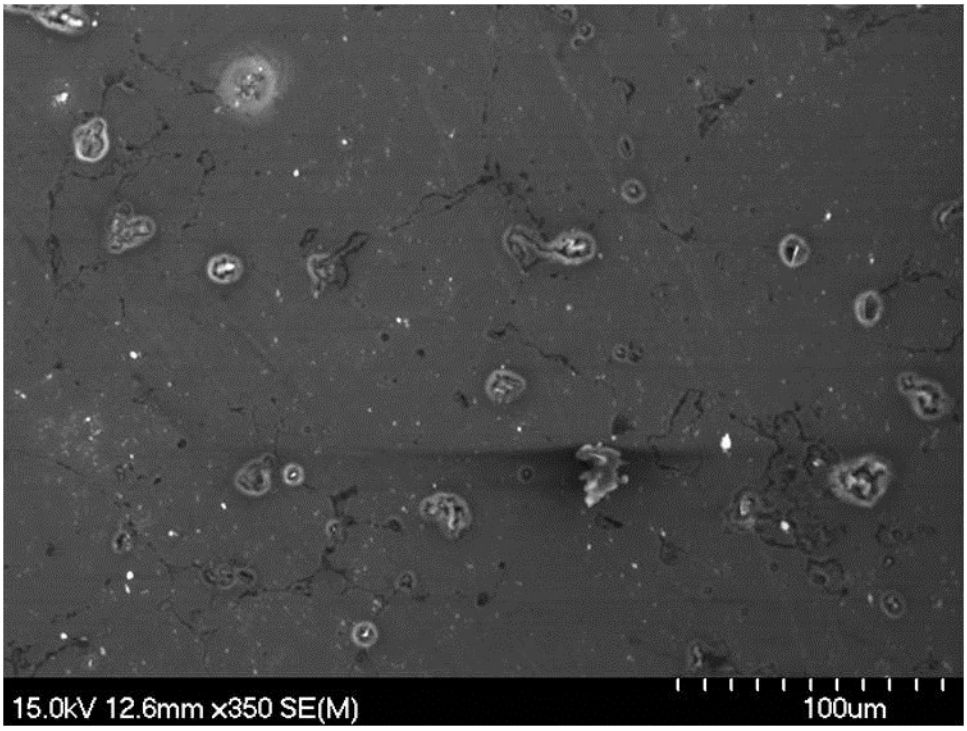

Figure 4-76 SEM micrograph of corroded Alumix 321 alloy showing initiation of pitting around intermetallic particles.

Figure 4-77, Figure 4-78 and Figure 4-79 show the spot used for the analysis, the EDS spectrum and the mapping chemical analysis of the intermetallic particles, respectively. The EDs spectra show the presence of iron, silicon and aluminum in addition to small amount of copper and magnesium. This observation is similar to what we have obtained in AA6061 wrought alloy.

Figure 4-77 SEM micrograph shows the corroded surface of Alumix 321 PM alloy and the location at which EDS was performed.

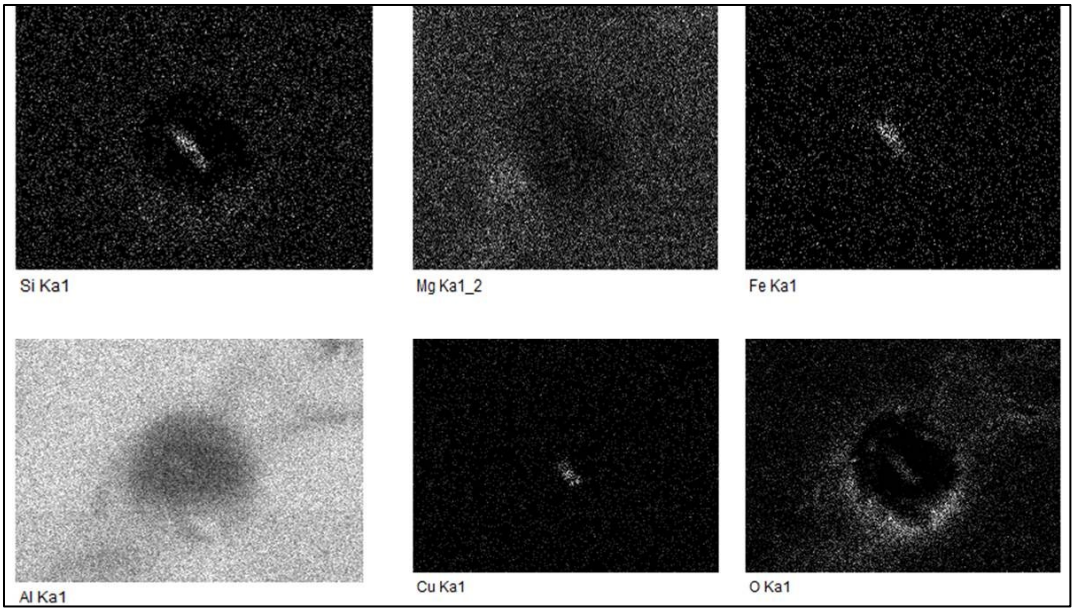

Figure 4-78 X-ray mapping analysis showing the chemical composition of the intermetallic particle.

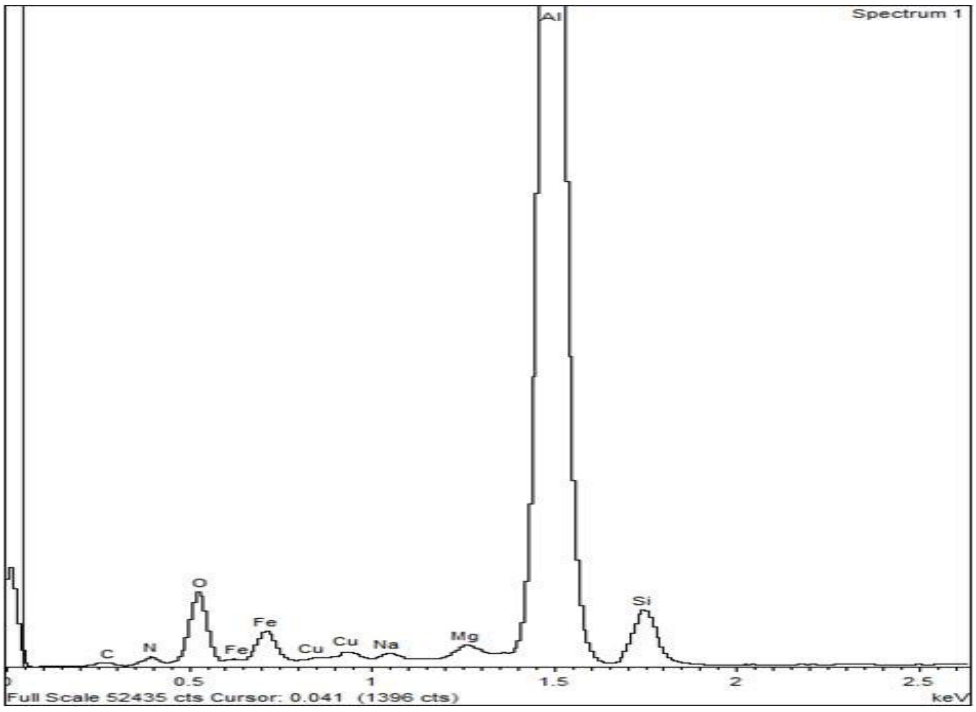

Figure 4-79 EDS spectra of the intermetallic particles found in the corroded surface of Alumix 321 PM alloy.

In addition to pitting, Intergranular corrosion (IGC) was observed in Alumix 321 PM samples after the exposure to 3.5 wt% NaCl solution. Figure 4-80 illustrates the corroded surface of Alumix 321 where IGC is clearly visible. To obtain more information about the nature of the corrosion process along the grain boundaries, EDS line scan was also performed to see if there is any variation of the alloying elements along the grain boundaries compared to the matrix. Figure 4.81 shows the EDS line scan results obtained along the grain boundaries. The results show that there is no clear variation in alloying elements concentration between the matrix and the grain boundaries. The only exception was the oxygen which clearly shows higher concentration at the grain boundaries relative to its concentration in the matrix. This higher amount of oxygen is due to the corrosion that takes place and the formation of aluminum oxide as a corrosion product.

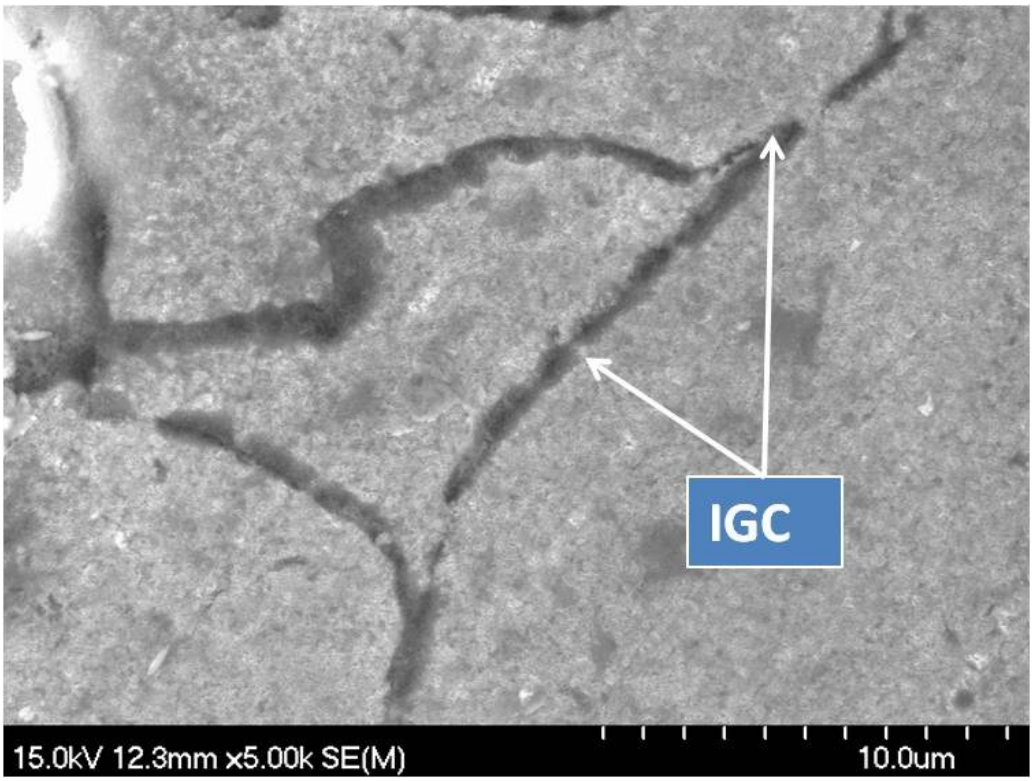

Figure 4-80 Corroded surface of Alumix 321 PM alloy showing IGC after the exposure to 3.5 wt% NaCl solution.

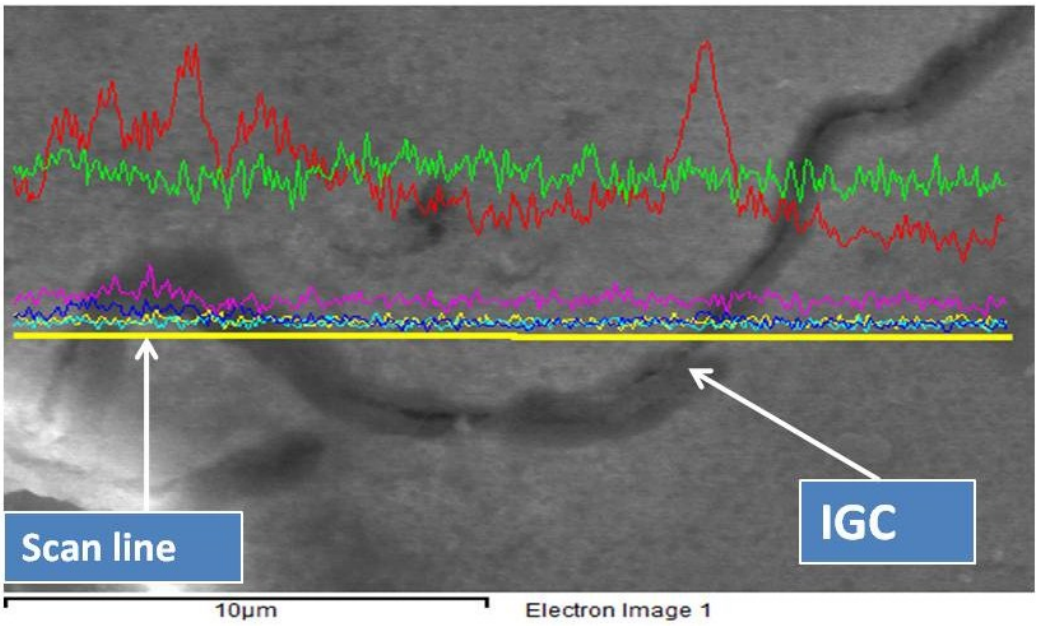

Figure 4-81 EDS line scan through the grain boundary of Alumix 321 PM alloy, O=red, Mg=green, Fe=Yellow, Cu=light blue, N=dark blue, Si=Purple.

Close and careful examination of Alumix 321 sintered samples shows an interesting observation. Back-scattered electron images taken for Alumix 321 PM samples show signs of diffusion of intermetallic particles to the grain boundaries. Figure 4-82 shows that intermetallic particles diffused to the grain boundary region. The cross sign indicates the spot where WDS analysis was performed, the results confirmed that those particles are Al-Fe-Si particles. The explanation is that during sintering and liquid phase formation, these particles were able to diffuse in the liquid phase region: the possibility of melting of these particles is highly unlikely due to their high melting point. This observation is very important because the presence of these particles was found to affect Alumix 321 corrosion behaviour. Figure 4-83 shows formation of pits around these particles, it is clearly seen that much severe attack can be observed around these particles compared to other regions in the grain boundaries.

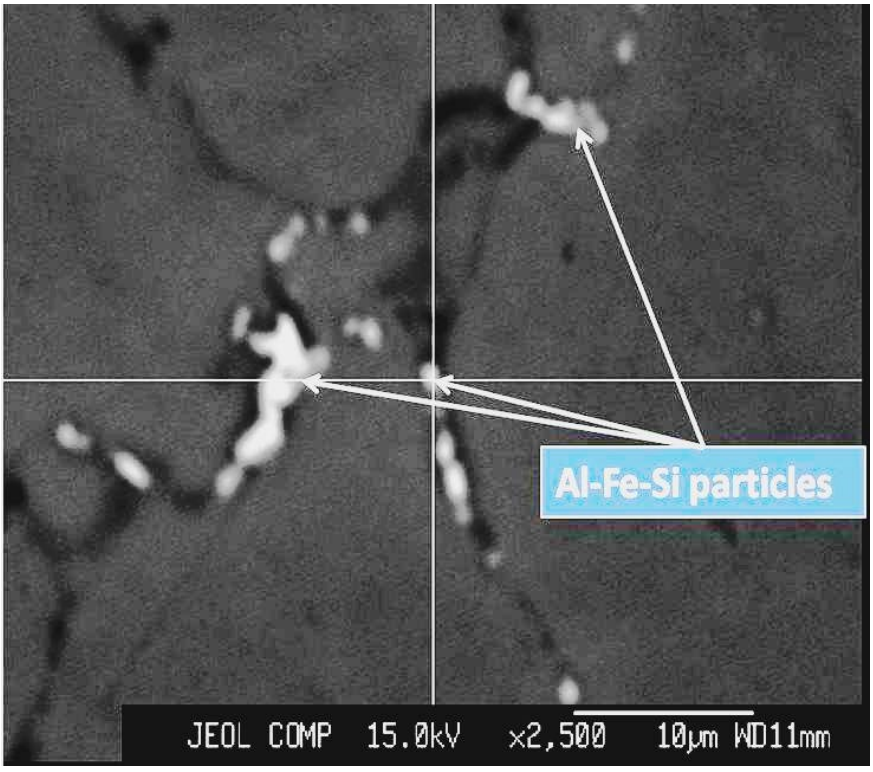

Figure 4-82 Back scattering image showing diffusion of intermetallic particles to the grain boundaries of Alumix 321 PM alloy.

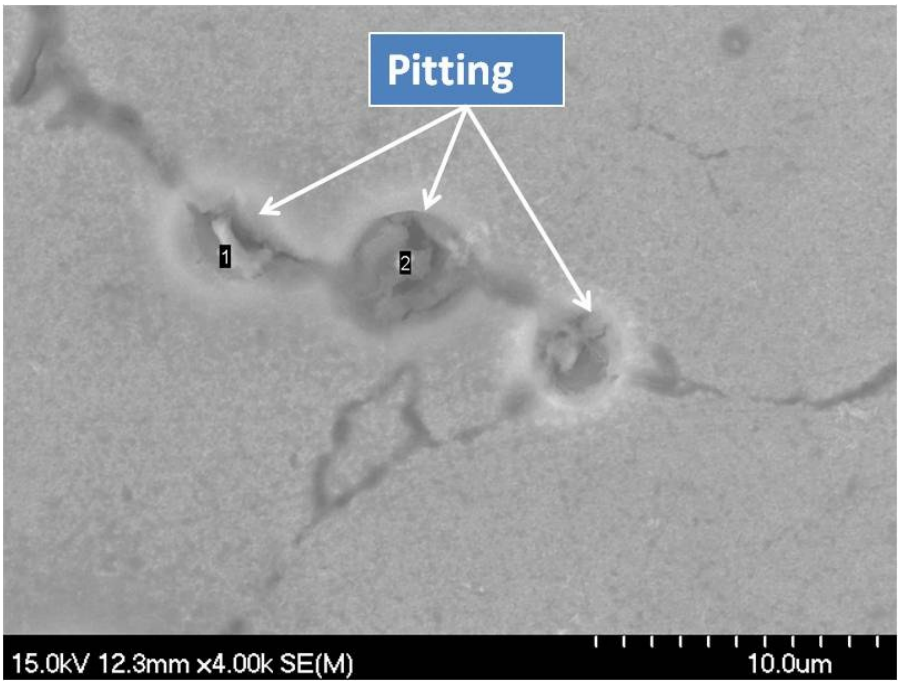

Figure 4-83 SEM micrograph showing pits formed around intermetallic particles, spot 1 and 2 indictete the spot analysis for EDS analysis.

To further understand IGC of Alumix 321 PM samples, corroded Alumix 321 samples were polished and then scanned using the SEM. The aim was to trace the source of IGC. Figure 4-84 shows the polished surface of corroded Alumix 321 sample in which the IGC attack accelerated through the grain boundary. As a result, the isolated pores become connected and reduce the corrosion and mechanical performance of this alloy.

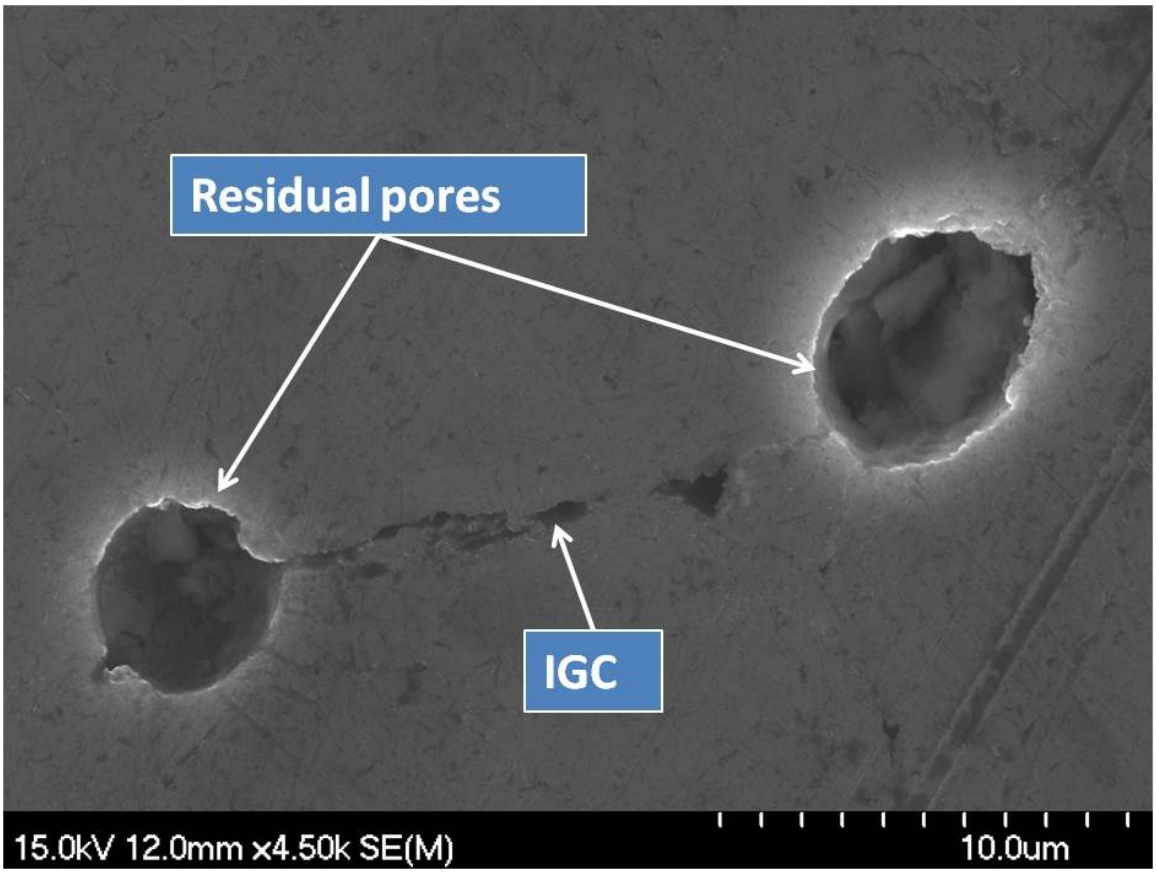

Figure 4-84 SEM of polished Alumix 321 surface after the exposure to 3.5 wt% NaCl solution showing the effect of IGC on isolated pores.

4.8 EFFECT OF HOT SWAGING

Hot swaging was used as a post sintering technique on Alumix 321 to study the effect of this treatment on corrosion properties. Prior to corrosion testing, Alumix 321 samples were pressed cold isostatically at 30,000 PSI (207 MPa), sintered at 630 °C and then swaged. Prior swaging, the samples were heated to 500 °C for 1 hr. As a result of swaging, the total cross sectional reduction of 34% was achieved. The aim is to investigate the effect of swaging process on the corrosion behaviour of the Alumix 321 PM alloy.

4.8.1 *OPEN CIRCUIT POTENTIAL (OCP)*

Figure 4-85 shows the effect of hot swaging on open circuit potential. Alumix 321 samples before swaging show a continuous drop in potential as a function of time. This continuous drop is a sign of a corrosion reaction that takes place at the surface and most likely inside the pores. The relatively lower pressure used during cold iso-static pressing produced a structure that is containing interconnected porosity. The decline in potential continues and finally reaches a plateau where the samples become stable at a potential of -0.895±0.030 V/SCE. It is worth noting here that this behaviour is similar to the behaviour observed in the Alumix 321 PM samples pressed at 100 MPa and were uni-axially pressed. The similarity is attributed to the lower pressure used in both cases and to the nature of porosity and microstructure. Comparing to non swaged sample, Alumix 321 after swaging shows a very stable and more positive OCP. The value obtained after swaging was -0.765±0.003 V/SCE which indicates more tendency toward passivation.

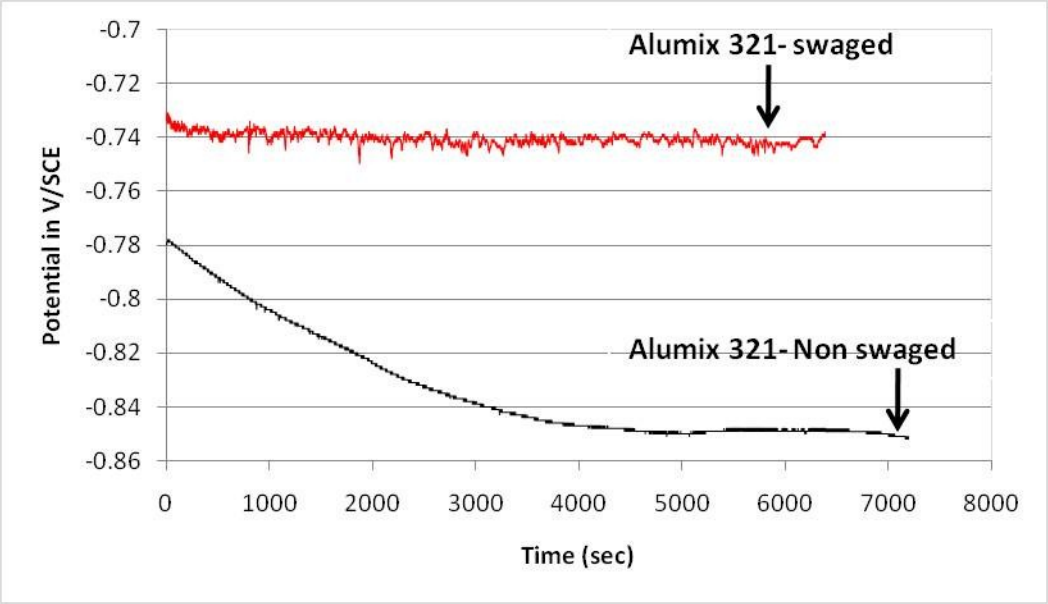

Figure 4-85 OCP variation of swaged and non swaged Alumix 321 PM alloy in 3.5 wt% NaCl solution.

4.8.2 *TAFEL EXTRAPOLATION (TE)*

Tafel extrapolation was used to measure the effect of swaging on corrosion current. Figure 4-86 shows the Tafel extrapolation graph of swaged Alumix 321 in 3.5 wt% NaCl solution. The graph shows clearly the impact of swaging on Alumix 321. The impact was clearly seen in the corrosion current. Corrosion current density of swaged Alumix 321 decreases from $6.56X10^{-6}$ A/cm^2 before swaging to $6.4X10^{-7}$ A/cm^2 after swaging. Figure 4-87 shows the comparison of corrosion current of swaged, non swaged Alumix 321, and AA6061 wrought alloy. Results show that the corrosion current of the non swaged Alumix samples was higher than both the wrought AA6061 and swaged Alumix 321. The process of swaging was very affective and led to a corrosion current that was even lower than the wrought samples. This good performance of the swaged samples is attributed to the remarkable changes in the microstructure that was combined with a high density values as it will be explained in more detail during the discussion of the microstructure of the corroded samples.

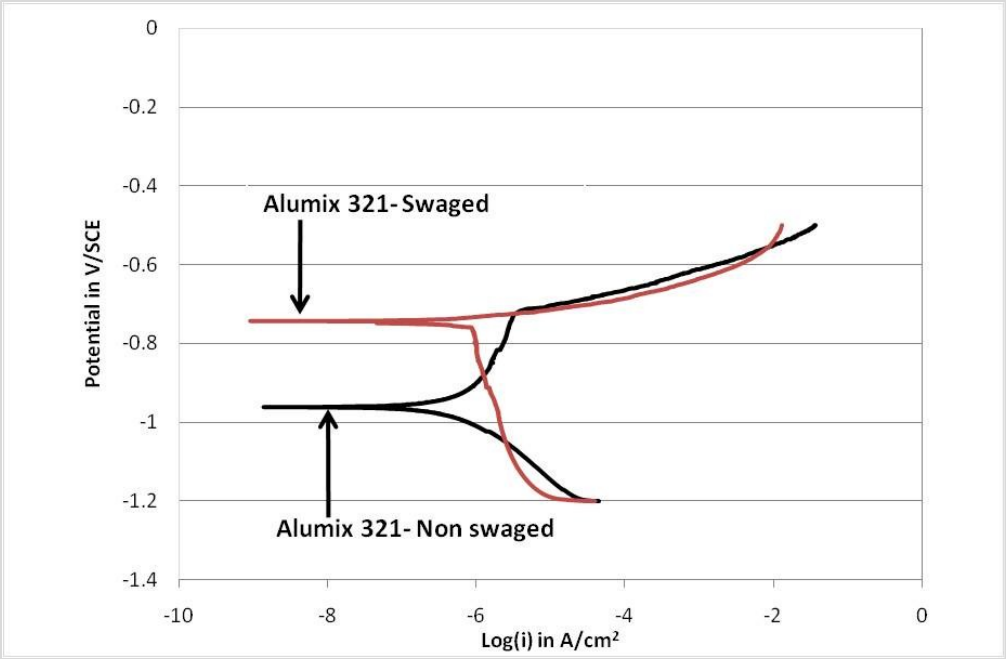

Figure 4-86 Tafel extrapolation of Alumix 321 before and after swaging in 3.5 wt% NaCl solution.

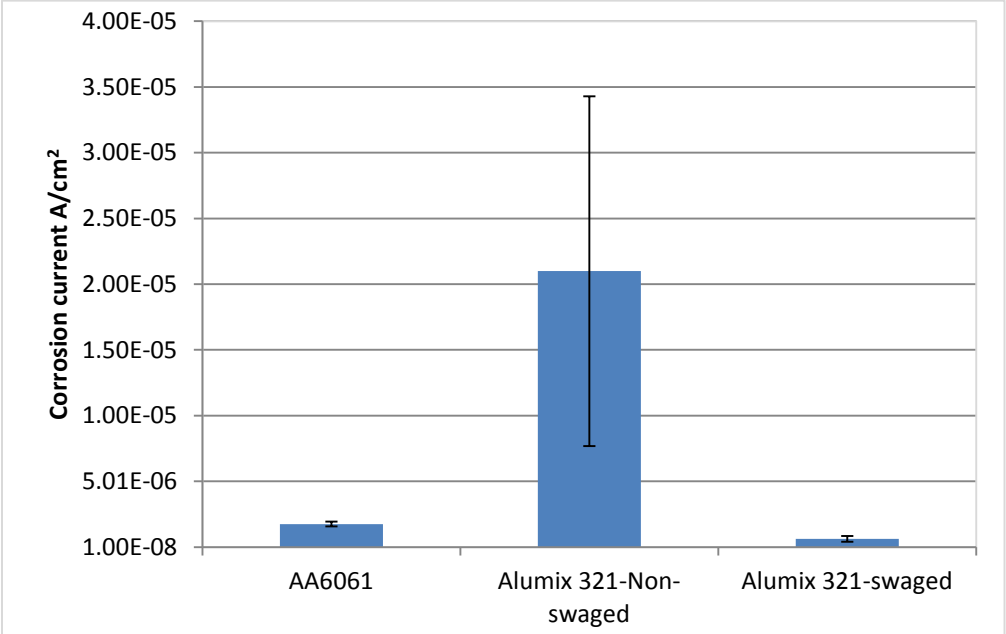

Figure 4-87 Comparision of average corrosion current values for swaged and non swaged Alumix 321 PM samples to the wrought AA6061 samples in 3.5 wt% NaCl solution.

It is worth noting that the Alumix 321 non swaged samples show a large scattering in corrosion current. Error bar for non swaged Alumix 321 samples indicates that scattering. However, all corrosion current values were higher than those of swaged samples and none of the non swaged samples showed a better performance than the swaged samples.

4.8.3 *CYCLIC POLARIZATION (CP)*

Cyclic polarization test was performed on Alumix samples before and after swaging. Figure 4-88 illustrates that Alumix 321 in the as sintered condition shows more negative corrosion potential, it also shows a gradual increase in anodic current as a function of potential. In comparison to the as sintered non swaged sample, the swaged Alumix 321 shows more positive corrosion potential and more sharp increase in anodic current that started at the corrosion potential. Similar to the corrosion current, corrosion potential of non swaged Alumix 321 samples showed a large error values. For non swaged Alumix 321 samples the Corrosion potential recorded to be -0.947±0.121 V/SCE. This value increases to -0.745±0.003 V/SCE for the swaged samples. The lower error values recorded during testing of swaged samples is possibly due to the homogeneous and dense microstructure obtained after hot swaging.

Despite the lower corrosion potential of the non swaged samples, cyclic polarization graph shows that the pitting potential of both samples is almost the same. Pitting potential was -0.727 V/SCE and -0.745 V/SCE for non swaged and swaged Alumix 321, respectively. Cyclic polarization graph also shows that the repassivation potential was almost the same, values recorded were -1.057 V/SCE and -1.066 V/SCE for non swaged and swaged, respectively.

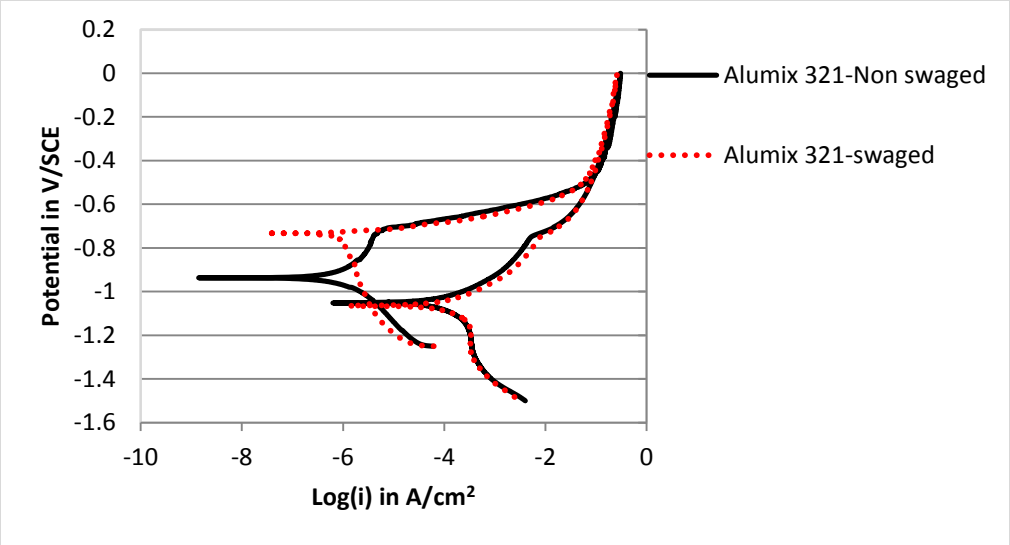

Figure 4-88 Cyclic polarization plot of swaged and non swaged Alumix 321 in 3.5 wt% NaCl solution.

4.8.4 *STAIR STEP POLARIZATION (SP)*

Stair step polarization was applied to achieve a slower scanning rate which provides enough time for crevice corrosion to take place. Figure 4-89 shows the variation of corrosion current of swaged and non swaged Alumix 321 samples as a function of potential. The graph shows a gradual increase in current as a function of potential. At certain potential, a sharp increase in current can be observed which indicates pitting potential. It is very clear that the pitting potential of swaged samples is higher than that of non swaged samples. Pitting potential increases from -0.731 V/SCE in non swaged samples to -0.720 V/SCE of the swaged samples. Figure 4-90 shows the variation of stair step potential and current versus time. At the beginning of the experiment, the current values were very small until it reached a certain potential at which a fast increase in current can be observed. It was pointed before that pitting potential obtained from the cyclic polarization plot of swaged and non swaged samples was almost the same. It was also mentioned that pitting potential is coincide with the corrosion potential, which makes difficult to distinguish between these two values. Results obtained from the stair

step polarization indicate that the slower scan stair step polarization is able to give us clear difference between swaged and non swaged samples.

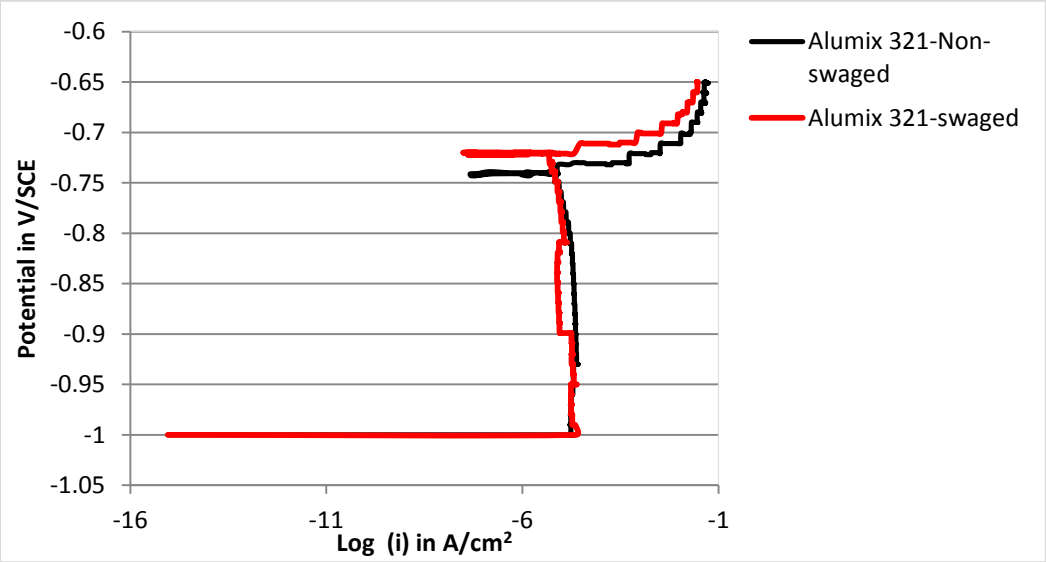

Figure 4-89 Stair step polarization graph of swaged and non swaged Alumix 321 in 3.5 wt% NaCl solution.

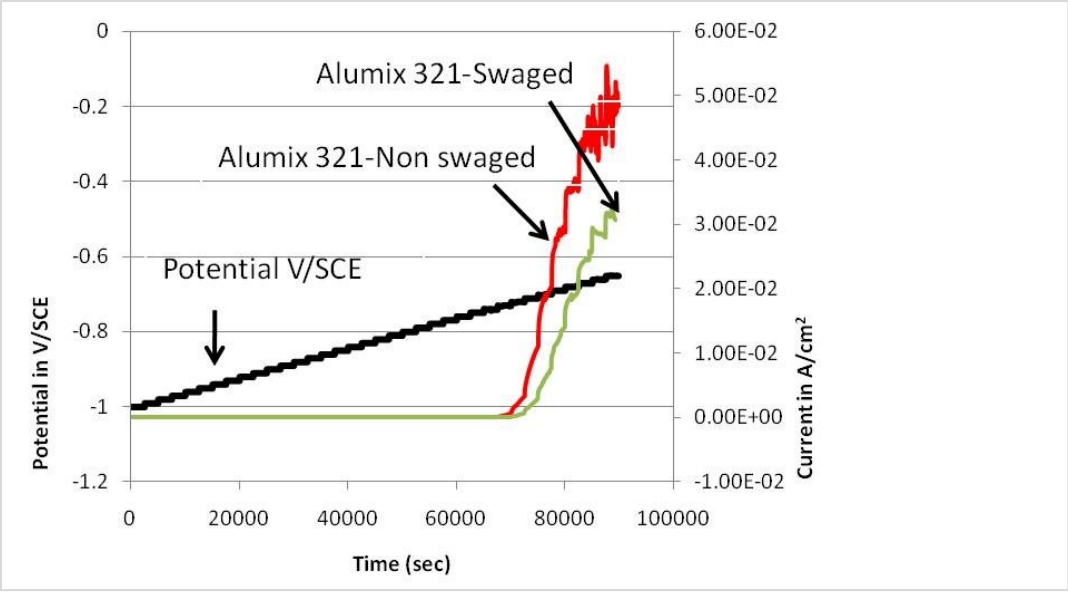

Figure 4-90 Stair step potential variation as a function of time and current of swaged and non swaged Alumix 321 PM alloy in 3.5 wt% NaCl solution.

4.8.5 *CHARACTERIZATION OF SWAGED ALUMIX 321 CORRODED SAMPLES*

In 4.5.2 the impact of hot swaging on the microstructure of Alumix 321 and how hot swaging treatment produced a very homogeneous microstructure. Figure 4-91 shows an optical micrograph of Alumix 321 that shows this variation was discussed. It is clearly visible how the microstructure has changed and consequently corrosion behaviour and other properties will be changed. Samples made of Alumix 321 were exposed to 3.5 wt% NaCl solution for 48 hours and then examined using optical and scanning microscopy. The goal here was to see how swaging affected the corrosion behaviour of Alumix 321. Figure 4-92 shows corroded samples before and after swaging. As sintered non swaged samples show that most of the corrosion reactions took place inside the interconnected porosity which provides a large surface area for corrosion reactions to take place. Some of the interconnected pores were connected to other pores and form what so called tunnel type of attack. Very small pits can be observed on the matrix of the swaged Alumix 321 samples which suggest that most of the corrosion reactions take place on the matrix. However, some closed and interconnected pores still exist even after swaging.

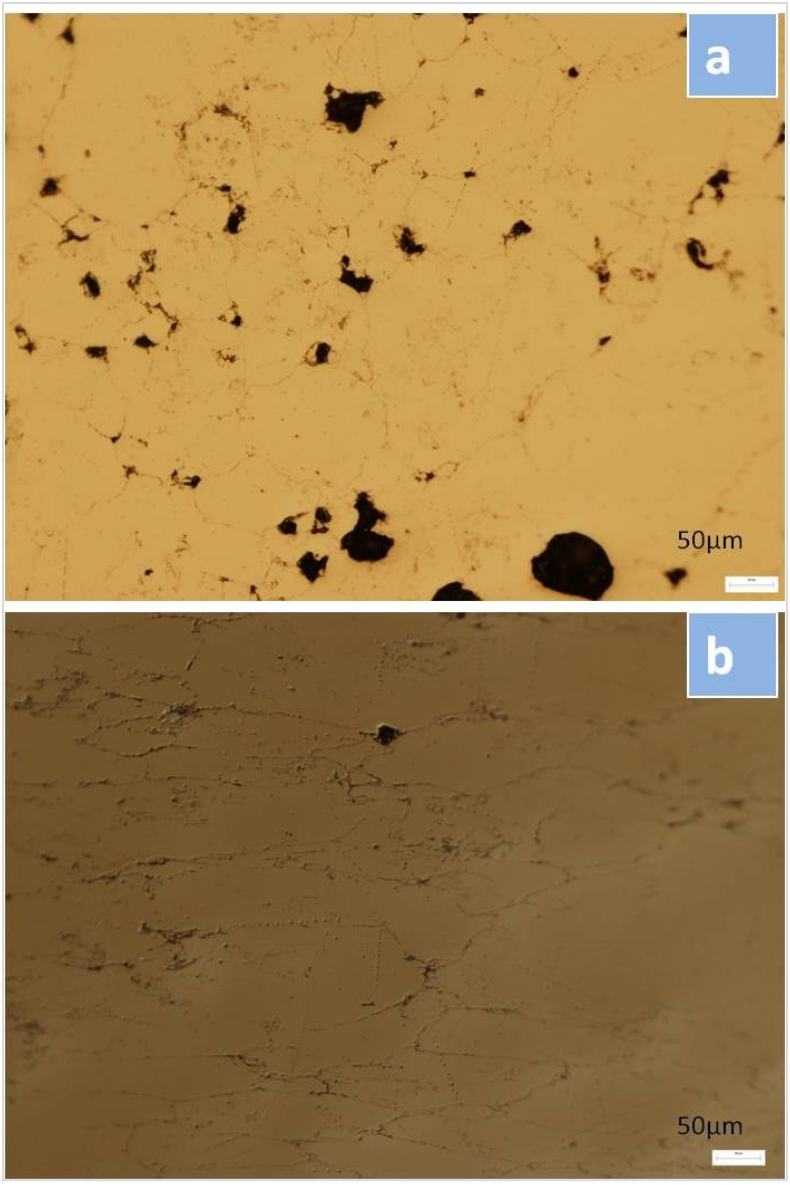

Figure 4-91 Optical micrograph of Alumix 321 PM alloy. a) befor swaging, b) after swaging.

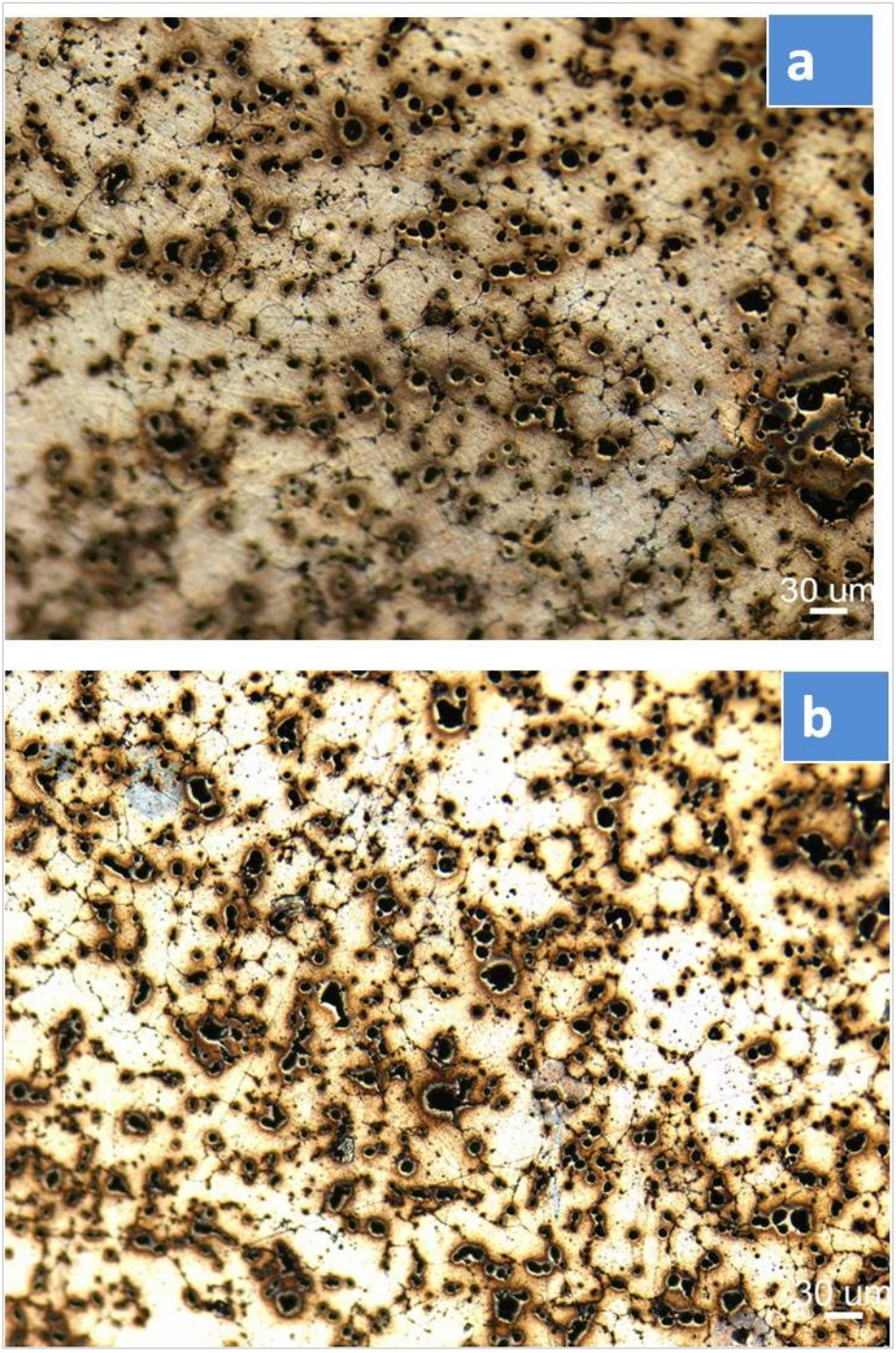

Figure 4-92 Optical micrograph of Alumix 321 PM alloy in 3.5 wt% NaCl solution, a) before swaging, b) after swaging.

Figure 4-93 and 4-94 show a low magnification SEM micrographs of Alumix 321 PM alloy before and after swaging, respectively. SEM micrographs of the non swaged samples

show a surface that is corroded and evidence of local corrosion spots which are either due to pitting or due to crevices corrosion. The fewer corrosion spots observed of swaged samples is a result of the changes in microstructure after swaging. Higher magnification SEM images (Figure 4-95) of the corroded surface of non swaged Alumix 321 alloy shows that in addition to the crevice corrosion that takes place inside the pores, intergranular corrosion can also be clearly observed. Interconnected pores are large and sometimes are linked to each other. Pitting due to the presence of iron rich particles was less observed. Figure 4-96 shows a corroded surface of swaged Alumix 321 sample in 3.5 wt% NaCl solution. Generally, the severity of attack was less than that observed in the non swaged samples. However, the same three types of corrosion mechanisms, pitting, IGC, and crevice corrosion can be observed. It is observed that the pits with round nature are more frequently exist and the intergranular corrosion was less severe.

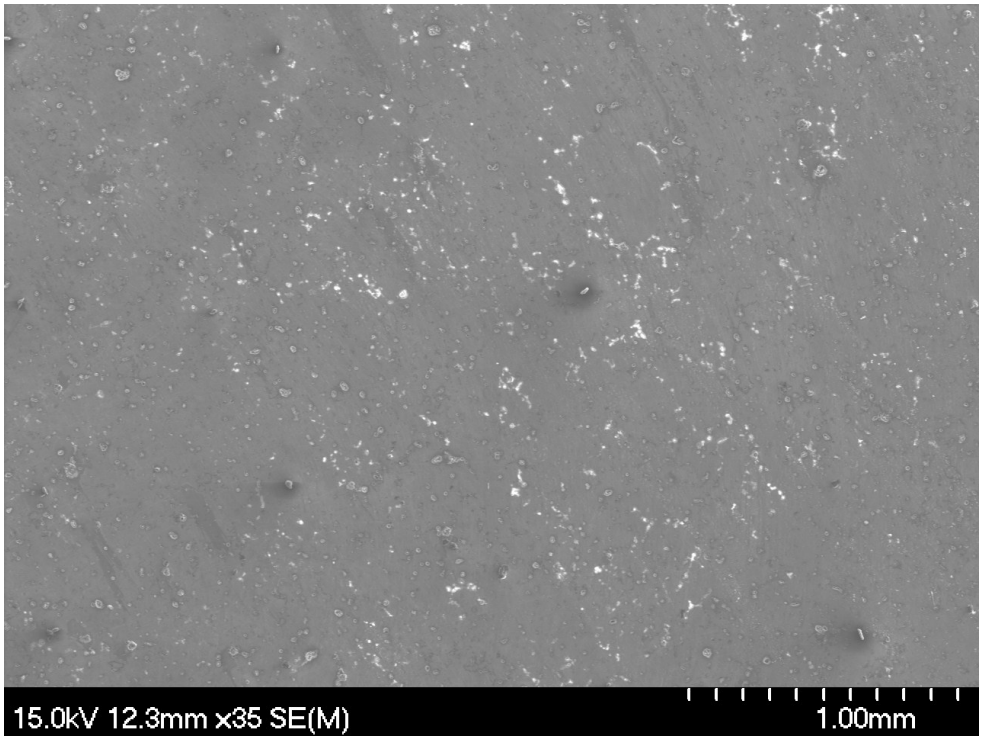

Figure 4-93 SEM of the corroded surface of non swaged Alumix 321 PM alloy in 3.5 wt% NaCl solution.

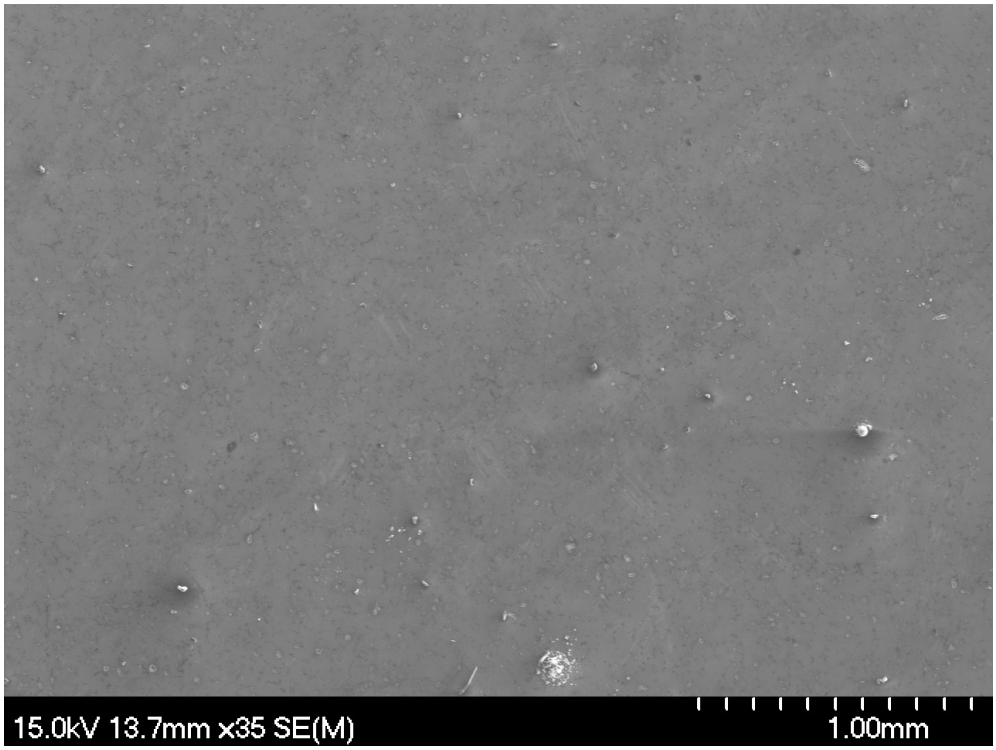

Figure 4-94 SEM of the corroded surface of Alumix 321 PM alloy after swaging in 3.5 wt% NaCl solution.

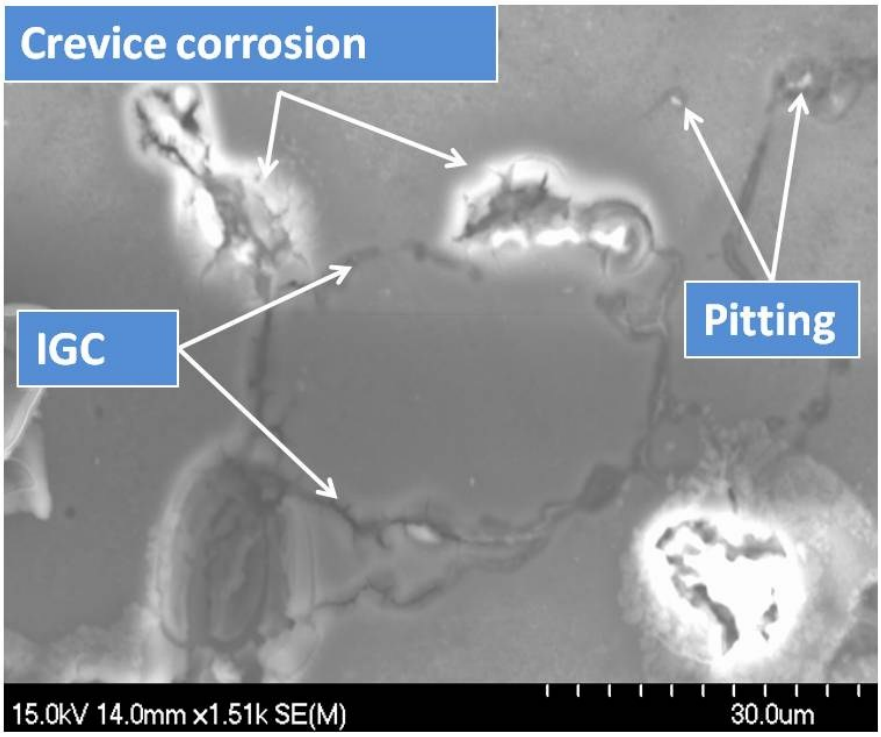

Figure 4-95 SEM micrograph shows differnt corrosion mechanisms of non swaged Alumix 321 PM alloy in 3.5 wt% NaCl solution.

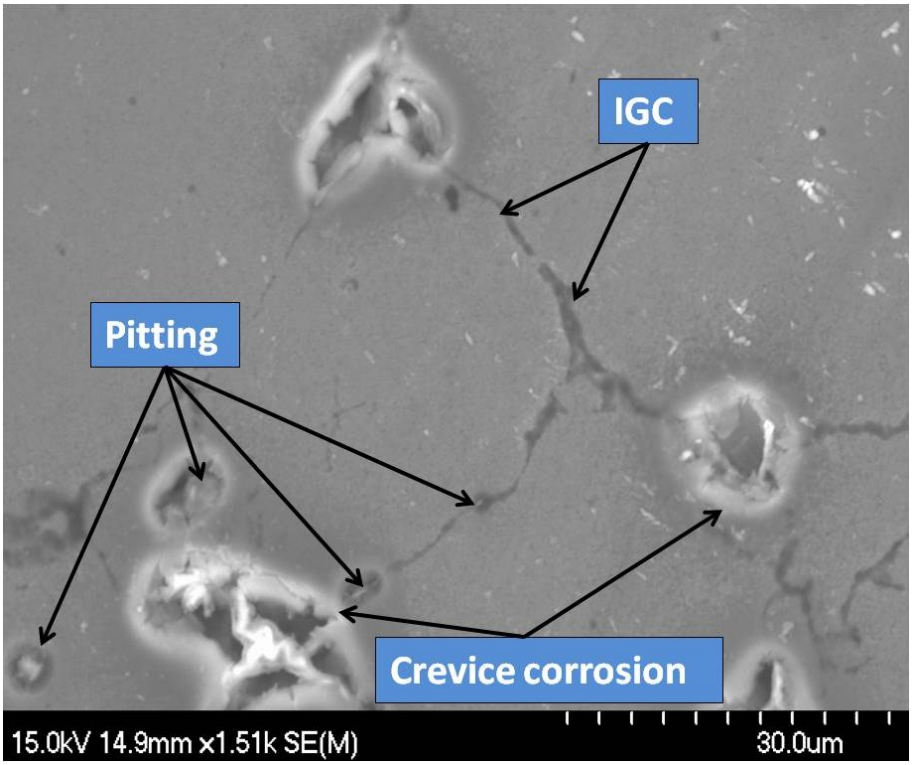

Figure 4-96 SEM micrograph of swaged Alumix 321 PM alloy in 3.5 wt% NaCl solution.

4.9 EFFECT OF HOT ROLLING

Hot rolling was applied on Alumix 321 PM sintered samples and its effect on corrosion behaviour was observed. Alumix 321 powder was uni-axially pressed at 500 MPa, sintered at 630 °C, and then hot rolled. Prior to rolling, Alumix 321 slabs were heated at 500°C for 1 hour. As a result of rolling a total reduction in thickness was 27%. After rolling, slabs were machined into disk samples, heat treated to T6 condition, and then tested for corrosion performance. Different electrochemical techniques were applied to study the effect of hot rolling on corrosion.

4.9.1 *OPEN CIRCUIT POTENTIAL (OCP)*

Open circuit potential was conducted to follow the variation of potential of Alumix 321 as a function of time. Alumix 321 samples in as sintered and rolled condition were placed in a cell and the open circuit potential was recorded. Figure 4-97 shows the variation of the open circuit potential for both rolled and non rolled Alumix 321 samples in 3.5 wt% NaCl solution.

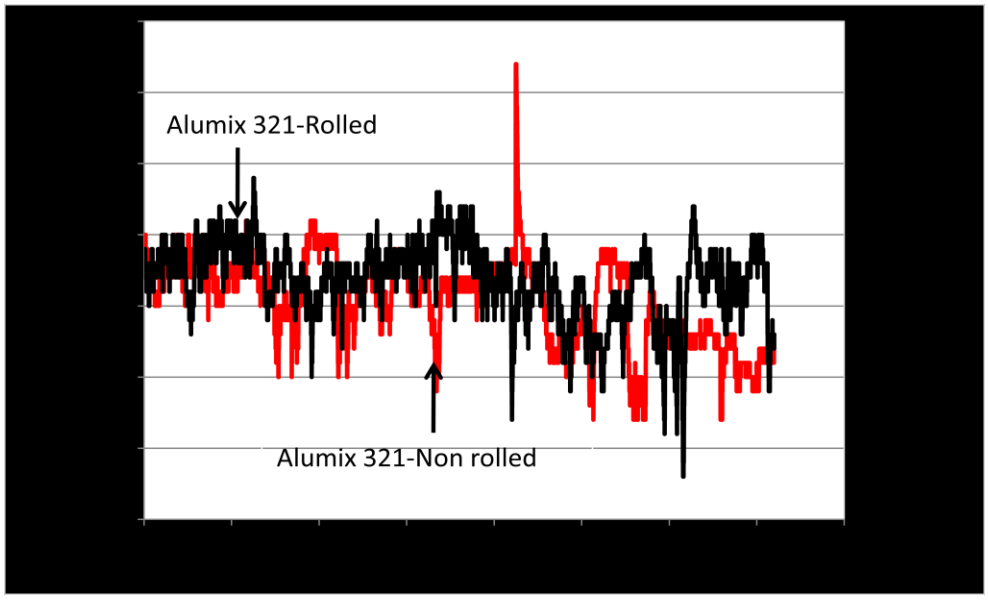

Figure 4-97 Open circuit potential of rolled and non rolled Alumix 321 PM alloy in 3.5 wt% NaCl solution.

The plot shows that the hot rolling treatment has not affected the open circuit potential that much. However, hot rolled samples show slightly higher positive potential than the non rolled samples. The average OCP of non rolled Alumix 321 was -0.758±0.006 V/SCE, and it was -0.756± 0.002 V/SCE for rolled samples. Comparing to hot swaging which was the other way used to hot deform the Alumix 321, the difference between the OCP was not very big, it was expected to see this kind of trend because the non rolled samples were pressed at higher pressure which was 500 MPa and the deformation due to rolling may not affect very much the material microstructure. On the other hand, the changes in the microstructure due to swaging were very noticeable and the difference between non swaged and swaged was very clear.

4.9.2 *TAFEL EXTRAPOLATION (TE)*

Figure 4-98 shows the Tafel plot of Alumix 321 before and after hot rolling. The plot shows that both alloys show a similar anodic current while they show different cathodic current. Corrosion current measured for non rolled and rolled Alumix 321 was 4.5180E-6 and 8.4763E-07, respectively. Figure 4-99 shows the corrosion current of rolled and non rolled Alumix 321 and AA6061. The rolling treatment clearly reduces the corrosion current; the resultant corrosion current after rolling was even lower than the wrought equivalent AA6061.

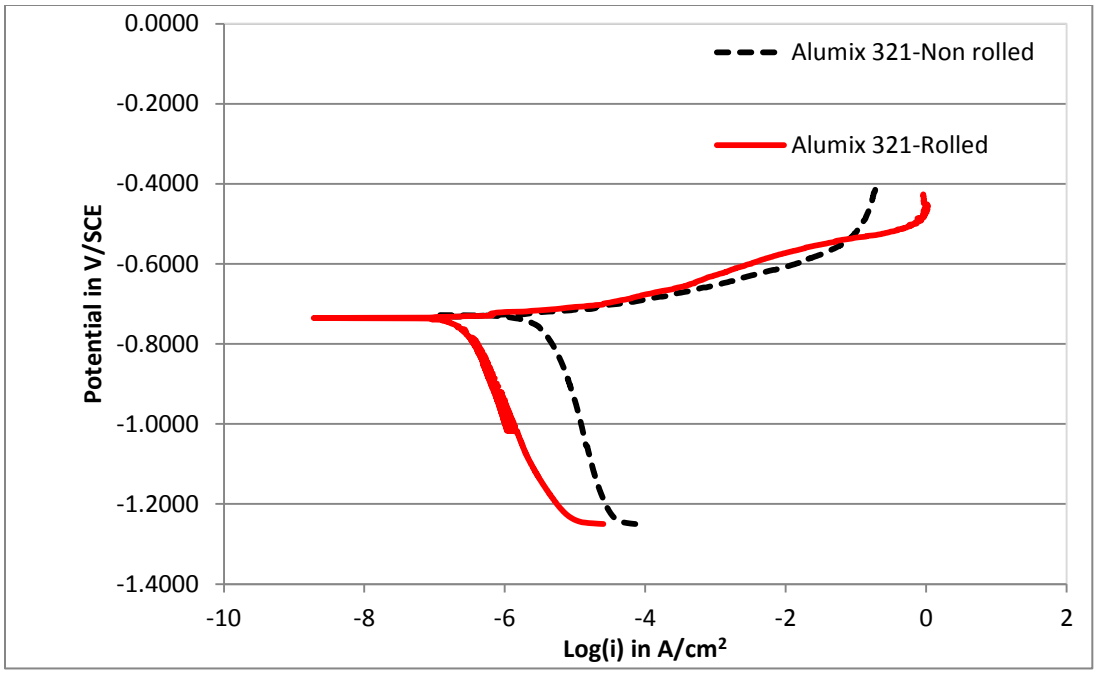

Figure 4-98 Tafel plot of Alumix 321 in 3.5 wt% NaCl solution before and after rolling.

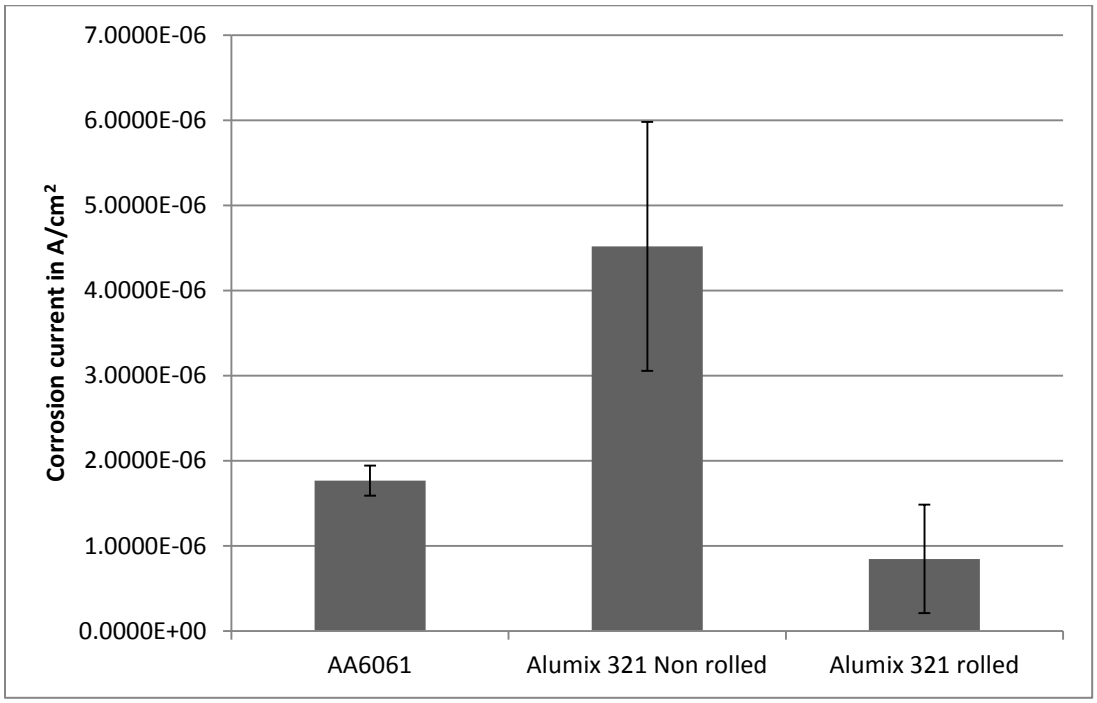

Figure 4-99 Comparision of average corrosion current of rolled and non rolled Alumix 321 PM alloy in 3.5 wt% NaCl solution to the wrought AA6061 alloy.

4.9.3 *CYCLIC POLARIZATION (CP)*

Figure 4-100 illustrates the cyclic polarization curve of Alumix 321 before and after hot rolling in 3.5 wt% NaCl solution. The graph shows that anodic portion of the polarization curve of both rolled and non rolled alloys increases sharply at a value which is very close to the corrosion potential. It shows also that pitting take place at the same potential for both systems. Corrosion potential recorded was -0.740±0.017 V/SCE and -0.737±0.004 V/SCE for non rolled and rolled Alumix 321, respectively. Similar to the values obtained in the corrosion current and open circuit potential, the error recorded in the non rolled samples was higher than that recorded in rolled samples indicating more homogeneity and less scattering in the data recorded. The cathodic part of the cyclic polarization curve shows lower corrosion current of rolled than non rolled samples. The plot also shows a repassivation potential at which the reverse current shows a smaller value. The repassivation potential recorded was -1.036±0.006 and -1.040±0.005 for the non rolled and rolled alloys, respectively.

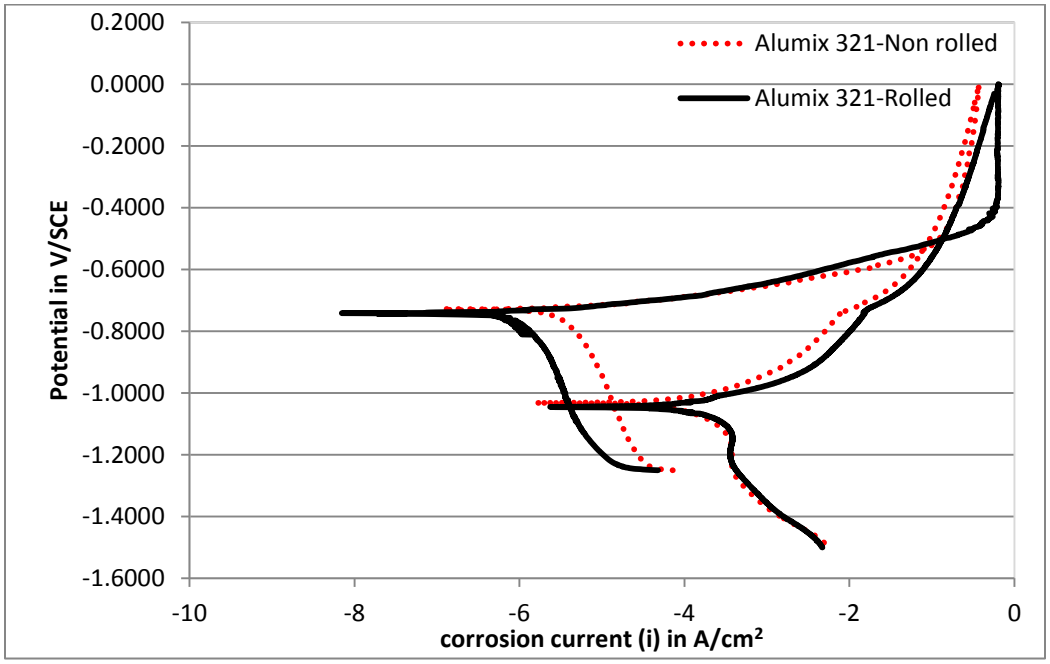

Figure 4-100 Cyclic polarization graph of rolled and non rolled Alumix 321 in 3.5 wt% NaCl solution.

4.9.4 *STAIR STEP POLARIZATION (SP)*

A slower scan rate stair step polarization was applied for both rolled and non rolled samples. Figure 4-101 shows the variation of current as a function of stair step potential. As the potential increases in the anodic direction slight gradual increase in current can be observed in both systems. However, the current recorded for non rolled alloy was higher than that for rolled alloy which is the same result obtained from linear polarization scan. The main observation here is the fast increase in current which took place at about -0.730 V/SCE. The fast increase in current is an indication of pitting. Pitting potential for both rolled and non rolled coincide and it is difficult to distinguish between them.

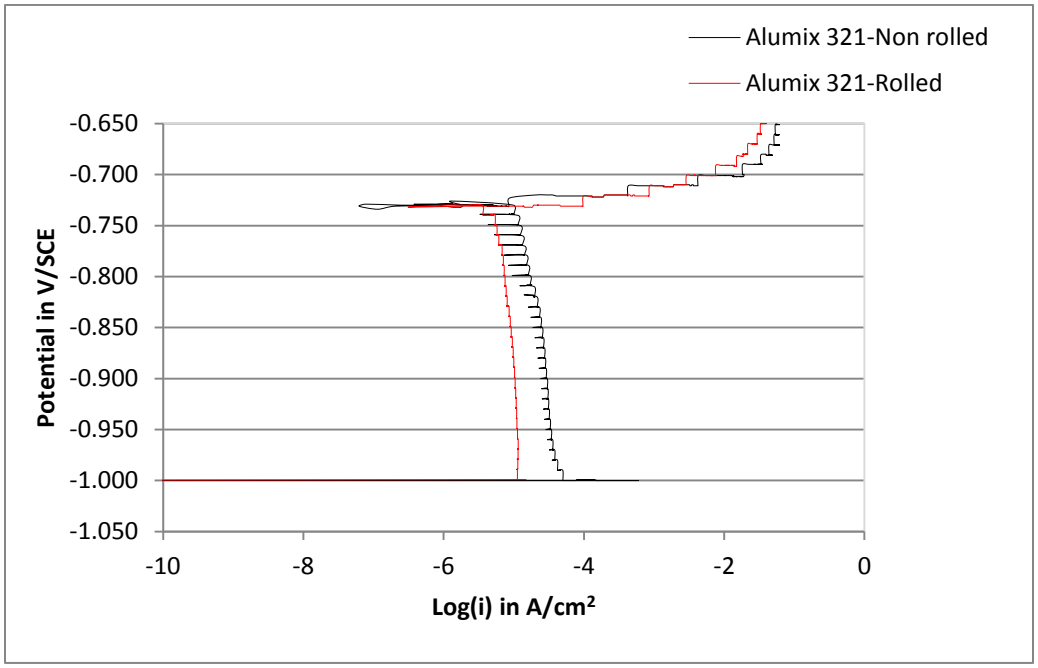

Figure 4-101 Stair step polarization graph of rolled and non rolled Alumix 321 in 3.5 wt% NaCl solution.

The variation of potential as a function of time and current for rolled and non rolled Alumix 321 is shown in Figure 4-102. One axis shows a step wise increase in potential as a function of time and the secondary axis shows the variation of current. At the beginning of the scan the current recorded was very small and continues until a dramatic increase was recorded. The graph shows that the onset of high current was the

same for both rolled and non rolled alloys. This result is in a good agreement with the observation from the linear polarization plot in which the pitting potential for the two systems was almost the same.

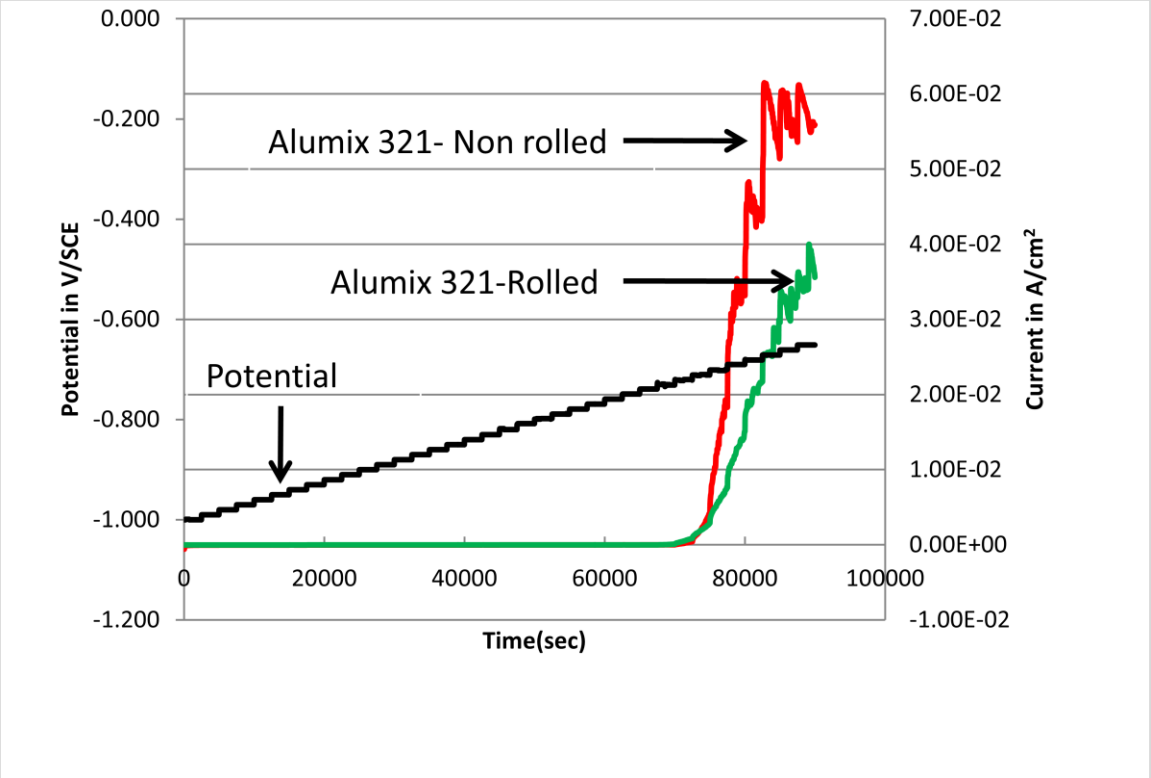

Figure 4-102 Variation of stair step potential as a functon of time and current for rolled and non rolled Alumix 321 in 3.5 wt% NaCl solution.

4.9.5 *CHARACTERIZATION OF ROLLED ALUMIX 321 CORRODED SAMPLES*

Corroded samples prepared from Alumix 321 were examined before and after hot rolling. Figure 4-103 shows SEM micrographs of a corroded surface of Alumix 321 alloy before and after hot rolling taken at low magnification. The corroded surfaces show that the corrosion attack in the case of hot rolled samples was less than that of the non rolled samples. Higher magnification SEM images of the corroded surface show that the hot rolling process reduces the amount of porosity and produced a microstructure that more likely facilitates the corrosion attack that takes place on the surface rather than

inside the pores. Figure 4-104 shows SEM micrograph of hot rolled Alumix 321 corroded surface and indicates that large portion of the exposed surface area is pore free at which pitting can be observed.

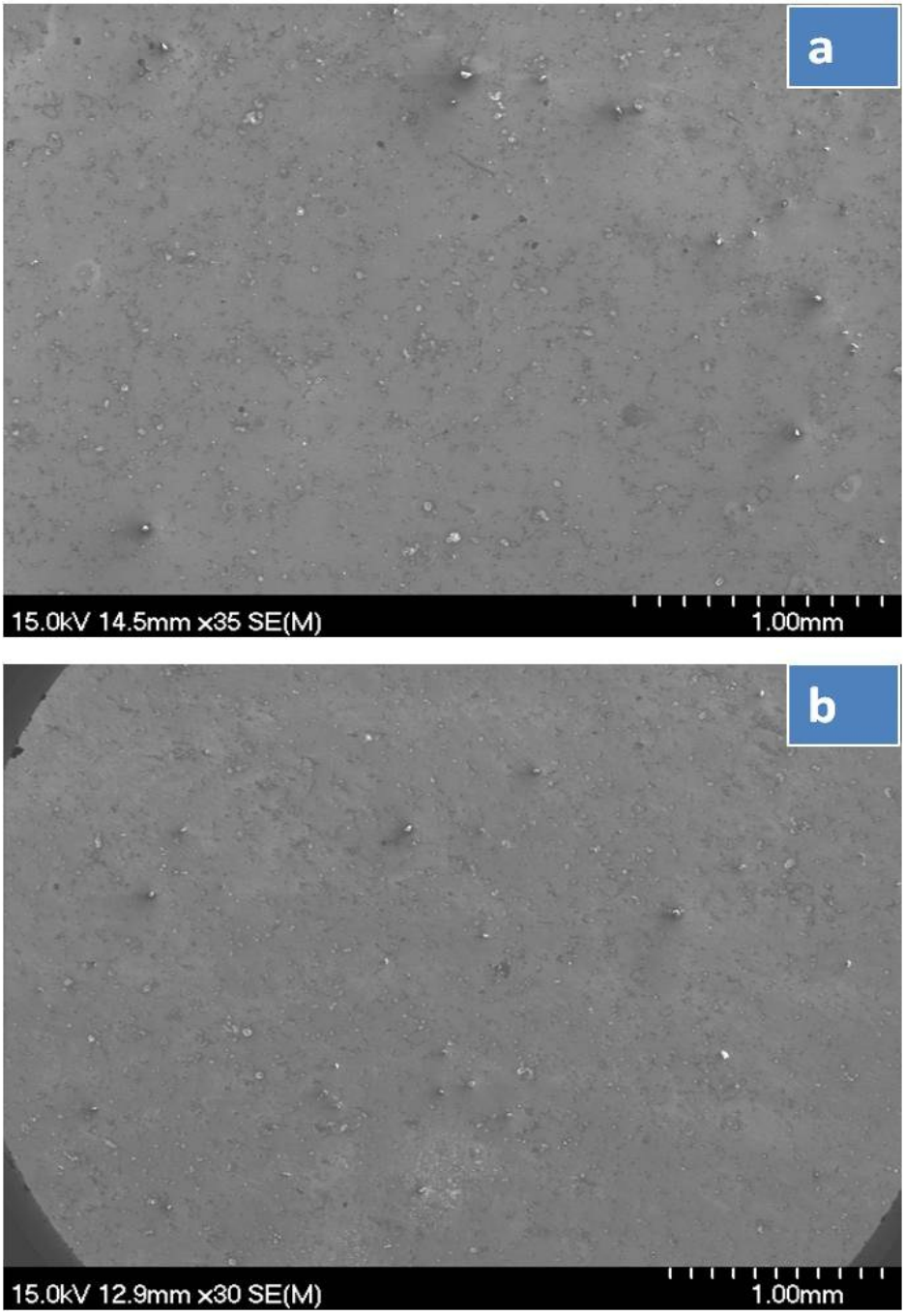

Figure 4-103 SEM micrograph shows the coroded surface of Alumix 321 PM alloy in 3.5 wt% NaCl solution a) before hot rolling , b) after hot rolling.

Despite the changes in the microstructure due to the effect of hot rolling, similar corrosion mechanisms to the other PM samples were observed. Pitting, crevice and intergranular corrosion were detected. Figure 4-105 shows these three types of attack. Crevice corrosion is expected to happen inside interconnected and closed pores while pitting most likely to happen on the surface of the alloy. Those pits have a round shape and in some cases were formed at the vicinity of the iron rich intermetallic particles.

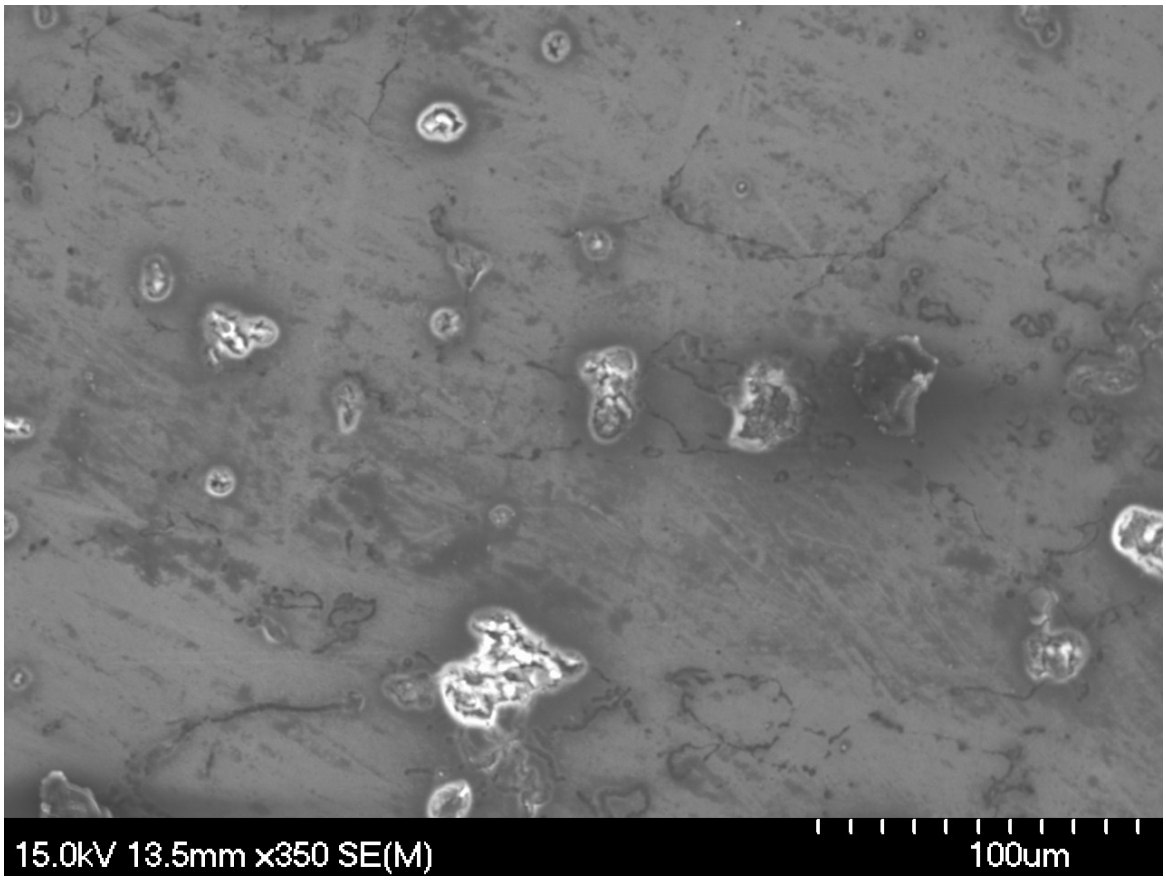

Figure 4-104 SEM showing corroded surface of hot rolled Alumix 321 PM alloy in 3.5 wt% NaCl solution.

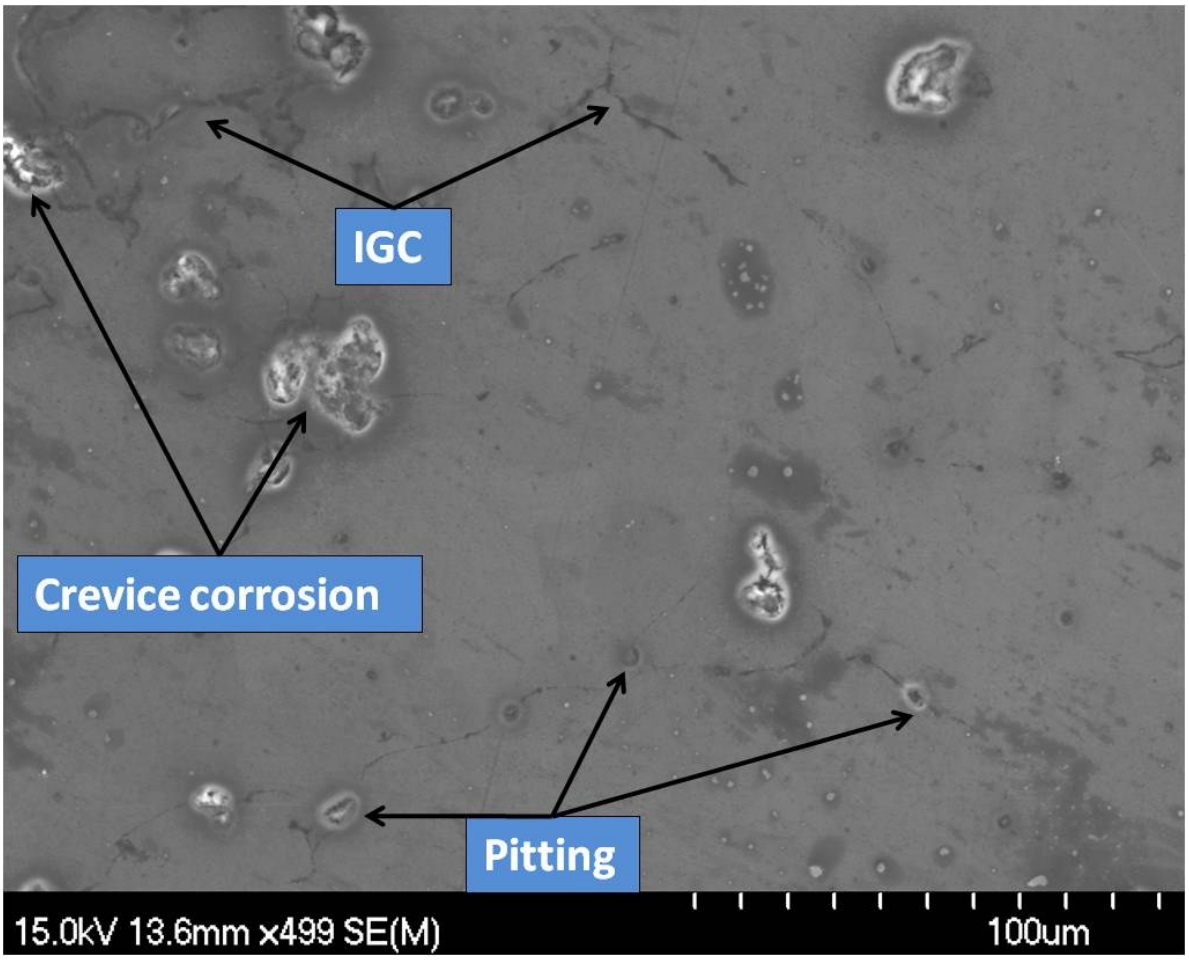

Figure 4-105 SEM showing corrosion morphology of hot rolled Alumix 321 in 3.5 wt% NaCl solution.

4.10 EFFCET OF SHOT PEENING

It has been noted from the observation of sintered and the surface modified Alumix 321 PM corroded samples the important role of porosity on the corrosion behaviour. The idea behind applying shot peening was to modify the surface and observe how this technique will affect the corrosion behaviour of the Alumix 321 PM alloy. Prior to corrosion experiments, samples made of Alumix 321 PM alloy were uniaxially pressed at 500 MPa, sintered at 630 °C, heat treated to T6 condition, and then shot peened.

4.10.1 *OPEN CIRCUIT POTENTIAL (OCP)*

Figure 4-106 shows the open circuit potential of Alumix 321 samples before and after shot peening. The graph shows that the as sintered samples show more positive OCP than the shot peened samples. The value recorded for the as sintered non peened samples was -0.753±0.005. After shot peening the Alumix 321 samples show more negative OCP. The results show that the OCP of shot peened Alumix 321 was -0.769±0.020 V/SCE. The more negative potential is an indication that shot peened samples have higher tendency for corrosion than the as sintered samples which is due to the effect of deformed layer formed after the shot peening treatment.

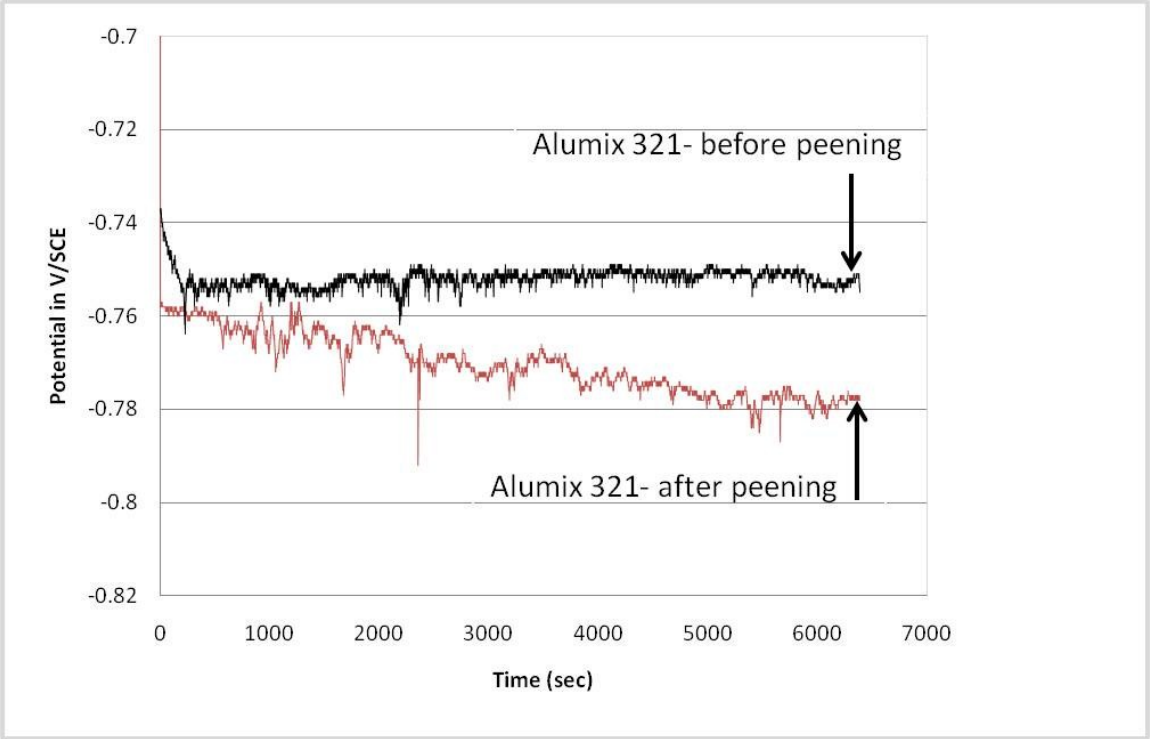

Figure 4-106 OCP of Alumix 321 before and after shot peening in 3.5 wt% NaCl solution.

4.10.2 *TAFEL EXTRAPOLATION (TE)*

Tafel extrapolation was used to calculate the effect of shot peening on corrosion current. Figure 4-107 shows the Tafel extrapolation plot of Alumix 321 before and after shot peening. The results show that the corrosion current recorded was 3.2069E-07 A/cm^2 and 7.86E-06 A/cm^2 for shot peened and as sintered samples, respectively. In

addition of the effect of shot peening on corrosion current, shot peening treatment also affects the corrosion potential. Tafel extrapolation plot also shows that the corrosion potential of the shot peened samples is more negative than the corrosion potential of the as sintered not peened samples. This trend is similar to that observed of the OCP and was attributed to the formation of the deformed layer that was initiated after the shot peening process.

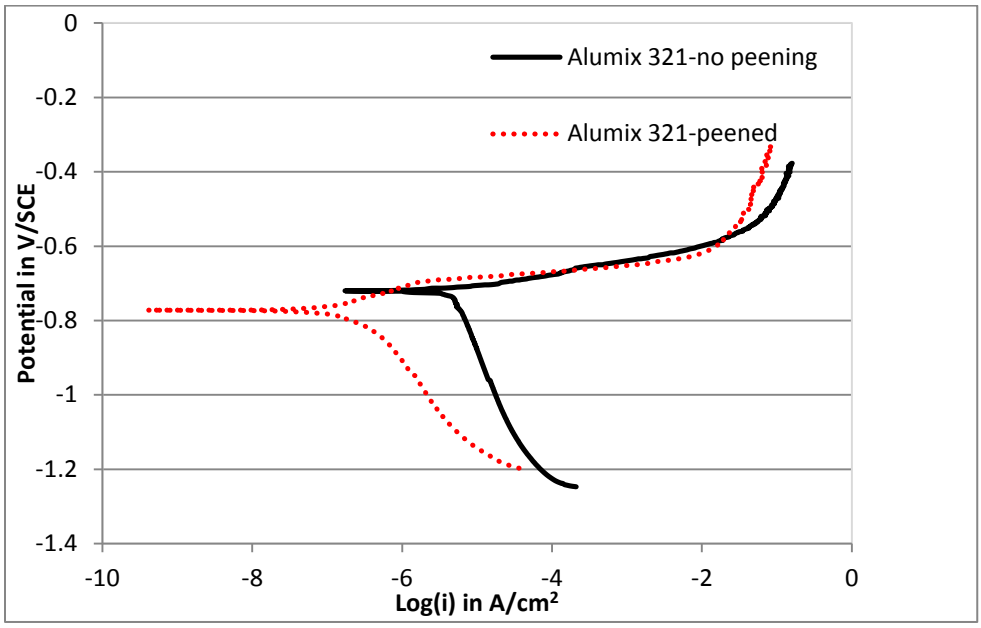

Figure 4-107 Tafel extrapolation plot of Alumix 321 before and after shot peening in 3.5 wt% NaCl solution.

The corrosion current of Alumix 321 before and after shot peening was compared to the corrosion current of their equivalent AA6061 wrought aluminum alloy. Figure 4-108 shows that the corrosion current of the shot peened Alumix 321 PM samples is even lower than that of the wrought form. This better performance is attributed to the effect of shot peening treatment on the surface of the Alumix 321 samples.

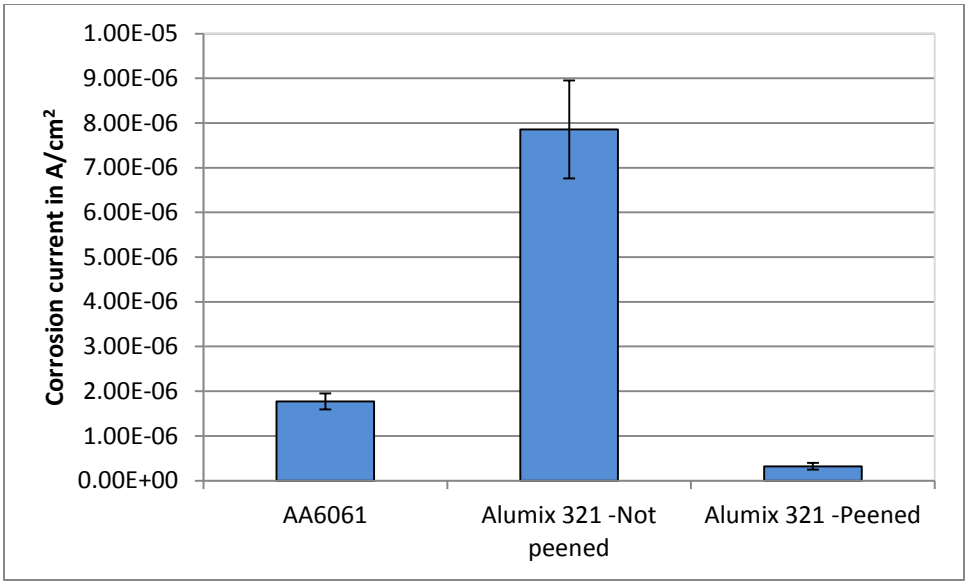

Figure 4-108 Comparision of average corrosion current of shot peened and non peened Alumix 321 PM alloy in 3.5 wt% NaCl solution to the AA6061 wrought alloy.

4.10.3 *CYCLIC POLARIZATION (CP)*

Cyclic polarization plot shows that the shot peened samples demonstrate different behaviour than the as sintered not peened samples. Figure 4-109 illustrates the effect of shot peening treatment on the cyclic polarization plot. The anodic portion of the graph shows that the corrosion current increases gradually and not very sharply as in the case of as sintered samples. Despite the difference in the slope of the current, pitting takes place almost at the same potential for both peened and sintered samples. However, slightly higher pitting potential was recorded in shot peened samples. Pitting potential of the shot peened samples was found to be -0.716±0.011 V/SCE. The repassivation potential was almost the same for Alumix 321 before and after, the value recorded was -1.0502±0.001 V/SCE. The plot again shows that the corrosion potential in case of shot peened samples is more negative than that of as sintered samples. The corrosion potential of the as sintered Alumix 321 samples was recorded to be -0.719±0.016 V/SCE while the value obtained was more negative and found to be -0.762±0.025 V/SCE.

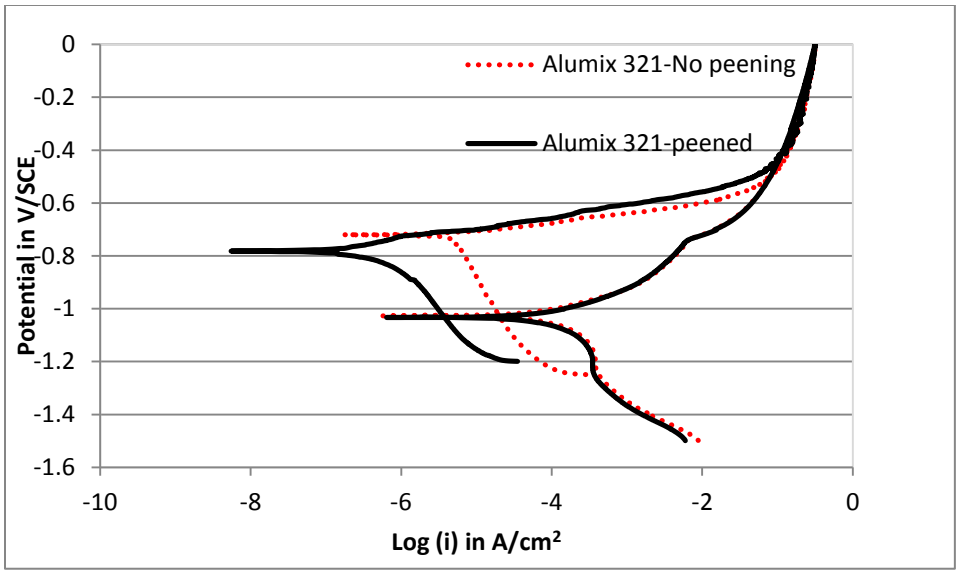

Figure 4-109 Cyclic polarization plot of Alumix 321 PM alloy in 3.5 wt% NaCl solution before and after shot peening.

4.10.4 *STAIR STEP POLARIZATION (SP)*

Figure 4-110 shows the stair step polarization plot of Alumix 321 in 3.5 wt% NaCl solution before and after shot peening. The plot shows that for both peened and non peened samples the current at lower potential was very small, and it is almost the same. The current then increases rapidly at certain potential. Generally, the potential at which this current increase was higher in case of shoot peened samples than for non peened samples. The higher pitting potential for the shot peened samples indicates that shot peening can improve the pitting resistance as well. The better pitting characteristics after shot peening can be attributed to the surface modification and alteration that happened after shot peening. Bombarding the porous surface leads to closing off appreciable amount of surface porosity and leads to a better performance. More explanation will be given about the effect of this process on the surface and the microstructure during the discussion of characterization of the corroded samples.

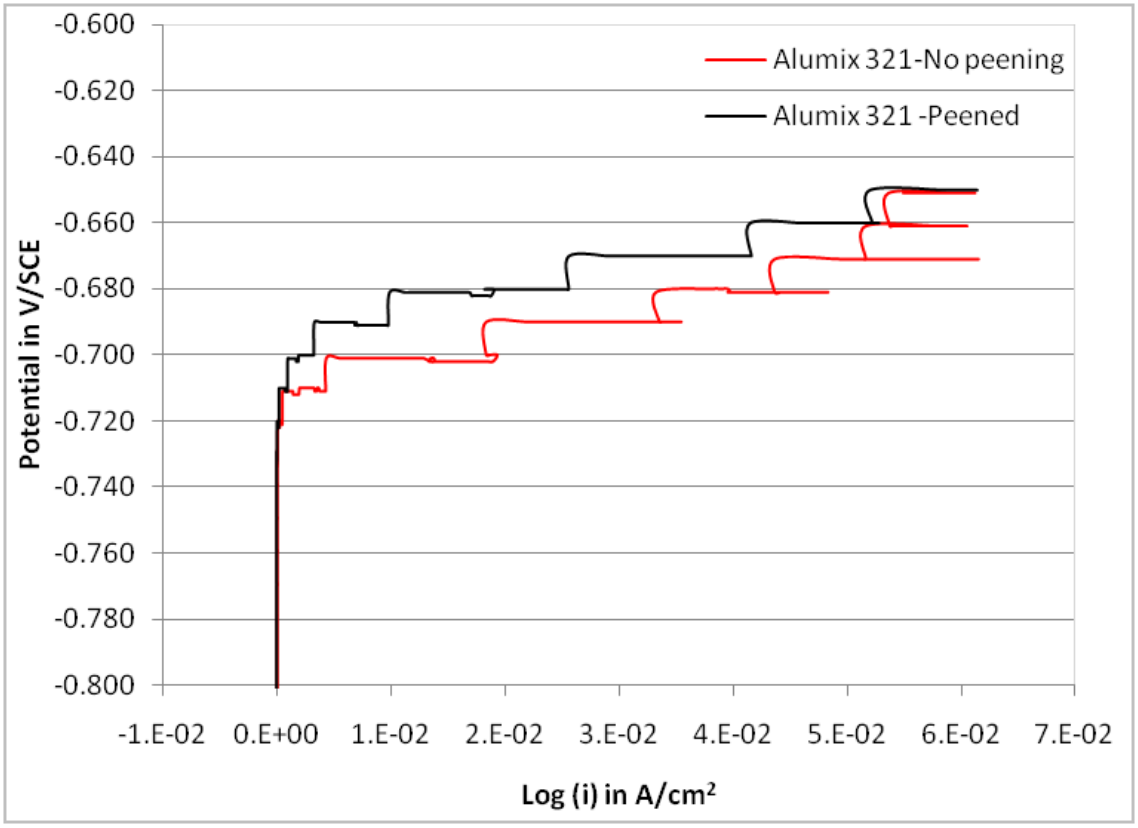

Figure 4-110 Stair step polarization plot of peened and non peened Alumix 321 in 3.5 wt% NaCl solution.

Figure 4-111 shows the variation of current as a function of stair potential and time. The graph shows the behaviour of Alumix 321 samples before and after shot peening. At lower stair potential the value of the current was constant and very small. At certain potential, dramatic increase in current can be observed. This rapid increase is associated with pitting. The plot clearly shows that the shot peened samples show better performance. Shot peened Alumix 321 samples have a higher pitting potential and consequently a better pitting resistance than non peened samples. The better performance of the Alumix 321 after peening is attributed to the modified surface that resulted from the interaction between the high speed peening particles and the sample surface. Data collected after the stair step polarization indicates that the shot peening surface treatment increases the pitting potential of the Alumix 321 samples from -0.711 V/SCE to -0.690 V/SCE.

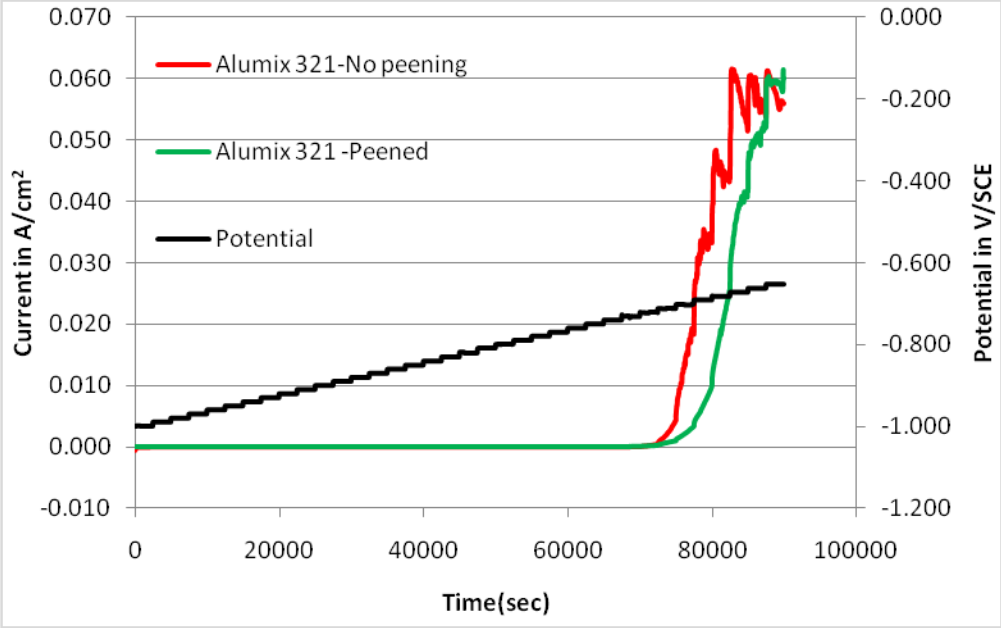

Figure 4-111 Stair step polarizatio plot showing the variation of potential and current as a function of time of Alumix 321 in 3.5 wt% NaCl solution.

4.10.5 *CHARACTERIZATION OF CORRODED SHOT PEENED SAMPLES*

Figure 4-112 shows a low magnification optical micrograph of a corroded shot penned Alumix 321 sample after exposing to 3.5 wt% NaCl solution. The Figure illustrates that the effect of shot peening is almost even all over the samples even though some islands of the base metal were not affected by the peening process. It can be seen that pitting corrosion is quit visible and clear. Some pits were formed inside the dimples. Only minor attack can be seen inside some dimples which suggest the possibility that those pores were closed due to the peening effect. Figure 4-113 shows a higher magnification optical micrograph of shot peened Alumix 321. The Figure shows clearly that pits were formed inside some dimples that were formed initially after peening. It also shows that a shot peened free area still exist in which clearly round pits can be seen. The presence of un deformed islands will create an interesting situation in terms of solution stagnancy and oxygen concentration. Un deformed areas will be at different level compared to the bottom of those dimples, in addition, dimples themselves are at different level than the interconnected and closed pores where the solution is more static and stagnant. This

condition will create different aeration cells which are far more complicated than the simple different aeration cell.

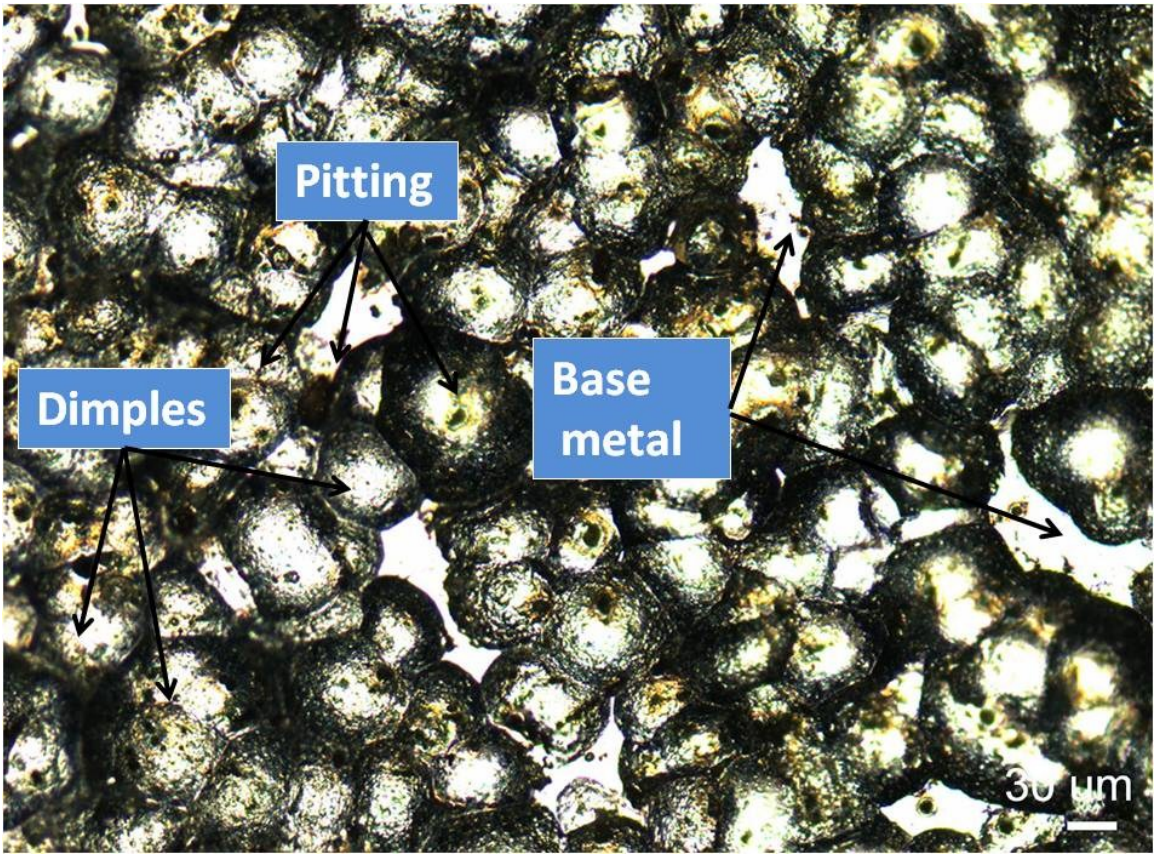

Figure 4-112 Optical micrograph of the corroded surface of shot peened Alumix 321 in 3.5 wt% NaCl solution.

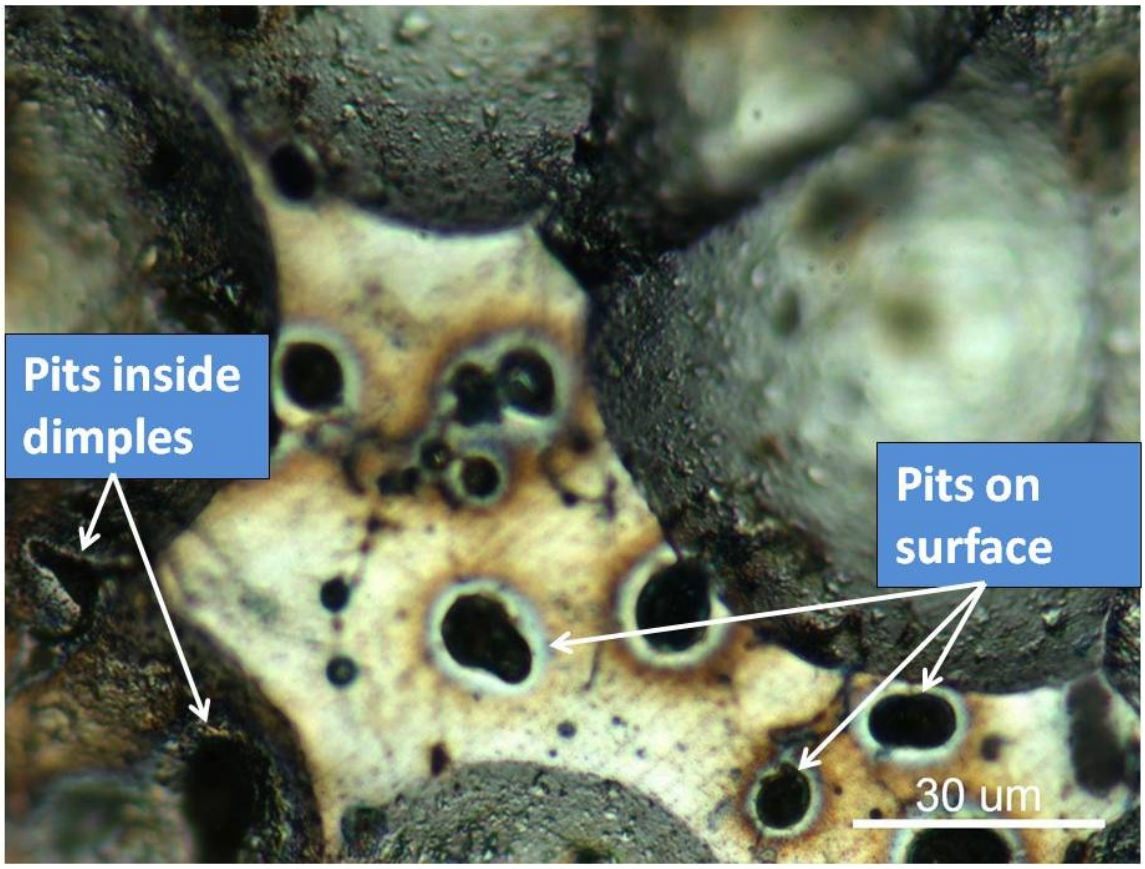

Figure 4-113 High magnification optical micrograph of the corroded surface observed on shot peened Alumix 321 in 3.5 wt% NaCl solution.

Figure 4-114 is an optical micrograph that shows the as received and as shot peened and corroded Alumix 321 samples after exposing to 3.5 wt% NaCl solution. It appears that shot peening is efficient in terms of reducing corrosion spots, this reduction reflects the lower corrosion rate of shot peened samples compared to non peened samples. Shot peening collapsed some interconnected pores and close some channels which will prevent the saline solution from reaching new areas. Shot peening as a surface alteration technique was combined by an increase in toughness. Optical profilometry shows that roughness increases from 0.033±0.003 µm before shot peening to 3.95±0.232 µm after shot peening. Despite the increase in roughness and the deformed layer that formed on the surface which may affect the corrosion behaviour of the material, shot peening resulted in lower corrosion current and higher pitting potential.

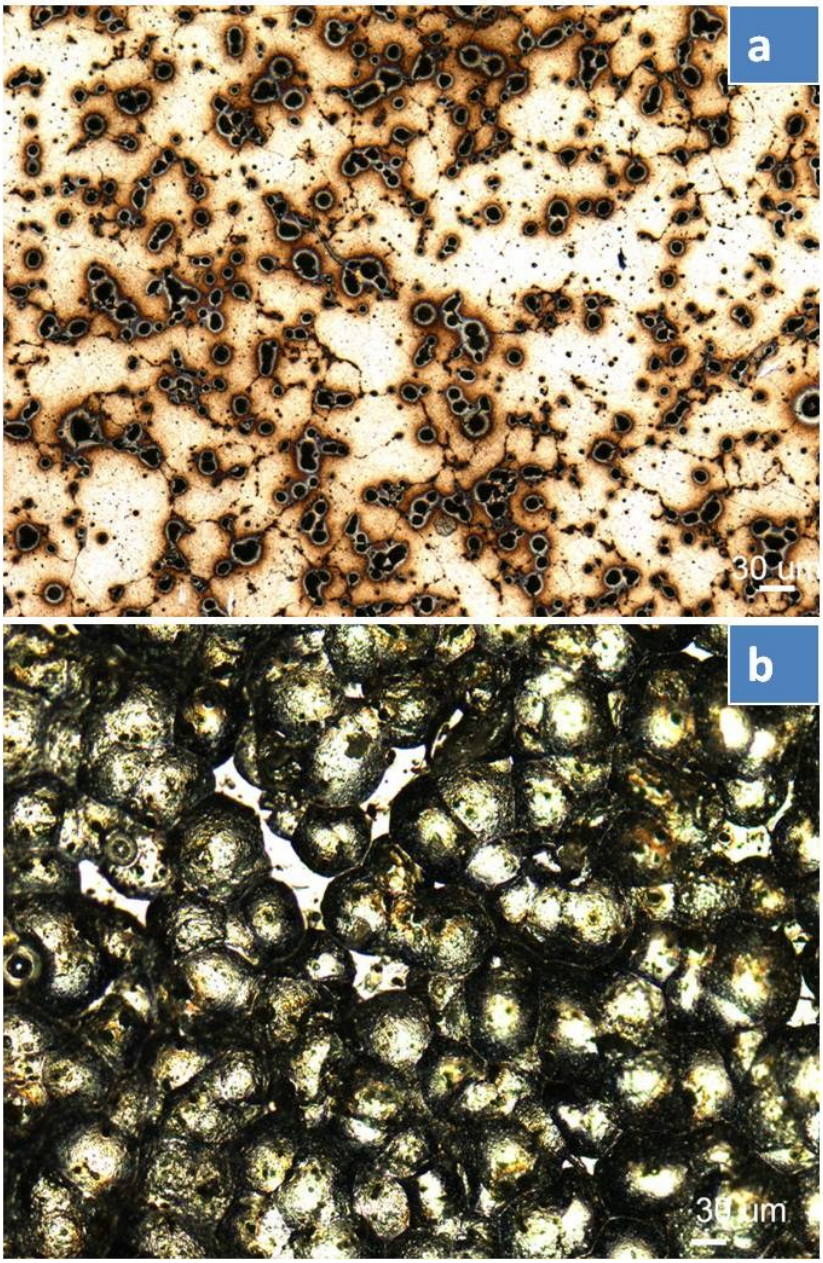

Figure 4-114 Optical micrograph shows the corroded surface of Alumix 321 in 3.5 wt% NaCl solution a) before shot peening, b)after shot peening.

Figure 4-115 and Figure 4-116 shows low magnification scanning electron micrographs of corroded surface of Alumix 321 in 3.5 wt% NaCl solution. The images show clearly the effect of peening process. Dimples are very clear as a main feature of the sample topography. At this magnification, only a few corrosion spot can be observed which

probably due to corrosion reactions inside some large pores that were not affected by shot peening.

Figure 4-117 illustrates higher magnification scanning electron micrograph of corroded Alumix 321 surface after shot peening. The image shows round pitting sites that formed around iron rich particles. The presence of these pits inside the dimples suggests that peening process was not successful to close off all the pores and some of them remain open to the surface. Similar to the non peened samples, the other corrosion mechanism is the crevice corrosion which takes place inside large and interconnected porosity. In addition to pitting and crevice, intergranular corrosion mechanism was also observed after shot peening.

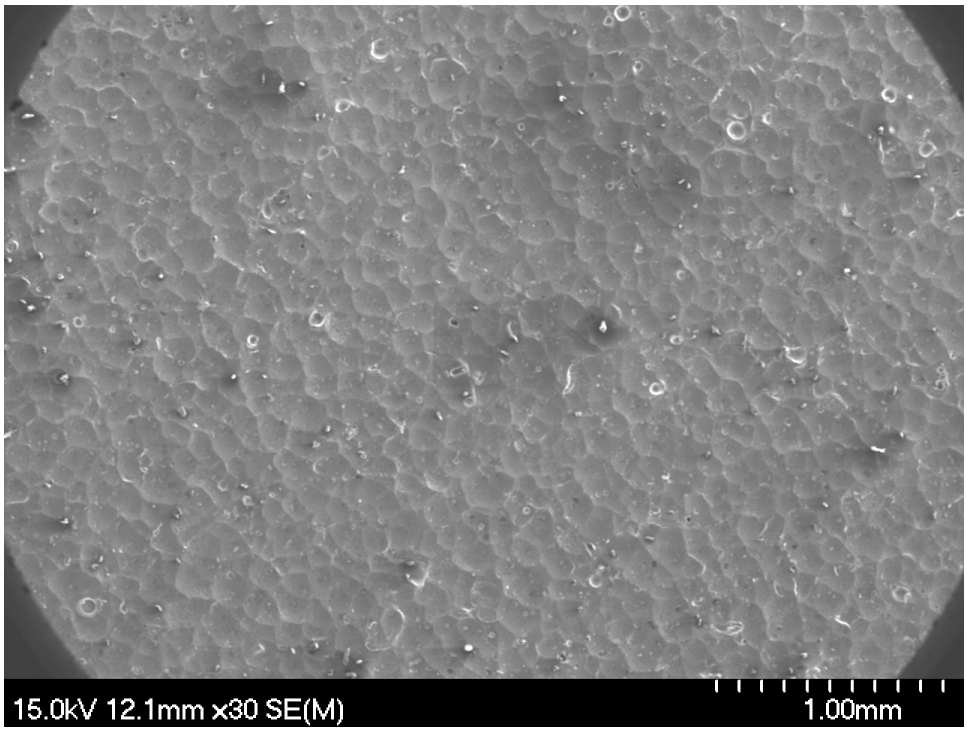

Figure 4-115 SEM micrograph shows a corroded surface of shot peened Alumix 321 PM alloy in 3.5 wt% NaCl solution.

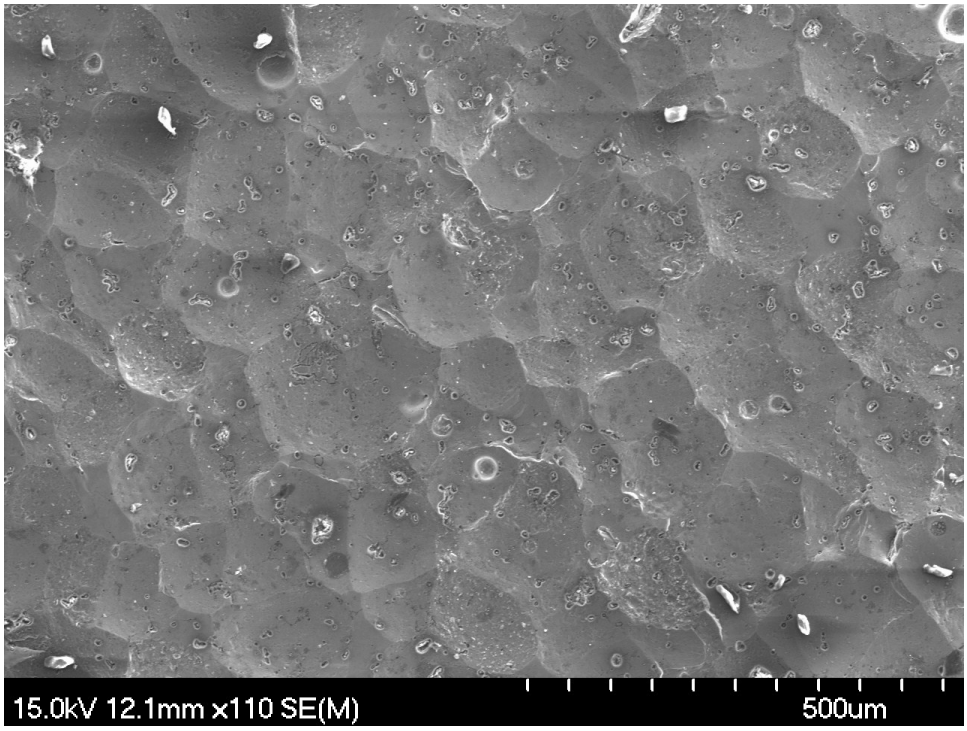

Figure 4-116 Corroded surface of shot peened Alumix 321 PM alloy in 3.5 wt% NaCl solution.

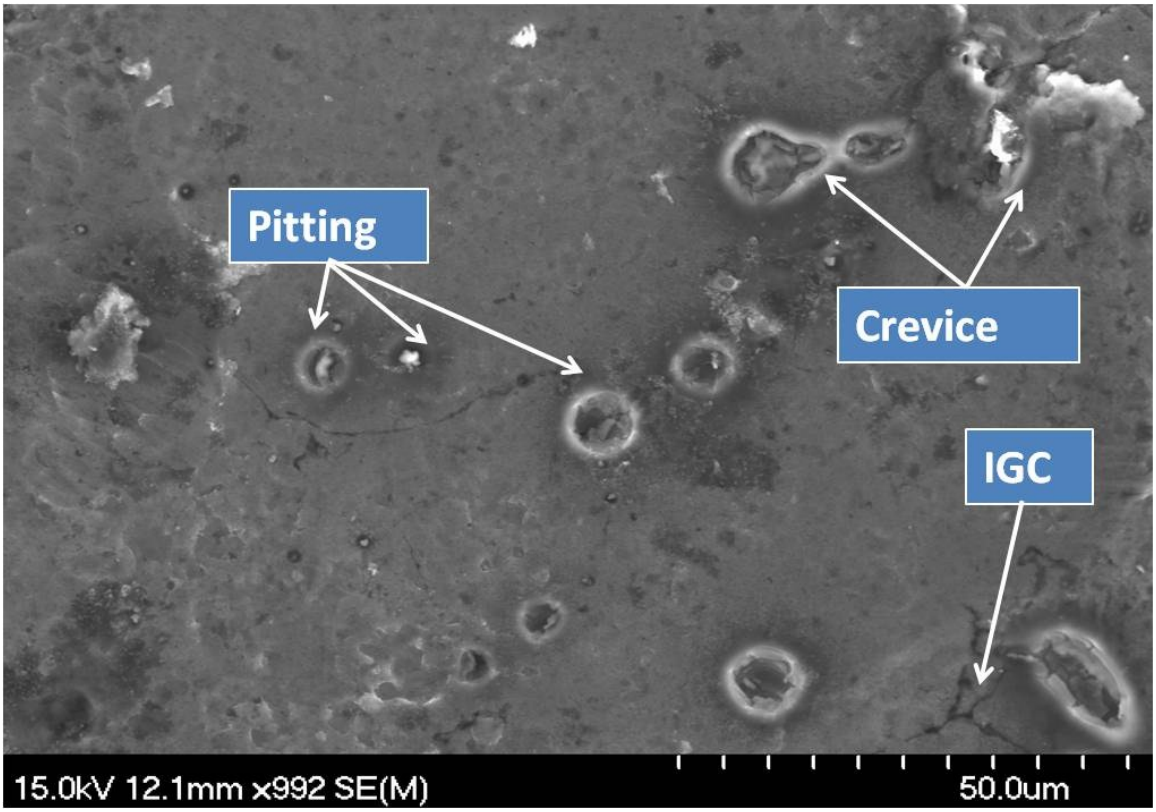

Figure 4-117 SEM micrograph of the corroded surface of shot peened Alumix 321 in NaCl solution.

4.11 EFFECT OF SIZING

The corrosion behaviour of Alumix 321 PM alloy was evaluated after sizing. Three different sets of samples were tested in which different pressing and sizing pressures were used. The samples were pressed at 100, 300, 500 MPa, sintered at 630 °C, and then sized at 50, 100, 180 MPa, respectively. It is worth noting that the sized samples were tested in the as sintered condition (T1) in order to facilitate the sizing process.

4.11.1 *OPEN CIRCUIT POTENTIAL (OCP)*

Figure 4-118 shows the OCP plot of Alumix 321 samples pressed at different pressure and then sized. Similar to the trend of the samples before sizing, the samples pressed at 100 MPa and sized show more negative potential than the other two sets of samples. In addition to the more negative potential, the samples show also continuous drop in potential. It is worth noting that the drop in potential was not as severe as in the case before sizing. The open circuit potential after sizing was recorded to be -0.878 V/SCE. However, the values before sizing show a large degree of scattering with more negative potentials and the OCP of the samples pressed at 100 MPa before sizing was -0.9235 V/SCE. The more positive potential after sizing is most likely due to the effect of sizing pressure in reducing the effect of interconnected porosity. Contrary to the trend of the samples pressed at 100 MPa, the samples pressed at 300 MPa and 500 MPa and then sized at 100, and 180 MPa, respectively, show different response after sizing. The OCP values recorded were -0.776 V/SCE and -0.772 V/SCE for samples pressed at 300 and 500 MPa, respectively. The values before sizing were more positive and recorded to be -0.735 V/SCE and -0.748 V/SCE for the samples pressed at 300 and 500 MPa, respectively. This behaviour can be explained based on the fact of how the sizing pressure affects the samples. In the case of the samples pressed at 100 MPa, it is suggested that the pressure was used to close some of the interconnected pores and not much bulk deformation was attributed, while in the case of the samples pressed at 300 MPa and 500 MPa the pressure was enough to cause a noticeable amount of deformation that shifts the open circuit potential to more negative values.

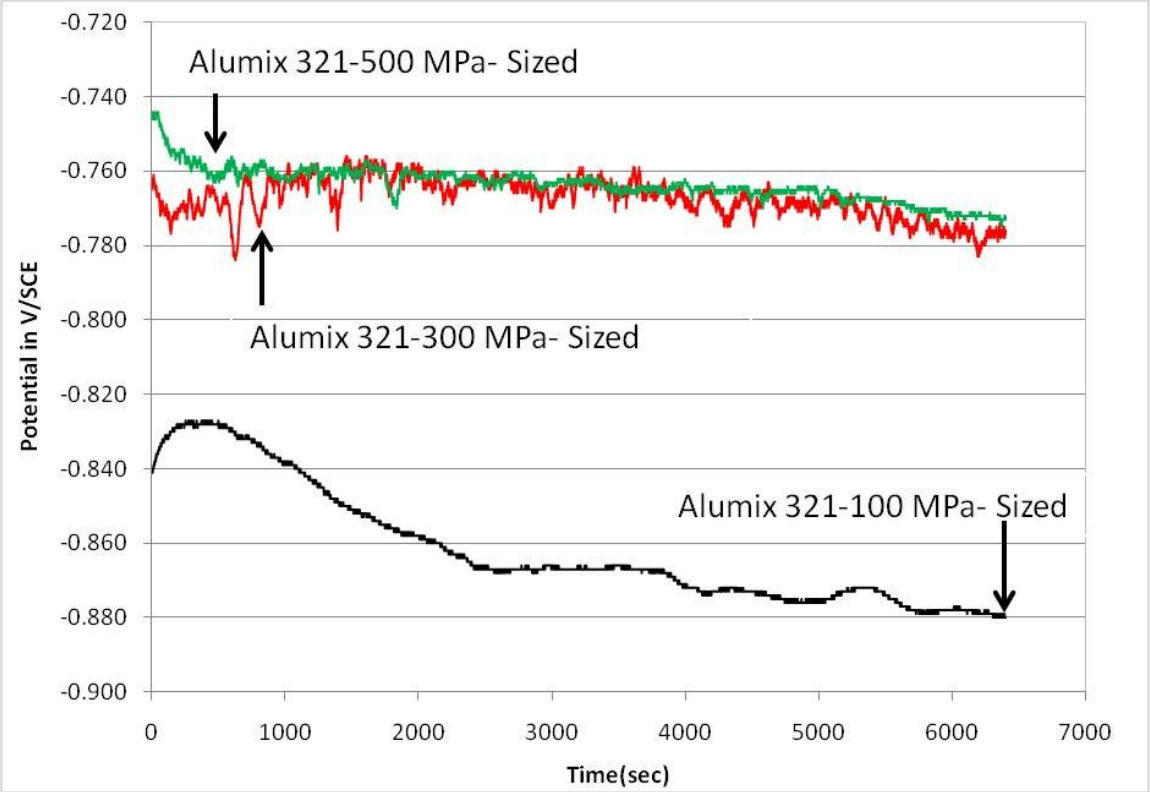

Figure 4-118 Variation of OCP as a function of time of Alumix 321 sized at different pressures in 3.5 wt% NaCl solution.

4.11.2 *TAFEL EXTRAPOLATION (TE)*

Tafel extrapolation technique was used to calculate the corrosion current of Alumix 321 PM samples pressed at different pressures and then sized. The samples were pressed at 100, 300, and 500 MPa. Samples pressed at 100 MPa and then sized at 50 MPa show a lower corrosion current than those not sized. Similar to the other samples pressed at this pressure, the anodic portion of the plot shows gradual increase in current followed by a sharp increase in current at a potential associated with pitting. Figure 4-119 shows the effect of sizing on the Tafel plot of this set of samples. Applying Tafel extrapolation technique verify that sizing treatment decreases the corrosion current from 6.8775E-06 A/cm^2 to 1.6415E-06 A/cm^2, both values were higher than the value for the wrought AA6061 alloy.

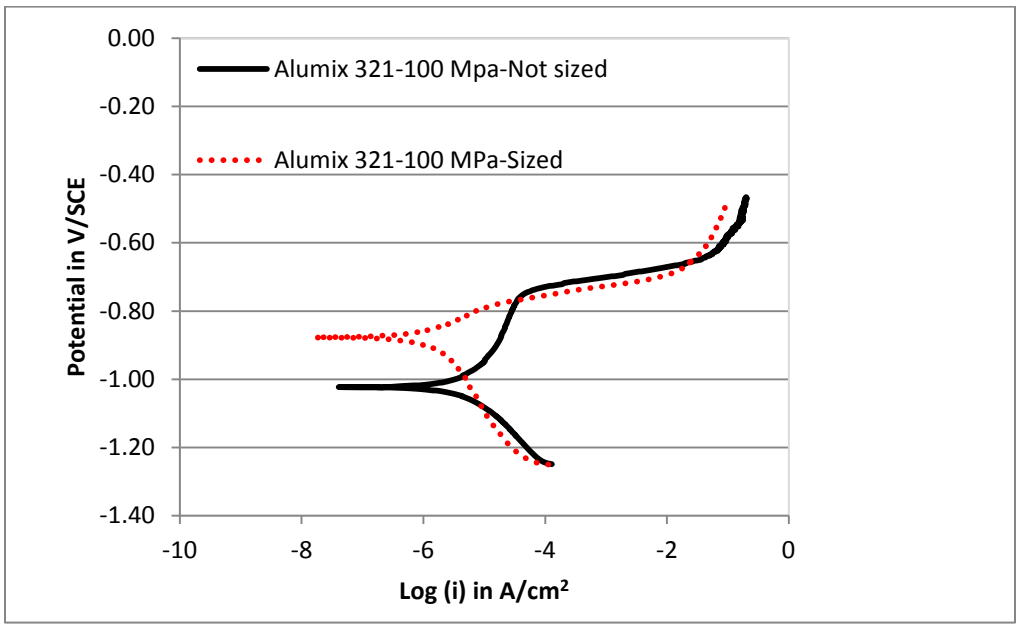

Figure 4-119 Effect of sizing on Tafel plot of Alumix 321 in 3.5 wt% NaCl solution.

For the set of samples pressed at 300 MPa and then sized at 100 MPa, the sizing treatment was beneficial in terms of the corrosion current. The corrosion current of the sized samples was lower and recorded to be 2.5 E-06 A/cm^2 compared to 4.58E-06 A/cm^2 for non sized samples, and again both the sized and non sized corrosion current was higher than the corrosion current of their equivalent AA6061 wrought alloy.

The third set of samples were pressed at 500 MPa and then sized at 180 MPa. The trend was similar to the samples pressed at 300 MPa in which a sharp increase in current took place right at the corrosion potential. Tafel extrapolation technique shows that sizing improves the corrosion resistance. The corrosion current for this set of samples decreases from 5.21E-06 A/cm^2 before sizing to 2.32E-06 A/cm^2. Figure 4-120 shows the Tafel plot of the Alumix samples after sizing. The corrosion current of Alumix 321 samples pressed and sized at different pressure were compared to their equivalent AA6061 wrought alloy, the result is shown in Figure 4-121.

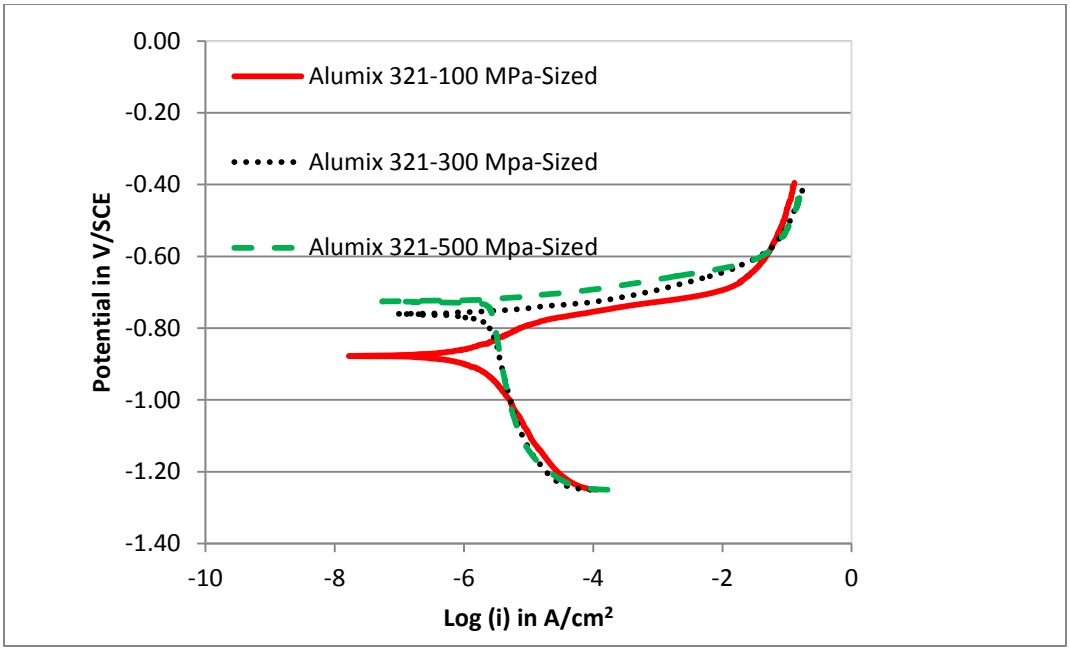

Figure 4-120 Tafel extraploation plot of Alumix 321 PM alloy after sizing at different pressures.

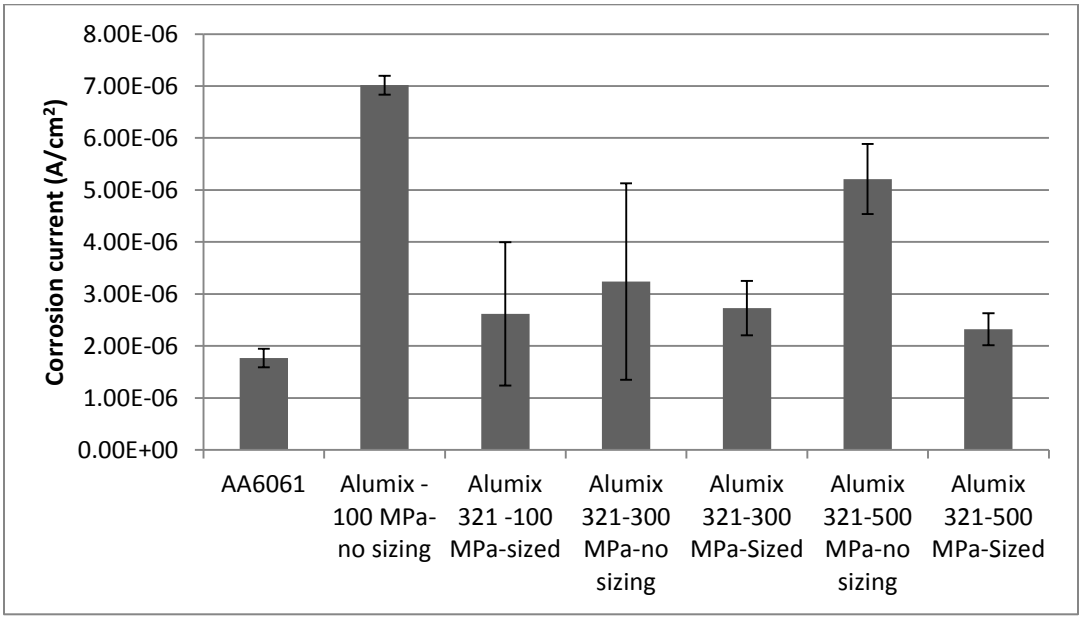

Figure 4-121 Comparision of the corrosion current of Alumix 321 PM alloy as a function of sizing.

4.11.3 *CYCLIC POLARIZATION (CP)*

Figure 4-122 shows the cyclic polarization plot of Alumix 321 alloy pressed at 100 MPa before and after sizing. Similar to the results obtained before, the 100 MPa samples and despite the sizing effect show noticeable negative corrosion potential. In addition to the lower corrosion potential, sized and not sized Alumix 321 samples demonstrate gradual increase in corrosion current. The gradual increase in current starts at the corrosion potential and continuous until sharp increase is observed which indicates pitting. The value of the pitting potential of the sized and un sized Alumix 321 was recorded to be -0.788 V/SCE and -0.876 V/SCE, respectively. For those samples were not subjected to the sizing treatment, the gradual increase is steadier and the corrosion current was higher. In accordance with OCP results the corrosion potential of the sized samples is more positive compared to those not sized. The corrosion potential increases from -1.023 v/SCE before sizing to -0.876 V/SCE after sizing. Sizing treatment did not affect the repassivation potential of Alumix 321 very much and the values were approximately the same, the values were -0.995 V/SCE and -1.000 V/SCE before and after sizing, respectively.

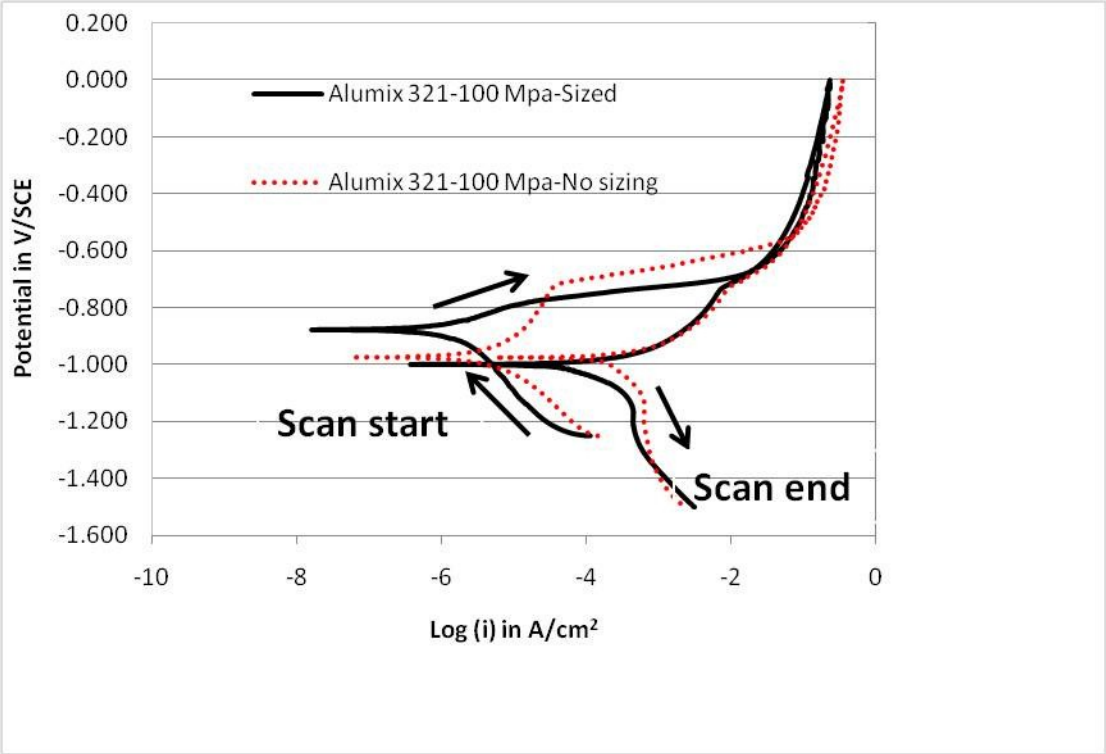

Figure 4-122 Cyclic polarization plot of Alumix 321 PM alloy in 3.5 wt% NaCl solution before and after sizing.

Another set of samples were pressed at 300 MPa and then sized at 100 MPa. Figure 4-123 illustrates the effect of sizing treatment on the cyclic polarization plot of Alumix 321 in 3.5 wt% NaCl solution. This set of sized samples behave differently than that pressed at 100 MPa, they show more negative corrosion potential and sharper anodic current variation. Contrary to the previous set of samples, the corrosion potential after sizing is more negative. The values recorded before and after sizing were -0.698 V/SCE and -0.761 V/SCE, respectively. This drop in potential can be explained on the effect the deformation caused during sizing. The more negative corrosion potential of the sized samples was combined by lower pitting potential even though the overlapping makes it difficult to distinguish the exact value of pitting corrosion from the corrosion potential. On the other hand, repassivation potential was the same and it was -1.032 V/SCE.

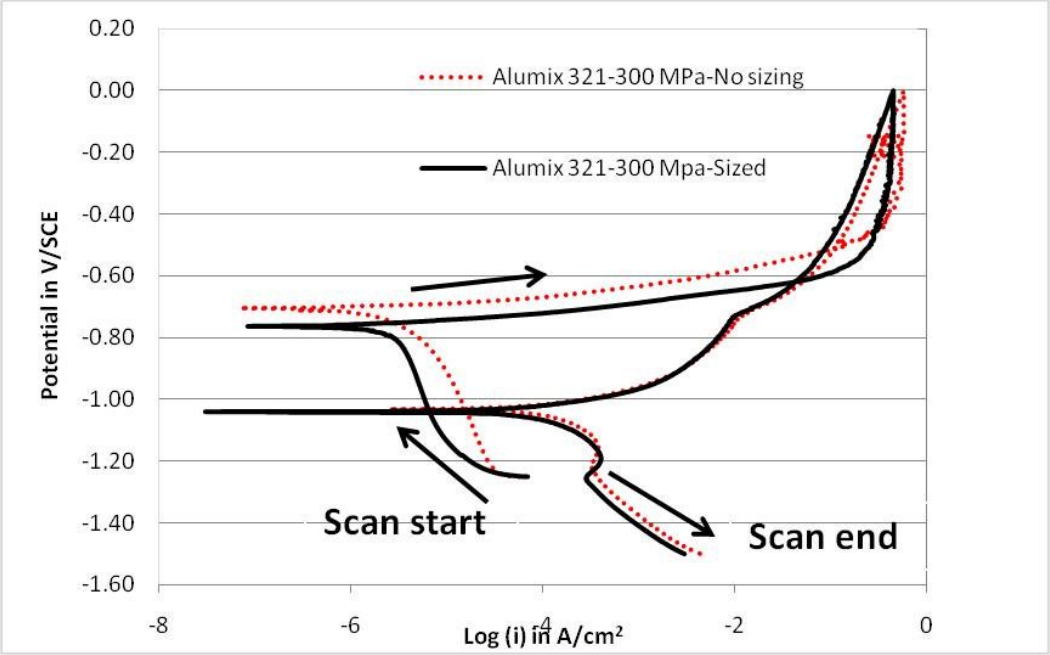

Figure 4-123 Cyclic polarization plot of Alumix 321 alloy pressed at 300 MPa and then sized at 100 MPa in 3.5 wt% NaCl solution.

The third set of samples were pressed at higher pressure (500 MPa) and then sized at 180 MPa. The behaviour of this set was similar to the set pressed at 300 MPa and sized at 100 MPa and quite different than those samples pressure and sized at lower pressure. Figure 4-124 shows the cyclic polarization plot of this set. Corrosion potential before and after sizing was -0.702±0.009 V/SCE and -0.728±0.002 V/SCE, respectively. The sharp increase in potential of both sized and not sized suggests that pitting happens at a potential that coincides with the corrosion potential. However, samples before sizing show higher pitting potential in general. Similar to the samples pressed at 300 MPa and sized at 100 MPa, this set of samples show only small difference in repassivation potential between sized and not sized samples, the values were -1.028 V/SCE and-1.038 V/SCE before and after sizing, respectively.

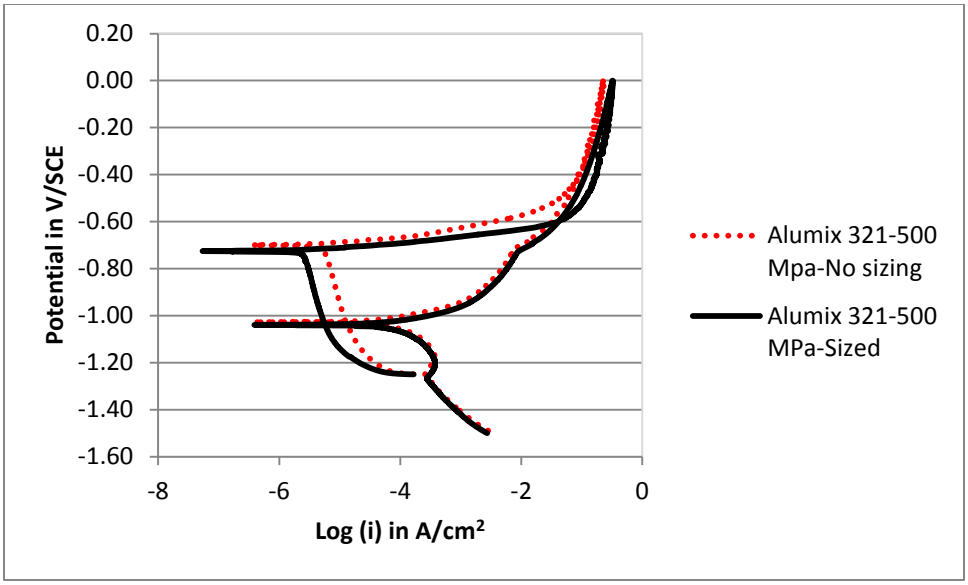

Figure 4-124 Cyclic polarization plot of Alumix 321 PM alloy after sizing at 180 MPa in 3.5 wt% NaCl solution.

4.11.4 *STAIR STEP POLARIZATION (SP)*

In order to study the pitting behaviour at slower scanning rate, stair step polarization was carried out. In this experiment samples pressed at 300 MPa and then sized at 100 MPa were tested. Figure 4-125 shows the variation of current as a function of stair step potential. At the beginning of the scan the potential was very small and almost constant. As the stair potential approaches the corrosion potential value, a sharp increase in current takes place as an indication of the onset of the pitting. Similar to most of the samples tested, the corrosion and pitting potentials were coincident and it is very difficult to distinguish between these two values. However, due to the slower rate and small increment in potential, stair step shows better ability to distinguish between these two values especially in the case of the sized samples. Generally, Alumix 321 PM samples before sizing shows higher pitting potential than the sized samples. The pitting potential of the sized and not sized samples were -0.741 V/SCE and -0.721 V/SCE, respectively.

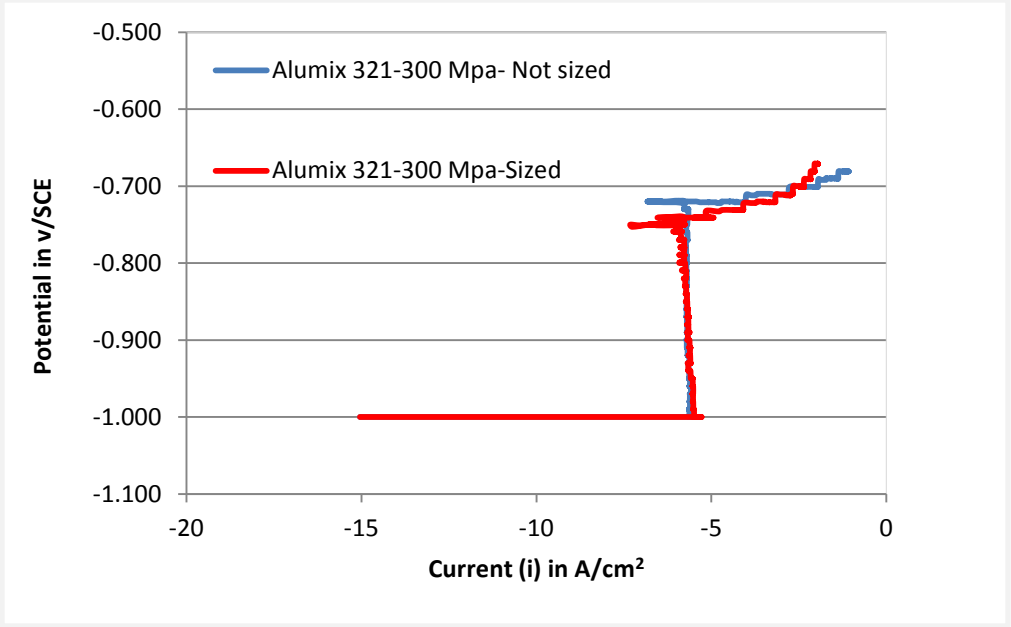

Figure 4-125 Stair step polarization of Alumix 321 in 3.5 wt% NaCl solution before and after sizing.

Figure 4-126 shows the variation of potential and current as a function of time during stair step polarization scan. Dramatic increase in current can be seen at a potential corresponding to pitting. The pitting potential of sized samples was lower than that of not sized ones. This result in agreement with the results obtained from the cyclic polarization plot which shows that Alumix 321 samples before sizing show a higher pitting potential than sized samples. It is worth noting that in all the set of samples, cyclic polarization technique shows that pitting potential of the Alumix 321 before sizing is better than those after sizing. Actually, the amount of deformation created in this treatment is not as high as that created during the other surface modification techniques such as rolling and swaging. This makes it difficult to relate these results to the deformation effect. Two factors may over shadow the sized samples results, the first is the heat treatment condition and the second is the sizing process conditions. Sizing was performed on the as sintered samples which is the T1 condition, all the rest of the samples were tested in the as heat treated T6 condition. The other possible reason is the affect of lubrication solution that was used to facilitate the sizing process. Despite

the cleaning step that was performed, it is highly likely that this solution may entrap inside the porosity and affect the electrochemical reactions inside those pores.

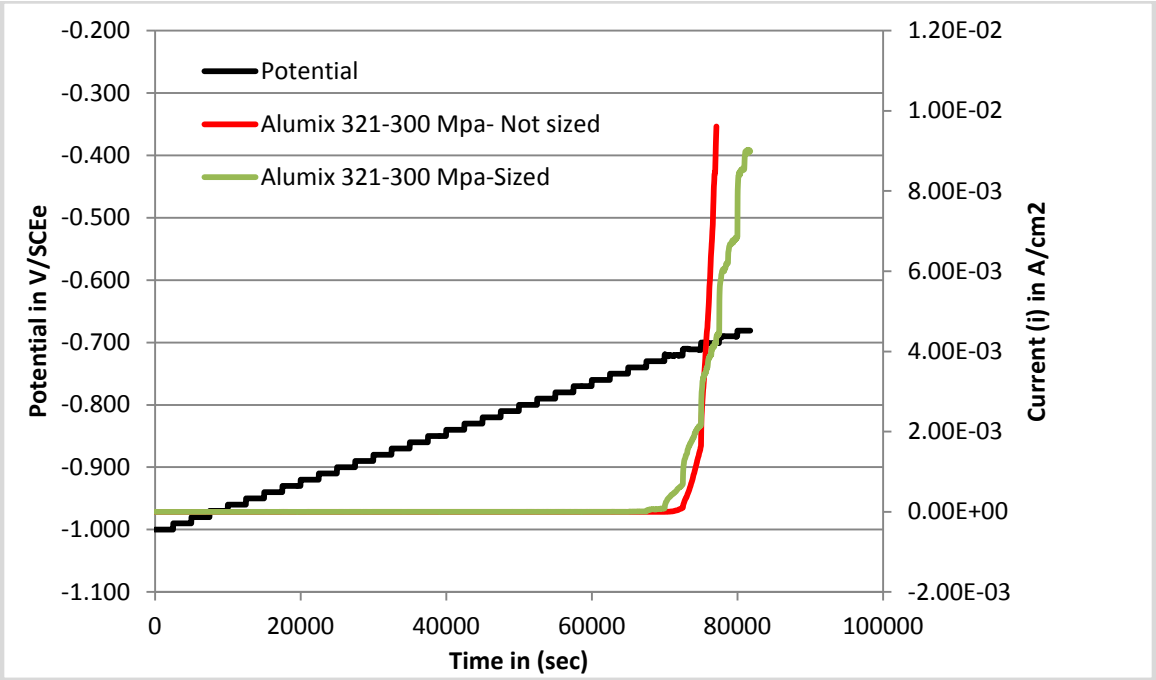

Figure 4-126 Variation of potential and current as a function of time during stair step polarization of Alumix 321 in 3.5 wt% NaCl solution.

4.11.5 *CHARACTERIZATION OF SIZED CORRODED SAMPLES*

Corroded Alumix 321 samples that were sized at different conditions were investigated using optical and scanning electron microscope. Figure 4-127 shows an optical micrograph of corroded of Alumix 321 samples pressed at 100 MPa and sized at 50 MPa. The effect of sizing is not very clear mainly because the low pressure used. However, more round corrosion spots can be seen in the sized samples which can be attributed to the effect of sizing treatment on the interconnected porosity.

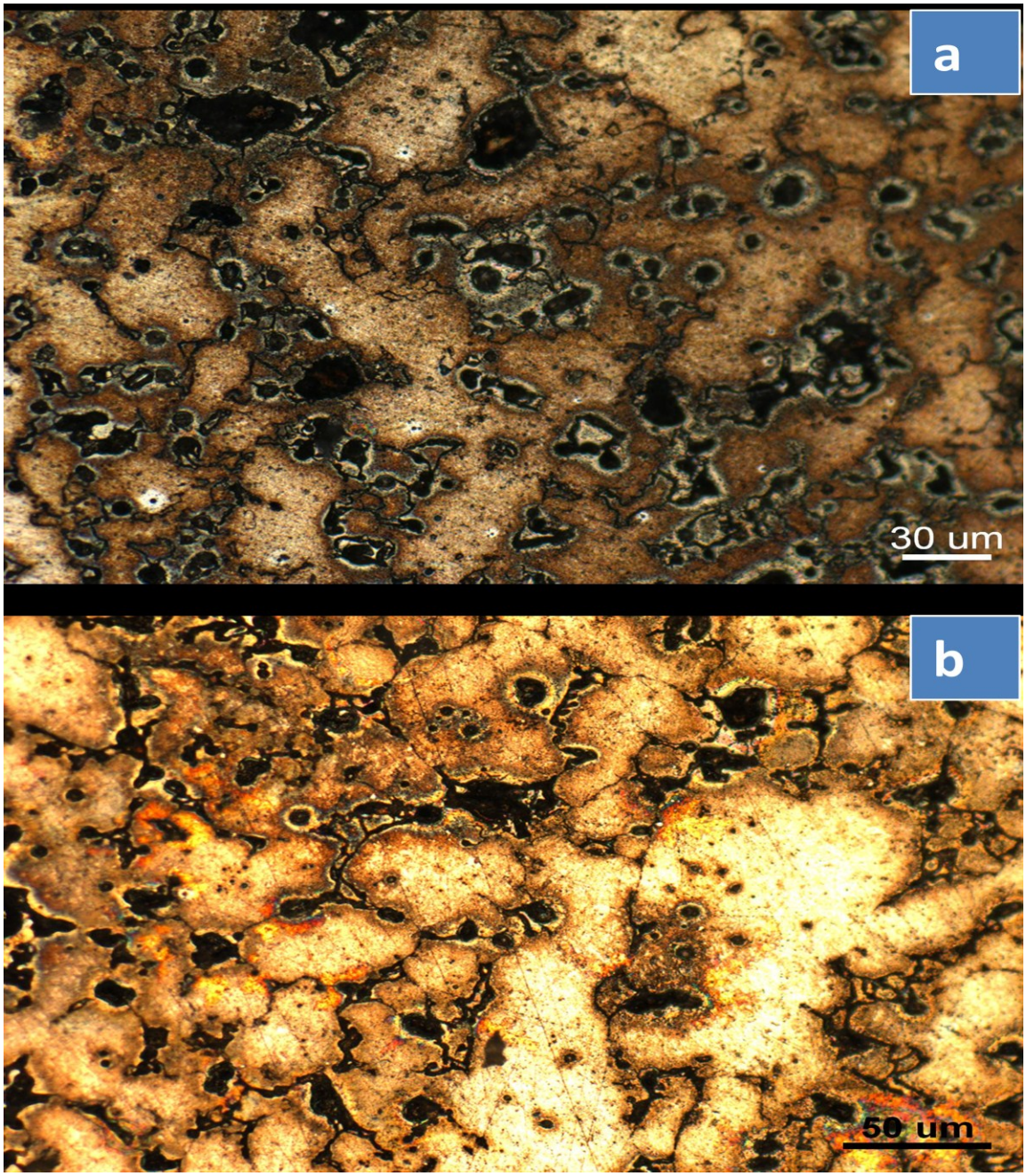

Figure 4-127 Corroded surafce of Alumix 321 PM alloy a) As sintered b) As sintered and sized.

Figure 4-128 shows a higher magnification optical micrograph of Alumix 321 sample pressed at 100 Mpa and then sized at 50 MPa. The Figure shows that the corrosion attack is quite severe and appear clearly in the interconnected porosity. Thsee interconnected porosity is a common feature of all samples pressed at lower pressure (100 MPa). It can be concluded that the sizing treatment was not able to make a remarkable change in the nature of these pores. However, closing some paths in the inteconnected pores is possible.

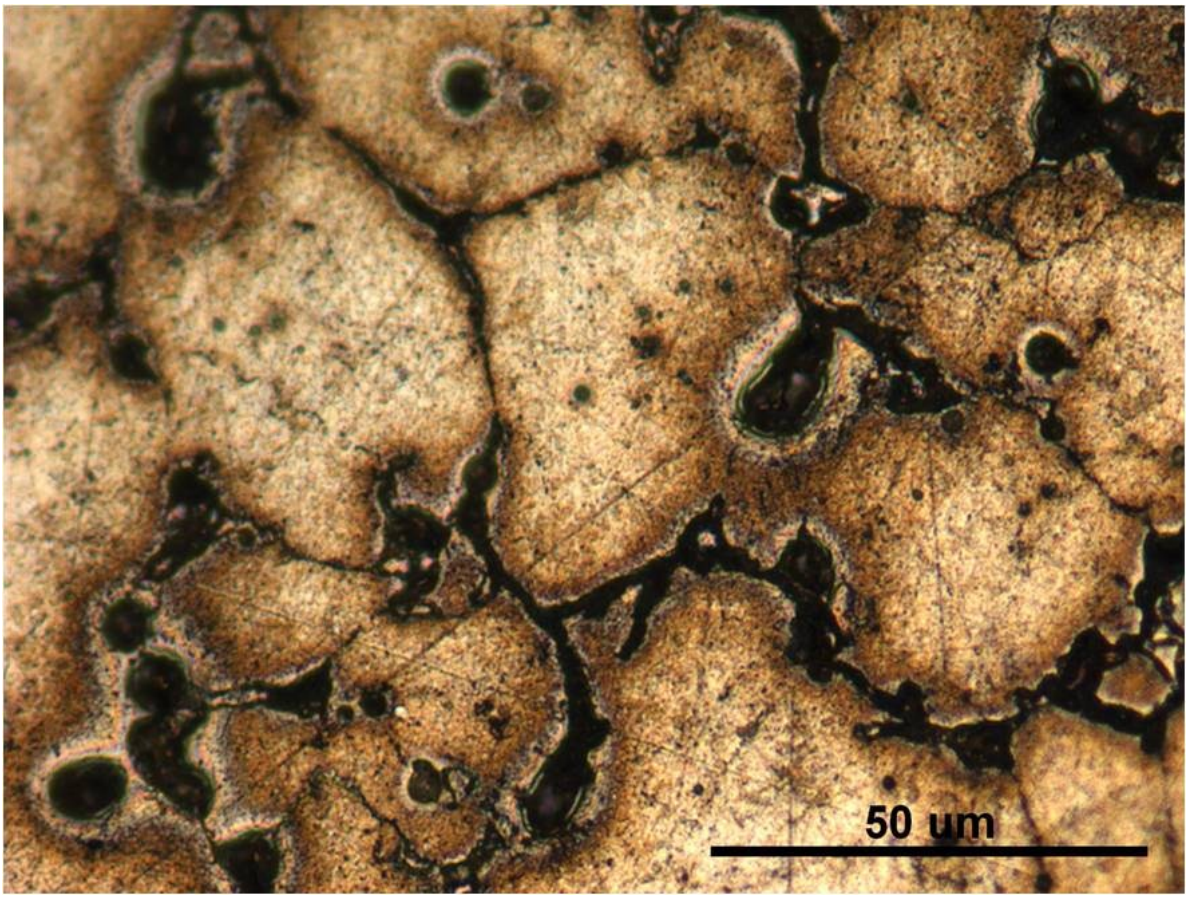

Figure 4-128 Optical micorgraph of corroded Alumix 321 PM alloy after sizing.

Compared to the samples pressed at lower pressure, the corroded samples that were pressed at 300 MPa and sized at 100 MPa show different type of attack after corrosion. Most of the corrosion attack takes place inside the round closed pores and only small evidence of corrosion inside the interconnected pores can be seen. This observation is in agreement with the higher density values of samples pressed at 300 MPa compared to those samples pressed at 100 MPa. Samples pressed at higher pressure show more round closed type of pores compared to interconnected pores in the case of samples pressed at lower pressure. In addition to pitting corrosion that takes place inside the grains, other evidence of corrosion at grain boundary can be seen in the samples pressed at 300 MPa. Figure 4-129 shows the corroded surface of Alumix 321 PM sized samples pressed at different pressures.

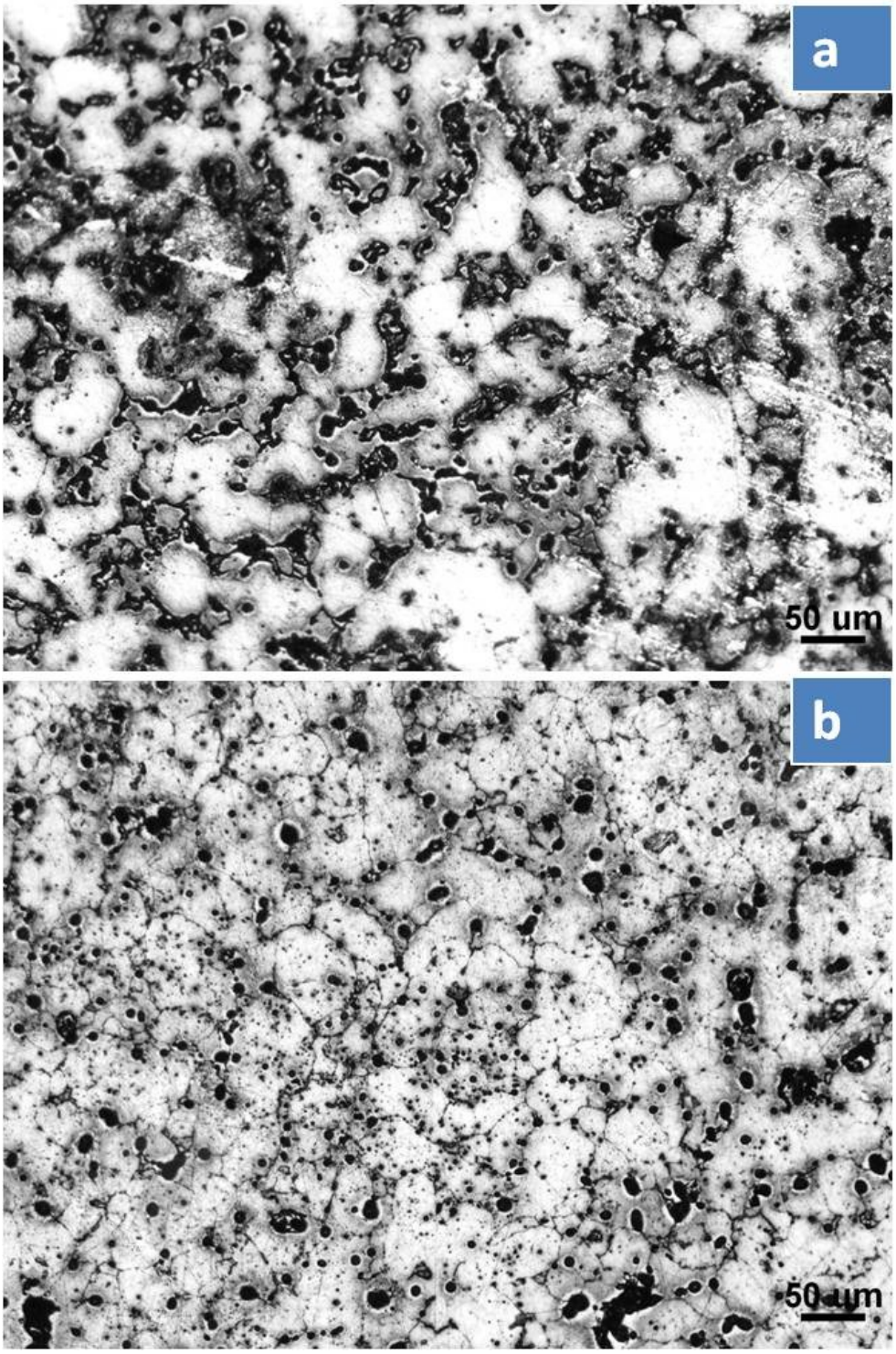

Figure 4-129 Optical micrograph of coroded Alumix 321 PM alloy after sizing at diiferent pressures. a) pressed at 100 MPa and sized at 50 MPa, b)pressed at 300 MPa and sized at 100 MPa.

Samples pressed and sized at higher pressure show more evidence of corrosion attack in the closed pores and less appearance of interconnected porosity attack. The samples pressed at 500 MPa and then sized at 180 MPa show that most of the corrosion attack appears to happen inside the grains as a result of better densification conditions that facilitate reducing the existence of both closed and interconnected porosity. However, corrosion attack can be seen inside some retained round pores. The corrosion morphology of the sample pressed at 500 MPa and then sized at 180 MPa is shown in Figure 4-130.

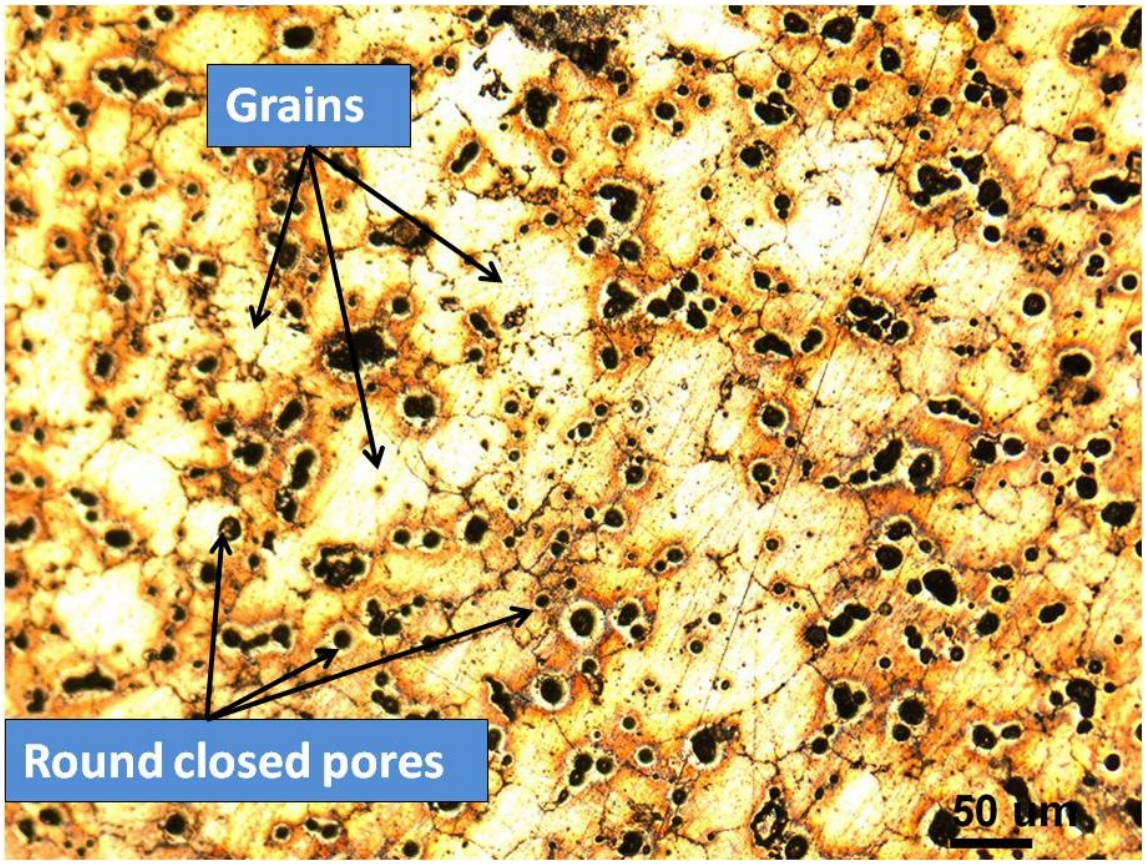

Figure 4-130 Optical micrograph of Alumix 321 PM alloy pressed at 500 MPa and sized at 180 MPa.

Figure 4-131 shows the optical micrograph of the corroded surface of Alumix 321 samples pressed at 100, 300, and 500 MPa and then sized at 50, 100, 180 MPa, respectively. The samples pressed and sized at lower pressure (pressed at 100 MPa and sized at 50 MPa) illustrates a corrosion attack inside the interconnected pores, the attack was sever up to the point where it outlined some grains completely. As the pressing and sizing pressure increases (pressing at 300 MPa, sized at 100, and pressing at 500 MPa, sized at 180 MPa), more signs of corrosion attack inside closed porosity and more evidence of pitting inside the grains and not along the grain boundaries as it was the case in samples pressed and sized at lower pressure.

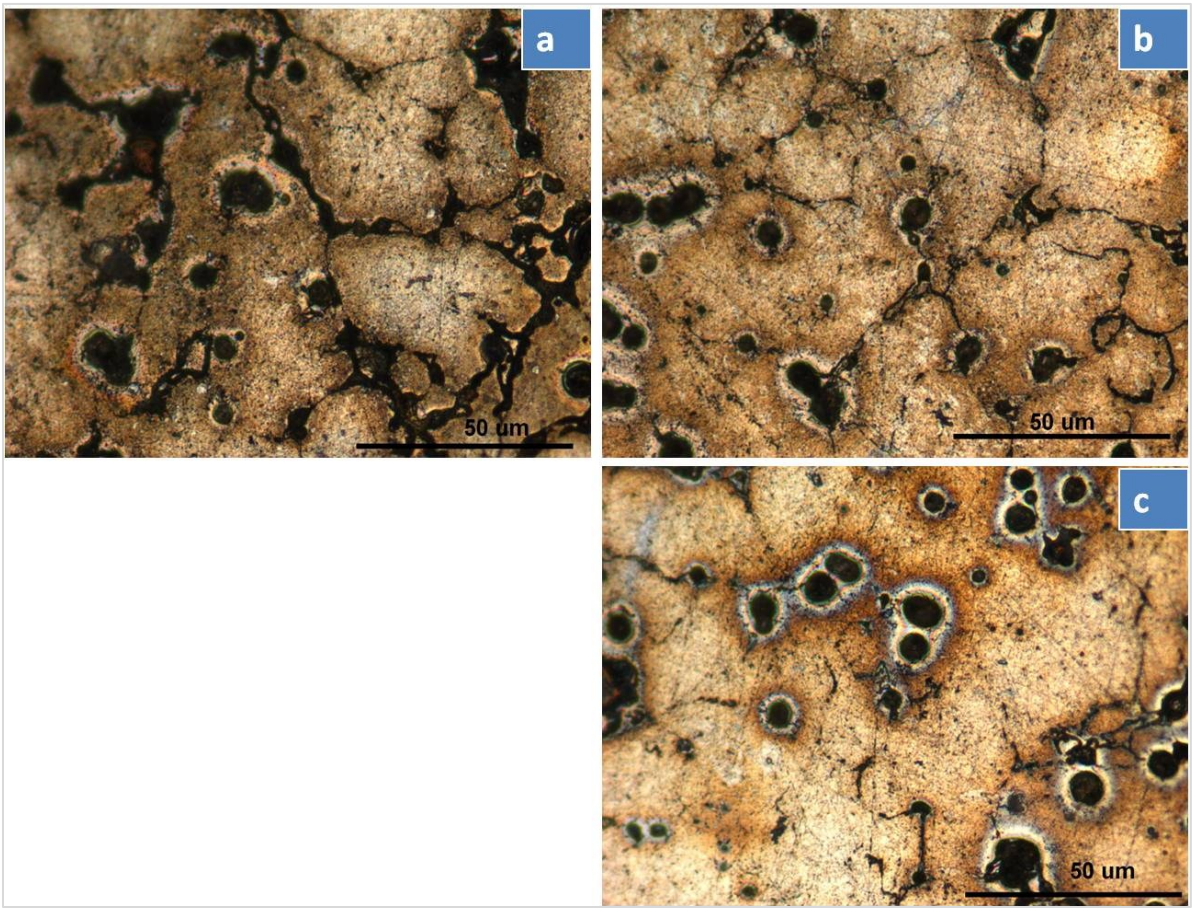

Figure 4-131 Optical micrograph showing the corroded surafce of Alumix 321 PM alloy in 3.5 wt% NaCl solution a) pressed at 100 and sized at 50 Mpa, b) pressed at 300 and sized at 100 MPa, c) pressed at 500 MPa and sized at 180 MPa.

Scanning electron microscope was used to study the corrosion attack aiming to help identify the corrosion mechanisms exist. Figure 4-132 shows an SEM micrograph of the Alumix 321 PM sample pressed at 500 MPa and then sized at 180 MPa. The main type of the attack is the pitting corrosion. Most of the corrosion attack appears in a form of hemispherical pits which initiated most likely inside the grains. Higher magnification SEM microscopy was used to identify the possible corrosion mechanisms. Figure 4-133 shows the SEM images of Alumix 321 PM sample pressed at 500 MPa and then sized at 180 MPa. It is obvious that pitting exist as a main corrosion mechanism. Some pits formed around iron rich particle which is the same mechanism observed in other wrought and PM samples. In addition to pitting, intergranular corrosion is noticeably seen. It was observed that the intergranular corrosion is not as severe as in the case of samples pressed at lower pressure. The higher pressure used in pressing and later in sizing helps to produce more dense structure and less interconnected pores.

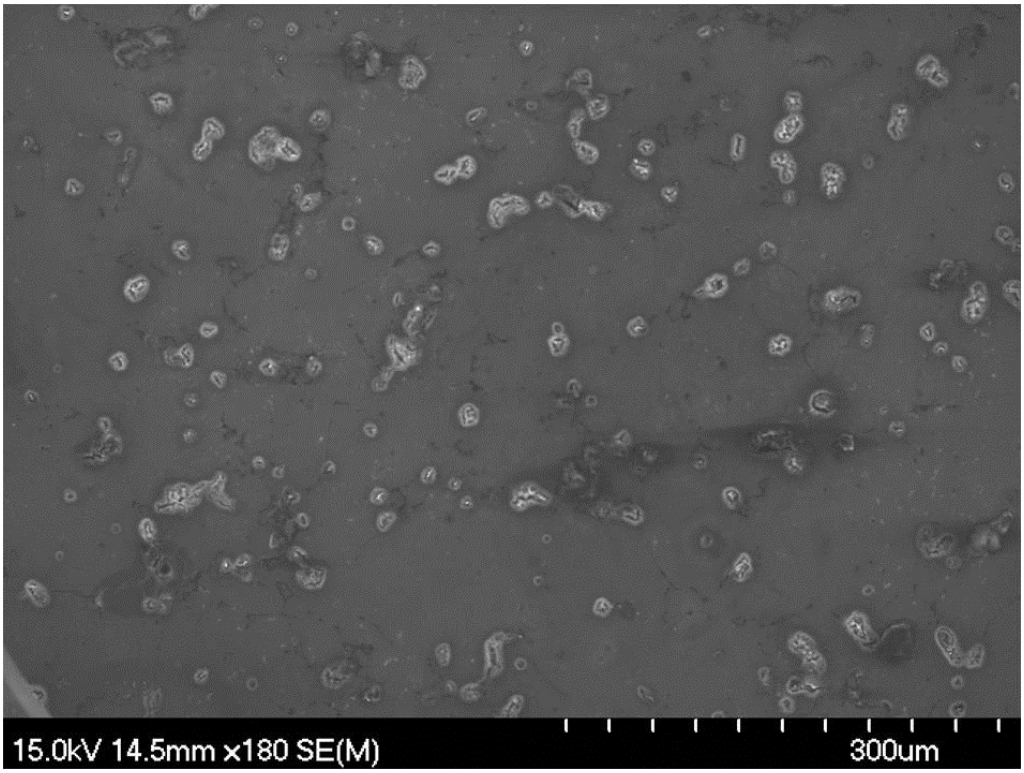

Figure 4-132 SEM micrograph of the corroded surface of Alumix 321 PM alloy after sizing.

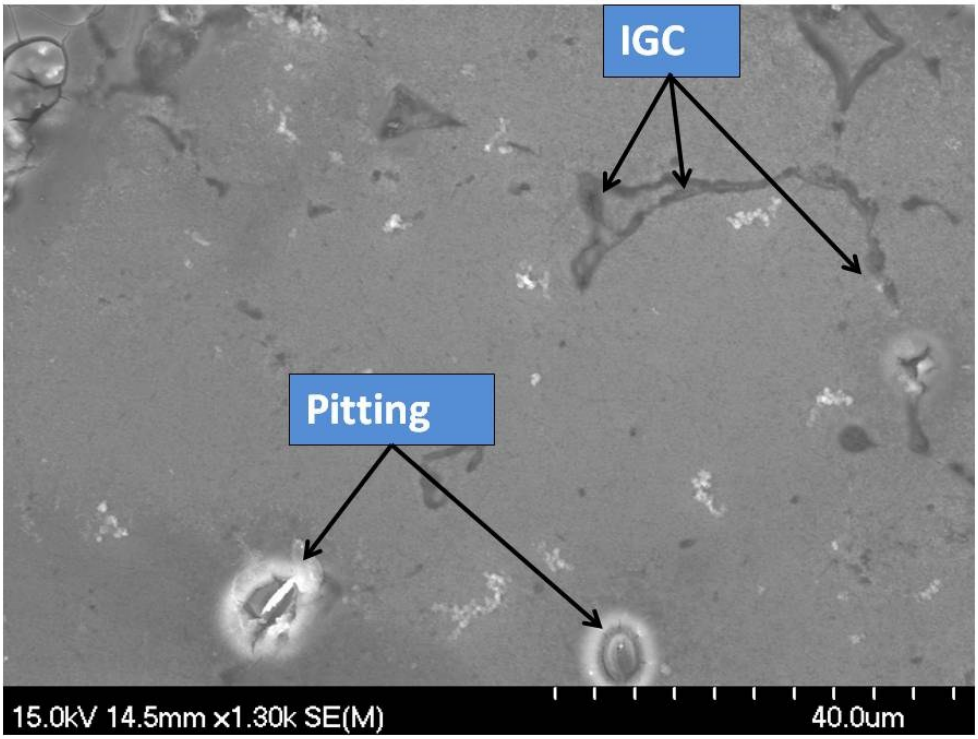

Figure 4-133 SEM micrograph showing corrosion mechanisms observed in sized Alumix 321 PM alloy (pressed at 500 MPa, sized at 180 MPa) in 3.5 wt% NaCl solution.

4.12 EFFCET OF RESIN IMPREGNATION

Resin impregnation was used as a surface modification technique for two purposes, the first purpose is to close off open pores and the second is to get an idea about the real exposed surface area that remains after resin impregnation. Prior to corrosion experiments, Alumix 321 powder was pressed at 100 MPa, sintered at 630 °C, the samples then were ground, polished, cleaned and then epoxy resin was applied. Image analysis technique was used to measure the area that was filled with a resin and consequently, the area that is exposed to the saline solution.

4.12.1 *OPEN CIRCUIT POTENTIAL (OCP)*

Alumix 321 PM samples used in this experiment were subjected to the corrosion experiments after they were pressed, sintered and then impregnated. Figure 4-134 shows the open circuit potential of Alumix 321 before after resin impregnation. Alumix

321 PM samples before resin impregnation show more negative and continuous drop in potential. It was showed before that samples pressed at 100 MPa have lower density than samples pressed at higher pressure. Small density values resulted in interconnected porosity and large surface area exposed to the solution. Additionally, the time needed for the saline solution to penetrate in the samples is very long which probably explains why the equilibrium time was difficult to be achieved. At the end of the experiment the OCP recorded for this sample is -0.883 V/SCE.

Resin impregnated sample show less negative OCP. The OCP of the resin impregnated Alumix 321 PM samples recorded to be -0.749 V/SCE. The less negative potential of the impregnated samples is a good sign that the impregnation processes was successful in closing off most of the pores and reduce the area exposed to the solution. Stable OCP can be clearly seen from the variation of potential as a function of time.

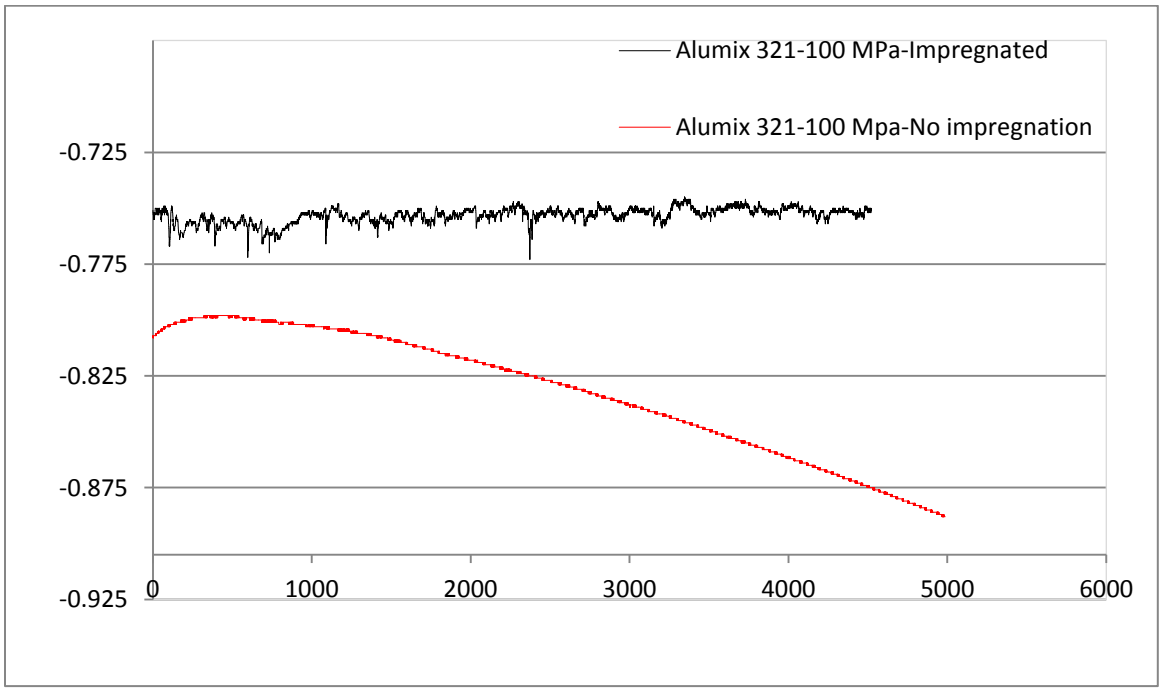

Figure 4-134 OCP variation of Alumix 321 PM alloy before and after resin impregnation.

4.12.2 *TAFEL EXTRAPOLATION (TE)*

Tafel extrapolation technique was used to measure the corrosion rate of Alumix 321 PM samples before and after resin impregnation. Figure 4-135 shows the effect of resin impregnation on the corrosion current of Alumix 321 in 3.5 wt% NaCl solution. Alumix 321 PM sample before resin impregnation shows more negative corrosion potential and gradual increase in potential for both the anodic and the cathodic part of the curve. The anodic part of the curve shows a gradual increase in potential until certain potential was reached. The potential at which the dramatic increase in current appears is defined as pitting potential. Results show that the effect of impregnation is clearly visible on Alumix 321 PM alloy. The main observation of the impregnated sample is the sharp increase in current that takes place at the corrosion potential. It is the same trend that was observed for Alumix 321 PM samples pressed at higher pressure. The conclusion here is that resin impregnation has affected the samples the same way the higher pressure has done which is mainly reducing interconnected porosity and produces more dense structure.

In order to get a better idea on how the surface area affects the corrosion current, image analyzing technique was used to measure the pore area fraction of the impregnated samples. The area fraction of pore was 5.26%; the area was then subtracted from the total surface area and used as the effective surface area during the corrosion experiments. Tafel extrapolation technique was used to evaluate the effect of resin impregnation on the corrosion current of Alumix 321 PM alloy. The corrosion current decreases from 7.0228E-06 A/cm^2 before impregnation to 2.5786E-06 A/cm^2 after impregnation.

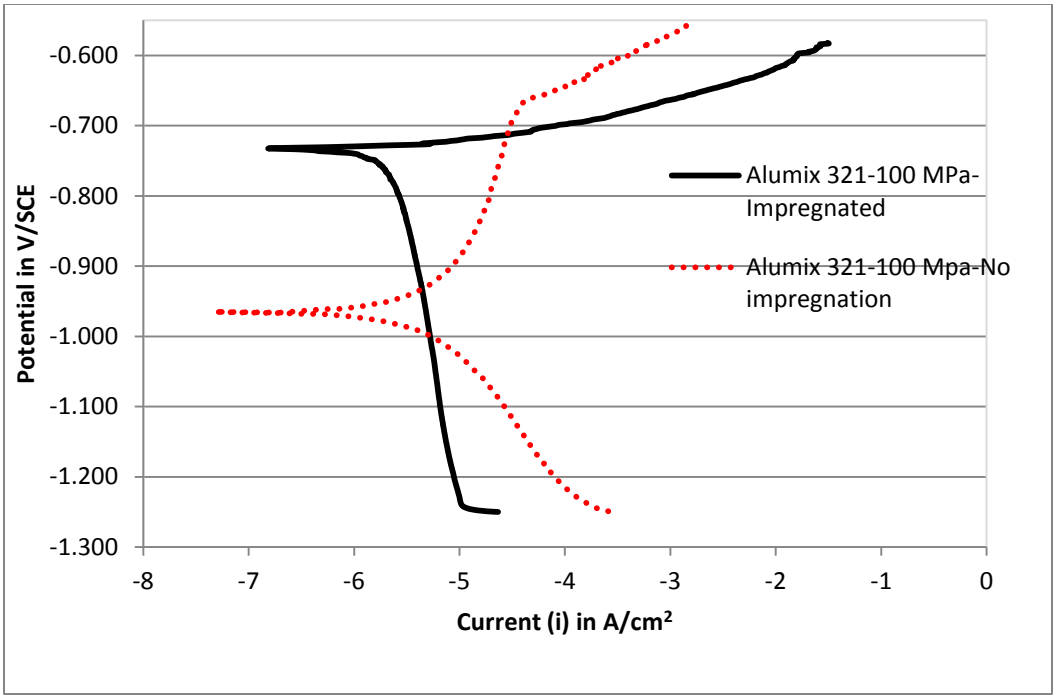

Figure 4-135 Effect of resin impregnation on Tafel plot of Alumix 321 PM alloy in 3.5 wt% NaCl solution.

4.12.3 *CYCLIC POLARIZATION (CP)*

Figure 4-136 shows the effect of resin impregnation on the cyclic polarization plot of Alumix 321 PM alloy in 3.5 wt% NaCl solution. Alumix 321 sample before impregnation shows more negative corrosion potential. The anodic current increases gradually before it is sharply rose at pitting potential. The pitting potential recorded was -0.677 V/SCE. The behaviour of the Alumix 321 PM sample after resin impregnation was different. The anodic current part of the plot shows sharp increase at a potential coincident with the corrosion potential. The potential associated with this sharp increase in current is defined as a pitting potential and recoded to be -0.739 V/SCE. This behaviour is similar to the behaviour observed in the Alumix 321 samples that were pressed at higher pressure. Metallographic analysis of the resin impregnated samples provided strong evidence that the resin was impregnated inside the pores. Resin Impregnation closes off noticeable percentage of pores and reduces the effective exposed surface area. The other characteristic potential that was recorded is a repassivation potential. Alumix 321

samples before impregnation shows more positive potential than the samples after impregnation. The repassivation potential recorded to be -1.017 V/SCE and -1.057 V/SCE for Alumix 321 samples before and after impregnation, respectively.

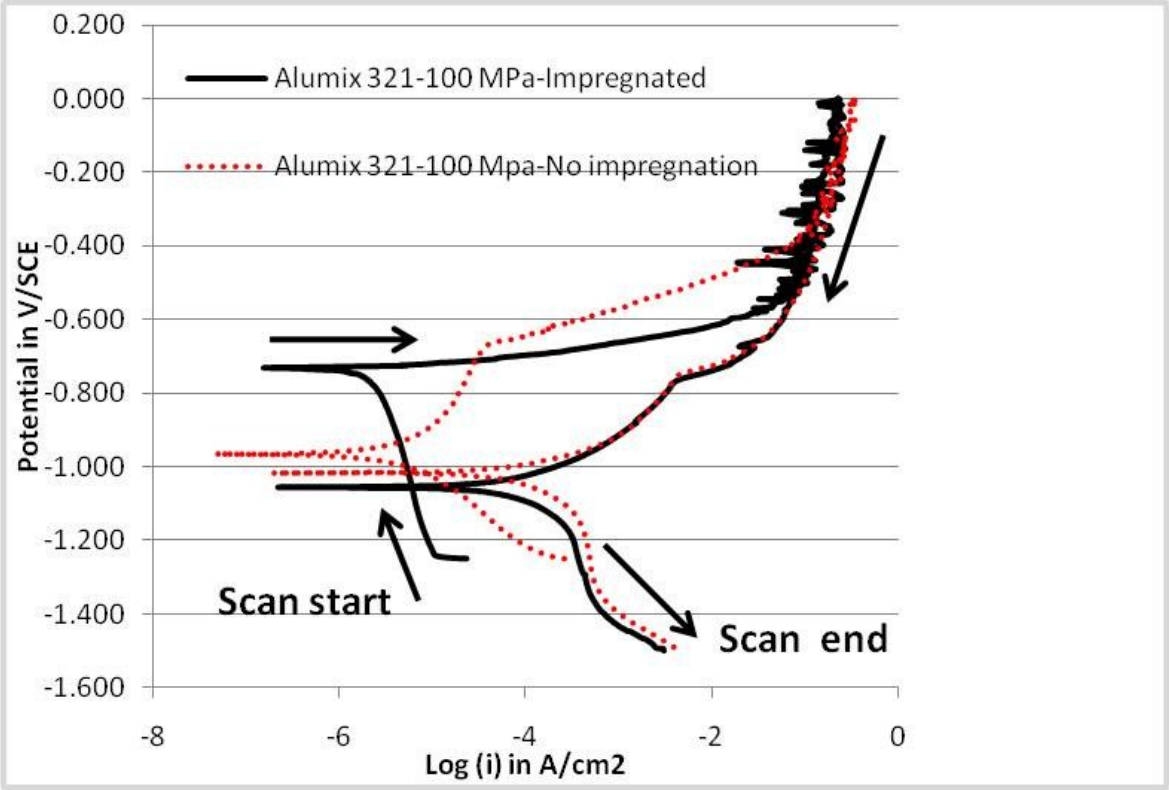

Figure 4-136 Effect of impregnation on the cyclic polarization plot of Alumix 321 PM alloy in 3.5 wt% NaCl solution.

4.12.4 *CHARACTERIZATION OF RESIN IMPREGNATED CORRODED SAMPLES*

Impregnation of the Alumix 321 samples was successfully performed. Optical and scanning microscopy shows that a large portion of pores were impregnated successfully. Figure 4-137 shows an optical micrograph of the Alumix 321 samples pressed at 100 MPa after impregnation. It is clear that the resin impregnated effectively and was very recognizable especially for interconnected and large pores. However, the resin was difficult to be detected in small pores.

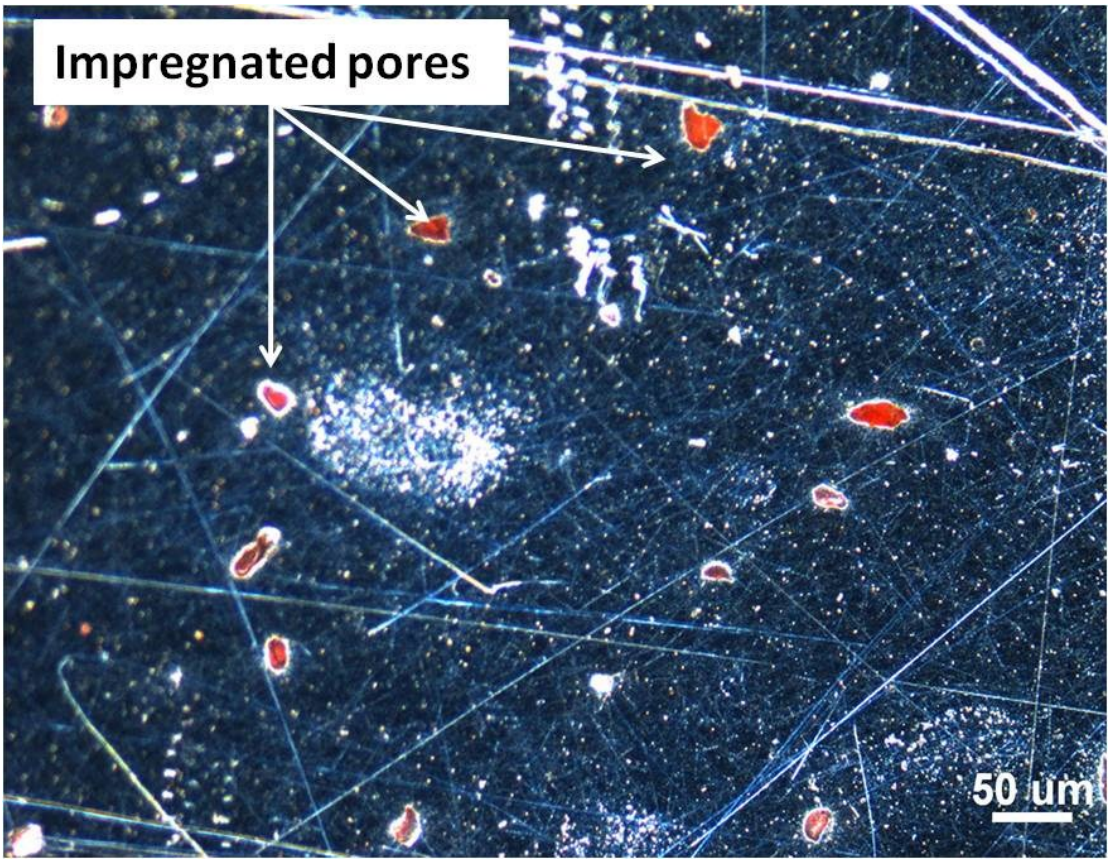

Figure 4-137 Dark field illumination optical micrograph of impregnated Alumix 321 PM alloy.

Figure 4-138 shows an optical micrograph of the corroded Alumix 321 PM sample. The image shows the corrosion product, base metal and impregnated pores. The image shows clearly that the interconnected pores in the base metal were impregnated by the resin. There was also an area that was partially attacked due to incomplete exposure to the solution. The nature of the corrosion attack in this region shows that most of the corrosion attack takes place at the interconnected porosity, and as a result some grains were left insulated. Additionally, the resin can be seen clearly around some corroded grains. The corrosion product shows a porous and spongy form and signs of resin residual after corrosion.

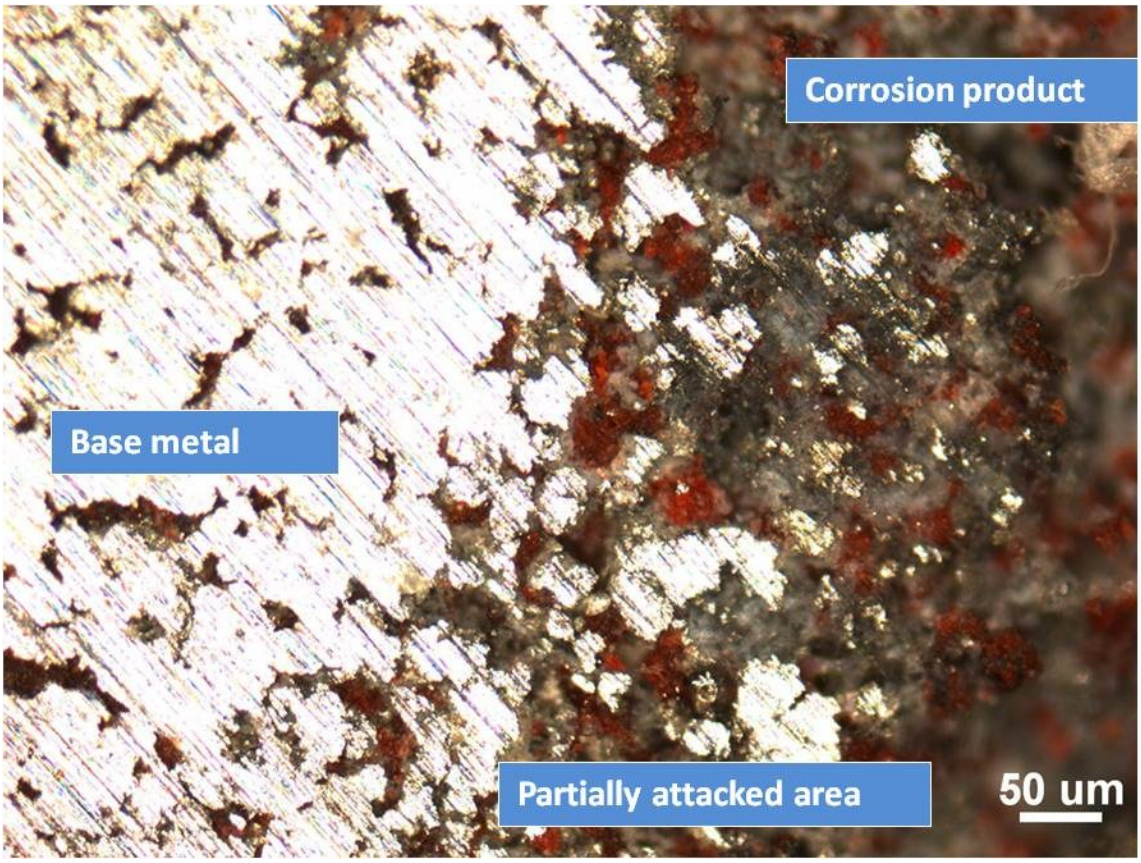

Figure 4-138 Optical micrograph of resin Impregnated Alumix 321 alloy after exposure to 3.5 wt % NaCl solution.

Examining the corroded samples shows that most of the corrosion takes place in the interconnected porosity. Some grains were outlined with a corrosion product and form a tunnel like attack. The severity of the corrosion attack was noticeably less when those interconnected were effectively impregnated. Figure 4-139 shows the corrosion morphology of Alumix 321 PM alloy in 3.5 wt% NaCl solution. Figure 4-140 illustrates the corroded surface of Alumix 321 alloy after the exposure to saline solution. It is unmistakably seen that the resin that appears as a red colour was impregnated and helps to resist the corrosion attack. Despite the presence of deep spots where the corrosion was very severe, some Islands remain almost pristine and covered with the resin. It is clearly seen that the resin was mixed with the corrosion product and covers some areas after the metallic matrix was attacked and eventually corroded. It is highly

likely that the metallic matrix was preferentially corroded and that is why the resin was left behind mixed with the corrosion product. Impregnated samples show a similar corrosion mechanism to the samples before impregnation as shown in Figure 4-141. Knowing that these set of samples were pressed at relatively lower pressure (100 MPa), the interconnected pores which are predominant are the preferred sites for crevice corrosion. Microstructural examination shows that a noticeable amount of those pores were impregnated and consequently isolated from the solution, which in turn gave a lower corrosion rate as was confirmed using the potentiodynamic polarization techniques.

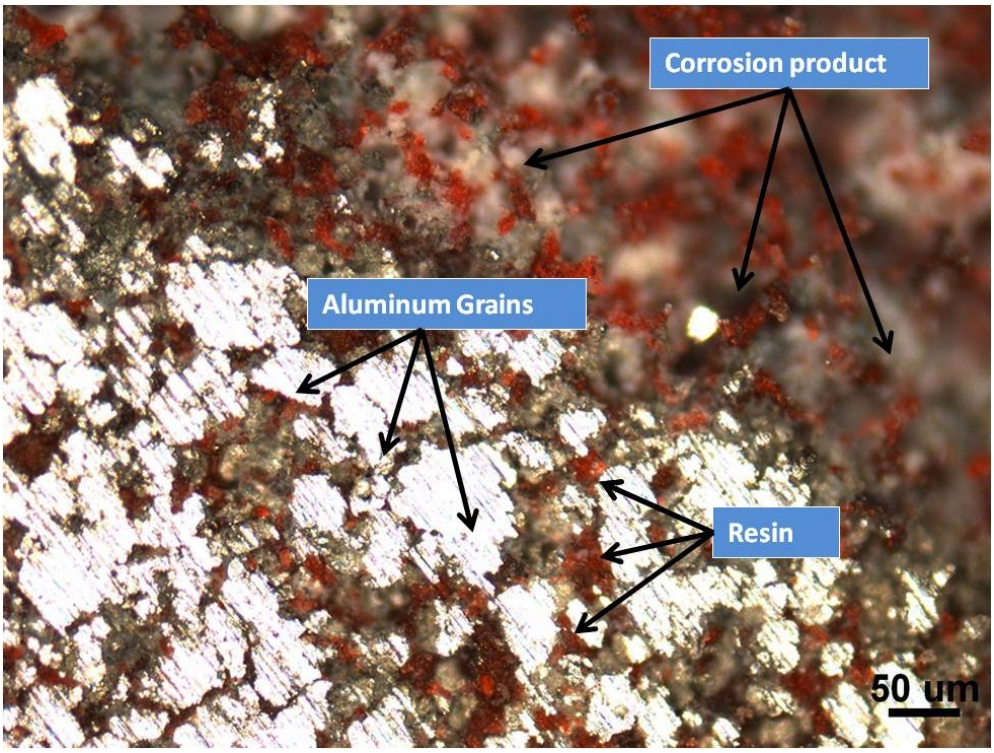

Figure 4-139 Corroded surface of Alumix 321 PM alloy in 3.5 wt% NaCl solution.

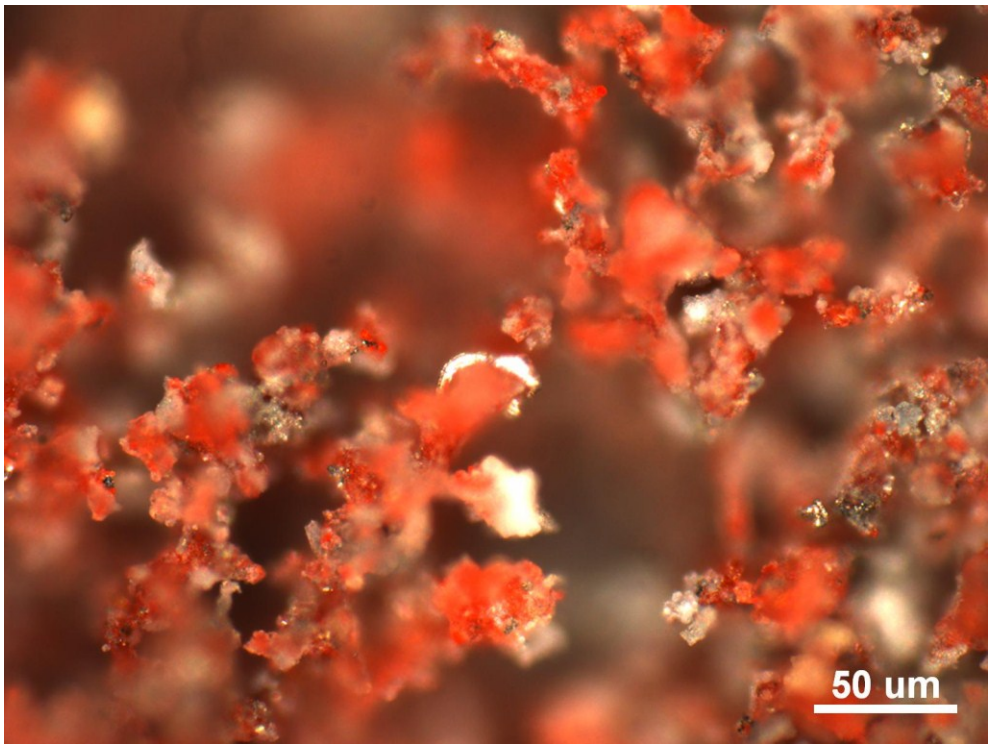

Figure 4-140 Dark field illumination optical micrograph showing the corrosion product of resin impregnated Alumix 321 PM alloy in 3.5 wt% NaCl solution.

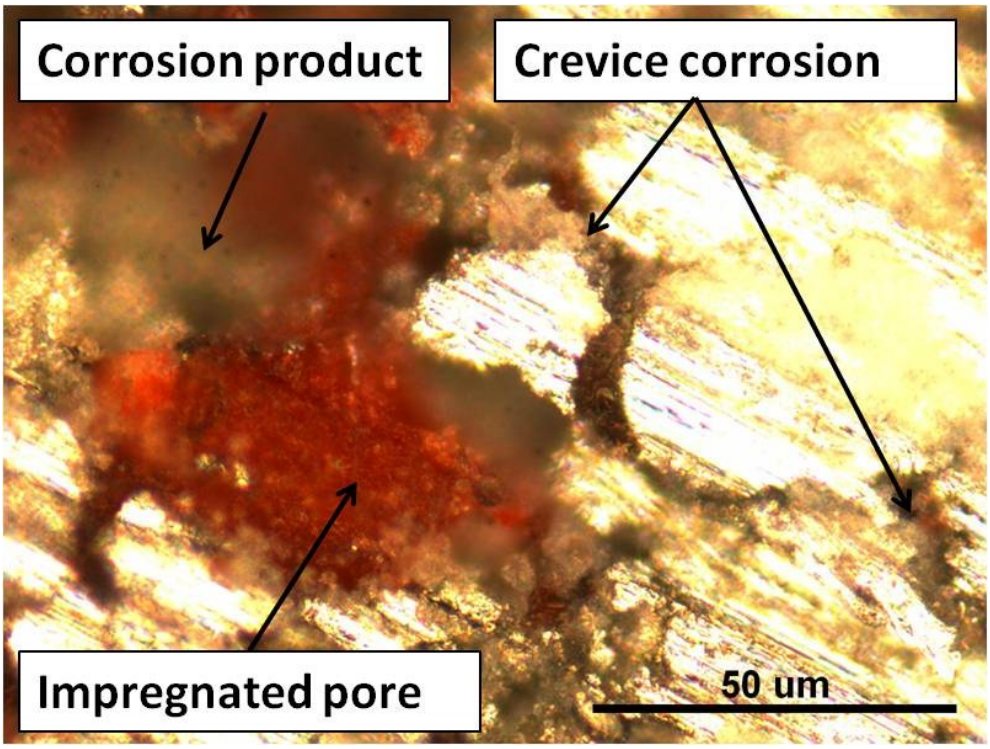

Figure 4-141 Optical micrograph of the corroded surafce of Alumix 321 PM alloy in 3.5 wt% NaCl solution.

SEM was used to analyze the surface of impregnated Alumix 321 after corrosion. Figure 4-142 shows a corroded surface of impregnated Alumix 321 PM sample in 3.5 wt% NaCl solution. The Figure shows an area that was totally corroded which is spongy and porous. This area is the exposed area during the corrosion experiment. This area is the same area that was presented in Figure 4-140 where the matrix is severely attacked by the solution leaving behind corrosion product mixed with the resin. The second area is the base metal. Base metal was not attacked and shows clearly the effect of the resin impregnation. The impregnated pores appear white color due to the charging effect. Partially attacked area is the area where there was limiting exposure to the solution. It shows some grains were attacked at the grain boundaries. In most of the cases grain boundaries were preferred sites for corrosion due to the presence of interconnected porosity which work as preferred sites for crevice corrosion. Figure 4-143 shows a higher magnification SEM image of the partially corroded area of the resin impregnated Alumix

321 PM alloy. It is very clear that the resin was impregnated inside some pores. However, not all of the pores were successfully impregnated. Evidence of corrosion inside some interconnected pores can be clearly seen. Other important observation is the evidence of corrosion at the interface between the resin and the metallic matrix. It is worth noting here that this resin was designed and manufactured for samples cold mounting and it was used in this research to examine how the impregnation can be used as a surface modification technique. Some physical and chemical consideration need to be evaluated before using a resin for such an application, these considerations is out the scope of this research.

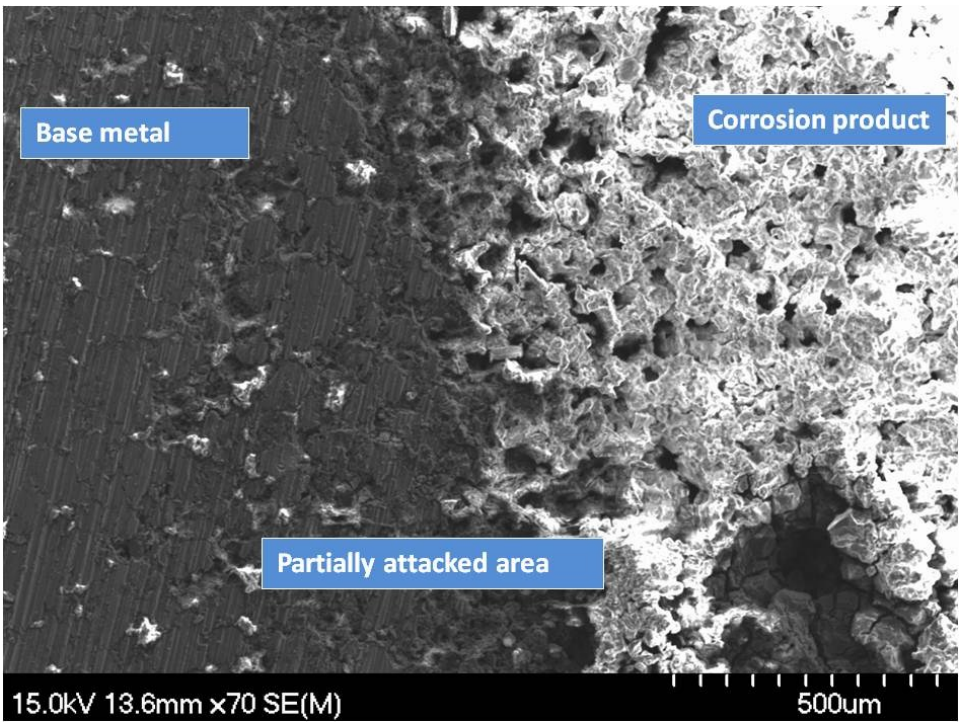

Figure 4-142 SEM of the corroded surafce of resin impregnated Alumix 321 in 3.5 wt% NaCl solution.

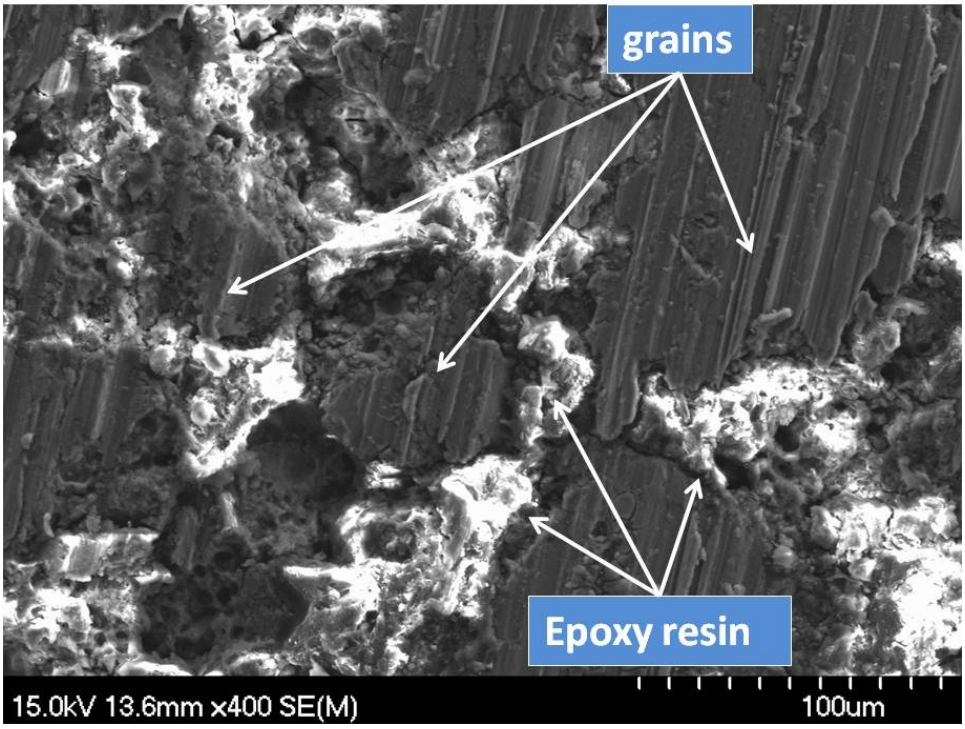

Figure 4-143 Higher magnification SEM micrograph showing the partially attacked area of resin impregnated Alumix 321 PM alloy.

4.13 SUMMARY OF CORROSION BEHAVIOUR OF ALUMIX 321 PM ALLOY AND AA6061 WROUGHT ALLOY

From the results obtained it can be concluded that all post sintering treatments applied were effective in reducing the corrosion current and hence improving the corrosion resistance. However, the effect of these treatments on the corrosion potential was different. Table 4-10 summarizes the corrosion results on both wrought and PM alloys.

Table 4-10 Corrosion parameters of Alumix 321 PM alloy and AA6061 wrought alloy in 3.5 wt% NaCl solution.

Corrosion parameter / Material	E_{corr}	E_{pit}	E_{rep}	E_{SS}	E_{ocp}
AA6061-T6	-0.714	-0.714	-1.039	NA	-0.736
Alumix 321-100 MPa	-0.971	-0.704	-1.023	-0.73	-0.874
Alumix321-200 MPa	-0.737	-0.717	-1.031	-0.73	-0.76
Alumix 321-300 MPa	-0.701	-0.701	-1.037	-0.73	-0.747
Alumix 321-400 MPa	-0.72	-0.702	-1.031	-0.73	-0.748
Alumix 321-500 MPa	-0.717	-0.717	-1.031	-0.73	-0.754
Alumix 321-hot swaged	-0.946	-0.726	-1.056	-0.731	-0.895
Alumix 321- hot swaged	-0.745	-0.745	-1.065	-0.72	-0.765
Alumix 321-not rolled	-0.74	-0.74	-1.036	-0.73	-0.758
Alumix 321-hot rolled	-0.737	-0.737	-1.039	-0.73	-0.756
Alumix 321-500-un peened	-0.719	-0.716	-1.05	-0.711	-0.753
Alumix 321-500-peened	-0.762	-0.716	-1.05	-0.69	-0.769
Alumix 321-100-no impregnation	-0.966	-0.677	-1.017	NA	-0.883
Alumix 321-100-impregnated	-0.739	-0.739	-1.057	NA	-0.749
Alumix 321-300-no sized	-0.698	-0.698	-1.032	-0.721	-0.735
Alumix 321-300-sized	-0.761	-0.761	-1.032	-0.741	-0.776
Alumix 321-500-no sized	-0.702	-0.702	-1.028	NA	-0.748
Alumix 321-500-sized	-0.728	-0.728	-1.038	NA	-0.772
Alumix 321-100-no sized	-1.023	-0.876	-0.995	NA	-0.923
Alumix 321-100-sized	-0.876	-0.788	-1	NA	-0.878

CHAPTER 5 CONTRIBUTION TO ORIGINAL THOUGHT

The needs for new materials that meet certain requirements make it necessary to develop new alloys. One of the growing industries is the powder metallurgy. Strict and tight environmental regulations make it necessary to develop new materials with light weight and good properties. Aluminum and aluminum alloys are widely used in structural, automotive, and aerospace industry. Aluminum alloys produced by Powder metallurgy technique are competing with traditionally produced aluminum alloys. One of the well known aluminum alloys is the Al-Mg-Si which has moderate mechanical properties but good corrosion resistance. In addition to the processing parameters, corrosion behaviour of this system prepared by powder metallurgy technique needs to be evaluated.

As a new area of research, processing and corrosion behaviour of Alumix 321 PM alloy was studied in this research. Different routes of production technique were used and the effect of these different routes on some mechanical and corrosion behaviour was evaluated. The main contribution in this research is the study on how different processing and surface modification techniques affect mechanical and corrosion properties of this alloy. There is controversy in the literature about the corrosion performance of aluminum powder metallurgy alloys. In this research, some concepts such as the corrosion mechanisms, importance of the real surface area, and scanning rate were addressed as important factors when we test or use aluminum powder metallurgy alloys.

The other main contribution is the use of surface modification techniques to improve the corrosion resistance of aluminum powder metallurgy alloys. Effect of shot peening on corrosion behaviour of aluminum powder metallurgy alloys has never been published before. The other promising technique is the resin impregnation. Although this technique is known for corrosion control, using electrochemical techniques and microstructural analysis to evaluate the effect of impregnation on corrosion resistance is one of the main contributions of this research.

Effect of post sintering techniques such as rolling, extrusion, and sizing are rarely presented in previous work. Working parameters of these treatments were assigned and their impacts on microstructure and corrosion behaviour were studied.

CHAPTER 6 FUTURE WORK

Most of the previous work that was done on aluminum powder metallurgy in general and specifically on Alumix 321 PM alloy has primarily focused on characterization and developing the early stages of PM processing, such as powder characterization, compaction and sintering. In this research, different post sintering techniques were applied. The great impact that several post sintering techniques that were used have had on the properties of the Alumix 321 PM alloy suggests studying these techniques in more details.

The issue of how the pores affect the corrosion performance of Alumix 321 PM alloy was addressed. For more understanding, good characterization of porosity and its affect need to be studied. Using the FIB technique is recommended. This technique will enable to cut sections in isolated pores, interconnected pores and grain boundaries and investigate the internal surface before and after exposure to the sodium chloride solution. There is also a need to use a technique for the surface area measurement in order to get representative corrosion parameters.

Shot peening post sintering technique is promising. It is cheap, easy to be applied, and efficient. The main drawback is its effect on the corrosion potential due to the presence of the deformed layer. In our research the intensity was kept constant, operating parameters can be changed to produce different intensities that enable closing off the pores as well as reduce the effect of the deformed layer.

Epoxy resin impregnation found to be effective in reducing the corrosion rate. However, this resin was not designed for this purpose. Testing other types of resins with different chemical and physical properties may lead to better performance of the impregnation processes.

The role of iron containing particles on the corrosion performance was very clear. It is suggested to study the effect of manganese on the corrosion behaviour of this system. Manganese alloys reacts with iron and reduces the tendency of iron to influence the corrosion.

CHAPTER 7 CONCLUSIONS

1. The optimal compaction pressure for Alumix 321 powder was determined to be 500 MPa, resulting in a compact of higher green density and green strength of 2.5768 g/cc, 10 MPa, respectively. The optimal sintering procedure for Alumix 321 consisted of a ramp to 390 °C where the temperature was held for 30 min to remove the lubricant from the compacts. This was followed by heating to 630 °C to sinter for 30 min. The samples were then subjected to a furnace cooling.
2. Disk samples made of Alumix 321 powder pressed at 500 MPa and sintered at 630 °C show a linear relationship between pressure and sintered density, while this relation was not clear in the case of TRS samples. Disk samples made of Alumix 321 powder and pressed at 100 MPa produced samples with density 2.57150 g/cc which is 95.6% of the theoretical density, while samples pressed at 500 MPa gave a density of 2.645 which produces a theoretical density of 98.4%.
3. Tensile properties of Alumix 321 PM alloy were compared to the standard properties established by a commercial 601AB alloy. The tensile properties of Alumix 321 were comparable to the 601AB alloy, except the percentage of elongation that showed lower values than the standard 601AB alloy.
4. SEM and EPMA proved the presence of iron containing particles in both T1 and T6 Alumix PM Samples as well as in the wrought AA6061.
5. Hot rolling was performed successfully; the percentage of reduction was 27%. Density changed from 2.5895 g/cc to 2.6658 g/cc which produces a theoretical density of 99.01%. Hardness changed from 30 HRE to 53 HRE in T1 temper and from 93 HRE to 106 HRE in T6. Hot swaging was performed successfully on Alumix 321 PM alloy. Density changed from 2.485 g/cc to 2.673 g/cc which produces a theoretical density of 99.39. Hardness was also improved in both T1 and T6 as a result of swaging; theoretical density improves from 92.41 to 99.39 and hardness from 88 HRE to 96 HRE. On contrary, sizing produced smaller amounts of deformation than hot rolling and swaging and was kept between 3-5 %. Shot peening was used as a surface modification technique. Shot peening

has a noticeable effect on the microstructure and average equivalent roughness.

6. Corrosion behaviour of AA6061-T6 was studied. Corrosion parameters recorded were, E_{OCP}=-0.736 V/SCE, E_{corr}=-0.714 V/SCE, I_{corr}=1.77E-06 A/cm^2, E_{pit} = -0.714 V/SCE, Erep=-1.039 V/SCE, C_R=19X10^{-3} mmpy. The main corrosion mechanism observed for AA6061 alloy was pitting corrosion. Iron rich particles that contain Al and Si found to work as a pitting initiation sites. Two mechanisms of pitting were observed, hemispherical, and crystallographic pitting.
7. Stabilization time during open circuit potential experiments for Alumix 321 PM alloy was much longer than wrought AA6061 alloy. Alumix 321 PM samples pressed at 200, 300, 400, and 500 MPa show similar trend. However, ranking the corrosion current of these alloys based on the density was not clear. Samples pressed at 100 MPa show continuous drop in the OCP, more negative corrosion potential and the highest corrosion current which was 1X10^{-5} A/cm^2.
8. Two characteristic values were indicated for all Alumix 321 PM samples using cyclic polarization. The points are pitting and repassivation potential which were further confirmed by using potentiostatic technique. Stair case polarization did not show clear trend on how pressing pressure affects the corrosion current.
9. The effect of pressing pressure on the microstructure was very clear. Samples pressed at 100 MPa show different microstructure and consequently different corrosion mechanism than the samples pressed between 200-500 MPa, the difference in corrosion mechanism was clearly proven by the electrochemical experiments.
10. Comparing to AA6061 wrought alloy, Alumix 321 PM alloy corroded samples show pitting, crevice and intergranular corrosion. However, wrought AA6061 shows only pitting corrosion. On the other hand, for both systems wrought and PM alloys, iron rich particles work as a pitting initiation sites. The only different observation is the migration of these particles to the grain boundaries in the

case of the Alumix 321 PM alloy; this observation was not seen in the case of wrought AA6061.

11. Hot swaging improves the corrosion resistance of Alumix 321 PM alloy. Corrosion current decreases from 6.56E-06 A/cm^2 to 6.4E-07 A/cm^2 as a result of swaging, while corrosion potential increases from -0.947 V/SCE to -0.745 V/SCE. Stair step polarization results show that hot swaging produces better pitting resistance. Hot rolled samples show almost the same OCP before and after rolling. Although corrosion current decreases by rolling from 4.5180E-06 A/cm^2 to 8.4763 E-07 A/cm^2. This value was even lower than that of wrought AA6061 alloy. Hot rolling does not show very much affect on corrosion potential. Similar to the other corrosion parameters, stair step polarization did not show clear difference in pitting potential as a result of hot rolling.
12. Shot peening surface treatment produces a deformed surface layer and a dimple type microstructure, as a result of the peening process roughness increases from 0.033 µm to 3.95 µm. Shot peening samples show more negative OCP than sintered samples. Shot peening reduces the corrosion current from 7.86E-06 A/cm^2 to 3.2069E-07 A/cm^2, the corrosion current after shot peening was lower than the value recorded for the wrought AA6061 alloy. Pitting potential of Shot peened samples was higher than samples before peening. Stair step polarization indicates better pitting resistance after peening comparing to the as sintered samples. Similar to the other Alumix 321 PM samples, pitting, crevice, and intergranular corrosion mechanisms were observed in the peened corroded samples.
13. Alumix 321 PM samples pressed and sized at lower pressure show a less negative potential. The OCP of the samples pressed at 100 MPa and sized at 50 MPa increases from -0.923 V/SCE to -0.878 V/SCE. Corrosion potential follows the same trend. Contrary, samples pressed and sized at higher pressure show more negative potential for both OCP and E_{corr} after sizing. All the sized samples show more negative pitting potential using cyclic polarization. Similarly, more

negative pitting potential was recorded using the stair step polarization. Despite the pressing and sizing pressure, sizing decreases the corrosion current and similar corrosion mechanisms to other Alumix 321 PM samples were observed.

14. Resin impregnation was applied successfully on Alumix 321 PM samples. OCP moves to more positive values. Corrosion current decreases as a result of the resin impregnation from 7.0228E-06 A/cm^2 to 2.5786E-06 A/cm^2 after impregnation. As a result of impregnation, pitting potential became more negative, pitting potential of Alumix 321 PM alloy was recorded to be -0.739 V/SCE before impregnation and it was recorded to be -0.677 V/SCE after impregnation. The repassivation potential of the impregnated samples was more negative compared to the samples before impregnation.

15. Stair step polarization was applied successfully. The results obtained indicated that this technique can be applied to bridge the gap between classical immersion and electrochemical corrosion experiments.

REFERENCES

1. E. Ghali, *Corrosion Resistance of Aluminum and Magnesium Alloys; Understanding, Performance, and Testing,* Hoboken, New Jersey: John Wiley & Sons, 2010.
2. I. Polmear J, *Light Alloys; from Traditional Alloys to Nanocrystals,* Linacre House, Jordan Hill, Oxford OX2 8DP: Butterworth-Heinemann, 2006.
3. R. Cayless B, *Metals Handbook,* Materials Park, OH, USA: ASM international, 1990.
4. J. R. Pickens, Techniques for assessing the corrosion properties of aluminum powder metallurgy alloys, Presented at Rapidly Solidified Powder Aluminum Alloys: A Symposium, Philadelphia, Pa, 4-5 April 1984, pp. 381-409. 1986.
5. E. W. James, *ASM Metals Handbook,* Metals Park, Ohio 44073, USA: American Society of Metals, 1984.
6. J. R. Pickens, Aluminum powder metallurgy technology for high-strength applications, *J. Mater. Sci. 16(6),* pp. 1437-1457. 1981.
7. R. M. German, *Powder Metallurgy Science,* 105 College Road East, Princeton, New Jersy, USA: Metal powder industrial federation, 1994.
8. R. M. German, *Powder Metallurgy & Particulate Materials Processing,* 105 College Road East, Princeton, New Jersy: metal powder industrial federation, 2005.
9. S. J. Kang, *Sintering: Densification, Grain Growth, and Microstructure,* Amesterdam: Elsevier, 2005.
10. R. N. Lumley, Surface oxide and the role of magnesium during the sintering of aluminum, *Metallurgical and Materials Transactions .A, Physical Metallurgy and Materials Science 30(2),* pp. 457-463. 1999.
11. G. B. Schaffer, Powder processed aluminum alloys, *Mater Forum 28*pp. 65-74. 2004.

12. M. Youseffi, Sintering and mechanical properties of prealloyed 6061 al powder with and without common lubricants and sintering aids, *Powder Metallurgy 49(1),* pp. 86-95. 2006.
13. G. Sutradhar, Closed die axisymmetric forging of sintered aluminum preforms, *J. Mater. Process, Technol. 68(1),* pp. 19-22. 1997.
14. J. Park, An experimental study on the optimization of powder forging process parameters for an aluminum-alloy piston, *J. Mater. Process. Technol, 113(1),* pp. 486-492. 2001.
15. A. Bose and W. B. Eisen, *Hot Consolidation of Powders & Particulate,* 105 College Road East, Princeton, New jersy, USA: Metal powder industries federation, 2003.
16. ASTM standard B243-10, *Standard Terminology of Powder Metallurgy,* West conshohocken, PA: ASTM international, 2010.
17. U. Zupanc, Effect of pitting corrosion on fatigue performance of shot-peened aluminum alloy 7075-T651, *J. Mater. Process. Technol, 210(9),* pp. 1197-1202, 2010.
18. O. Linen, The effects of sintering and shot peening processes on the fatigue strength, *Materialwissenschaft Und Werkstofftechnik 41(4),* pp. 202-212, 2010.
19. J. R. Davis, ASM International, Handbook Committee, *Metals Handbook* (Desk ; 2 ed.) 1998.
20. V. S. Sastri, E. Ghali and M. Elboujdainui, *Corrosion Preventation and Protection Practical Solutions,* Southern Gate, Chchester, West Sussex PO19 8SQ, England: John Wiley & Sons, Ltd, 2007.
21. J. R. Davis, *Corrosion: Understanding the Basics, ASM International,* Materials Park, OH 44073-0002, 2000.
22. W. D. Callister and D. G. Rethwisch, *Materials Science and Engineering: An Introduction* (8th ed.) 111 River street, Hoboken, NJ, USA, John Wiley & Sons Ltd, 2010.
23. D. A. Jones, *Principles and Prevention of Corrosion* (2nd ed.), Prentice Hall, Upper Saddle River, NJ, 1996.

24. P. A. Christensen and A. Hamnett, *Techniques and Mechanisms in Electrochemistry* (1st ed.), Blackie Academic & professional, London; New York, 1994.
25. M. Noel and K. Vasu, *Cyclic Voltammetry and the Frontiers of Electrochemistry,* 1990.
26. Princeton applied research, A review of techniques for electrochemical analysis, Application note E-4.
27. A. J. Bard and L. R. Faulkner, *Electrochemical Methods : Fundamentals and Applications, John Wiley & Sons Ltd, New York,* 1980.
28. P. Marcus and F. Mansfeld, *Analytical Methods in Corrosion Science and Engineering, CRC/Taylor & Francis, Boca Raton, Fla,* 2006.
29. J. Koryta, J. Dvořák and L. Kavan, *Principles of Electrochemistry, John Wiley & Sons Ltd, Chichester, New York,* 1993.
30. J. R. Davis, *Corrosion of Aluminum and Aluminum Alloys, ASM International, Materials Park, OH 44073, USA, 1999*.
31. P. R. Roberge, *Corrosion Engineering: Principles and Practice, McGraw Hill, New York,* 2008.
32. K. Srinivasa Rao, Pitting corrosion of heat-treatable aluminum alloys and welds: A review, *Transactions of the Indian Institute of Metals 57(6),* pp. 593-610, 2004.
33. K. P. Wong, Local chemistry and growth of single corrosion pits in aluminum, *J. Electrochem. Soc, 137(10),* pp. 3010-15, 1990.
34. Z. Szklarska-Smialowska, Pitting corrosion of aluminum, *Corros. Sci, 41(9),* pp. 1743-1767, 1999.
35. D. W. Buzza, Growth of corrosion pits on pure aluminum in 1M NaCl, *J. Electrochem. Soc, 142(4),* pp. 1104-1104, 1995.
36. A. Betts and L. Boulton, Crevice corrosion: Review of mechanisms, modelling, and mitigation, *Br. Corros. J. 28(4),* pp. 279-295, 1993.
37. M. Baumgärtner and H. Kaesche, The nature of crevice corrosion of aluminum in chloride solutions, *Materials and Corrosion 39(3),* pp. 129-135, 1988.

38. R. Baboian, *Corrosion Tests and Standards: Application and Interpretation, ASTM International, West Conshohocken, Pa,* 2005.
39. A. Ul-Hamid, CORROSION REPORT-electrochemical behaviour of al alloys in aerated and deaerated NaCl solution, *Corros. Prev. Control 48(4),* pp. 151, 2001.
40. P. Trzaskoma, E. McCafferty and C. Crowe, Corrosion behavior of SiC⁄ al metal matrix composites, *J. Electrochem. Soc. 130,* pp. 1804, 1983.
41. D. M. Aylor, Pitting corrosion behavior of 6061 aluminum alloy foils in sea water, *J. Electrochem, Soc. 133(5),* pp. 949-51, 1986.
42. C. Blanc and G. Mankowski, Susceptibility to pitting corrosion of 6056 aluminum alloy, *Corros. Sci. 39(5),* pp. 949-959, 1997.
43. R. Buchheit, R. Grant, P. Hlava, B. McKenzie and G. Zender, Local dissolution phenomena associated with S phase (Al2CuMg) particles in aluminum alloy 2024-T3, *J. Electrochem. Soc, 144(8),* pp. 2621-2627, 1997.
44. N. Birbilis and R. Buchheit, Electrochemical characteristics of intermetallic phases in aluminum alloys, *J. Electrochem. Soc, 152*pp. B140, 2005.
45. B. Shaw, M. McCosby, A. Abdullah and H. Pickering, The localized corrosion of al 6XXX alloys, *JOM Journal of the Minerals, Metals and Materials Society 53(7),* pp. 42-46, 2001.
46. R. Buchheit, A compilation of corrosion potentials reported for intermetallic phases in aluminum alloys, *J. Electrochem. Soc, 142*pp. 3994, 1995.
47. M. H. Larsen, J. C. Walmsley, O. Lunder, R. H. Mathiesen and K. Nisancioglu, Intergranular corrosion of copper-containing AA6xxx AlMgSi aluminum alloys. *J. Electrochem. Soc, 155*pp. C550, 2008.
48. M. H. Larsen, J. C. Walmsley, O. Lunder and K. Nisancioglu, Effect of excess silicon and small copper content on intergranular corrosion of 6000-series aluminum alloys, *J. Electrochem. Soc, 157*pp. C61, 2010.
49. F. Eckermann, T. Suter, P. J. Uggowitzer, A. Afseth and P. Schmutz, Investigation of the exfoliation-like attack mechanism in relation to al-mg-si alloy microstructure, *Corros. Sci, 50(7),* pp. 2085-2093, 2008.

50. F. Eckermann, T. Suter, P. J. Uggowitzer, A. Afseth, M. Stampanoni, F. Marone and P. Schmutz, In situ microtomographically monitored and electrochemically controlled corrosion initiation and propagation in AlMgSi alloy AA6016, *J. Electrochem. Soc, 156*pp. C1, 2009.
51. J. Park, C. Paik, Y. Huang and R. Alkire, Influence of fe-rich intermetallic inclusions on pit initiation on aluminum alloys in aerated NaCl, *J. Electrochem. Soc,146*pp. 517. 1999.
52. A. Aballe, M. Bethencourt, F. J. Botana, M. Marcos and J. M. Sánchez-Amaya, Influence of the degree of polishing of alloy AA 5083 on its behaviour against localized alkaline corrosion, *Corros. Sci, 46(8),* pp. 1909-1920, 2004.
53. A. M. Bastaweesy, Effect of surface finish on the corrosion characteristics of 6061-T 6-al-alloy in saline waters, *Bulletin of Electrochemistry.Karaikudi 11(9),* pp. 412-417, 1995.
54. W. Badawy, F. Al-Kharafi and A. El-Azab, Electrochemical behaviour and corrosion inhibition of al, al-6061 and al-cu in neutral aqueous solutions, *Corros. Sci. 41(4),* pp. 709-727, 1999.
55. W. A. Badawy and F. M. Al-Kharafi. The inhibition of the corrosion of al, al-6061 and al-cu in chloride free aqueous media: I. passivation in acid solutions, *Corros. Sci. 39(4),* pp. 681-700, 1997.
56. J. Datta, C. Bhattacharya and S. Bandyopadhyay, Influence of cl-, br-, NO 3-and SO 4 2-ions on the corrosion behaviour of 6061 al alloy, *Bull. Mater. Sci. 28(3),* pp. 253-258, 2005.
57. H. Allachi, F. Chaouket and K. Draoui, Protection against corrosion in marine environments of AA6060 aluminum alloy by cerium chlorides, *J. Alloys Compounds 491(1-2),* pp. 223-229, 2010.
58. A. Sameljuk, O. Neikov, A. Krajnikov, Y. V. Milman and G. Thompson, Corrosion behaviour of powder metallurgical and cast al-zn-mg base alloys, *Corros. Sci. 6(1),* pp. 147-158, 2004.

59. A. Sameljuk, O. Neikov, A. Krajnikov, Y. V. Milman, G. Thompson and X. Zhou, Effect of rapid solidification on the microstructure and corrosion behaviour of al-zn-mg based material, *Corros. Sci. 49(2),* pp. 276-286, 2007.
60. S. Sunada, N. Nunomura and K. Majima, Corrosion behavior of 6000 series aluminum alloys produced by conventional and powder extruded process through electrochemical impedance method, Materials Science Forum. 654-656. pp 1964-1967, 2010.
61. J. McIntyre, R. Garrett and R. Conrad, Pitting corrosion behavior of powder metallurgy mechanically alloyed IN-9052, *Metallurgical and Materials Transactions A 22(4),* pp. 938-941, 1991.
62. O. Vanegas, I. Castro, W. Barona and H. Sanchez Sthepa, Mechanical and chemical behavior of sintered 6061 powder aluminium alloy reinforced with CuAl2 particles, *Physica Status Solidi (c) 4(11),* pp. 4145-4150, 2007.
63. S. Majado, A. Morales, J. Torralba, ,Corrosion resistance of powder metallurgical 2124 aluminum alloys in saline aqueous solution, *The European Corrosion Congress,* Lisbon, Portugal, 4-8 September 2005, 2005.
64. D. Bishop, J. Cahoon, M. Chaturvedi, G. Kipouros and W. Caley, On enhancing the mechanical properties of aluminum P/M alloys, *Materials Science and Engineering A 290(1-2),* pp. 16-24, 2000.
65. L. Christodoulou, J. Gordon and J. Pickens, Effect of co content on the stress-corrosion cracking behavior of 7091-type aluminum powder alloys, *Metallurgical and Materials Transactions A 16(5),* pp. 945-951, 1985.
66. E. Lunarska, Pitting corrosion of powder metallurgy AlZnMg alloys, *Corrosion 43(6),* pp. 219-228, 1987.
67. M.J. Topolski, V. Agarwala, M. J. koczak, Electrochemical and microstructural characteristics of 7000 and 3000 series powder metallurgy aluminum alloys, The *13th National SAMPE Technical Conference, Society of aerospace material and process engineers, Covina, Calif,* pp. 559-570, 1981.

68. S. Sanchez-Majado, J. M. Torralba and A. Jiménez-Morales, Assessment of the corrosion behavior of a sintered al-cu-mg alloy in aeronautical environments as a function of the heat treatment, Presented at Materials Science Forum, 2007.
69. P. Searson and R. Latanision, The corrosion and oxidation resistance of iron-and aluminium-based powder metallurgical alloys, *Corros. Sci. 25(10),* pp. 947-968, 1985.
70. MPIF Standard, Test Methods for Metal Powders and Powder Metallurgy Products, MPIF, Princeton, New Jersey, 1999.
71. MPIF Standard 15, Determination of Green Strength for Unsintered Compacted Powder Metallurgy Materials, MPIF, Princeton, New Jersey, 1997.
72. MPIF Standard 10, Determination of the tensile Properties of Powder Metallurgy Materials, MPIF, Princeton, New Jersey, 2000.
73. Ecka Alumix 321, *Metal Powder Technology*, A technical brochure from Ecka granules, herr Hans-Claus Neubing, D-91235 Velden, Germany,
74. ASM Handbook. *Vol 13, Corrosion, ASM international, Materials Park, OH,* 1987.
75. B. Zaid, Effects of pH and chloride concentration on pitting corrosion of AA6061 aluminum alloy, *Corros. Sci, 50(7),* pp. 1841-7, 2008.
76. A. Standard. G102-89, *Calculation of Corrosion Rates and Related Information from Electrochemical Measurements, Annual Book of ASTM Standards, ASTM International, West Conshohocken, PA,* 2004.
77. Z. Ahmad, A review of corrosion and pitting resistance of al 6061 and 6013 silicon carbide composites in neutral salt solution and seawater, *Corr. Rev. 19(2),* pp. 119-156, 2001.
78. G. E. Kiourtsidis, Pitting corrosion of artificially aged T6 AA2024/SiC_p composites in 3.5wt.% NaCl aqueous solution, *Corros. Sci, 49(6),* pp. 2711-25, 2007.
79. NACE/ASTM, ASTM NACE/ASTMG193-11a standard terminology and acronyms relating to corrosion, *ASTM International, West Conshohocken, PA, 2010.*

80. D. Sun, Y. Jiang, Q. Xiang, C. Zhong, J. Gong, L. Zhang and J. Li, Ex situ TEM observation of localized attack on AA 6061, *Materials and Corrosion 61(2),* pp. 105-110, 2010.
81. F. Birol and Y. Birol, Corrosion behavior of twin-roll cast al-mg and al-mg-si alloys, 9th International conference on aluminum alloys, 4-8 August, Brisbane, Australia, 2004.
82. Y. L. Cheng, Study of the potential electrochemical noise during corrosion process of aluminum alloys 2024, 7075 and pure aluminum, *Materials and Corrosion, 54(8),* pp. 601, 2003.
83. M. Dlapka, Defining the pores in PM components, *Metal Powder Report 65(2),* pp. 30, 2010.
84. K. H. W. Seah, The influence of pore morphology on corrosion, *Corros. Sci. 40(4),* pp. 547, 1998.
85. L. Fedrizzi, Corrosion mechanisms of an AISI type 316L sintered stainless steel in sodium chloride solution, *Materials and Corrosion 42(8),* pp. 403, 1991.
86. H. Hack, Potentiostatic technique for corrosion studies, presented at corrosion 85, March 25-29, Boston, USA, 1985.

APPENDIX A- CHEMICAL COMPOSITION

Table A-1 Chemical composition of Alumix 321 raw powder.

Element	Composition (mg/kg)
Ag	<2
Al (Measured)	966988
Al (By Difference)	980882
As	44
Ba	<2
Be	<2
Bi	130
Ca	45
Cd	<5
Co	1
Cr	5
Cu	3179
Fe	952
K	<20
Li	<5
Mg	13089
Mn	18
Mo	7
Na	34
Ni	66
P	<100
Pb	19
S	17
Sb	<100
Se	<100
Si	5000
Sn	322
Sr	<1
Te	<10
Ti	34
Tl	<100
V	108
Zn	45
Zr	12

Table A-2 Chemical composition of AA6061.

Element	Composition (mg/kg)
Ag	0.1
Al (Measured)	996154
Al (By Difference)	976026
As	<10
Ba	5
Be	<1
Bi	185
Ca	56
Cd	<5
Co	<5
Cr	708
Cu	3038
Fe	3417
K	<20
Li	<5
Mg	9311
Mn	314
Mo	8
Na	36
Ni	61
P	<100
Pb	66
S	<10
Sb	<100
Se	<100
Si	6090
Sn	<100
Sr	<1
Te	<100
Ti	137
Tl	<100
V	84
Zn	447
Zr	10

APPENDIX B-EPMA DATA

Table B-1 EPMA of speciifc areas within the microstructure of AA6061-T6.

Material	Mg	Al	Cu	Si	Fe	Ag	Total
Matrix 1	0.665	94.461	0.226	0.586	0.022	0	95.96
Matrix 2	0.644	93.299	0.222	0.542	0.009	0	94.716
Matrix 3	0.63	93.651	0.212	0.606	0.008	0	95.107
Irregular Fe particle 1	1.215	75.505	0.793	2.953	8.726	0	89.192
Irregular Fe particle 2	1.906	72.467	1.159	4.066	14.082	0	93.68
Irregular Fe particle 3	0.905	78.696	0.87	3.009	9.373	0	92.853
Circular particles 1	1.208	80.821	0.577	1.91	5.377	0	89.893
Circular particles 2	1.033	82.895	0.501	1.438	3.632	0	89.499
Circular particles 3	1.027	82.876	0.463	1.557	3.99	0	89.913
Black particles	12.736	75.812	0.373	11.252	1.986	0	102.159

Table B-2 EPMA of speciifc areas within the microstructure of Alumix 321-T1

Material	Mg	Al	Cu	Si	Fe	Ag	Total
Matrix 1	0.467	95.752	0.266	0.39	0.011	0	96.886
Matrix 2	0.578	95.545	0.229	0.406	0.011	0	96.769
Matrix 3	2.086	85.837	0.684	2.246	5.236	0	96.089
White Irregular particle 1	2.34	84.255	0.819	2.491	6.087	0	95.992
White Irregular particle 2	2.974	68.534	1.378	3.524	8.159	0	84.569
White Irregular particle 3	1.117	84.226	1.043	2.476	6.323	0	95.185
White round particles 1	*4.983*	*79.129*	1.056	3.636	5.239	0	94.043
White round particles 2	*7.898*	*75.199*	0.192	3.298	0.01	0	86.597
White round particles 3	2.614	63.815	2.496	6.395	19.795	0	95.115

Table B-3 EPMA of specific areas within the microstrcuture of Alumix 321-T6.

Material	Mg	Al	Cu	Si	Fe	Ag	Total
Matrix 1	0.76	98.587	0.187	0.537	0.012	0	100.083
Matrix 2	0.734	98.812	0.255	0.475	0.046	0	100.322
Matrix 3	0.729	98.757	0.221	0.474	0.006	0	100.187
Irregular particle 1	2.088	68.331	1.446	5.484	19.96	0	97.309
Irregular particle 2	1.292	89.705	0.846	3.239	10.387	0	105.469
Irregular particle 3	1.904	76.672	1.22	4.411	15.968	0	100.175
Round particles 1	1.708	69.573	1.234	4.338	15.103	0	91.956
Round particles 1	1.887	88.712	0.751	2.821	8.324	0	102.495
Round particles 1	0.771	90.598	0.209	0.834	0.053	0	92.465
Round black particles 1	3.947	90.115	0.259	0.467	0.029	0	94.817
Round black particles 2	0.705	93.286	0.221	0.556	0	0	94.768
Round black particles 3	2.91	86.286	0.25	0.512	0.003	0	89.961

APPENDIX C-EDS CHARTS

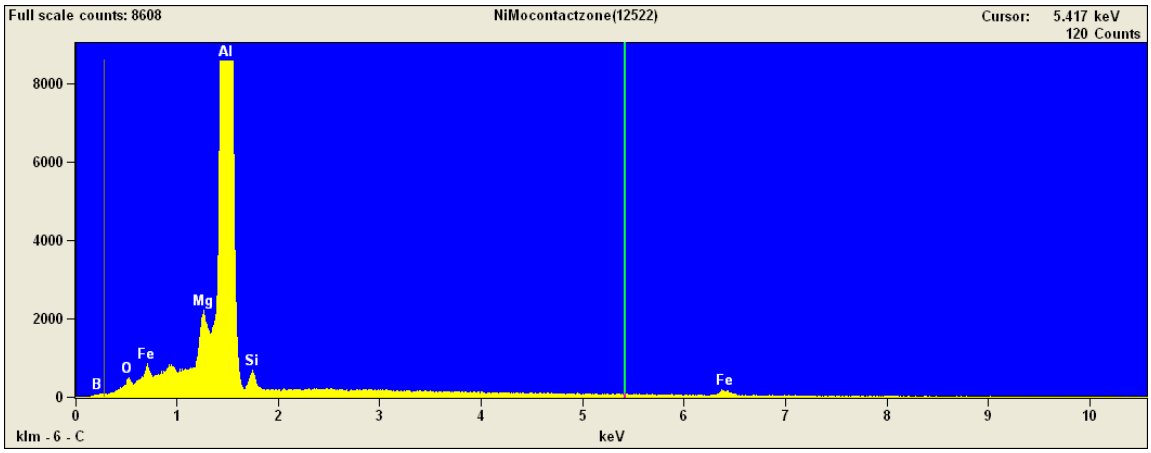

Figure C-1 EDS spectrum of gray spherical particle in AA6061-t6 alloy.

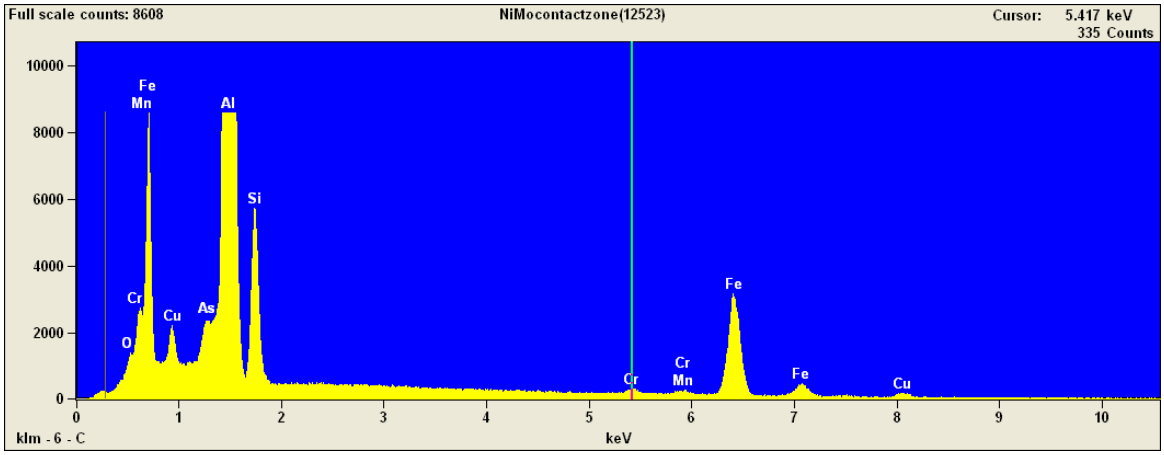

Figure C-2 EDS of white Chinese script particle in AA6061-T6 alloy

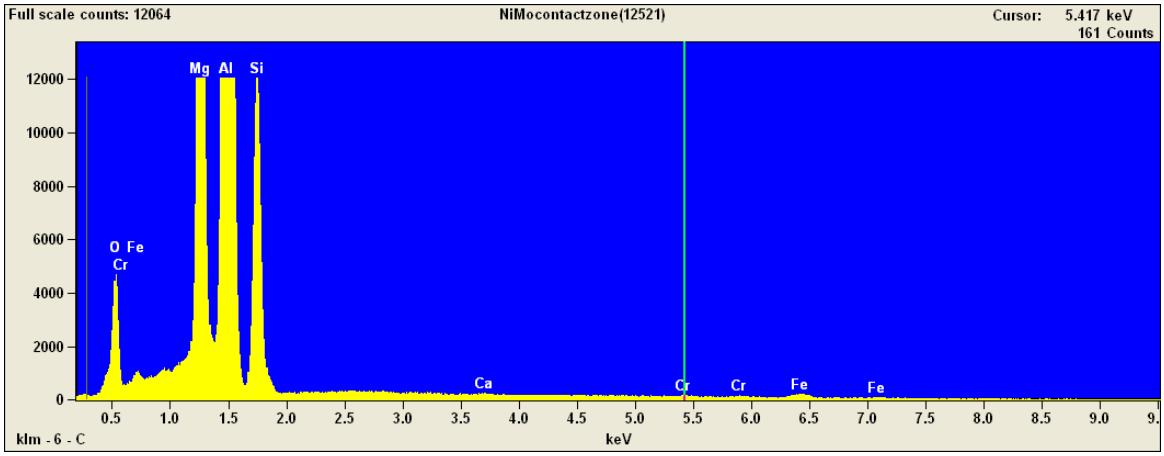

Figure C-3 EDS of black particle in AA6061-T6 alloy.

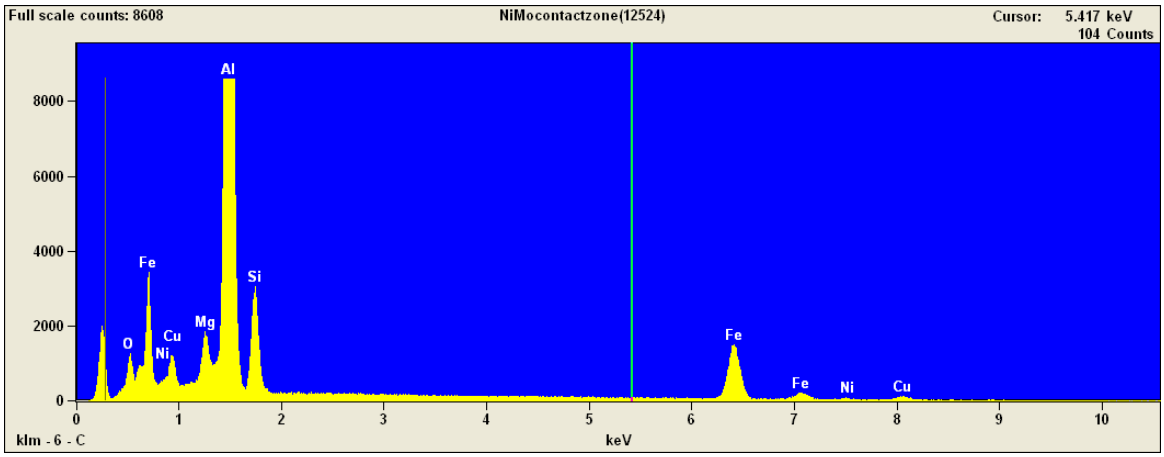

Figure C-4 EDS spectrum of white irregular particle in Alumix 321-T6 alloy.

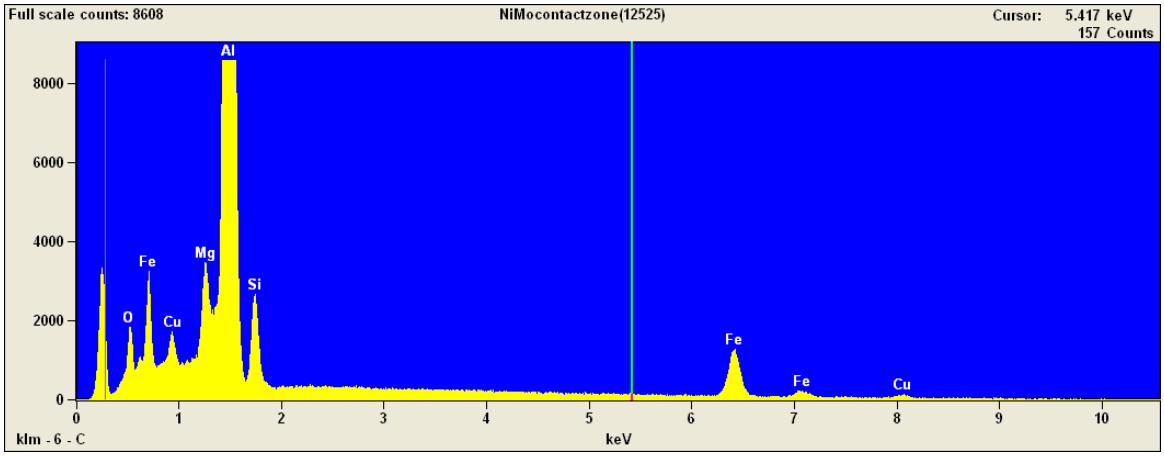

Figure C-5 EDS spectrum of elongated white particle in Alumix 321-T6 alloy.

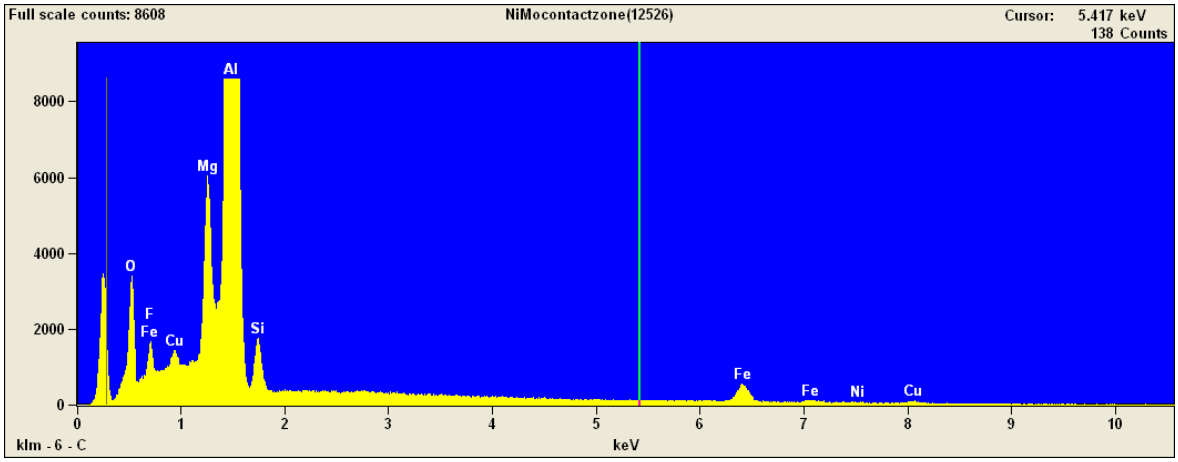

Figure C-6 EDS spectrum of small gray particle in Alumix 321-T6 alloy.

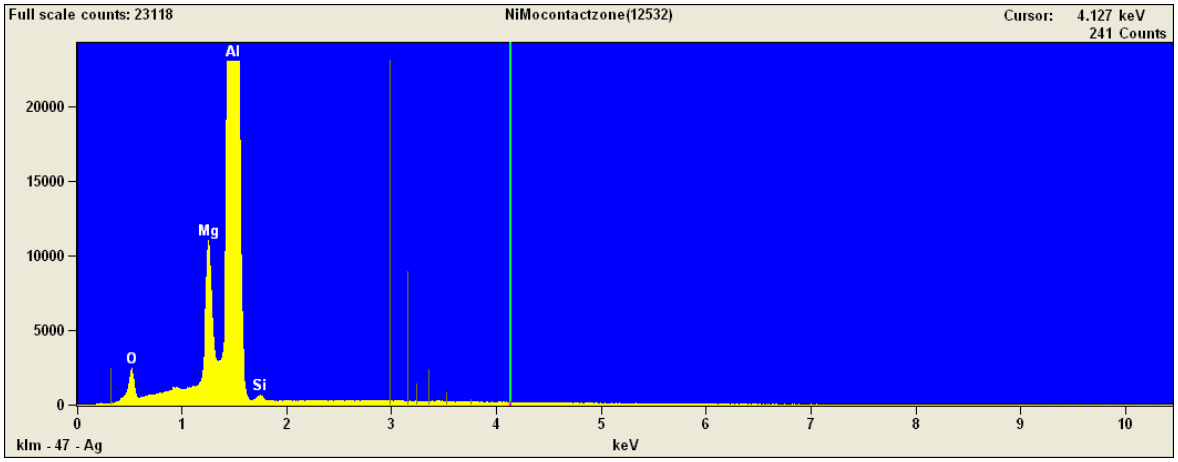

Figure C-7 EDS spectrum of black spherical particle in Alumix 321-T6 alloy.

APPENDIX D-SINTERING PROFILE OF ALUMIX 321PM ALLOY

Table D-1 Dimensional variation, mass variation, and sintered density of Alumix 321 PM alloy.

Material	No	Δ OAL%	Δ W %	Δ L%	Δ M %	DENSITY (g/cc)
-Alumix 321	33	-0.024980016	-0.055083	0	-1.19771863	2.458107109
-TRS	34	0.43493476	0.0707992	0.598425197	-1.17555251	2.444769586
-P=200 MPa	35	0.154567212	0.0078691	-0.251730648	-1.1949962	2.452479412
-T=610 °C	36	0.194397368	0.0865596	-0.125904942	-1.19914603	2.454685906
Alumix 321	37	0.527104542	0.3460208	0.346347607	-1.26592381	2.519026114
-TRS	38	0.418064516	0.1966027	0.157480315	-1.2686128	2.519560594
-P=400 MPa	39	0.718680523	0.2280053	0.157331655	-1.25862121	2.516635926
-T=610 °C	40	0.527895663	0.3224284	0.125865324	-1.26615142	2.520825729
-Alumix 321	17	-0.7383387	-0.51928	-0.50267044	-1.2385	2.48805357
-TRS	18	-0.1646624	-0.16524	-0.06289308	-1.21416	2.471978432
-P=200 MPa	19	-0.2945288	-0.39277	-0.31486146	-1.21349	2.476863779
-T=620 °C	20	-0.379924	-0.48692	-0.03149606	-1.20869	2.478616942
Alumix 321-	21	0.17083398	0.062839	0.094458438	-1.31687	2.529064774
-TRS	22	0.36831457	-0.0157	0.125904942	-1.30909	2.533066157
-P=400 MPa	23	0.25347887	-0.0157	-0.09425071	-1.31028	2.528023681
-T=620 °C	24	0.20172762	0.141565	0.125865324	-1.30524	2.530420023
-Alumix 321	1	-0.60592459	0.0786968	0.377595972	-0.24679763	2.494154772
-TRS	2	-0.68941399	-0.007862	0.157133878	-0.09113214	2.495455546
-P=200 MPa	3	-0.52910052	0.212498	-0.094250707	0.056021849	2.497910137
-T=630 °C	4	-0.60987802	0.1495004	-0.062912866	0.107066381	2.516113598
-Alumix 321	5	-0.518161563	-0.031454	-0.156739812	-1.35022788	2.548219422
-TRS	6	-0.155730897	-0.078623	-0.219642297	-1.33314623	2.54439596
-P=400 MPa	7	-0.124223602	-0.172779	-0.125786164	-1.33377326	2.541576424
-T=630 °C	8	-0.124191462	-0.09428	-0.062952471	-1.34239592	2.542998606
Alumix 321-	25	-4.57764037	-2.21838	-1.225259189	-1.2851646	2.650181246
-TRS	26	-3.63563724	-2.20091	-1.763779528	-1.2831411	2.646372985
-P=200 MPa	27	-3.58106083	-2.10087	-1.040025213	-1.2800896	2.648410506
-T=640 °C	28	-4.0475121	-2.30273	-1.700251889	-1.2778499	2.647978787
Alumix 321-	29	-1.92655338	-1.09277	-0.378071834	-1.3427907	2.641027937
-TRS	30	-1.98963731	-1.38932	-0.409836066	-1.3321865	2.64143081
-P=400 MPa	31	-2.00794921	-1.11556	-0.409706902	-1.3182731	2.632217008
-T=640 °C	32	-1.96291131	-0.99057	-0.662042875	-1.3425431	2.64245825

Table D-2 Hardness of Alumix 321 PM alloy as a function of pressure and sintering

Material	Temper	Sample No	Side 1	Side 2	Side 1	Side 2	Average Hardness (HRE)
Alumix 321 -TRS -P=200 MPa -T=610 °C	**T1**	35	23.8	17.8	18.7	15.7	**18.8625**
		36	20.9	17.2	20.8	16	
	T6	33	87.7	84	81.4	90.3	**81.3875**
		34	76.8	74.2	81.5	75.2	
Alumix 321 -TRS -P=400 MPa -T=610 °C	**T1**	39	22.6	26.2	30.2	22.7	**27.175**
		40	31.9	29.8	27.1	26.9	
	T6	37	94.5	85.2	87.4	81.9	**87.05**
		38	84.4	88.9	90.3	83.8	
Alumix 321 -TRS -P=200 MPa -T=620 °C	**T1**	19	30.9	22.1	18.8	22.8	**22.575**
		20	23.6	20.3	19.2	22.9	
	T6	17	82.5	85.4	83.6	90.2	**84.675**
		18	82.7	81.2	88.9	82.9	
Alumix 321 -TRS -P=400 MPa -T=620 °C	**T1**	23	25.2	27	27.6	26	**27.4**
		24	27.6	26.6	31.7	27.5	
	T6	21	85.4	84.8	88.3	84.3	**86.2375**
		22	89.1	85.9	87.3	84.8	
Alumix 321 -TRS -P=200 MPa -T=630 °C	**T1**	11	35	36.3	34.7	31	**37.0625**
		12	38.6	39.7	41.6	39.6	
	T6	9	96.8	96.7	94.1	96.1	**92.0125**
		10	90.9	86.3	86.2	89	
Alumix 321 -TRS -P=400 MPa -T=630 °C	**T1**	15	33.4	32	26.3	32.3	**32.0375**
		16	37.2	33.7	34.8	26.6	
	T6	13	62.8	89.6	90.7	92.7	**87.725**
		14	89.1	92.2	91.8	92.9	
Alumix 321 -TRS -P=200 MPa -T=640 °C	**T1**	27	46.5	48.7	47.7	46.5	**47.4125**
		28	46.7	47.1	49	47.1	
	T6	25	98.8	98.1	97.2	97.8	**98.9625**
		26	97.4	105	99.7	97.7	
Alumix 321 -TRS -P=400 MPa -T=640 °C	**T1**	31	42.1	43.1	43.9	43.4	**43.4625**
		32	45.4	44.5	40.1	45.2	
	T6	29	96	96.9	97.9	101.1	**98.925**
		30	102.8	101.5	96.7	98.5	